Barrels, jets and smoke-rings: Understanding the bizarre shapes of radio supernova remnants

Bryan Malcolm Gaensler

A thesis submitted for the degree of
Doctor of Philosophy
at the
University of Sydney

February 1999

To Dr Michael Bishop,

For showing me where to start

Abstract

This thesis considers the various morphologies of radio supernova remnants (SNRs), and attempts to determine whether their appearance results from the properties of the progenitor star and its supernova explosion, or from the structure of the interstellar medium (ISM) and ambient magnetic field into which a SNR consequently expands. High-resolution observations of Supernova 1987A show a young remnant whose appearance and evolution are completely dominated by the structure of its progenitor wind. A statistical study of the Galactic population of bilateral SNRs demonstrates that the symmetry axes of these remnants run parallel to the Galactic Plane. This result can be explained by the interaction of main sequence stellar wind-bubbles with the ambient magnetic field; expansion of SNRs into the resulting elongated cavities results in a bilateral appearance with the observed alignment. Radio observations of SNR G296.8–00.3 show a double-ringed morphology which is best explained by expansion either into an anisotropic main-sequence progenitor wind or into multiple cavities in the ISM. Data on SNRs G309.2–00.6 and G320.4–01.2 (MSH 15–5*2*) make a strong case that the appearance of both remnants is significantly affected by collimated outflows from a central source; for G309.2–00.6 the source itself is not detected, but for G320.4–01.2 there is now compelling evidence that the remnant is associated with and is interacting with the young pulsar PSR B1509–58. I conclude that, while the youngest SNRs are shaped by their progenitor's circumstellar material, the appearance of most SNRs reflects the properties of the local ISM and magnetic field. Remnants which interact with an associated pulsar or binary system appear to be rare, and are easily distinguished by their unusual and distorted morphologies.

"And now I understand the supernova scene, Oh-a-oh"

— "Video Killed The Radio Star"
The Presidents Of The United States Of America, 1998.

Acknowledgements

It's hard to believe that after three long years it's all finally over. It was stressful, but it was lots of fun too. Ever since I was young I've enjoyed talking to people and asking lots of questions, and nothing has changed. So not surprisingly, an enormous number of people have all played some part in helping me get here.

The biggest thanks must go to my two supervisors, Anne Green and Dick Manchester. Anne has spent the last three years picking me up when I'm in a rut, then keeping my feet on the ground whenever I get carried away. Without her organisation, advice, encouragement and support I could never have made it. Dick is the consummate scientist, and over the course of my thesis has been the one to teach me what research is all about. Our lively debates over scientific issues have been some of the highlights of my candidature, and I'm deeply grateful for the time he has continually put aside for me despite his busy schedule.

Next on the list come the denizens of Room 86, Bob Sault and Neil Killeen. Their stoic endurance of my questions, bug reports and suggestions has been tremendous, and most of what I have learnt about interferometry has been through them. (Special thanks to Neil for some fascinating discourses on the Spice Girls.) Many other people have helped me with data reduction and analysis: I'm particularly grateful to Richard Gooch, Vince McIntyre, Tom Oosterloo and Warwick Wilson for their time and patience. On the scientific side, I've picked everyone's brain I could — special mentions to my collaborators during the course of my thesis: Karen Brazier, Simon Johnston, Mike Kesteven, John Reynolds, Lister Staveley-Smith and Tasso Tzioumis. I also appreciate conversations and correspondence with Lori Allen, Veta Avedisova, Matthew Bailes, Lewis Ball, John Blondin, Michael Burton, Jim Caswell, Roger Chevalier, You-Hua Chu, David Crawford, Froney Crawford, John Dickel, John Dickey, Richard Dodson, Gloria Dubner, Dale Frail, Miller Goss, Andrew Gray, Charlene Heisler, Jeff Hester, Lloyd Higgs, Helen Johnston, Vicky Kaspi, Bärbel Koribalski, Tom Landecker, Denis Leahy, Stuart Lumsden, Doug Milne, David Moffett, Michael Norman, Serge Pineault, Steve Reynolds, Rob Roger, Ray Stathakis, Tony Turtle, Andrew Walker, Mark Walker, Brad Wallace, Mark Wardle and Rosa Williams, all of whose suggestions and ideas ended up in here somewhere. A special mention to Dan Briggs, who did all the hard work on the super-resolution of SN 1987A, and made numerous comments on the text of Chapter 2. Sadly, I never had the opportunity to meet Dan in person: he will be sorely missed.

I have been a frequent visitor to Narrabri, and my trips there have always been a lot of fun. Biggest thanks must go to Chris Forbes, Margaret Guest and Chris Wilson for keeping me well-fed whenever I'm up there, and to Tina Earle, Kylee Forbes and Leona Hardman for regular pick-ups from the airport and train station. Robin Wark endured my endless remote observing runs and taught me most of what I know about the ATCA; now if only I could learn to juggle. Thanks also to Graham Baines, Dave McConnell, Derek McKay, Nuria McKay and Mark Wieringa for dealing with late-night phone calls with good grace, and to all the Duty Astronomers who took their time to support my numerous observing runs.

The ATNF Higher Degree Programme is a fantastic idea, and participating in it has been a very stimulating experience. Thanks must go to all the Epping staff for their time and support. Those not already mentioned include Shaun Amy, Joan Archer, Mark Calabretta, Matthias Ehle, Ron Ekers, Dorothy Goddard, Raymond Haynes, Henrietta May, Ray Norris, Elaine Pacey and Betty Siegman. At the University of Sydney, Ferg Brand, Lawrence Cram, Dick Hunstead, Don Melrose, Gordon Robertson and Elaine Sadler have all given of their time at some stage. Special thanks to Vicky Moore for her tireless efforts in the Physics Library — although she is still yet to convince me that Hercules is better than Xena.

The traumas of a PhD thesis are only bearable because one shares the load with fellow students. The late-night dinners, the gossip sessions and the Friday lunches at the pub are all part of the experience, and I'm grateful for all the friendly faces along the way. Special acknowledgement must go to all those I've shared an office with over the years: David Abbott, Martin Anderson, Sebastian Juraszek, Lucyna Kedziora-Chudczer, Vince McIntyre, Alan McPhail and David Morgan-Mar, and to my buddies Gene ("Super Kiwi") Davidson and Tracy ("Galaxy Girl") Getts. Deepest thanks and love go to Kate ("I'm A Princess") Brooks for our regular rendezvouses at the Indian Home Diner on Oxford Street, and to Tanya ("Me Me Me") Hill for always being there. Other astro types who've made the last few years great fun include Ivan Baldry, Saskia ("Go Aussie / Go Kiwi") Besier, Douglas ("Bloody Disgrace") Bock, Julia Bryant, Martin Bureau, Churnie Churnster, Sonia Cianci, Michelle Doherty, Chris ("Use The Force") Fluke, Lisa Germany, Andrew ("Queenslander") Haigh, Stephen Hardy, Andrew ("The Elephant Man") Hopkins, Sally ("Goldilocks") Houghton, Mel ("Secret Squirrel") Hulbert, Andrew Jacob, Andreas ("Gone Sailing") Kelz, Lisa Kewley, Sung-Eun Kim, Jung-Kyu Lee, Joe Liske, John ("Stuff") McMahon, Brenda Matthews, Andrew Melatos, Daniel ("Choadal Lord") Mortlock, Eileen ("Chicken") O'Hely, Mary Putman, Dave Rayner, Andrew ("Freddie") Reid, Katrina Sealey, Snežana Stanimirović, Ben Stappers, Ann Maree Tabone and Anne Thorsley. Hopefully I haven't left anyone out. Thanks also to the mob at Sydney Observatory — Richard Berry, Andrew Constantine, Jeanie Kitchener, Nick Lomb, Rod Somerville and Geoff Wyatt — all of whom have made sure I remember that astronomy is a lot of fun.

One goes insane thinking only astronomy, and all my friends "on the outside" deserve my deep appreciation for their patience and understanding in putting up with my panic attacks, late nights and crazy schedule. There are too many people to mention them all, but I particularly would like to thank Jonathan Ackerman, Wendy ("I Need Some Coffee") Chung, Graham & Kate Carey, Sam Chambers, Geoff ("Burger Time") Facer, Sean ("Here's Your 20 Cents") Flanagan, Clinton Grant, Catherine ("Get Out Your Diary") Harris, Darryl Hoffman, Brett & Lexie ("Slimy Yet Satisfying") Hooker, Phil & Ayn Hopper, Jen ("Manly Groupie") Howley, Jason Jones, Tara ("Hakuna Matata") Kelly, Ben ("Hold This Diode For Me") Kremer, Astrid ("I Like To Win") Kuchel, Myfi ("I Forgot The Flash") Kuchel, Bob Lang, Susan McMahon, Alex Merchant, Glenn Mitchell, Tanya & David Monro, Mike Morony, Lisa Murray, Heather Patterson, Troy & Kym Phillips, Stephen & Rebecca

Shead, Nick Simpson, Varya Smith, David Tanner, Jess Try, Kelly ("Spice Up Your Life") Tsoi, Jackie Vilensky, Mim Walter, Mike ("Hawaiian Shirt") Winter and Brendon Yenson for all trying to keep me sane. For inspiration and magic moments I thank Jodie Foster, Deborah & Willy, and of course the mighty Manly-Warringah Sea Eagles.

Lastly, I am indebted to my family — thank-you to my extended clan, all of whom have provided much enthusiasm and support for what I've been doing. My brother Adam is everything I'm not, but somehow we click pretty well — thanks for all the crazy conversations, mind-games and music. Finally, my parents kept me clothed and fed for more than twenty years, and, knowingly or not, set me on this career path with one of the first books they ever bought me. Thanks to both of you for everything.

I acknowledge the following sources of funding for travel abroad:

- The Dominion Radio Astrophysical Observatory for assistance in attending The Second Naramata Summer School on the Interstellar Medium in Naramata, Canada in 1996 Aug.
- The Support for Access to Major Research Facilities Programme, administered by the Australian Department of Industry, Science and Tourism, for travel to the VLA in 1996 Sep–Oct.
- The Local Organising Committee, the ATNF, the Astronomical Society of Australia, the Faculty of Science of the University of Sydney and the Astrophysics Department of the University of Sydney for travel to the conference "SN 1987A: Ten Years After" held in La Serena, Chile, in Feb 1997.
- The Science Foundation for Physics within the University of Sydney for travel to the conference "The Evolution of Shell Supernova Remants" held in Minneapolis, USA, in Mar 1997.
- The Local Organising Committee, the Science Foundation for Physics within the University of Sydney, the R. and M. Bentwich Scholarship and the James Kentley Memorial Scholarship for travel to the conference "The Relationship Between Neutron Stars and Supernova Remnants", held in Elba, Italy in Jun 1998.

During my candidature I received the financial support of an Australian Postgraduate Award. I made frequent use of NASA's Astrophysics Data System Abstract Service and of the SIMBAD database, operated at CDS, Strasbourg, France. The Australia Telescope is funded by the Commonwealth of Australia for operation as a National Facility managed by CSIRO. The VLA is part of the National Radio Astronomy Observatory, a facility of the National Science Foundation operated under cooperative agreement by Associated Universities, Inc. This thesis was typeset by the author using the LaTeX document preparation system (Lamport 1994). Most figures were created using the `PGPLOT` Graphics Subroutine Library (Pearson 1997).

Statement of Originality

This thesis describes work carried out in the Department of Astrophysics at the University of Sydney and at CSIRO's Australia Telescope National Facility between 1995 and 1998. Except where otherwise acknowledged, the work presented in this thesis is my own. Significant contributions from other people are as follows:

- Chapter 2: Some observations and data reduction (particularly before 1995) were carried out by other members of the ATNF programme on Supernova 1987A. Current members of this project are Dick Manchester, Lister Staveley-Smith, Tasso Tzioumis, John Reynolds and Mike Kesteven. The *HST* image was supplied by John Krist.
- Chapter 3: Miller Goss and Dale Frail helped with the VLA proposal, scheduling and data reduction. Roy Duncan carried out the observations and reduction associated with the Parkes radio telescope. Various published radio images were supplied by Gloria Dubner, Andrew Gray, Tom Landecker and Mike Kesteven. David Moffett suggested to me the possibility that stellar wind-bubbles might be influenced by the ambient magnetic field.
- Chapter 4: Bärbel Koribalski provided H I data on PSR B1154–62.
- Chapter 5: Andrew Walker carried out and reduced the optical observations. *IRAS* data were supplied by the IPAC HIRES facility, while X-ray data were obtained through the HEASARC Online Service, provided by the NASA/Goddard Space Flight Center.
- Chapter 6: OH observations were carried out by Douglas Bock. *ROSAT* images of G320.4–01.2 were provided by Karen Brazier, Chris Greiveldinger and Silvano Massaglia. Froney Crawford communicated the rotation measure of PSR B1509–58.

Bryan Malcolm Gaensler
Sydney, Australia
February 1999

Publications

Apart from minor changes made for consistency of spelling and style, Chapters 2 through 5 of this thesis are exact reproductions of papers published in refereed journals. Chapter 6 is a slightly longer and more detailed version of a paper to appear in a refereed journal.

- Chapter 2: Gaensler, B. M., Manchester, R. N., Staveley-Smith, L., Tzioumis, A. K., Reynolds, J. E., & Kesteven, M. J., 1997, ApJ, **479**, 845

- Chapter 3: Gaensler, B. M., 1998, ApJ, **493**, 781

- Chapter 4: Gaensler, B. M., Manchester, R. N., & Green, A. J., 1998a, MNRAS, **296**, 813

- Chapter 5: Gaensler, B. M., Green, A. J., & Manchester, R. N., 1998b, MNRAS, **299**, 812

- Chapter 6: Gaensler, B. M., Brazier, K. T. S., Manchester, R. N., Johnston, S., & Green, A. J., 1999, MNRAS, in press

Acronyms, Abbreviations and Conventions

`AIPS`	Astronomical Image Processing System
ASCA	*Advanced Satellite for Cosmology and Astrophysics*
ATCA	Australia Telescope Compact Array
AXAF	*Advanced X-ray Astrophysics Facility*
b	Galactic Latitude
BSG	Blue Supergiant
CSM	Circumstellar Medium
Dec., δ	Declination
DM	Dispersion Measure
erg	Unit of energy: 1 erg $\equiv 10^{-7}$ J
gauss, G	Unit of magnetic flux density: 1 G $\equiv 10^{-4}$ T
FWHM	Full Width at Half Maximum
HST	*Hubble Space Telescope*
IRAS	*Infrared Astronomical Satellite*
ISM	Interstellar Medium
jansky, Jy	Unit of flux density: 1 Jy $\equiv 10^{-26}$ W m^{-2} Hz^{-1}
l	Galactic Longitude
LSR	Local Standard of Rest
$M_\odot$	Unit of mass: 1 $M_\odot \equiv 1$ solar mass $\simeq 1.99 \times 10^{30}$ kg
`MIRIAD`	Multichannel Image Reconstruction Image Analysis and Display
MOST	Molonglo Observatory Synthesis Telescope
NGST	*Next Generation Space Telescope*
parsec, pc	Unit of distance: 1 pc $\simeq 3.09 \times 10^{16}$ m
PA	Position Angle (measured north through east)
PSR	Pulsar
PWN	Pulsar Wind Nebula
RA, α	Right Ascension
RM	Rotation Measure
RMS	Root Mean Square
ROSAT	*Roentgen Satellite*
RSG	Red Supergiant
RSN	Radio Supernova
SKA	Square Kilometre Array
SN(e)	Supernova(e)
SNR	Supernova Remnant
VLA	Very Large Array
VLBI	Very Long Baseline Interferometry
XMM	*X-ray Multi-mirror Mission*

Spectral index: The radio spectral index, α, of a source is defined by $S_\nu \propto \nu^\alpha$, where S_ν is the flux density received at a frequency ν.

Contents

Chapter 1

Introduction

1.1 Preamble

"Guest stars" have been known since antiquity — stars of dazzling brightness which would suddenly intrude on the unchanging sky before fading away over a period of months or even years. Regarded by the ancients as signs or omens, the most energetic of these outbursts are now termed *supernovae* (SNe), and are known to be vast explosions marking the death of stars.

Supernovae might not affect our lives as directly as the ancients believed. Nevertheless, they are a possible trigger for star formation (Öpik 1953; Herbst & Assousa 1977) and are probably the only source in the Universe of all the heavy elements (Burbidge et al. 1957; Cameron 1957) — without them we simply would not be here. SNe also play an important role in cosmology as distance indicators (Kirshner & Kwan 1974; Perlmutter et al. 1998), while their remnants structure and energise the Galaxy's interstellar medium (ISM) (Cox & Smith 1974; Thornton et al. 1998) and are thought to be the origin of cosmic rays of energies up to 100 TeV (Blandford & Ostriker 1978; Koyama et al. 1995).

1.2 Supernovae and Supernova Remnants

There are several different types of SN, classified on the basis of optical spectrum at maximum light (see review by Weiler & Sramek 1988). The main criterion is whether or not hydrogen lines are seen in this spectrum: SNe with no observable hydrogen are classed as Type I, while those with hydrogen are Type II. Further subdivision of Type I SNe into Ia and Ib is based on the presence or lack of silicon absorption respectively (Branch 1986). Type II is subdivided into II-L and II-P based on whether or not the light curve shows a linear (L) or a plateau (P) phase after maximum (Barbon et al. 1979).

The progenitor of a Type Ia SN is thought to be a white dwarf star in a binary system. Such a star accretes mass from its companion, until a critical mass is reached and the star explodes with $\sim 10^{51}$ erg of kinetic energy. The explosion completely

disrupts the star and no compact core remains (Woosley & Weaver 1986). On the other hand, the progenitors of Type Ib and II SNe are thought to be massive stars (heavier than $8M_{\odot}$). The iron core formed by progressive episodes of nuclear fusion eventually collapses under its own weight, releasing $\sim 10^{53}$ erg of gravitational energy in neutrinos. These neutrinos weakly couple to the outer layers of the star, ejecting them at high velocity (Woosley & Weaver 1986). The resulting explosion liberates $\sim 10^{51}$ erg of kinetic energy, while the collapsed core is left behind as a neutron star (Baade & Zwicky 1934). Occasionally, the core is sufficiently massive to collapse further into a black hole (Brown & Bethe 1994).

The rate of SNe in the Milky Way can be estimated from statistics on extragalactic SNe. Current estimates put this rate at one supernova per 30–50 years, of which 80–90% are Type Ib or II (van den Bergh et al. 1987; Tammann et al. 1994; Cappellaro et al. 1997). Because of dust extinction over much of the Galactic Plane, no Galactic supernova has been observed since Kepler's SN of 1604.

The identification of the Crab Nebula (M 1, NGC 1952) as the remnant of the supernova of 1054 (Lundmark 1921; Duyvendak 1942; Mayall & Oort 1942) demonstrated that the expanding remains of SNe could be observed long after the event. Since then, more than 200 Galactic *supernova remnants* (SNRs) have been detected (Green 1996). SNRs emit across the entire electromagnetic spectrum, but the majority have so far been detected only at radio wavelengths. They are thought to last for 10^5–10^6 yr before dissipating into the surrounding ISM.

1.3 The Supernova Blast Wave

Approximately 80% of known SNRs are classed as "shells", appearing in the radio as limb-brightened rings of emission (see Figure 1.1). The perimeter of a shell SNR corresponds to the expanding shock wave produced by the explosion. Shell SNRs have high levels of linear polarisation and steep spectra ($\alpha \sim -0.6$, $S_\nu \propto \nu^\alpha$), indicating that they emit via *synchrotron radiation*, produced by ultra-relativistic electrons gyrating in a magnetic field. In old SNRs, strong compression of the ambient magnetic field by radiative shocks is thought to boost the emissivity of the Galactic background to observable levels (van der Laan 1962a). In younger SNRs, the maximum compression ratio the shock can produce is four, so that field compression cannot account for their radio emission. Rather, it is thought that emission results from both acceleration of electrons by the shock front (Bell 1978) and turbulent field-amplification and particle-acceleration behind the shock (Gull 1973; Cowsik & Sarkar 1984).

Where absorption by the intervening medium is weak, thermal X-ray emission can be detected from shell SNRs, corresponding to hot gas behind the shock. In some SNRs these thermal X-rays trace the radio shell, while in others the X-rays are centrally peaked (Rho 1995). An emerging class of SNRs also shows X-ray synchrotron emission from the perimeter, believed to be a result of shock-accelerated electrons as for the radio shell (Reynolds 1996). Cooling clumps behind the shock

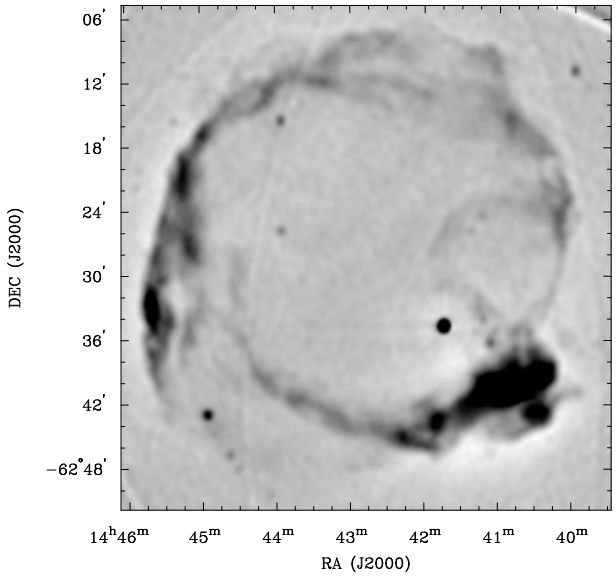

Figure 1.1 A radio image of SNR G315.4–02.3 (RCW 86), a typical shell SNR (Whiteoak & Green 1996).

emit in various optical lines, while shock-heated dust produces infra-red emission.

The simplest model for a shell SNR treats the ejecta as a spherical supersonic piston, propagating into a homogeneous surrounding medium. The evolution of the SNR can then be approximated by four phases (Woltjer 1972; Reynolds 1988):

- **Free Expansion:** The mass swept up from the ISM is negligible compared to that ejected by the explosion. The SNR expands at constant velocity, and is dominated by the properties of the explosion.
- **Adiabatic Expansion:** The mass swept up from the ISM is now considerably greater than that of the ejecta, and the shock begins to decelerate. Radiative losses are negligible and kinetic energy is conserved. For a monatomic gas with a specific heat ratio of 5/3, it can be shown that in this phase (Sedov 1959):

$$R_s = 1.17(E_0/\rho)^{1/5}t^{2/5}, \tag{1.1}$$

  where R_s is the radius of the shock as a function of time t, E_0 is the kinetic energy of the explosion, and ρ is the ambient density. This stage of evolution is sometimes known as the *Sedov-Taylor phase*.
- **Radiative Phase:** The remnant age is comparable to the time-scale for radiative cooling in the shock. The SNR now rapidly decelerates, and the compression ratio in the shock can become very large. Pressure is no longer a dominant factor, and momentum is conserved. The radius-time dependence is now $R_s \propto t^{1/4}$. This stage is also known as the *snowplow phase*.
- **Dissipation:** The velocity of the shock falls below the sound velocity of the ambient medium, and the remnant merges into the ISM.

1.4 Pulsars

In 1967, radio pulsations with a period of 1.34 seconds were detected from a source in Vulpecula (Hewish et al. 1968). In the three decades since, hundreds more of these "pulsating radio sources", or *pulsars*, have been discovered (Taylor et al. 1993). They are believed to be highly magnetised, rapidly rotating neutron stars. Baade & Zwicky (1934) had predicted that neutron stars would be formed when massive stars went supernova, a claim which was stunningly proved when pulsars were quickly discovered in both the Vela (Large et al. 1968) and Crab (Staelin & Reifenstein 1968) supernova remnants. However, in the thirty subsequent years the number of convincing associations between pulsars and SNRs has only grown to perhaps six or seven (Bailes & Johnston 1993; Kaspi 1996). It is still an open question as to whether the paucity of associations is merely a result of observational selection effects (Gaensler & Johnston 1995c; Brazier & Johnston 1999) or is an indication that many supernovae form neutron stars which are not detectable as pulsars (Gotthelf et al. 1997; Kouveliotou et al. 1998).

Radio emission from pulsars is believed to originate from above the star's magnetic poles. If the magnetic axis is not aligned with the rotation axis and is favourably oriented towards Earth, then regular radio pulsations are produced at the rotation period (the "lighthouse" model). The radio pulses are dispersed by the ISM as they propagate, and the resulting difference in arrival time of pulses at two different frequencies, together with a model for the distribution of electrons in the Galaxy, can be used to estimate a pulsar's distance (Taylor & Cordes 1993). All pulsars are slowing down; if the pulse period is P and the rate of slow-down is $\dot{P}$, then the pulsar's characteristic age, τ_c, is defined by (Manchester & Taylor 1977):

$$\tau_c = \frac{P}{2\dot{P}}. \tag{1.2}$$

However, this assumes that a pulsar slows down by pure magnetic dipole radiation (which is known not to be true), and that its initial period is much smaller than P (also not necessarily true). Thus τ_c should only be regarded as an approximation to a pulsar's true age. The observed spin-down indicates that pulsars are losing rotational kinetic energy, at rates between 10^{30} and 10^{39} erg s^{-1}. This energy is believed to be carried away from the pulsar in a magnetised relativistic wind (e.g. Michel 1991).

1.5 Crab-like SNRs

It has long been clear that the Crab Nebula is quite different from most other SNRs. It has a filled-centre rather than a shell-like appearance, its spectral index is flatter ($\alpha \sim -0.3$) than for most SNRs, its fractional linear polarisation is high, and measurements of its expansion indicate an acceleration rather than deceleration. These and other properties of the Crab can be understood in terms of an interaction

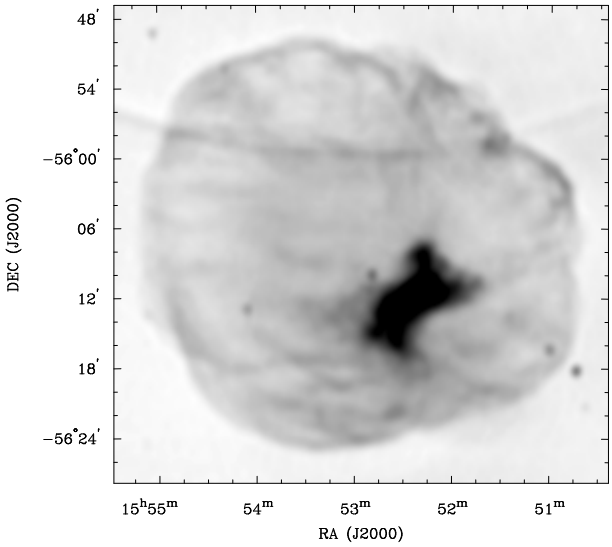

Figure 1.2 A radio image of SNR G326.3–01.8 (MSH 15–5*6*), the original "composite" supernova remnant. The outer, limb-brightened, and the inner, centrally-peaked, components are both visible (Whiteoak & Green 1996).

between ejected material and the relativistic wind powered by the central pulsar (Pacini & Salvati 1973; Reynolds & Chevalier 1984). Indeed the total bolometric luminosity of the Crab is a significant fraction of the rate at which its pulsar is losing energy.

Observations show that ∼20% of SNRs have a centrally-peaked component resembling the Crab Nebula. In most of these, the Crab-like component is surrounded by a shell component. Such remnants are termed *composite SNRs*, and have been shown to correspond to two separate sources of energy: the expanding blast wave and the central neutron star (see Figure 1.2). Less than a dozen Galactic SNRs, like the Crab, show no surrounding shell and are termed *filled-centre SNRs*, or *"plerions"* (Figure 1.3). The "traditional" explanation for the lack of a shell component in these SNRs is that they represent an explosion into a low density region of the ISM, so that the shell is yet to sweep up an appreciable amount of material (Chevalier 1977; Bhattacharya 1990; Sankrit & Hester 1997). However, there is evidence that at least some filled-centre SNRs are the remnants of low-energy supernovae in which no fast-moving ejecta were produced (Nomoto 1987; Wallace et al. 1997).

Every SNR that can be conclusively associated with a pulsar is either composite or plerionic. But the reverse is not true: there are many SNRs with filled-centre components (including those shown in Figures 1.2 and 1.3) for which no pulsar has yet been found. This can be simply explained by the fact that the radio beams of some pulsars never cross our line-of-sight (Frail & Moffett 1993). On the other hand, the energetics of some filled-centre SNRs suggest that their central pulsars have evolved in a non-standard away or have switched off (Green & Scheuer 1992; Woltjer et al. 1997).

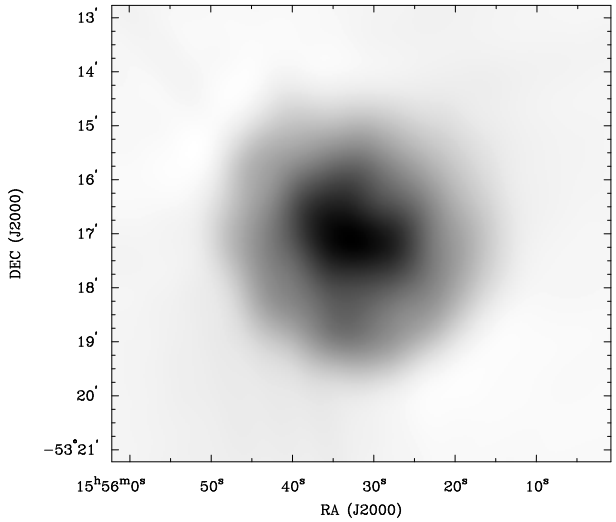

Figure 1.3 A radio image of SNR G328.4+00.2 (Kes 27), a filled-centre SNR (Whiteoak & Green 1996).

1.6 Supernova Remnant Morphologies

1.6.1 Observations

Even from the earliest maps (Harris 1962; Gardner & Milne 1965; Whiteoak & Gardner 1968; Milne 1970), it was clear that supernova remnants[1] are not uniformly limb-brightened shells. Observations of increasingly higher resolution and sensitivity continue to demonstrate the incredible levels of complexity in these objects. While no two SNRs are alike, certain persistent traits emerge amongst them. A far-from-exhaustive list of morphological categories include:

- **Blow-outs:** In SNRs such as that shown in Figure 1.4, part of the shell appears to have expanded more rapidly than the rest.
- **Bilateral SNRs:** Bilateral or "barrel" SNRs have a clear axis of symmetry. Radio emission around the shell is faintest where this axis intersects the shell, and is bright on either side. Bilateral SNRs are often also elongated along their axis, as is the case in Figure 1.5.
- **Double-rings:** Double-ringed, or biannular, SNRs have two (and sometimes more) overlapping rings of emission. An example is given in Figure 1.6.
- **One-sided:** Many SNRs are noticeably brighter along one side, as shown in Figure 1.7.

[1]Unless specifically stated otherwise, the term "supernova remnant" should be taken from here on to indicate radio emission from a shell-type SNR.

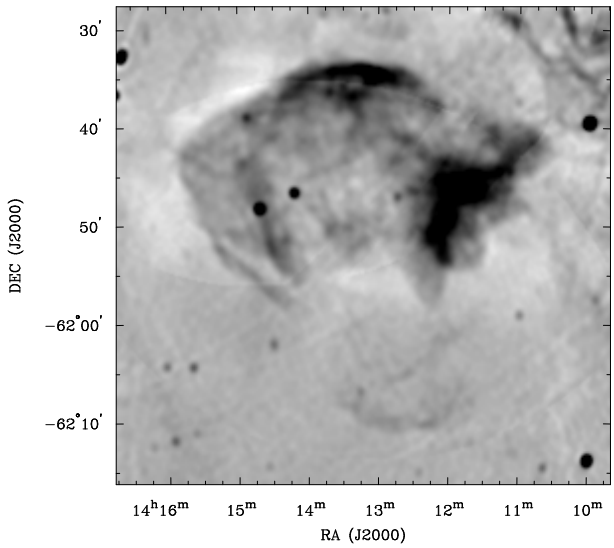

Figure 1.4 A radio image of SNR G312.4–00.4 (Whiteoak & Green 1996). The southern part of the shell has "blown out".

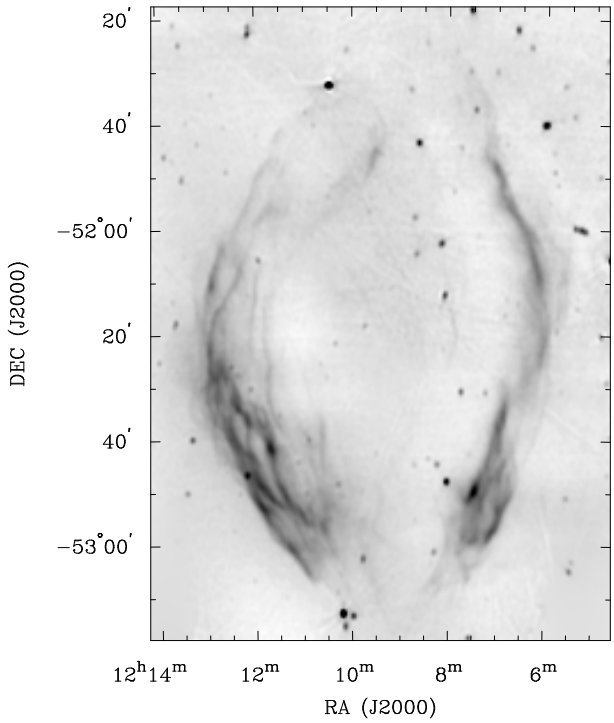

Figure 1.5 SNR G296.5+10.0 (PKS 1209–51/52), a classic "barrel" SNR (Kesteven & Caswell 1987).

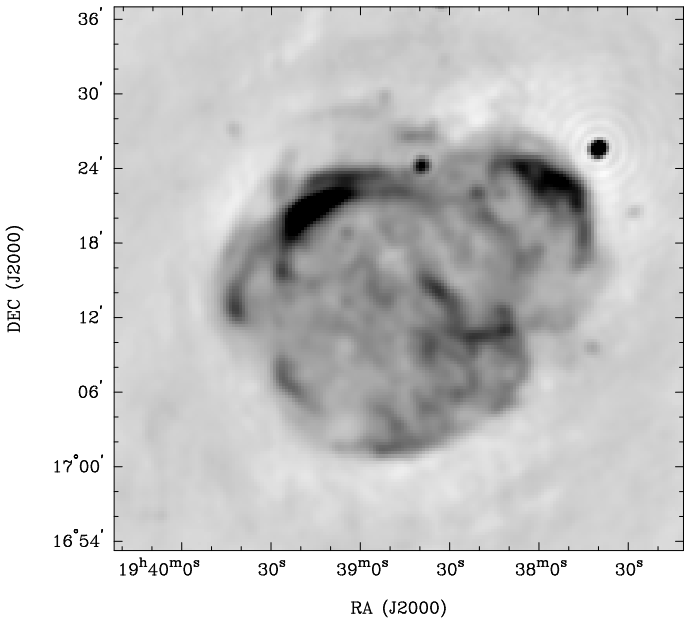

Figure 1.6 SNR G053.6–02.2 (3C400.2), which consists of two overlapping rings of different radii (Dubner et al. 1994).

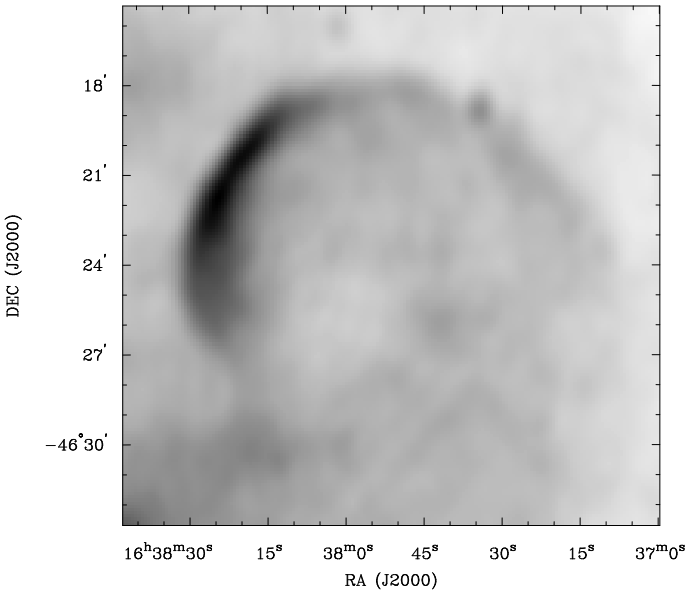

Figure 1.7 SNR G338.1+00.4, a faint shell with a bright north-eastern rim (Whiteoak & Green 1996).

1.6.2 Explanations

Clearly, this rich diversity of morphologies is telling us something about the explosion, its aftermath, and its environment. But what? The host of different explanations proposed for the appearances of SNRs can be grouped roughly into two classes: effects due to the ISM and ambient magnetic field can be considered "extrinsic" to the SNR, while the explosion itself, the circumstellar wind and any associated pulsar or binary system are "intrinsic" to the progenitor. I now review each of these possibilities in detail.

The Interstellar Medium

The assumption made in Section 1.3 of a homogeneous ISM is clearly unrealistic. The ISM is known to consist of many components, including hot ionised gas, cooler neutral gas and dense molecular material (see Hartquist 1994 for a recent review). The temperature, density and magnetic field strength within each component is quite different, and the appearance of a SNR will depend greatly upon its environment (Kafatos et al. 1980; Wheeler et al. 1980; Bhattacharya 1990). For Type Ib/II progenitors, this environment is likely to be particularly complicated, populated with molecular clouds from which these stars were born, and hot bubbles and cavities produced by their energetic winds. Thus the appearance of *every* SNR reflects, at least at some level, the simple fact that the ISM is inhomogeneous.

SNRs with blow-outs are easily explained if one part of the remnant encounters a region of the ISM of lower density than the rest (Milne et al. 1989; Pineault et al. 1997). Double-ringed SNRs can be explained similarly, by considering a low-density cavity adjacent to the remnant. When the shock breaks through into this cavity it rapidly expands across it, taking on its dimensions. Thus one sees a loop of emission corresponding to the original SNR, and another loop corresponding to the interaction of the shock with the walls of the cavity (Braun & Strom 1986; Pineault et al. 1987). If a SN explosion occurs *within* a non-spherical cavity, the remnant will quickly expand to take on the cavity's shape. If such a cavity is elongated along a particular axis, a SNR with a bilateral morphology can result (Bisnovatyi-Kogan et al. 1990).

Under certain simplifying assumptions, the synchrotron emission from a SNR will be brightest where the surrounding material is densest (Dickel & Jones 1985). One-sided SNRs can thus be explained in terms of a density gradient in the ambient medium. Indeed interaction with dense material has been conclusively demonstrated for at least some one-sided SNRs (Frail et al. 1994a; Wilner et al. 1998), while it has been argued that the overall density gradient of gas in the disk of the Milky Way causes SNRs to generally appear brighter on their side closest to the Galactic Plane (Caswell 1977).

Magnetic Fields

Synchrotron emission can only be produced in the presence of a magnetic field, and variations in the strength and structure of the ambient field can thus affect a SNR's radio morphology. For example, a simple gradient in field strength across a SNR will cause one side of the remnant to appear brighter than the other (Caswell & Lerche 1979; Reynolds & Fulbright 1990).

Only the component of the field normal to the direction of the shock is compressed. Thus even in a uniform magnetic field, variations in the angle between the shock and the field can cause brightness variations around the SNR. In a uniform field which is largely perpendicular to the line-of-sight, a SNR will be brighter on two opposite limbs, generating a bilateral appearance (van der Laan 1962b; Whiteoak & Gardner 1968; Shaver 1969; Ferrière & Zweibel 1991). It is not clear whether this mechanism is sufficient to produce the extreme ratios in brightness seen in some bilateral SNRs (Fulbright & Reynolds 1990; Ratkiewicz et al. 1994). However, it has been argued that the efficiency of shock-acceleration depends strongly on the angle between the shock and the magnetic field (Jokipii 1987; Roger et al. 1988), a mechanism which can produce a bilateral appearance with the appropriate brightness ratios (Fulbright & Reynolds 1990).

For typical ISM field strengths, the magnetic energy density is well below that of the SNR and the field is dynamically unimportant (Manchester 1987; Bisnovatyi-Kogan et al. 1990). But in extremely strong fields (such as might be found near the Galactic Centre) or for large SNRs, the field can significantly affect the evolution and shape of a SNR (Insertis & Rees 1991; Mineshige et al. 1993; Różyczka & Tenorio-Tagle 1995), impeding expansion across field lines. This can produce the elongation seen in some bilateral SNRs.

The Supernova Explosion

Both the high space velocities of pulsars (Shklovskii 1970; Cordes & Chernoff 1998) and asymmetries in the explosions themselves (Karovska et al. 1989; Spyromilio 1994) provide good evidence that supernovae are not spherically symmetric in their distribution of ejecta. Specifically, it has been proposed that material is preferentially ejected in the equatorial plane of the progenitor star, which could potentially produce a bilateral appearance in the resulting SNR (Bodenheimer & Woosley 1983; Kesteven & Caswell 1987). However, simulations suggest that any effect of the original distribution of ejecta on the shape of a SNR quickly vanishes once the remnant begins to interact with surrounding material (Bisnovatyi-Kogan & Blinnikov 1982; Blondin et al. 1996). Indeed, asymmetries were observed in the ejecta from SN 1993J, but the resulting radio remnant appeared circular and undistorted just eight months later (Marcaide et al. 1995a).

The Progenitor Wind

For most of their lives, the massive stars which are the progenitors of Type Ib/II SNe generate strong ($\gtrsim$ 2500 km s^{-1}) winds which blow large (up to 100 pc in radius) bubbles in the surrounding medium. For a single star with no significant space velocity or rotation, such a wind is isobaric and consequently spherically symmetric (Weaver et al. 1977). Although the evolution of a SNR propagating through such a wind bubble will be different from the simplified picture of Section 1.3 (Chevalier 1982a; Chevalier & Liang 1989; Ciotti & D'Ercole 1989; Tenorio-Tagle et al. 1991), the remnant, if visible, will still have a spherical and symmetric appearance in the radio. However, there are three possible factors which can induce deviations from spherical symmetry.

Firstly, a star with a significant space velocity can produce an elongated and distorted wind bubble, and will also result in a supernova which is off-centre, or even outside, the bubble. The interaction of the blast wave with this cavity can then produce a whole range of SNR shapes, including one-sided, bilateral and double-ringed morphologies (Różyczka et al. 1993; Brighenti & D'Ercole 1994).

Secondly, a progenitor which is rotating significantly, or which has a companion, can generate a wind which is denser in the equatorial plane than at the poles (Luo & McCray 1991; Bjorkman & Cassinelli 1993; Owocki et al. 1994). Expansion of a supernova remnant through such a medium can produce a biannular, bilateral or elongated morphology (Manchester 1987; Igumenshchev et al. 1992; Storey et al. 1992; Blondin et al. 1996), although it is unclear whether this appearance will persist once the SNR expands beyond this axisymmetric region and into the surrounding ISM (Bisnovatyi-Kogan & Blinnikov 1982; Blondin et al. 1996).

Finally, a wind-driven bubble can have a well-ordered magnetic field, usually with a toroidal geometry (Chevalier & Luo 1994). The structure of this magnetic field can affect the distribution of emissivity around the surface of the SNR, producing a bilateral appearance when viewed at certain angles (Zhang et al. 1996).

Pulsars and Binary Systems

Pulsars are high velocity objects, and can eventually catch up with and overtake their associated shell SNR. When this happens, interaction with the pulsar's relativistic wind can re-energise the SNR, brightening and distorting one side (Shull et al. 1989; Frail et al. 1994c).

In some theoretical models, jets of relativistic particles flow out along a pulsar's magnetic axis (Benford 1984; Sulkanen & Lovelace 1990), a possibility supported by high-resolution X-ray images of the regions around the Crab pulsar (Hester et al. 1995) and PSR B1509–58 (Brazier & Becker 1997). Therefore even if a pulsar is still well within its associated SNR, such jets can collide with the perimeter of the remnant, brightening the regions of impact and (depending on viewing angle and the geometry of the outflow) giving the SNR a bilateral or double-ringed appearance (Manchester & Durdin 1983; Manchester 1987; Willingale et al. 1996).

Most supernova progenitors are in binary systems, and some can stay bound to their companion after the supernova event. In some such systems, matter is accreted from the companion onto the neutron star or black hole, forming an accretion disk around the compact remnant and relativistic jets along the axis of rotation. The most well-known instance is the X-ray binary SS 433, whose twin relativistic ($v = 0.26c$) jets precess every 164 days (Hjellming & Johnston 1981a). SS 433 sits at the centre of the SNR G039.7–02.0 (W 50), and its jets propagate over many parsecs to collide with the SNR shell and give the remnant a distorted and elongated appearance (Begelman et al. 1980; Downes et al. 1986; Elston & Baum 1987; Murata & Shibazaki 1996). Only eight binaries with jets are known (Fender et al. 1997), and none except SS 433 are within a SNR. However, it has been argued that the biannular and bilateral morphologies of some shell SNRs could be explained if these remnants contain binaries like SS 433 (Gregory & Fahlman 1983; Manchester 1987).

1.6.3 Scope of This Thesis

In this thesis, I set out to explain deviations from spherical symmetry in radio SNRs. Given all the competing factors which might affect a remnant's appearance, it is obviously unrealistic to look for a single cause which can explain the shape of every known SNR. Rather, this thesis has three aims:

1. To explain the appearance of specific SNRs of interest.
2. Where appropriate, to consider how this explanation applies to the morphological category into which a SNR falls.
3. To explore the conditions under which extrinsic or intrinsic effects dominate.

There have certainly been previous attempts to explain the appearance of radio SNRs (e.g. Shaver 1969; Kesteven & Caswell 1987; Manchester 1987), and certain properties and characteristics have been established for the different morphological categories. But the spatial resolution and sensitivity of the data in these studies were comparatively poor, possibly leading to the incorrect classification of specific SNRs, and to misleading statistics when considering the entire Galactic population.

A significant fraction of Galactic SNRs have now been observed at $\sim 1'$ resolution (e.g. Whiteoak & Green 1996; Dubner et al. 1996), allowing more precise statistical analyses and making it possible to easily identify interesting SNRs for detailed follow-up observations. In this thesis, I have used existing observations of intermediate resolution to identify SNRs of specific interest, which I have then observed at higher sensitivity and resolution with the Australia Telescope Compact Array (ATCA) or the Very Large Array (VLA).

Chapters 2 through 6 of this thesis are each the reproduction of a paper submitted to a refereed journal, and are presented in the order in which the work was carried out. In Chapter 2 I present a radio study of SN 1987A, a unique opportunity to study a SNR in its earliest stages of evolution. Chapter 3 contains new observations

of two bilateral SNRs, G003.8–00.3 and G350.0–02.0, and goes on to consider the entire sample of bilateral remnants. Chapter 4 describes results on the double-ringed SNR G296.8–00.3, while in Chapter 5 I consider the unusual SNR G309.2–00.6. In Chapter 6 results are presented on G320.4–01.2, a complicated SNR coincident with the young pulsar PSR B1509–58. In Chapter 7 I summarise the main findings of the thesis, consider the application of these results to the more general issues associated with SNR morphology, and suggest some prospects for future investigation.

Chapter 2

The Radio Remnant of SN 1987A

This Chapter has also appeared as Gaensler et al., 1997, "The asymmetric radio remnant of SN 1987A", ApJ, **479**, 845.

2.1 Introduction

SN 1987A in the Large Magellanic Cloud has presented a unique opportunity. The nearest ($\sim$50 kpc) supernova (SN) to have been detected since the invention of the telescope, its aftermath presents a detailed picture of its progenitor's circumstellar medium (CSM) and of the interaction of this CSM with the SN shock.

Since the discovery of radio supernovae (RSNe) over 25 yr ago (Gottesman et al. 1972), such objects have proven to be useful tools in probing the CSM of massive stars. The flux density from a typical RSN takes weeks to years to peak in its radio emission, then undergoes a slow power-law decay extending over a period of years or even decades (Weiler et al. 1996). This is representative of the SN shock sweeping up the dense, slow-moving wind generated by the red supergiant (RSG) progenitor (Chevalier 1982b).

However, SN 1987A's progenitor, Sk–69°202, was very different. It is believed to have evolved from a RSG into a *blue* supergiant (BSG) approximately 2×10^4 yr before the SN event (Crotts & Heathcote 1991). During the star's period as a BSG, the high-velocity BSG wind interacted with the slower RSG wind surrounding it, creating a cavity. Ground-based and *HST* optical observations of SN 1987A have revealed a complex nebulosity surrounding the explosion, consisting of a central circular ring of diameter $\approx 1\farcs6$ (0.4 pc), and two similar rings of diameter $\approx 3\farcs6$ (0.9 pc), one on either side. The whole system is inclined at $\sim 45°$ to the line of sight (Jakobsen et al. 1991; Plait et al. 1995). While the exact origin for this "triple ring nebula" is unclear, it appears to demarcate the interface between the BSG and RSG winds, material at the boundary being excited by the ultraviolet flash from the supernova (Luo & McCray 1991). The optical emission appears to indicate that the BSG wind bubble is bipolar in shape (Crotts et al. 1995), the "standard" model being that this is caused by an RSG wind which is denser at the equator than at

the poles (Luo & McCray 1991; Martin & Arnett 1995). Problems exist with this model however (Blondin 1994; Burrows et al. 1995), and many alternatives have been proposed (e.g. McCray & Lin 1994; Burderi & King 1995).

Radio emission from SN 1987A was detected at 0.843 GHz by the Molonglo Observatory Synthesis Telescope (MOST) on 1987 Feb 25, two days after the SN event. This emission reached a maximum four days after the explosion (Turtle et al. 1987), then followed a power-law decay to become undetectable less than a year later (Ball et al. 1995a). This radio outburst is understood to be a consequence of the rapidly moving, low-density BSG wind, which produced only a short-lived period of radio emission when hit by the SN shock (Storey & Manchester 1987; Chevalier & Fransson 1987).

After remaining quiescent for several years, radio emission from the remnant of SN 1987A was redetected by both the MOST and the Australia Telescope Compact Array (ATCA) in mid-1990 (Staveley-Smith et al. 1992, hereafter Paper S1), approximately 1200 days after the explosion. At 9 GHz, the ATCA's highest frequency, the remnant was just resolved, and by early 1992 the emission was found to deviate by $\sim$10% from spherical symmetry (Staveley-Smith et al. 1993a, hereafter Paper S2). Super-resolution of ATCA data at comparatively low signal-to-noise produced images of resolution $\approx 0\farcs5$ (Staveley-Smith et al. 1993b, hereafter Paper S3). In an image corresponding to observations made in 1993 January, radio emission is distributed around the rim of a shell, with up to 50% of the flux density originating from two bright limbs on the shell's eastern and western edges. To account for the size of the remnant at the second radio turn-on, a velocity of $\sim 35\,000$ km s^{-1} was required for the fastest ejecta. However, only a marginal increase in size was subsequently detected over a 20-month period, implying that the remnant had either decelerated significantly, or was rapidly changing shape. This emission, which has since been shown to be centred on the position of the SN (Reynolds et al. 1995), was still increasing in its intensity four years after its reappearance (Ball et al. 1995a; Staveley-Smith et al. 1996, hereafter Paper S4).

The second onset of radio emission has been interpreted as resulting from the shock encountering a sudden increase in the density of the CSM. The diameter of the emitting region is noticeably smaller than the inner optical ring, and so the shock is yet to reach the undisturbed RSG wind. Chevalier (1992a) has argued that the shock has reached the termination shock of the BSG wind, so that it is now progressing through a region of constant density. Such a theory is supported by more detailed modelling of the radio emission (Ball & Kirk 1992; Duffy et al. 1995, hereafter DBK). Chevalier & Dwarkadas (1995, hereafter CD95), have recently proposed an alternative model, that the dense region that the shock has encountered is actually an ionised component of the *RSG* wind located inside the optical ring. The greater density of this RSG component can better explain the appearance of X–ray emission from SN 1987A (Beuermann et al. 1994; Gorenstein et al. 1994), and also the large apparent deceleration of the SN shock suggested by the results of Paper S3.

Only two other remnants of supernovae (SNe) as young as SN 1987A have been sufficiently resolved at radio frequencies to reveal morphological details, namely

SN 1986J (Bartel et al. 1991) and SN 1993J (Bartel et al. 1994; Marcaide et al. 1995a), both using VLBI (resolution < 1 mas). While these supernovae are very different from SN 1987A in their luminosities, radio light curves and properties of their progenitor stars (e.g. Ball & Kirk 1995), the brightness distribution of both objects deviates from that of a uniform spherical shell, at least to some extent. Thus it is clear that SN 1987A is not unique in having an asymmetric radio morphology so early in its lifetime. However, SN 1987A *is* unique in that we have a considerable amount of information about the progenitor star and its environment which we can use to try and explain the observed radio structures. Also, SN 1987A appears be at a later, or at least different, stage in its evolution: the other two objects are still in the standard RSN phase, a phase which lasted just days in the case of SN 1987A.

Previous ATCA data published on SN 1987A consists of 4.8 and 8.6 GHz flux densities up to day 2300, and a single super-resolved 9 GHz image. Here we present the entire ATCA data-set, to date, on SN 1987A. Flux density measurements have been carried out at intervals of 1–2 months at 1.4, 2.4, 4.8 and 8.6 GHz from day 918 (1989 August) up to day 3325 (1996 April). These seven years of observations cover the entire second phase of the radio evolution up to this point. We have also obtained 9 GHz images of the remnant at four epochs from 1992 to 1995. With the increasing flux density of the remnant, these images are becoming progressively more reliable and detailed.

Such observations provide a key insight into the interaction of the SN shock with the CSM. The flux density of the remnant as a function of time and frequency is our best guide to conditions at the shock, such as the details of the acceleration mechanism and the properties of the material into which the shock is expanding. The radio images of the remnant demonstrate the non-spherical nature of the system, and can be interpreted in terms of the three-dimensional structure of the surrounding medium and of the explosion itself. From these data the true rate of expansion of the remnant can also be measured. The observations made in this project are discussed in Section 2.2. Results are presented in Section 2.3, and are discussed in terms of the properties of SN 1987A and its surroundings in Section 2.4.

2.2 Observations

All observations were made with the Australia Telescope Compact Array (Frater et al. 1992), an aperture synthesis telescope consisting of six 22m-diameter antennas located on a 6km, east-west baseline near Narrabri, New South Wales. Two types of observations have been made of SN 1987A using the ATCA: monitoring and imaging. All observations were continuum observations, measuring two frequencies simultaneously each with a bandwidth of 128 MHz. All Stokes polarisation parameters were recorded. Amplitudes were calibrated using the revised scale of Reynolds (1994), assuming a flux density for PKS 1934–638 of 15.0, 11.6, 5.8 and 2.8 Jy at frequencies of 1.4, 2.4, 4.8 and 8.6 GHz, respectively. Flux density measurements in Papers S1 & S4 used an earlier scale; measurements at 1.4, 2.4 and 4.8 GHz were

on a scale 8–12% higher, and those at 8.6 GHz 10% lower, than values quoted here. Phases were calibrated using the source PKS 0530–727 and also, in conditions of poor phase stability, PKS 0454–810 (see Reynolds et al. 1995).

2.2.1 Monitoring

An ATCA monitoring observation of SN 1987A normally gives a measurement of the flux density of the source at four frequencies. The ATCA can observe at two frequency bands simultaneously: earlier observations were at either 1.4/2.4 GHz or 4.8/8.6 GHz, while more recent observations used frequency switching between these two pairs. The integration time for an observation was typically 6–12 h.

Until 1995 May, monitoring data were reduced using the `AIPS` package. After this date, the `MIRIAD` package (Sault et al. 1995) was used. To check the consistency between these two, we reduced several observations using both packages. The corresponding difference in flux density was in all cases considerably less than the uncertainty.

Data were edited, calibrated and imaged. Baselines shorter than 3 kλ were often contaminated by emission from strong sources outside the primary beam (primarily 30 Doradus), and were discarded. Images were then deconvolved using the `CLEAN` algorithm (Clark 1980). Before day 1500, the flux density of SN 1987A was equated to the peak brightness of the source. After this date, the flux density was measured by fitting a Gaussian profile to the emission.

2.2.2 Imaging

Imaging observations were made three times a year from 1992 to 1995. The three observations in a given year were always made with different 6 km configurations to give increased radial coverage in the $u - v$ plane. Each observation used two simultaneous frequencies, both between 8.6 and 9.1 GHz, giving a diffraction-limited synthesised beam of $\approx 1''$. Integration times were long (12–16 h) to give increased sensitivity. To avoid possible artifacts, the phase centre was placed $10''$ south of SN 1987A. More information on these observations is contained in Table 2.1.

All imaging data were reduced using `MIRIAD`. Observations corresponding to earlier images (Paper S3) were completely reprocessed. Data were carefully examined for bad points, and observations during which the atmospheric phase stability was poor were rejected. The data were then calibrated and the three sets of observations for each year combined. Images centred on the remnant were produced using multi-frequency synthesis (Sault & Wieringa 1994), using a cell size of $0\farcs08$ in each coordinate and an image size of 512×512 pixels. As a compromise between natural and uniform weighting, Briggs' robustness parameter was used with a value of 0 (Briggs 1995). This suppressed stripes in the dirty map caused by the small cell size. Deconvolution was carried out using a maximum entropy (`MAXEN`) algorithm (Gull & Daniell 1978) with 1000 iterations, using a square window of side $\approx 4''$

Epoch	Date of Observation	Day No.	Observing Time (h)	Diffraction Limited Beam	RMS Noise (μJy beam^{-1})	$S_{9\,\mathrm{GHz}}$ (mJy)
1992	1992 Oct 21	2068	17	$1\farcs11 \times 0\farcs85$	44	5.4±0.1
	1993 Jan 04	2142	15	PA = 34°		
	1993 Jan 05	2143	7			
1993	1993 Jun 24	2314	13	$0\farcs98 \times 0\farcs92$	34	6.8±0.1
	1993 Jul 01	2321	13	PA = 12°		
	1993 Oct 15	2426	19			
1994	1994 Feb 16	2550	13	$0\farcs99 \times 0\farcs94$	30	7.3±0.1
	1994 Jun 27	2683	26[a]	PA = −78°		
	1994 Jul 01	2687	14			
1995	1995 Jul 24	3074	11	$1\farcs04 \times 0\farcs89$	33	10.8±0.1
	1995 Aug 29	3111	11	PA = 6°		
	1995 Nov 06	3178	12			

[a]spread over two days

Table 2.1 Imaging observations of SN 1987A with ATCA. Position angles are those of the major axis of the beam, and are measured north through east.

centred on the remnant. The `MAXEN` model was then convolved with two different restoring beams: the first was the diffraction-limited beam, the second was a super-resolved circular beam with FWHM 0$\farcs$4 as used in Paper S3. This model was then combined with the unscaled residuals, and then regridded at a pixel scale of 0$\farcs$01 in each coordinate to produce the final image.

2.3 Results

2.3.1 Monitoring

Monitoring data for SN 1987A at all four frequencies are shown in Figure 2.1. Two uncertainties are associated with each measurement: a random error, representative of the noise in the image and the uncertainty in the fitting process, and a systematic error of order 5–10%, estimated by examining the scatter in the flux density of a nearby ($\sim 4'$) unresolved source which we designate ATCA J053604–691844[1]. These errors are combined in quadrature to give the error bars shown in Figure 2.1.

The flux density at all frequencies has continued to increase essentially monotonically over the entire period of observations, and shows no sign of levelling off. A linear fit over the last two years of data gives a rate of increase of 33.5±3.1, 23.0±3.0, 10.9±1.4 and 4.2±1.5 μJy day^{-1} at 1.4, 2.4, 4.8 and 8.6 GHz, respectively. Short-time-scale variations are evident in the data — the significance of these is discussed

[1]This source is variable. However, the estimate of the systematic scatter in its light curve was made over a period of ∼400 days during which its flux density appeared to remain constant.

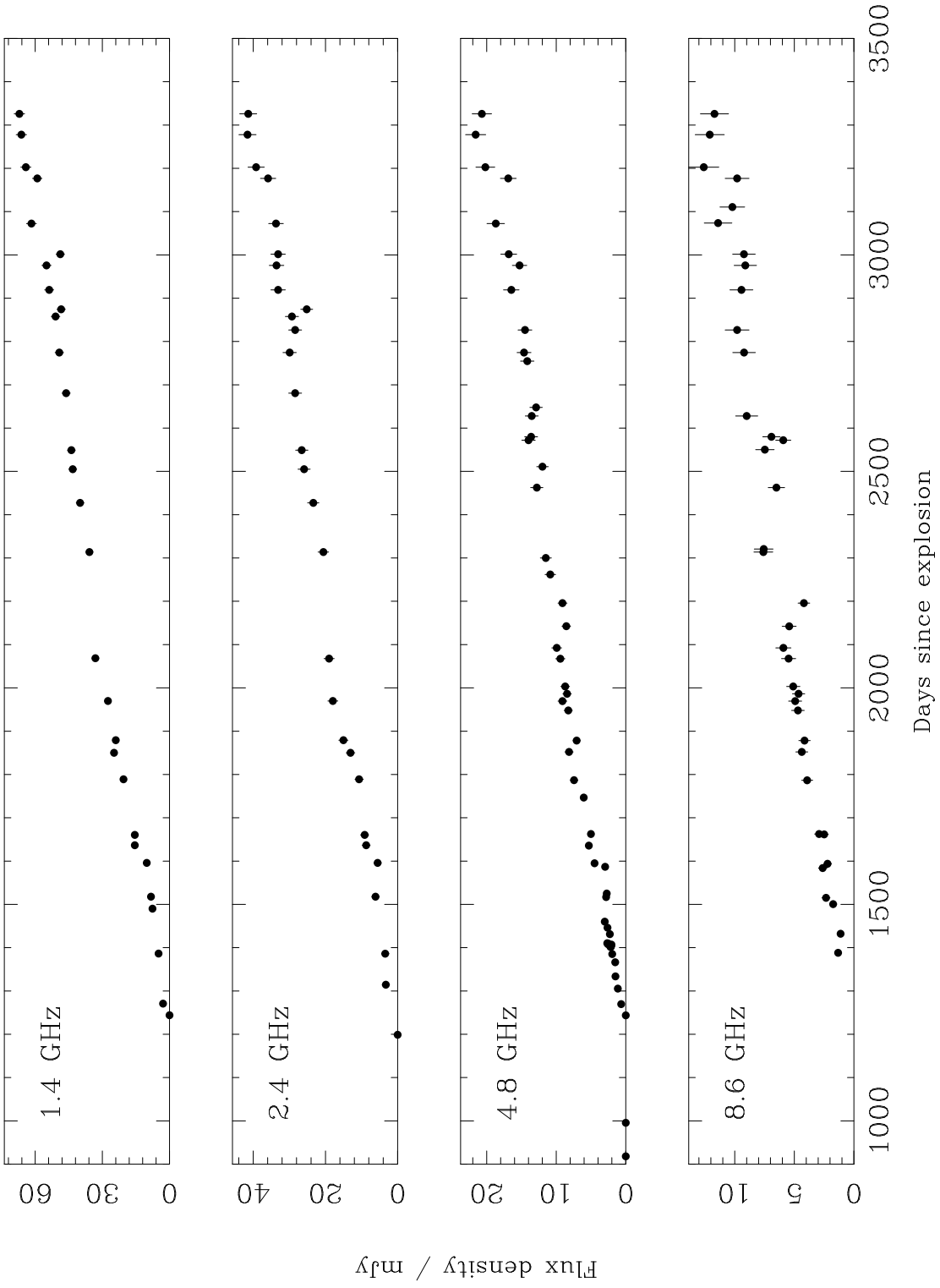

Figure 2.1 Light curves for the second radio turn-on of SN 1987A at four different frequencies. Where error bars are not shown, they are smaller than the plotted points.

in Section 2.4.1.

Spectra for SN 1987A at five epochs are shown in Figure 2.2. These observations are consistent with a constant spectral index $\alpha = -0.95 \pm 0.04$ over more than four years.

2.3.2 Imaging

Total Intensity

Two sets of total-intensity images are shown: first in Figure 2.3 the diffraction-limited images, then in Figure 2.4 the super-resolved images obtained by using a circular, $0\farcs4$ FWHM restoring beam. Only the inner $\approx 4''$ of each $40''$ image is shown, and no emission above the noise was seen outside this central region. More information on each image is given in Table 2.1. Figure 2.5 shows an SN 1987A difference image, produced by subtracting the super-resolved image made for the 1993 epoch from that made for 1995.

In the diffraction-limited images of the supernova, the source is clearly resolved. There is a distinct asymmetry associated with the emission, in that the peak is displaced east of centre. While the object increases in brightness with time, it does not appear to be getting noticeably larger — this is quantified below.

The super-resolved images show that, rather than being centrally peaked, the emission is restricted to the rim of an approximately circular shell. The 1992 image is (unsurprisingly) similar to that produced in Paper S3: two lobes are apparent on the east and west limbs of the remnant. In the 1993 and later images, the remnant continues to brighten, and takes on a more circular shape. For the 1995 epoch, the minimum of emission at the centre of the remnant is 330 μJy beam^{-1}, well above the noise, and this can be considered an upper limit on the flux density of a central point source. Using the `CLEAN` algorithm produces qualitatively similar images, although it is worth noting that `CLEAN` is *not* recommended for super-resolution (Briggs 1994).

The difference image in Figure 2.5 shows the two lobes or "hotspots" increasing in their intensity, the eastern hotspot clearly increasing in brightness more rapidly than the western one. In 1992 the ratio of peak brightness between the east and west lobes was 1.2, but by 1995 it was 1.8. Approximately 50% of the total flux density from the remnant is contained in these regions. In all images, the two hotspots are at consistent position angles of $\sim 100^\circ$ and $\sim 260^\circ$. The range in position angle of the diffraction limited beams in Table 2.1 is large, and indeed the beams for the 1993 and 1994 epochs are nearly circular. This is good evidence that the consistent orientation of the hotspots observed in the succession of super-resolved images is not an artifact driven by the $u - v$ coverage of the observations. Further tests on the reliability of such position angles under super-resolution have been carried out by Briggs (1995).

In the 1992 image, there appears to be an extension of emission towards the north of the remnant. This vanishes in later images and is likely to be an artifact introduced by super-resolution under conditions of low signal-to-noise ratio (cf.

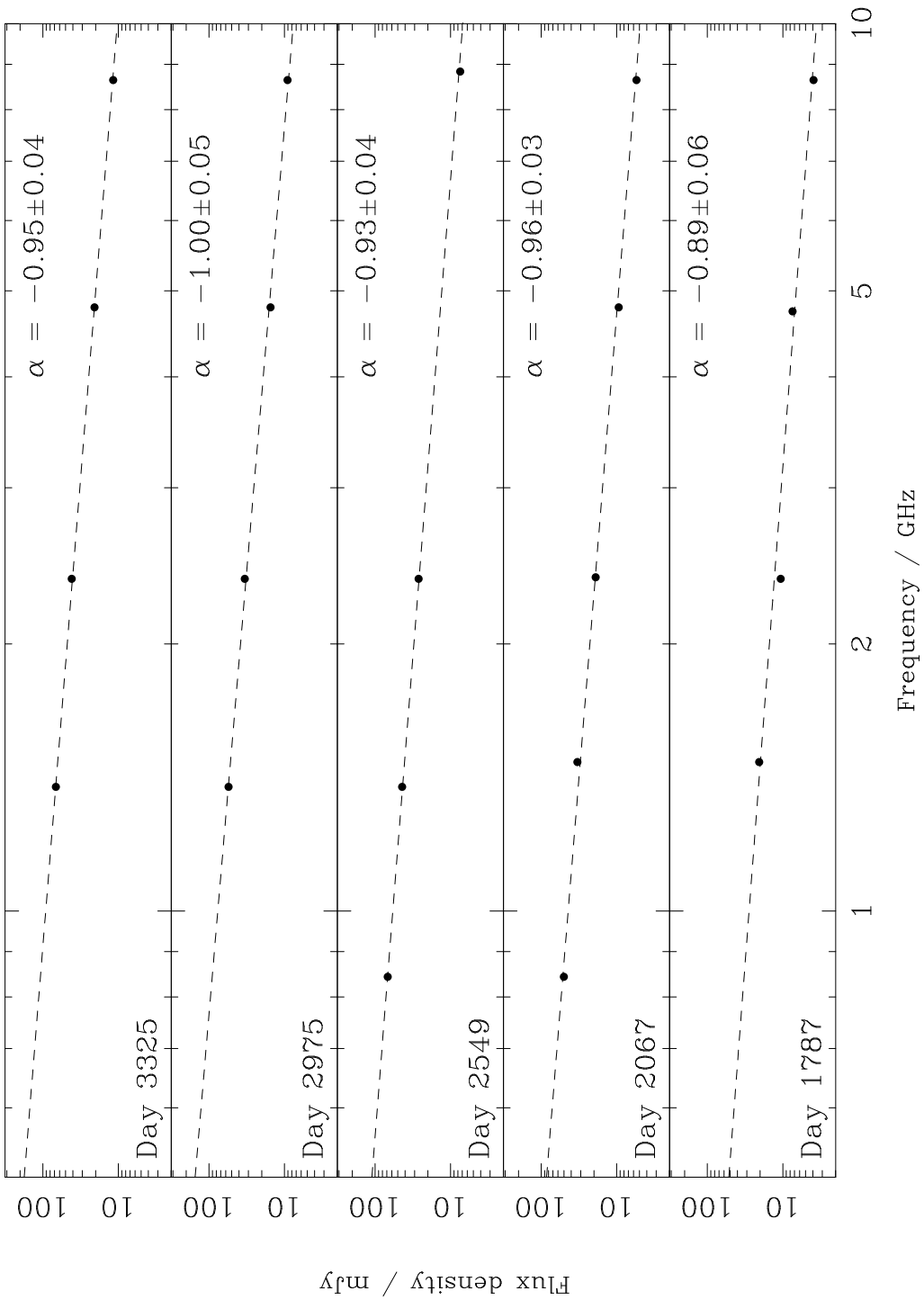

Figure 2.2 The radio spectrum of SN 1987A at five different epochs. The day number corresponds to the number of days since the explosion, and all observations were made within three days of the day number on each plot. Where available, 0.843 GHz MOST data (Ball et al. 1995a) have been included. The spectral index α ($S_\nu \propto \nu^\alpha$) has been calculated using a linear least-squares fit. Errors are no larger than the size of the plotted points.

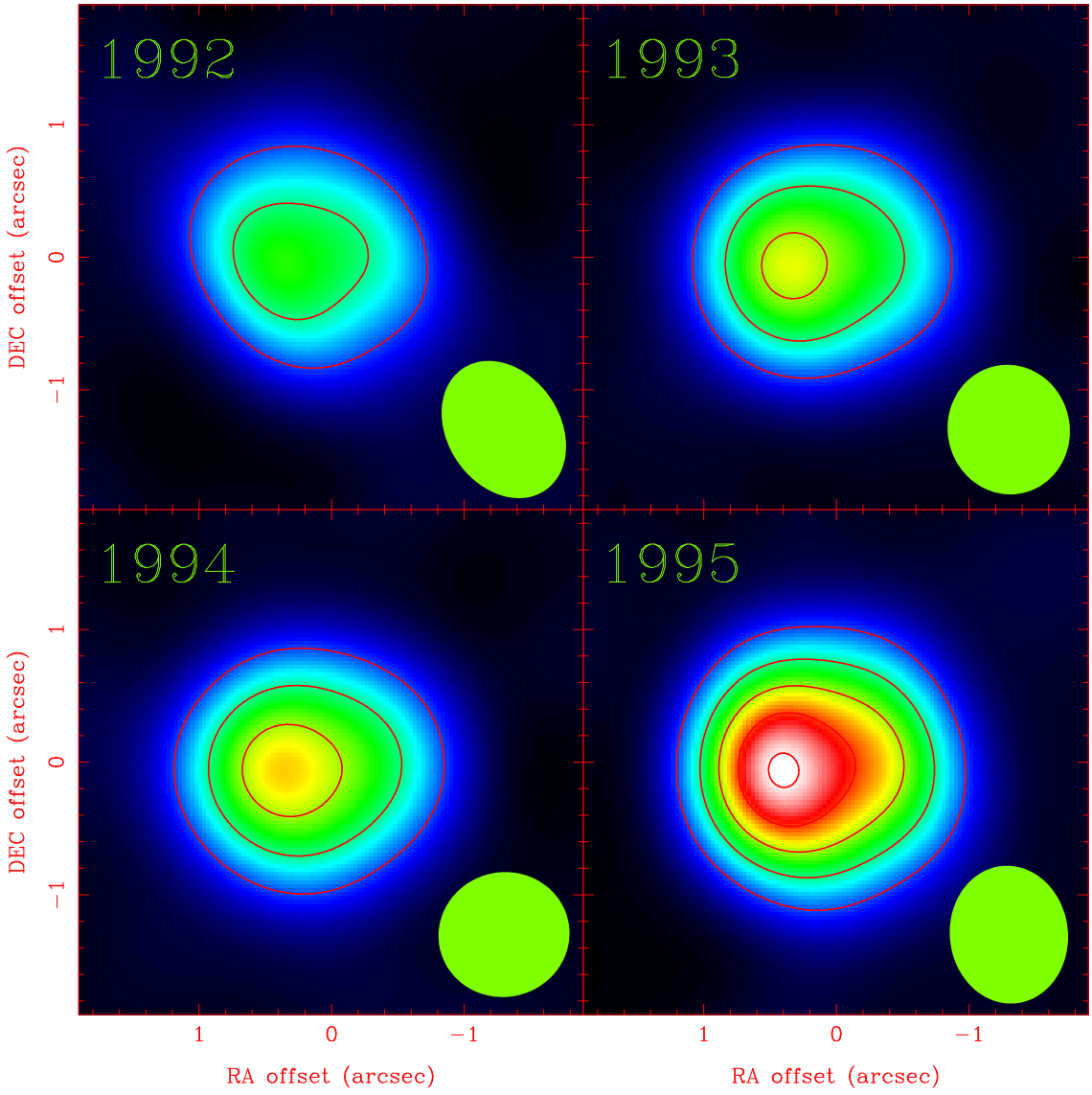

Figure 2.3 Diffraction-limited images of SN 1987A at 9 GHz, using data from epochs 1992 through to 1995 (see Table 2.1). An ellipse corresponding to the FWHM of the Gaussian restoring beam is shown at bottom right of each image. The colour map runs from –0.1 mJy beam^{-1} (black) to 5.1 mJy beam^{-1} (white), while the contours are at 1, 2, 3, 4 and 5 mJy beam^{-1}. Coordinates are given as offsets from RA $05^{\rm h}35^{\rm m}27\overset{\rm s}{.}97$, Dec. $-69°16'11\overset{''}{.}10$ (J2000).

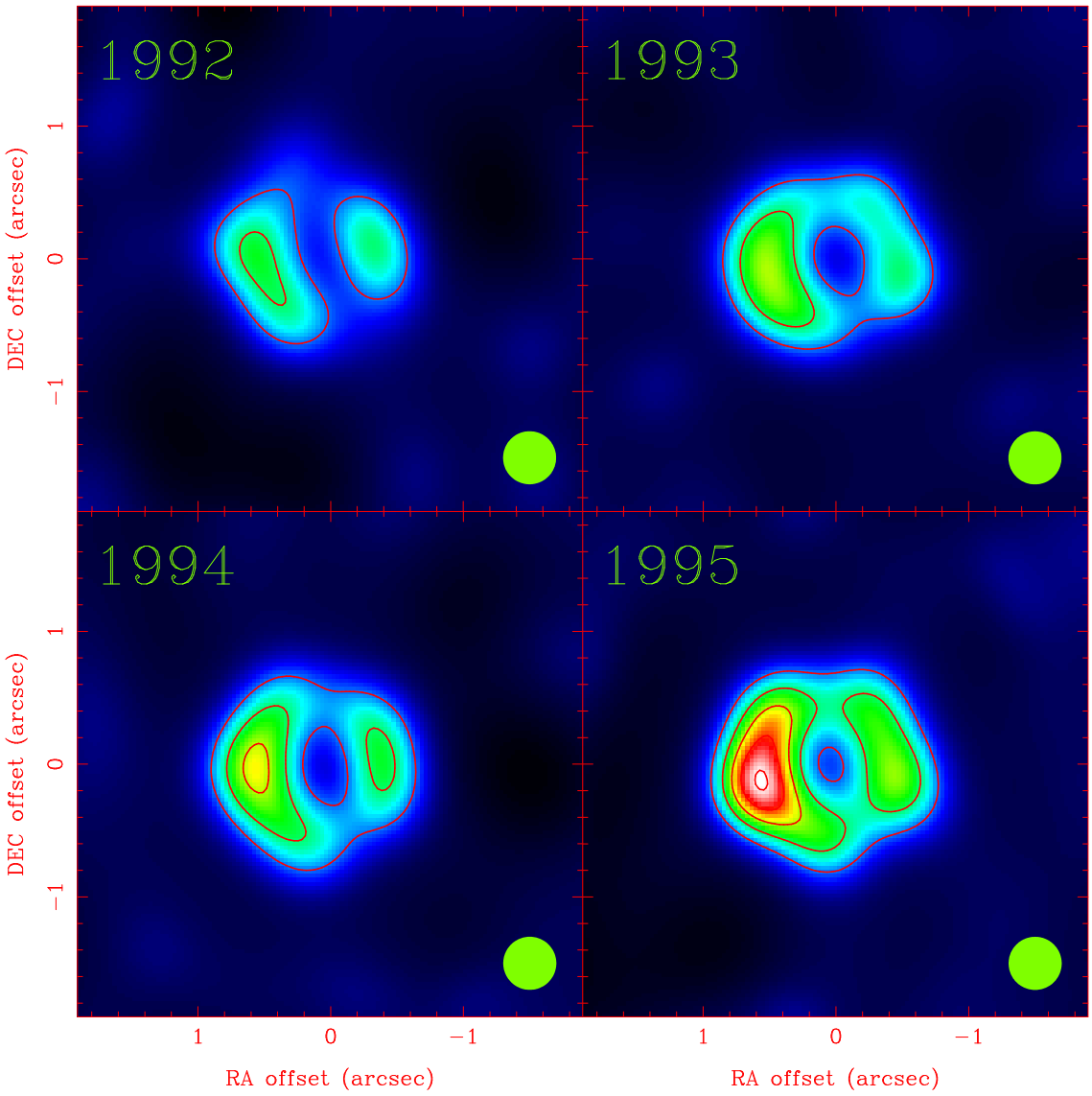

Figure 2.4 Super-resolved images of SN 1987A at 9 GHz, using data from Table 2.1. The colour map runs from –0.1 mJy beam^{-1} (black) to 2.0 mJy beam^{-1} (white), while the contours are at 0.4, 0.8, ... , 2.0 mJy beam^{-1}. Other features of the images are as in Figure 2.3.

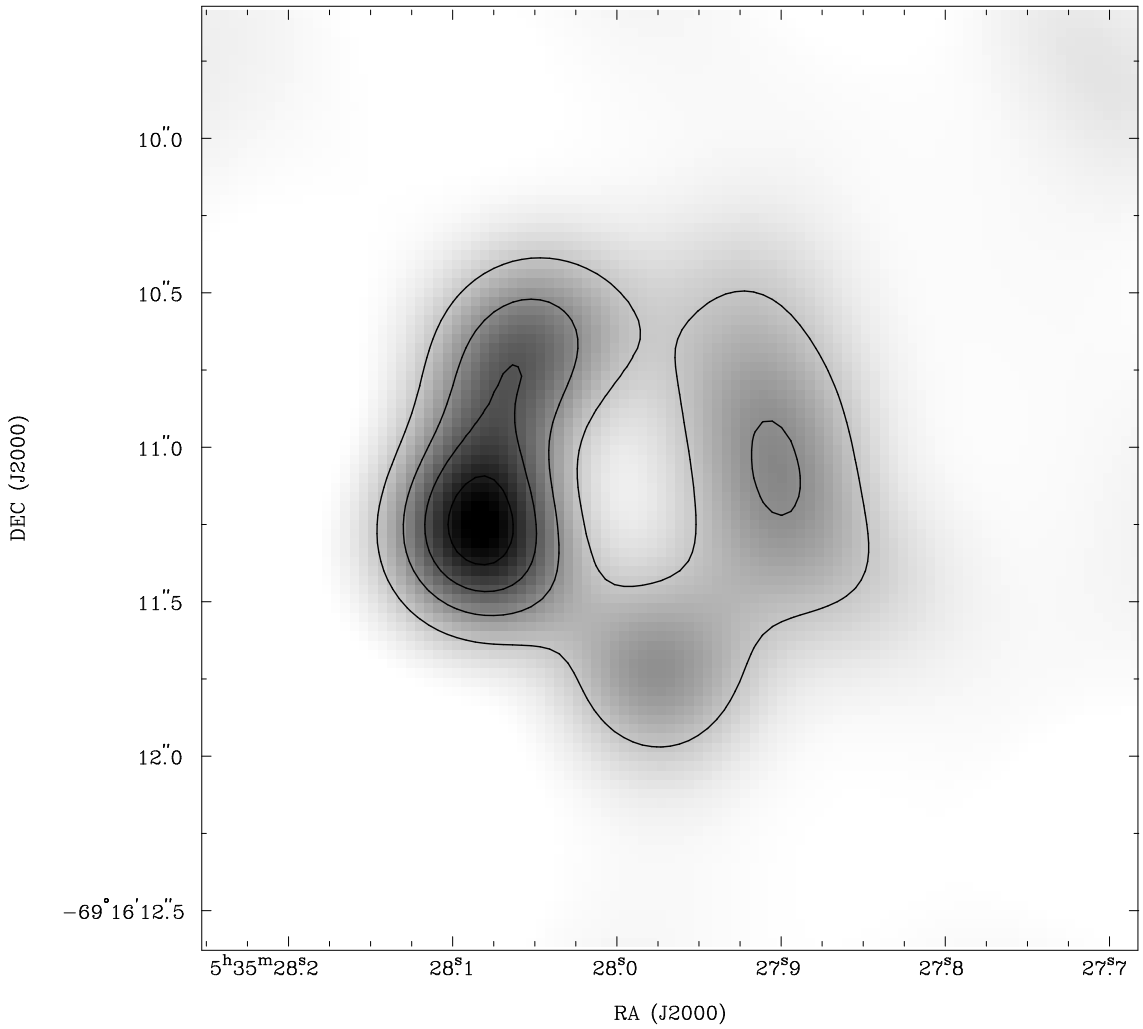

Figure 2.5 A difference map, produced by subtracting the super-resolved 1993 epoch image of SN 1987A from that corresponding to the 1995 epoch. The grey-scale ranges from 0.0 to 0.9 mJy beam^{-1}, while contour levels are at 0.2, 0.4, 0.6 and 0.8 mJy beam^{-1}.

Briggs 1994). In the 1994 and 1995 images, the eastern hotspot seems to extend towards the south, and the difference image in Figure 2.5 indicates that this may be a weaker, separate hotspot forming on the southern rim of the remnant.

Super-resolution is, in effect, an extrapolation of the u-v data out to projected interferometer spacings beyond those measured by the telescope. However, the long integration times, extensive u-v coverage obtained and the simplicity of the structure in the resultant images justify a moderate increase in resolution over that dictated by diffraction theory (Narayan & Nityananda 1986). The consistency of the results further adds to the credibility of the method: in 12 (three for each year) independent data-sets, each with different $u-v$ coverage and with differing noise levels, the same features are reproduced in Figure 2.4 — a roughly circular shell, with bright lobes to the east and west. For comparison, corresponding images of ATCA J053604–691844

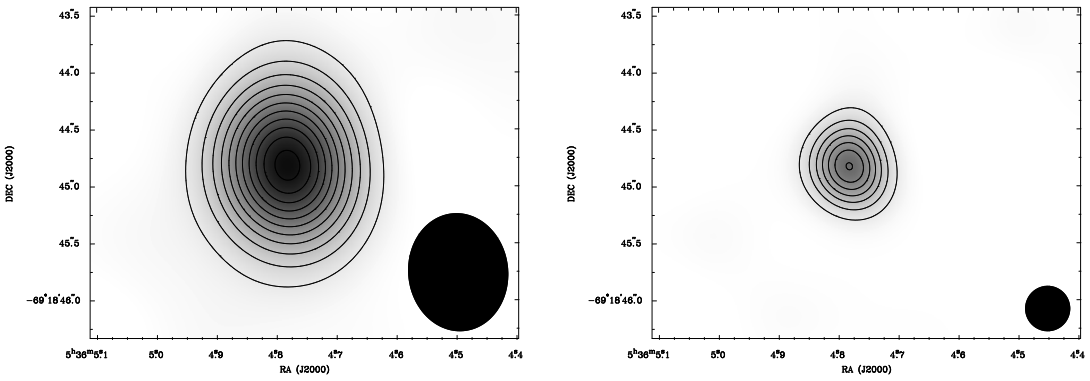

Figure 2.6 Diffraction-limited and super-resolved images of ATCA J053604–691844 at 9 GHz, using data from epoch 1995. For the diffraction-limited image, the grey-scale runs from –0.1 to 6.0 mJy beam^{-1}, and the contours run from 0.5 to 6.0 mJy beam^{-1} at 0.5 mJy beam^{-1} intervals. For the super-resolved image, the grey-scale is from –0.1 to 5.0 mJy beam^{-1}, with contours from 0.5 to 5.0 mJy beam^{-1} at 0.5 mJy beam^{-1} intervals. The FWHM of the restoring beam is shown at lower right in each case.

are shown in Figure 2.6. These show that for a simple unresolved source, super-resolution behaves as expected, producing a Gaussian region of emission with a reduced half-width and with an unchanged total flux density. A more in-depth study on the reliability of super-resolved images is described by Briggs (1994, 1995).

Figure 2.7 shows a comparison between the super-resolved radio image from 1995 and a *HST* WFPC2 image of the central source and the surrounding inner optical ring (Burrows et al. 1995). The images were aligned by first establishing an accurate position for the central source in the *Hipparcos* optical reference frame, and then linking this with the radio reference frame as determined by VLBI (Reynolds et al. 1995). The residual uncertainty between the VLBI reference frame and the ATCA image is $\sim 0\farcs05$. The position angles of the two opposed brightness enhancements in the radio image are similar to that of the major axis of the optical ring (PA $\approx 81°$). Although the minimum in the radio emission aligns closely with the central source, this is not so in earlier images, and is not considered significant.

Polarisation

Images were formed in the Stokes parameters Q, U and V, deconvolved using the `CLEAN` algorithm and restored with a diffraction-limited beam. A linear polarisation, L, image, was formed by combining Q and U. In the 1992, 1993 and 1994 data, no linear polarised emission was detected from the radio remnant. In the 1995 data, there is a marginal (2σ) detection from a region in the southwest of the remnant, corresponding to a total fractional polarisation of $\sim$0.01%. No circularly polarised emission was detected at any epoch.

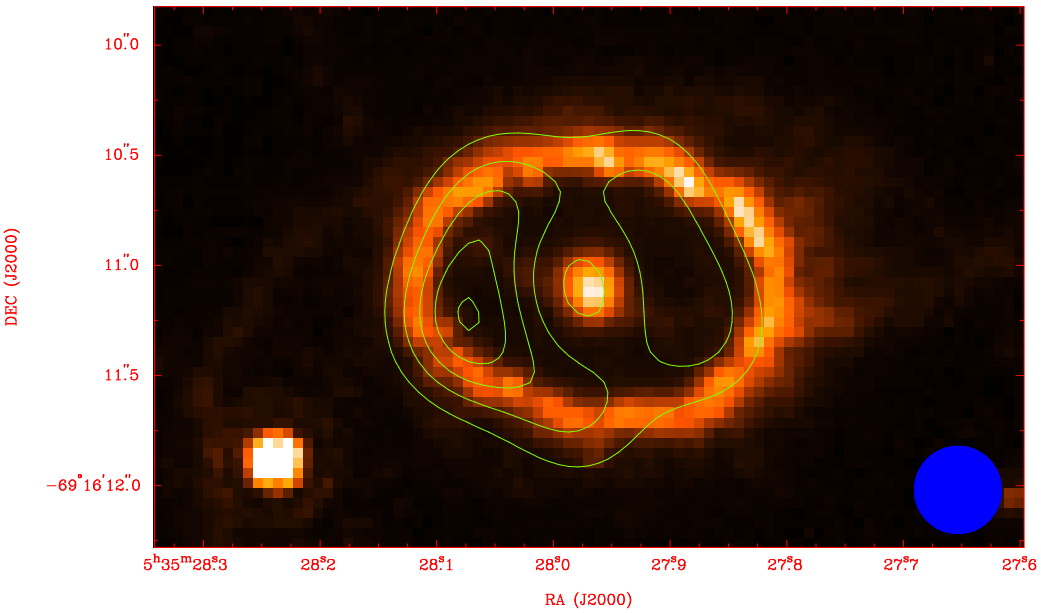

Figure 2.7 A comparison of *HST* and ATCA images of SN 1987A. Contours show the 1995 epoch of the super-resolved ATCA 9 GHz data. Contours run from 0.4 to 2.0 mJy beam^{-1} at 0.4 mJy beam^{-1} increments. At bottom right is shown the 0.″4 FWHM restoring beam. The grey-scale is a *HST* WFPC2 image of SN 1987A in Hα + [NII] (Burrows et al. 1995), to which the reference frame of Reynolds et al. (1995) has been applied. The point source at the lower left of the *HST* image is an unrelated field star (star 3 of Walker & Suntzeff 1990).

Expansion of the remnant

Using the method described in Paper S2, we obtain an estimate for the size of the radio remnant at each epoch by fitting a two-dimensional projection of a thin, spherical shell to 9 GHz u-v data. We have used all the data shown in Figure 2 of Paper S3, as well as that in Table 2.1. The results of the model fitting are shown in a plot of radius versus time in Figure 2.8. For the most recent (1995 Nov) data, a radius of $r = 0.''685 \pm 0.''005$ is obtained, 84% of the radius of the optical ring (Burrows et al. 1995).

A power-law fit to the data of the form $r/r_0 \propto (t/t_0)^m$ (where t is the time since the SN explosion and $t_0 = 1800$ d) gives $r_0 = 0.''641 \pm 0.''006$ and $m = 0.12 \pm 0.02$. At day 3200, this corresponds to an expansion rate of 9 ± 2 mas y^{-1}, which at a distance of 50 kpc translates to 2200±400 km s^{-1}. The value obtained for m is slightly less, but consistent with, the value $m = 0.17 \pm 0.08$ obtained using data up to day 2100 (Paper S3).

A power-law fit implies that the shock is currently decelerating. However, the data are equally well fitted by a straight line. This line does not pass through the origin, indicative of a rapid deceleration in the past but minimal deceleration in the present. Such a fit gives an expansion rate of 12 ± 2 mas y^{-1} (2800±400 km s^{-1}).

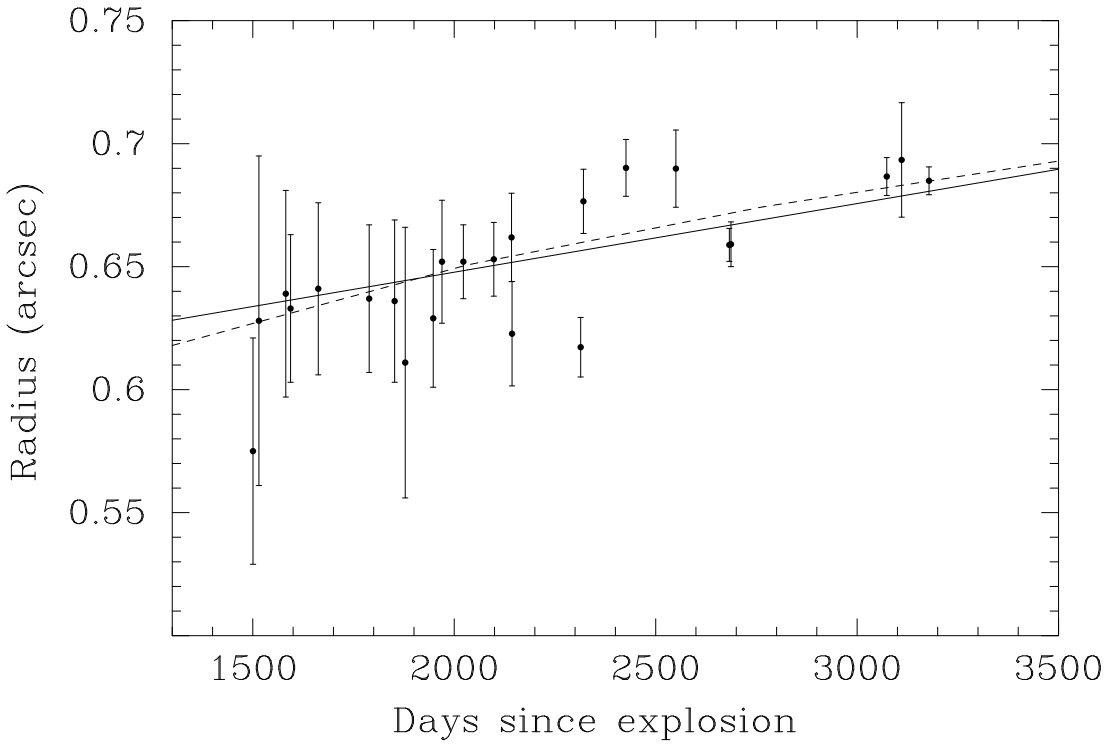

Figure 2.8 The radius of the radio remnant as a function of time, as determined by fitting a thin spherical shell of arbitrary position, flux density and radius to the $u-v$ data for 9 GHz observations in Paper S3 and in Table 2.1. The broken line is a power-law fit to the data of the form $r \propto t^m$, with $m = 0.12$. The solid line is a linear fit to the data, with slope 32 μas day^{-1} and with $r = 0\farcs642$ at $t = 1800$ days.

This is the value used in subsequent discussion.

Modelling directly in the u-v plane is a robust and consistent way of quantifying the relative size of the remnant as a function of time, and the results are not complicated by issues of deconvolution and resolution. However, it is clear that as time progresses, the approximation of a thin spherical shell becomes less and less justified, and measurements of the angular size may be skewed by the changing appearance of the remnant. Therefore, to confirm these results, the size of the remnant was also measured directly in the image plane.

For each super-resolved image of SN 1987A, the radius of the remnant was measured along lines joining the position of the central optical source (Reynolds et al. 1995) and the northern maximum, southern maximum, eastern saddle and western saddle, out to the point where the intensity falls to 50% of its value at the respective maximum or saddle. These measurements show no measurable expansion in any direction, with an upper limit of $\sim$7000 km s^{-1}. Although this method is somewhat crude, it is consistent with the result obtained from the $u-v$ fitting above.

We find that the eastern side of the remnant is $\approx 130 \pm 70$ mas further from the central source (in projection) than the other components. Reynolds et al. (1995)

noted a similar displacement by comparing the centre of symmetry of the 1992 epoch image to the position of the central source.

2.4 Discussion

2.4.1 Flux Density

Long-term Behaviour

The second turn-on in radio emission from SN 1987A (Paper S1) has generally been understood as being caused by the shock encountering a sudden increase in the density of the CSM, presumed to be the reverse shock of the BSG wind (Chevalier 1992a; Beuermann et al. 1994). Blondin & Lundqvist (1993) point out the possibility that no reverse shock exists, so that radio emission must somehow be generated by density enhancements of unknown origin in the free wind. However, the good fit to the radio light curve produced by both simple (Paper S4) and detailed (DBK) models, and the good evidence presented in Sections 2.3.2 and 2.4.2 for deceleration, are both strong arguments in favour of the shock having encountered a region of increased density.

Models of such an encounter with the shocked BSG wind predict that the flux density should level off or begin to decrease (Chevalier 1992a; DBK). Yet it is clear from Figure 2.1 that the flux density continues to rise. The ellipsoidal geometry of the BSG wind cavity may be a contributing factor, in that the distance to the density jump is greatest along the symmetry axis of the progenitor system (Blondin & Lundqvist 1993). The radio flare produced by the encounter of the shock with dense material is consequently spread out over a greater period of time before decaying. However, the morphology of the remnant suggests that emission along this axis does not contribute significantly to the total flux (see further discussion below in Section 2.4.4). Another possibility is that the presence of toroidal magnetic fields within the BSG wind-bubble serves to boost the radio emission (Chevalier & Luo 1994). This model can probably be ruled out though by the low level of linear polarisation observed, which argues against the presence of magnetic fields with such a well-defined geometry (Section 2.4.3 below). A recently proposed alternative is that the shock has encountered an ionised region of the RSG wind located inside the optical ring (CD95). This H II region is calculated to be $\approx$400 times more dense than the stagnation zone of the BSG wind. The large consequent deceleration experienced by the shock, combined with the increased particle injection, could sustain the radio flux density as is observed.

We do not attempt to model the radio light curves, other than to note that the simple model of Paper S4 for flux densities up to day 2300 still fits the data to a reasonable extent over the increased time period. The morphology of the remnant is becoming increasingly asymmetric with time — not only are there two strong hotspots, but they are brightening at different rates, and new features may be forming. Thus it is clear that the assumption made in earlier analyses of a spherical

emitting region (DBK; Paper S4) is no longer valid, and that more complex two- or three-dimensional modelling is now required. Such a study is beyond the scope of this Chapter.

Short-term Behaviour

In the ATCA data presented in Figure 2.1, small-scale fluctuations in SN 1987A's flux density are apparent at all four frequencies over time-scales of ∼100 days (comparable to the spacing between observations). This is in contrast with MOST data, for which Ball et al. (1995a) conclude that there have been no variations of amplitude >2% on time-scales between 30 and a few hundred days. In Paper S1, 4.8 GHz variations were reported at the level of ∼20% over a two-day period, six months after the radio emission reappeared. However, since then the sampling interval has been far coarser, and we are unable to determine if such short-period variability is still occurring.

The nature of the ATCA means that flux densities are not as accurate as those measured by the MOST. While the MOST has complete coverage in the $u-v$ plane over a full 12-h synthesis and obtains all spatial frequencies from 43λ to 4415λ, the ATCA has just 15 baselines spread over 6000 m. In addition, frequency switching and phase calibration means that only about a third of the time can be spent integrating on SN 1987A at a given frequency. These effects produce large sidelobes in the resultant images. Figure 2.1 suggests that flux density variations become more pronounced at higher frequencies. However, this is likely the result of atmospheric phase variations which, at 4.8 and 8.6 GHz, can cause the signal to decorrelate. There is the suggestion of some correlations between frequencies which were observed simultaneously (1.4/2.4 GHz or 4.8/8.6 GHz), but the factors discussed above will affect the data at both such frequencies similarly. We conclude that the small-scale changes in flux density seen in ATCA data are probably not significant — the light curve obtained by MOST is far more reliable.

Spectral index

Observations in the first year after the radio emission re-appeared showed significant variations in the spectral index (Paper S1). Correcting for the ATCA revised flux density scale (Reynolds 1994), the spectrum flattened from $\alpha < -1.6$ ($S \propto \nu^{\alpha}$) on day 1243 to $\alpha = -0.91 \pm 0.05$ on day 1517, before possibly steepening to $\alpha = -0.99 \pm 0.04$ on day 1595.

The data in Figure 2.2 show that within the uncertainties, the spectrum did not vary from day 1787 (1992 Jan) to day 3325 (1996 Apr). The average value over this period is $\alpha = -0.95 \pm 0.04$, consistent with the value at day 1595 (1991 Jul).

In the model of DBK, the shock compression ratio, $\rho = 1 - 3/2\alpha$, begins at its maximum value of 4 when the explosion occurs, and consequently decreases because the shock is modified by the acceleration of cosmic rays. The compression ratio then lies on a plateau ($\rho \approx 2.7$) for an extended period before then rapidly decreasing

again. In DBK's standard model, the plateau phase lasts until approximately day 2000, and by day ∼3000, $\rho < 2$ (α steeper than –1.5). However, observations imply that on day 3325, $\rho = 2.58 \pm 0.11$. For comparison, the spectrum on day 1517 corresponds to $\rho = 2.65 \pm 0.14$.

So, while we indeed observe a plateau, our results indicate that this phase is considerably more extended than predicted, and that accelerated protons are yet to smooth out the shock completely. In DBK's model, the behaviour of ρ as a function of time depends on the distance from the progenitor star of the density jump responsible for the radio emission. DBK's Figure 7 shows that if this jump is moved further from the star, the plateau region does become more extended. The model of DBK assumes that the density jump encountered is the termination shock of the BSG wind. However, if, as discussed above, the cause of the radio emission is an ionised region of the RSG wind, the greater distance of this component from the progenitor can, in the context of this model, explain the constant spectral index. CD95 roughly estimate that the contact discontinuity with the RSG wind is 20% further from the star than the termination shock of the BSG wind.

The increasingly asymmetric morphology of the remnant implies that a direct interpretation of the spectral index in terms of a single shock compression ratio may be overly simplistic. For example, because structural information is only available at 9 GHz, we are unable to determine if different regions in the remnant have different spectra, as is observed in SN 1993J (Marcaide et al. 1995b). If this is the case, an explanation for the observed constancy of the spectral index may require further insight.

2.4.2 Expansion of the Remnant

Between the SN event in 1987 Feb and the second radio turn-on in mid-1990, a mean expansion rate can be calculated for the remnant of ∼35 000 km s^{-1}. This is consistent with free expansion since the explosion (Hanuschik & Dachs 1987). However, by 1993 Jan, the remnant appeared to be expanding at only 4800±2300 km s^{-1} (Paper S3). While this seemed to indicate considerable deceleration, there was only a 20-month period over which measurements of the remnant's size had been made, and the low signal-to-noise ratio meant that the errors in these measurements were large. Also, an image was available at only one epoch, so that the possibility that the remnant was rapidly changing shape could not be ruled out.

However, over a period three times longer than previously possible, a low expansion velocity of 2800±400 km s^{-1} is still obtained. The succession of images demonstrates that the shell does not appear to be changing in its gross form — we therefore conclude that the explanation in Paper S3 for the observed deceleration is incorrect, and that the expansion speed obtained is realistic.

One explanation for the extremely low expansion velocity is that the emission observed is not from the shock at all, but from stationary or slowly moving clumps of material in the BSG wind. In this model, the shock is now considerably further from the star than the remnant we observe. However, the emission continues to

increase at all radio frequencies, and the spectral index is not steepening. Both these observations are difficult to explain if electrons are not continuing to be accelerated in the emitting regions. We therefore favour the alternative, that emission from the radio shell traces the expanding shock front.

The fastest ejecta contain only a small fraction of the total mass. For example, in the model of Luo et al. (1994), the ejecta have a density profile $n \propto v^{-9}$ for $v > 4000$ km s^{-1}. Thus it might be argued that while the fastest ejecta are responsible for the radio turn-on at day 1200 (and have since been decelerated), the main body of slower moving material has now caught up with this material, and that it is the relatively unimpeded expansion of these ejecta which we are now observing.

In a simple calculation, v, the mean velocity from day 0 to day t of ejecta currently at radius r, is given by

$$v = 18.6 \times 10^3 \text{ km s}^{-1} \left(\frac{r}{0\farcs687}\right) \left(\frac{t}{3200 \text{ days}}\right)^{-1} \tag{2.1}$$

where $r = 0\farcs687$ is the angular size of the remnant at $t = 3200$ days, using the linear fit in Figure 2.8. Since in reality ejecta may have decelerated in reaching a radius r, v is a *lower limit* on the initial velocity of the ejecta currently at this distance.

From Equation (2.1), we see that while the initial radio turn-on ($r \approx 0\farcs5$, $t \approx$ 1200 days) requires ejecta of velocity $\sim$35 000 km s^{-1}, emission from a thick shell at day 3200 still requires ejecta for which v = 10 000–20 000 km s^{-1}. The consequence of this is that most of the mass ejected by the supernova cannot yet have reached the radio emitting regions — the remnant is the result of rapidly moving material which was significantly decelerated at some time in the past, presumably around the time that radio emission was re-detected. Figure 2.8 is consistent with minimal deceleration from day 1500 to day 3500, but we cannot rule out the possibility that deceleration continues to take place.

This apparent deceleration would appear to be the best observational evidence yet that the shock has encountered a marked increase in density. CD95 argue that this deceleration is further evidence for an encounter with the dense, ionised RSG wind. From their model, we calculate a *mean* velocity for the shock while it is in this region of 6100$\pm$1200 km s^{-1}. If the remnant continues to decelerate, a still denser component may be required to explain the observations.

When the fastest ejecta reach the circumstellar ring, the system is expected to become a strong source of optical and UV line emission, and the X–ray and radio luminosity should show a rapid increase (Luo & McCray 1991; Luo et al. 1994). This has clearly not yet occurred, and limits even the fastest ejecta to a mean velocity of $\approx$22 000 km s^{-1} from day zero to day 3200. Assuming that the remnant continues to expand at its current rate, our results indicate that the shock will reach the ring in the year 2006$\pm$3, which agrees with the prediction of 2003 from X–ray observations (Hasinger et al. 1996). This is also consistent with hydrodynamic models (e.g. Suzuki et al. 1993; Luo et al. 1994), the most recent estimate being 2005$\pm$3 (CD95). However, further deceleration of the ejecta could delay the encounter considerably.

In Section 2.3.2, we suggested that the eastern region of the remnant may be further from the centre of the explosion than other regions. If this is the case, then this region either had the highest initial velocity, or has been decelerated the least. That it is also the brightest region favours the former. This could represent anisotropy in the explosion, as discussed below in Section 2.4.4.

2.4.3 Polarisation

The radio emission from the remnant is believed to be synchrotron emission (Ball & Kirk 1992; Paper S4), and so is expected to be associated with high degrees of linear polarisation. However, the remnant is comparable in size to the synthesised beam of the telescope, and so there may exist variations in position angle of the electric field vectors over spatial scales smaller than this beam. In addition, the projected direction of the magnetic field could also be varying along the line of sight. Both these effects can smear out any linear polarisation and give a low value for L. From the low level of polarisation observed, we can conclude that the magnetic field is disordered on a scale of $\sim 0\farcs5$ (0.1 pc), and certainly is not well organised within each hotspot.

2.4.4 Morphology of the Radio Emission

It is well established that the triple-ring optical nebula surrounding the supernova has cylindrical symmetry, with the axis inclined at $\approx 43^\circ$ to the line of sight and at a position angle of $\approx -9^\circ$ on the plane of the sky (Jakobsen et al. 1991; Burrows et al. 1995; Plait et al. 1995). The supernova event itself also appears to have had a similar symmetry, the envelope being extended along the axis of the cylinder (Karovska et al. 1989). It is generally accepted that the axisymmetric geometry observed coincides with the axis of rotation of the progenitor star, or possibly with the axis of a progenitor binary system.

An optically thin cylindrical shell of radio emission inclined at $\sim 45^\circ$ to the line of sight will show two brightness enhancements on the inclination axis. Thus in Figure 2.7, the alignment of the two opposed radio hotspots with the major axis of the optical ring argues that, to first order at least, the radio emission has the same symmetry as the optical nebula. However, the enhanced brightness from the eastern limb of the radio remnant breaks this symmetry, and indicates that the true geometry is still more complex. Models of the flux density cannot distinguish between ring and spherical geometries for the radio emission (Ball et al. 1995b). However, the non-zero level of emission in the centre of the radio shell argues that, unlike the inner ring, the remnant is quasi-spherical and extended in three dimensions.

DBK attribute the anisotropies observed in the 1992 image to minor variations in conditions at the shock, and assume that the system is essentially spherically symmetric. However, the persistence of these anisotropies, and the increase of the asymmetry with time, argue that the non-spherical nature of the morphology is significant. Bartel et al. (1991) suggest three explanations for the asymmetries

observed in the radio remnant of SN 1986J: a central pulsar could be affecting the morphology in some way, the explosion may have been asymmetric, or the CSM into which the shock is expanding is not isotropic. Each of these could also influence the evolution of SN 1987A, and we consider the three possibilities in turn.

Effect of a Central Pulsar

Neither pulsed emission (e.g. Manchester & Peterson 1996) nor a central compact source (Paper S1) has yet been detected in the remnant of SN 1987A. Although the detection of neutrinos from the initial explosion suggests that a neutron star was formed, it may have undergone subsequent collapse to form a black hole (Chevalier 1992b). If this is not the case, effects such as luminosity, beaming, scattering and absorption may still prevent the detection of pulsed emission (Manchester 1988).

While the radio emission observed is clearly not "plerionic", it has been proposed that the formation of two opposed regions of enhanced emission in shell supernova remnants (SNRs) can be explained by jets or cones of emission from a central neutron star (Manchester 1987; Willingale et al. 1996). However, the lack of radio emission for several years between the SN event and the second turn-on, the steep spectral index, and the increasing asymmetry between the eastern and western hotspots cannot be explained by this model in its simplest form, and we consider it an unlikely explanation for the radio emission. It is worth noting that a model involving a pulsar with precessing jets has been proposed to explain the optical triple-ring nebula (Burderi & King 1995).

An Asymmetric Explosion

There is reasonable evidence that supernova ejecta are not distributed isotropically. Models of SNe involving rotating progenitor stars produce excess ejecta in the equatorial plane (Bisnovatyi-Kogan 1971; Bodenheimer & Woosley 1983), and there is observational evidence to suggest that this can influence the morphology of an evolved SNR (Tuohy et al. 1982; Kesteven & Caswell 1987).

For a spherically symmetric ambient medium with no large-scale magnetic fields, the radio emission from the remnant will peak where the shock is strongest. Indeed, several authors have argued for a spherically symmetric BSG wind (e.g. Martin & Arnett 1995) and the lack of polarisation detected in the radio emission indicates that the magnetic field is disordered on small scales. With such simplifying assumptions, the alignment of the radio morphology with the presumed equatorial plane of the progenitor star suggests that the ejecta were predominantly toroidal. In addition, the shell is faintest in the north and the south, as would be expected if ejecta were primarily generated in the equatorial plane.

There are problems with this conjecture, however. First, the suggestion that a third, southern, hotspot may be forming in the shell (as shown in Figure 2.5) is difficult to explain. Second, the assumption that the CSM which the shock is encountering is spherically symmetric may well be a naive one, as discussed further

below. Finally, although there is much evidence from both optical polarimetry and asymmetry in the line emission from the supernova to suggest that the envelope and ejecta were axisymmetric (Cropper et al. 1988; Méndez et al. 1988; Karovska et al. 1989; Pun et al. 1995), most observations have extensions being produced predominantly in the *polar* directions. This is at odds with the equatorial dominance required here. However, the asymmetries represented in optical observations may only be of very low mass (e.g. Utrobin et al. 1995) and may not be representative of the overall shock front. VLBI observations of SN 1993J have indeed shown that early measurements of asymmetry in the SN event need not translate to the morphology of the radio shell (Marcaide et al. 1995a). Also, simulations of axisymmetric ejecta show that the resulting shock front is almost spherical (Blondin et al. 1996). Given these results, we cannot completely rule out this hypothesis.

Rather than producing a toroidal ejection of material, SNe can also be directional in their anisotropy, as evidenced by the kicks imparted to neutron stars (Kaspi et al. 1996a; Petre et al. 1996). In Section 2.3.2, it was shown that the eastern limb may have expanded slightly further than the western limb, which may be the result of more rapidly moving material being ejected in this direction. We note that optical spectroscopy of SN 1987A also gives evidence for such an event (Stathakis 1996).

Asymmetries in the CSM

The nature of the triple-ring nebula surrounding SN 1987A is not completely understood (Burrows et al. 1995; Burderi & King 1995; Panagia et al. 1996). However, it is generally agreed that its existence is consistent with the mass-loss history of the progenitor star Sk–69°202. Several authors have proposed as an explanation the interaction of an equatorially enhanced RSG wind with a spherically symmetric BSG wind (Luo & McCray 1991; Wang & Mazzali 1992; Martin & Arnett 1995; CD95). Other possibilities include a spherically symmetric RSG interacting with an axisymmetric BSG (Blondin 1994), the effect of a binary companion (Podsiadlowski et al. 1991; Lloyd et al. 1995) and the presence of a proto-stellar molecular disk (McCray & Lin 1994). In any case, it is accepted that the surrounding CSM is not spherically symmetric.

Chevalier & Luo (1994) have argued that the onset of radio emission from SN 1987A can be explained by toroidal magnetic fields in the BSG wind bubble. Only a slight enhancement in the magnetic field of the equatorial regions above the poles is required to produce the observed morphology (DBK). But as discussed in Section 2.4.3, the lack of observed polarisation makes this explanation unlikely.

A plausible explanation for the hotspots observed in the radio emission is that these parts of the shock have simply encountered denser regions of the CSM than the fainter regions. This could be because the transition to the shocked wind occurs closer to the star in the bright regions, or because the density of the shocked wind varies with polar angle. These two possibilities are not mutually exclusive, and we consider the implications of each below.

If the termination between the free and shocked winds is not spherical, but is

extended along the symmetry axis (Blondin & Lundqvist 1993; CD95), the equatorial regions of the SN shock encounter the denser, shocked wind before the polar regions do. The polar regions can also be expected eventually to reach the shocked component of the wind, at which time the remnant might begin to take on a more uniform brightness distribution. The suggestion in the 1994 and 1995 super-resolved images (Figure 2.4) and in the difference image (Figure 2.5) that the southern rim of the radio shell is now beginning to brighten may indicate that this is already happening.

The fact that the eastern hotspot is brighter than its western counterpart can be understood if this side of the expanding remnant reached the density jump first. This may correspond to the two-clump model of DBK, where the SN shock encounters two clumps of material with a ∼120 day delay between them. No third jump in the light curve is seen which might correspond to the formation of a new hotspot to the south (A. J. Turtle 1996, private communication), although its contribution to the total flux density would be low. This difference between the eastern and western sides of the remnant can be explained in terms of a break in the cylindrical symmetry of the surrounding CSM, although this could be at odds with the high degree of symmetry observed in the optical emission (Burrows et al. 1995). Light travel times may also have an effect (Ball et al. 1995b), but a more appealing prospect is that it is a result of the possible directional anisotropy in the initial explosion discussed above. If higher velocity ejecta were produced on the eastern side of the remnant, this can also explain why the eastern hotspot continues to brighten more rapidly than that in the west.

While the shocked wind is believed to have a constant density in the radial direction (e.g. DBK), it has been argued that the density may well vary with polar angle (Blondin 1994), so that even after all parts of the SN shock have reached the denser component of the wind, particle injection may be greatest around the equator. Such an axisymmetric density distribution in the CSM should produce extensions in the north-south direction (Paper S3; Blondin et al. 1996). Although such extensions are clearly not observed, Blondin et al. (1996) estimate that protrusions along the poles only become significant ∼10 yr after the explosion, and so may not necessarily be expected to occur at the current time.

It is worth noting that the amount of anisotropy in the CSM required to produce the observed morphology is low. Around any given circumference on the shell in the 1995 super-resolved image (Figure 2.4), the ratio of maximum to minimum brightness is no more than three. Using Equation (4.7) of Paper S4, this corresponds to a ratio of the ambient density between the equatorial and polar regions of ∼1.7. Most models can easily account for such a difference, even if the shock is yet to reach the densest regions (Luo & McCray 1991; Blondin & Lundqvist 1993).

Comparison to Other RSNe and SNRs

SN 1986J, one of the most luminous RSNe known, was imaged in 1988 by Bartel et al. (1991). It was then of comparable age to SN 1987A, and also had a radio

remnant quite similar in morphology; it too had two opposed hotspots, one brighter than the other, superimposed on a rough circular shell. SN 1986J also has several protrusions extending beyond the shell. These appear to extend from local minima in the rim, and might be representative of the features discussed by Blondin et al. (1996) which are produced by the expanding SN shock in the less dense, polar, regions of an axisymmetric progenitor wind. As noted above, such features may, with time, become apparent in SN 1987A.

Marcaide et al. (1995b) present a time sequence of images of the remnant of SN 1993J, taken between 6 and 18 months after the explosion. Unlike SN 1987A, clear expansion has been detected for this object — an expansion index of $m \approx 0.9$ ($r \propto t^m$) has been measured right from day zero, indicating minimal deceleration. At 8.3 GHz, the shell of SN 1993J is almost circular, and has relatively small (compared to SN 1987A) brightness variations around its circumference. Marcaide et al. (1995a) attribute these variations to small inhomogeneities in the CSM, possibly produced by a binary companion to the progenitor.

In SN 1993J, we have a remnant which has so far undergone minimal deceleration, and which is also reasonably uniform in its shape and brightness. If, from this, we argue that it is the same physical process which causes both the deceleration of a shock front and a non-uniform appearance for the radio remnant, then we are led to the conclusion that it must be a non-uniform CSM which gives SN 1987A its appearance.

The connection between radio supernovae and evolved supernova remnants is unclear (Weiler et al. 1986; Wilkinson & de Bruyn 1990), and there is the intriguing possibility that having long ago passed through its RSN stage, SN 1987A may be, as suggested in Paper S3, in the very early stages of an evolution corresponding to that of a classical SNR. Manchester (1987) has argued that the passage of the SN shock through the progenitor wind, as is occurring in the case of SN 1987A, can "imprint" a remnant with a morphology which it retains through to an evolved state. For example, the small-scale symmetry of SNR G296.5+10.0 is indicative of the remnant's being shaped by events early in its lifetime (Storey et al. 1992). However, it is clear that the large-scale ISM (Landecker et al. 1982a; Braun & Strom 1986), as well as possibly large-scale magnetic fields (Roger et al. 1988; Fulbright & Reynolds 1990), may both have a large effect on a remnant's morphology.

At low resolution, the bipolar, but asymmetric, appearance of older supernova remnants such as SNR G308.8–0.1 and SNR G320.4–1.2 (Whiteoak & Green 1996) is suggestive of the morphology of SN 1987A. Such a comparison is, at least for now, pure speculation, although continued observations of SN 1987A over the next decade and beyond may give hints as to what this object might one day become.

2.5 Conclusion

In this Chapter, we have reported on all ATCA observations of SN 1987A from 1989 up to mid-1996, with the following main results:

1. The total flux density has increased monotonically since radio emission was redetected in 1990.
2. The spectral index has remained constant since 1992 Jan at $\alpha = -0.95 \pm 0.04$.
3. Assuming that the observed radio emission traces the shock, the remnant is the product of initially rapidly moving ($v = 10\,000$–$35\,000$ km s^{-1}) ejecta, which have subsequently decelerated to $v \approx 3000$ km s^{-1}. Assuming continued expansion at this velocity, the shock will encounter the inner optical ring in the year 2006±3.
4. The eastern and western regions of the remnant align with the major axis of the optical ring, and are brighter than the northern and southern regions.
5. The eastern limb is brighter than the western limb, and is also increasing in brightness more rapidly.
6. Material on the eastern side of the remnant may have travelled further from the explosion than the rest of the remnant.

We propose the following basic theory. Points 1, 2 and 3 above are consistent with the shock reaching a sudden increase in the density of the CSM. This is believed to be either the termination shock of the BSG wind, or the contact discontinuity to the RSG wind. The increased density and distance from the star of the latter region can perhaps better explain the observations.

Point 4 is good evidence that the shocked wind is axisymmetric in its shape and/or density distribution. That deceleration of a remnant seems coupled with distortion of its morphology (cf. SN 1993J) is also a good indication that the CSM is probably the cause for the observed structure. We expect that as the shock further expands into this axisymmetric CSM, the polar regions will elongate and eventually brighten. If observations show these regions remaining faint and becoming retarded in their expansion, an alternative explanation could be a toroidal distribution of ejecta.

Points 5 and 6 can be explained by the shock on the eastern side of the remnant reaching the density jump first. We propose that this may indicate a directional anisotropy in the SN explosion.

Monitoring and imaging SN 1987A with the ATCA will continue. In addition, the forthcoming upgrade of the ATCA to operation at frequencies up to 25 GHz will allow diffraction-limited images of SN 1987A down to a resolution of $\sim 0\farcs4$. With such data, a better study of existing and new features will be possible. With resolved images at both 9 and 25 GHz, spectral index variations across the remnant will also be detectable, which may show differences in the energetics of hotspots and of the polar regions. For example, the brightest region of SN 1993J also appears to have the steepest spectrum (Marcaide et al. 1995b).

It is not clear exactly what will happen to the radio emission when the shock reaches the optical ring — much will depend on the nature of the unshocked RSG wind and its density distribution, an issue on which current models are undecided. It is entirely possible that the appearance of the remnant once it has passed into

this region will be quite different to what we see now. In any case, SN 1987A will likely become a spectacular object in all wavebands, and we will continue to observe it regularly in anticipation of this event.

Chapter 3

The Nature of Bilateral SNRs

This Chapter has also appeared as Gaensler, 1998, "The nature of bilateral supernova remnants", ApJ, **493**, 781.

3.1 Introduction

High resolution observations of radio supernova remnants (SNRs) have revealed exceedingly complex structures. The appearance of a SNR can tell us much about the supernova (SN) explosion itself, the nature of any central compact object, the circumstellar medium (CSM) of the progenitor, the surrounding interstellar medium (ISM), and the properties of the ambient magnetic field. Indeed the difficulty in interpreting SNR morphologies has always been in disentangling the competing effects and in determining which ones dominate during the different evolutionary stages.

Perhaps the longest running debate concerning SNR morphologies has been over the classification referred to as bilateral, bipolar, axially symmetric, or "barrel" SNRs. These remnants are characterised by a clear axis of symmetry, low levels of emission along this axis, and two bright limbs on either side (e.g. Gardner & Milne 1965; Whiteoak & Gardner 1968; Roger & Costain 1976; Kesteven & Caswell 1987, hereafter KC87; Roger et al. 1988; Caswell et al. 1992). It is generally accepted that bilateral SNRs represent an underlying cylindrical symmetry, the emitting regions corresponding to the curved walls of the cylinder (KC87). A bilateral appearance is then produced when the "barrel" axis is approximately in the plane of the sky, the two bright flanks running parallel to this axis.

Many mechanisms for generating a bilateral appearance have been suggested (see Bisnovatyi-Kogan & Silich 1995 for a review). However, it is not clear which of these models, if any, actually apply. Indeed, given the diversity in the environments and ages of Galactic SNRs, several of the mechanisms proposed may be valid. We emphasise that observations demonstrate that many SNRs are not bilateral. To some extent, this can be accounted for by viewing angle (see KC87 and Section 3.6.4 below), but it is important to keep in mind that whatever mechanism is invoked, the morphology may be dominated by small scale effects such as the inhomogeneity

of the local environment.

We now briefly outline previously proposed explanations for bilateral SNRs. Explanations can be divided up into two categories: "extrinsic", relating to the ambient ISM and magnetic field, and "intrinsic", relating to the progenitor, its CSM, the SN explosion itself, and any compact stellar remnant.

3.1.1 Extrinsic Explanations

The simplest model to explain a bilateral appearance is that it is the result of the density structure of the surrounding ISM. Simulations show that when a remnant expands inside an elongated, or tube-like, cavity, it quickly takes the shape of that cavity, and a bilateral appearance can be produced (Bisnovatyi-Kogan et al. 1990).

It has long been realised that the geometry of the ambient magnetic field can also affect the appearance of a SNR. We collectively refer to models relying on the ambient field as "magnetic". In a uniform magnetic field, the shock front produced by an expanding SNR will preferentially compress the field where the shock normal is perpendicular to the field lines. Thus, in a well-ordered ambient field with a significant component in the plane of the sky, enhanced emission along two limbs is generated, producing a bilateral appearance (van der Laan 1962b; Whiteoak & Gardner 1968).

Argument is divided as to whether this mechanism can produce the observed ratio of maximum to minimum intensity around the circumference of SNRs which are in the adiabatic phase of evolution (Fulbright & Reynolds 1990, hereafter FR90; Ratkiewicz et al. 1994). Thus, an extension of this model has been proposed, in which the efficiency of particle acceleration by the SN shock depends on the angle between the shock normal and the orientation of the ambient magnetic field (Jokipii 1987; Roger et al. 1988; FR90). FR90 argue that the bilateral appearance in the adiabatic phase can best be explained by "quasi-perpendicular" acceleration, in which acceleration is most efficient (and synchrotron emission strongest) where the shock normal and the field are at right angles. "Quasi-parallel" models (where the shock normal and the field are aligned) can also produce a bilateral appearance at some orientations, but at other orientations produce morphologies which are never observed (FR90, but see Zhang et al. 1996).

3.1.2 Intrinsic Explanations

There are a number of symmetry axes associated with the progenitor system and the explosion. Several mechanisms have been suggested by which these symmetries can produce a bilateral appearance. Models include a toroidal distribution of ejecta (Bodenheimer & Woosley 1983; KC87), the effect of a high velocity progenitor (Różyczka et al. 1993; Brighenti & D'Ercole 1994), the distribution of mass loss and magnetic field in the CSM produced by the progenitor (Manchester 1987; Igumenshchev et al. 1992; Storey et al. 1992; Zhang et al. 1996), and the influence

of outflows from a central compact object (Manchester & Durdin 1983; Willingale et al. 1996).

3.1.3 A Statistical Approach

Understanding the morphology of an individual SNR can be difficult, often requiring a concerted multi-wavelength campaign. Only a few bilateral SNRs can be considered to be well-studied (most notably G296.5+10.0 and G327.6+14.6) and even these objects provoke controversy (e.g. compare Roger et al. 1988 with Storey et al. 1992). An alternative approach is to consider the common properties of bilateral SNRs on a statistical basis.

There is reasonable evidence that at least for low latitudes, the Galactic magnetic field is well-ordered and generally runs parallel to the Galactic Plane when projected onto the sky (Mathewson & Ford 1970; Manchester 1974; Ellis & Axon 1978; Sofue & Fujimoto; Rand & Kulkarni 1989; Reid & Silverstein 1990; see also reviews by Sofue et al. 1986 and Beck et al. 1996). If a bilateral appearance is caused by a magnetic model, one might expect the structure of the Galactic magnetic field to manifest itself as a statistical alignment of the symmetry axes of bilateral SNRs with the Galactic Plane (Shaver 1969).

Given that such a result would be reasonably conclusive, several researchers have attempted to determine whether such an alignment exists. By creating an average circumferential profile from SNRs for which appropriate data was available at the time, Shaver (1969) found that SNRs appeared to have minima in their emission where the shell is intersected by a line of constant Galactic latitude, and argued that this was evidence for magnetic models. However, the statistical significance of the result was low, and the limited sample available was from observations of poor resolution and sensitivity.

In more recent years, the statistics of SNR samples have steadily improved, and other researchers have carried out various analyses investigating alignment between the axes of SNRs (defined in various ways) and the Galactic Plane (Shaver 1982; Manchester 1987; Leckband et al. 1989; Whiteoak & Green 1996, hereafter WG96). In all cases, no alignment was found, leaving the authors to conclude that either the magnetic field is not well-aligned with the Plane at such scales, or that the magnetic model is not valid.

However, some of these studies implicitly assume that *all* SNRs have a bilateral symmetry, and then assign an axis to every remnant in their sample. Others restrict their sample to SNRs with a symmetry axis, but include remnants where this symmetry is not necessarily bilateral. If only a small subset of remnants are truly bilateral, then these analyses will never show any alignment because any real effect will be swamped by the large number of randomly oriented axes corresponding to non-bilateral SNRs. In addition, the low resolution of many of the images available at the time caused a poor determination of the axis of symmetry.

There are now over 200 SNRs known in the Galaxy (Green 1996), and an increasing number of objects have been observed at high resolution. For almost the

entire Galactic population, observations are now of sufficient quality that one can determine which SNRs have a clear bilateral appearance (defined in some manner), and restrict analysis to this sample.

In Section 3.2, we describe high-resolution 1.4 GHz observations and analysis procedures for two Southern SNRs, G003.8–00.3 (formerly G003.7–00.2) and G350.0–02.0 (formerly G350.0–01.8). We present images of these remnants in Section 3.3, and argue that these SNRs are members of the bilateral class with their axes aligned along the Galactic Plane. The properties of these two SNRs are then briefly discussed in Section 3.4. In Section 3.5, we consider the Galactic population of bilateral SNRs, and demonstrate a clear tendency for the bilateral axis to align with the Plane. It is argued in Section 3.6 that the magnetic model can explain this alignment, but that there are difficulties accounting for the detailed morphologies of bilateral SNRs. An alternative model is proposed, in which the ISM is pre-processed by the ambient magnetic field to form structures running parallel to the Galactic Plane. SNRs then interact with this material, producing a bilateral appearance with the observed alignment.

3.2 Observations and Data Reduction

Interferometric observations were made with the Very Large Array (VLA) of the National Radio Astronomy Observatory, an aperture synthesis telescope consisting of 27 antennas in a "Y"-shaped array, located near Socorro, New Mexico (Napier et al. 1983). The dates and lengths of the observations are given in Table 3.1. Two bands were observed simultaneously, with centre frequencies of 1.385 GHz and 1.465 GHz, bandwidths of 50 MHz, in all four Stokes parameters. Because of its large angular extent, SNR G350.0–02.0 was observed in a mosaic of four pointings (see Table 3.3), with a cycle time of 24 minutes. Amplitudes were calibrated by assuming flux densities at 1.385 and 1.465 GHz respectively of 14.94 and 14.55 Jy for J1331+305 (3C286) and 16.32 and 15.62 Jy for J0137+331 (3C48). Phases were calibrated using the source J1751–253.

Date	Array	Source	Time on source (min)
1996 Jan 20	CnB	G003.8–00.3	165
		G350.0–02.0	90
1996 May 21	DnC	G350.0–02.0	24
1996 Jun 18	DnC	G003.8–00.3	31
		G350.0–02.0	24
1996 Jun 22	DnC	G003.8–00.3	47
		G350.0–02.0	40

Table 3.1 VLA observations.

The VLA data were edited and then calibrated in `AIPS` using standard techniques (Greisen 1996). The visibility data were then transferred to the `MIRIAD` package (Sault et al. 1995), and total intensity images formed using uniform weighting and a cell size of $4''$. For the mosaiced observations of G350.0–02.0, a joint image was formed from all four pointings (Cornwell et al. 1993; Sault et al. 1996), which was then corrected for the mean primary beam response of the VLA antennas.

The smallest projected spacing between antennas for the observations in Table 3.1 is 0.12 kλ , which corresponds to an angular scale of $\sim 30'$. Thus the VLA observations are not sensitive to emission on scales larger than this. These short spacings were obtained by making single-dish observations (in total intensity only) of both SNRs using the Parkes 64-m radio telescope. Amplitudes were calibrated using the source PKS B1934–638, assuming a flux density of 14.90 Jy. Except where noted in Table 3.2, observational techniques were the same as used in the 2.4 GHz survey of Duncan et al. (1995). Scans were made in both l and b, of regions surrounding both SNRs, at a scan rate of 6° min^{-1}. The Parkes observations were reduced in the manner described by Duncan et al. (1995), and the resultant images regridded and reprojected to match the higher resolution data.

Observing date	1996 Sep 07
Centre frequency	1.40 GHz
Bandwidth	40 MHz
System temperature	25 K
RMS noise	24 mJy beam^{-1}
Beam width (FWHM)	$14\farcm85 \pm 0\farcm25$
Map gridding	$6'$

Table 3.2 Parkes observations.

Data from the two telescopes were then combined by adding together the dirty images from each instrument. The flux density scale of the single dish data was preserved by weighting them by the inverse ratio of the beam areas (Ye et al. 1991; Stewart et al. 1993). Point spread functions were produced similarly, and the images then deconvolved using the maximum entropy algorithm (Gull & Daniell 1978). For G350.0–02.0, all pointings were deconvolved simultaneously using the `MIRIAD` task `MOSMEM` (Sault et al. 1996). The resulting models were then smoothed using a Gaussian restoring beam to produce the final images.

Because of the proximity of G003.8–00.3 to both the Galactic Plane and the Galactic Centre, single-dish observations of this source are dominated by diffuse emission from confusing sources and the Galactic background. The composite image has flux filling the entire field of view, and it is thus not possible to successfully deconvolve it. The image of G003.8–00.3 as presented in Section 3.3 therefore does not include the Parkes measurements. Since the angular extent of this SNR is significantly smaller than the largest spatial scale sampled by the VLA, we still

expect to recover almost all of the flux density from this object.

Images of linearly polarised emission were made from the interferometric data in Stokes Q, U and V. (Although no real emission is expected in circular polarisation, the V image provides a useful check of quality.) The Q and U images were then deconvolved using the `CLEAN` algorithm (Clark 1980), and a linear polarisation image, L, produced which was then corrected for non-Gaussian noise statistics (Killeen et al. 1986) using the `MIRIAD` task `IMPOL`.

3.3 Results

Total intensity images of G003.8–00.3 and G350.0–02.0 are shown in Figures 3.1 and 3.2 respectively. These images are of higher resolution, and in the latter case, of greater extent than in previous images. We are thus able to derive improved positions for the centres of these two SNRs, resulting in a change of name for both remnants.

Because the VLA is non-coplanar, the approximation of a flat sky used in standard synthesis imaging is invalid at large distances from the phase centre (Perley 1989). As a result, some point sources in Figure 3.2 have a triangular appearance.

Information about each image and its derived parameters are provided in Table 3.3. Flux densities and their uncertainties were determined by integrating within multiple polygons enclosing the emission from each SNR. The RMS noise in each image was measured by similarly integrating over a source-free region. In the case of G003.8–00.3, the given centre and diameter are those of a circle best fitting the outer perimeter of the emission. G350.0–02.0 is clearly non-circular, and so the centre is defined as that point equidistant from the boundaries of the SNR both along and at right angles to the bilateral axis. The diameter given is the maximum extent in these two directions.

3.3.1 SNR G003.8–00.3

SNR G003.8–00.3 (then G003.7–00.2) was discovered in the Galactic Centre Survey carried out with the Molonglo Observatory Synthesis Telescope (MOST) at 0.843 GHz (Gray 1994) and was classified as a SNR on the basis of its morphology. Using flux densities from Gray (1994) and from Table 3.3, we obtain a spectral index for G003.8–00.3 of $\alpha = -0.65 \pm 0.05$ ($S_\nu \propto \nu^\alpha$), confirming the non-thermal nature of this source.

The image of G003.8–00.3 (Figure 3.1) shows it to be a classic bilateral remnant, with a clear axis of symmetry defined by the two bright limbs, and a low level of emission along this axis (cf. KC87). The emitting regions appear to be composed of multiple filaments extended along the symmetry axis: on the north-west rim of the SNR, these filaments take the form of roughly parallel arcs, while in the south-east they overlap each other. The original 0.843 GHz image of this remnant seemed

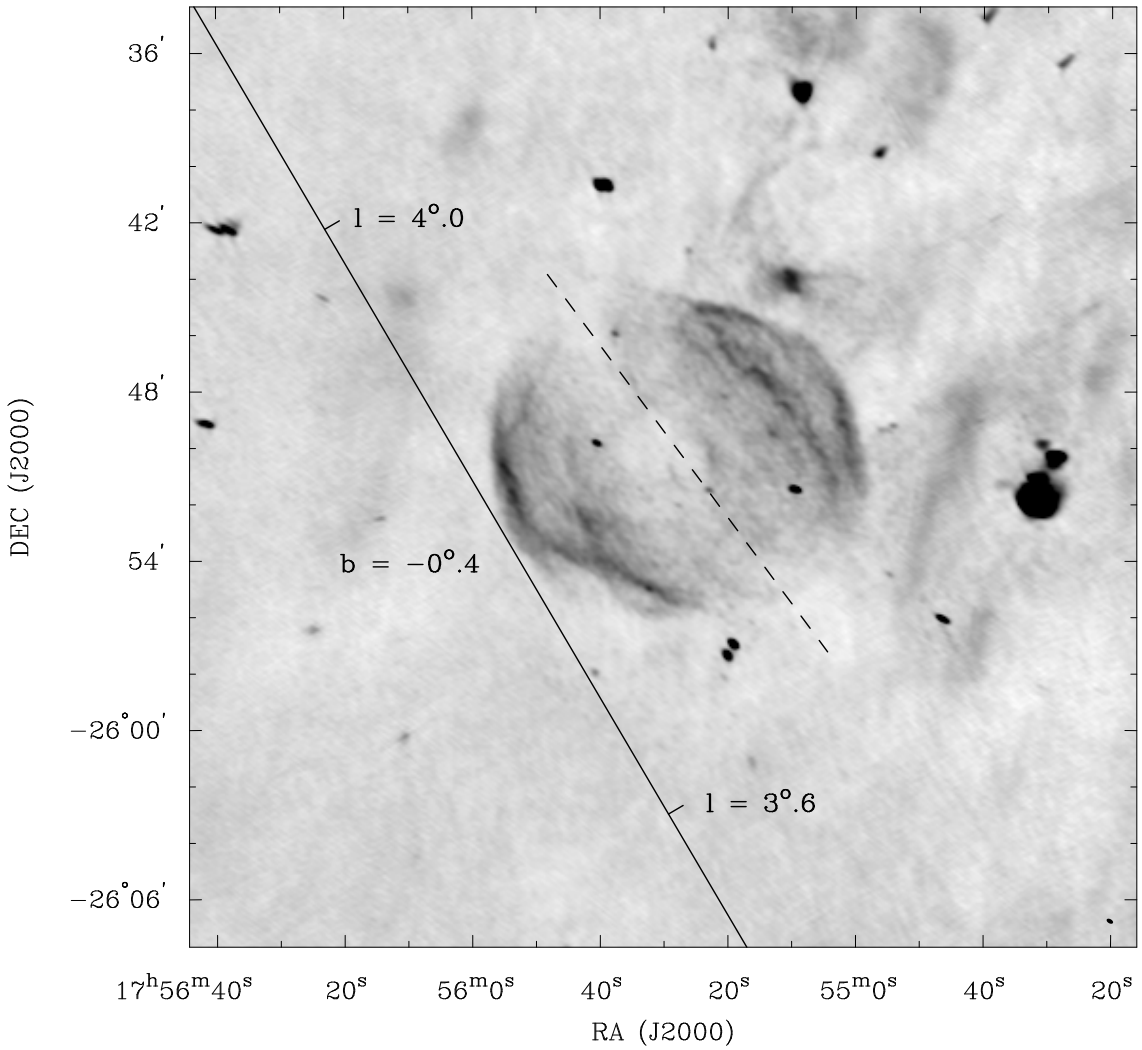

Figure 3.1 1.4 GHz VLA image of SNR G003.8–00.3. The linear grey-scale is from –0.5 to 3.0 mJy beam^{-1}, and the peak surface brightness in the image is 15.8 mJy beam^{-1}. The synthesised beam, shown at the lower right of the Figure, corresponds to a resolution of $15'' \times 9''$. The solid line represents a constant Galactic latitude $b = -0.^{\circ}4$. The dashed line represents the axis of symmetry for this SNR, as discussed in the text.

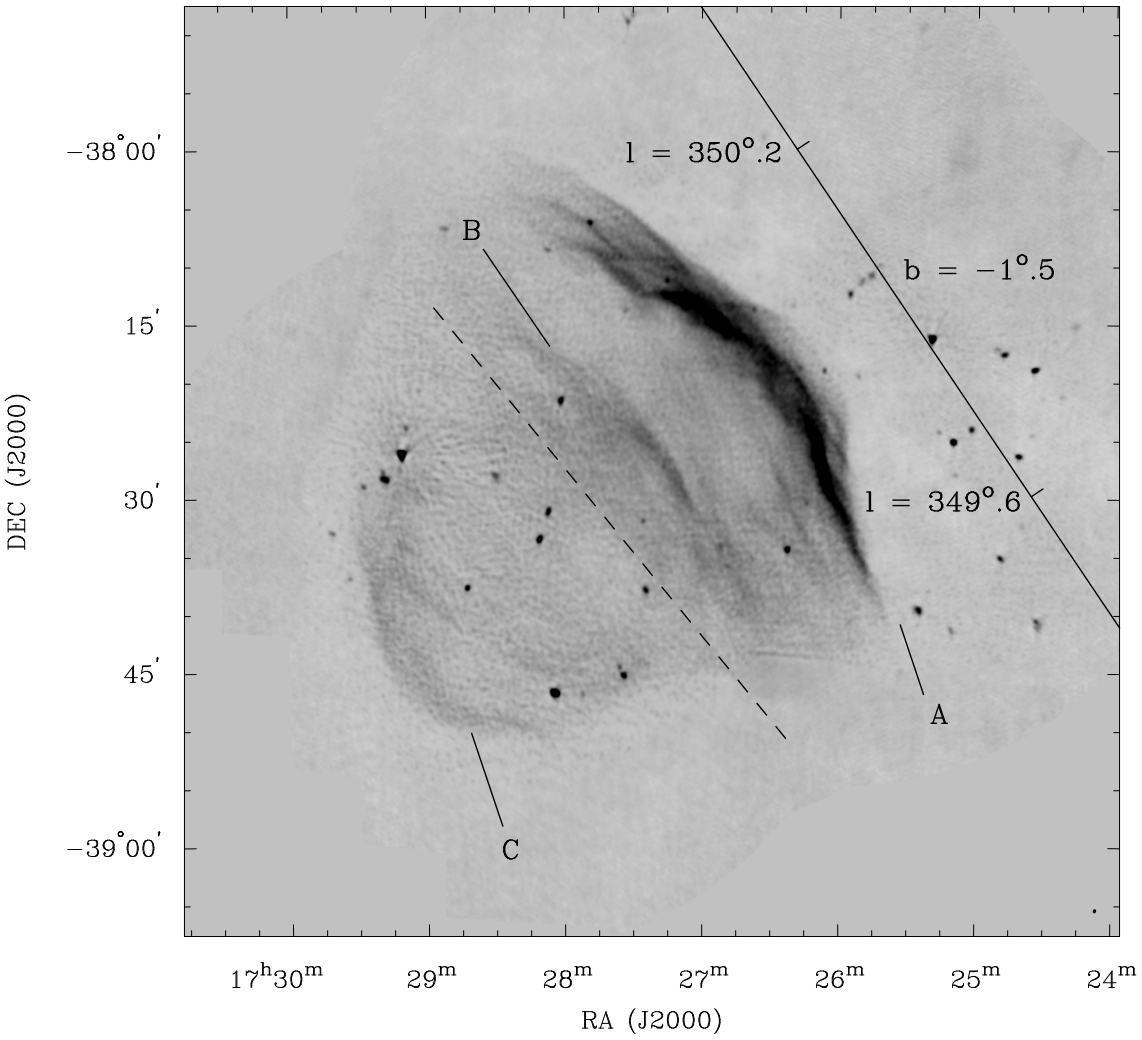

Figure 3.2 Image of SNR G350.0–02.0, produced by combining 1.4 GHz data from the VLA and from Parkes. The linear grey-scale is from –2.4 to 7.5 mJy beam^{-1}, and the peak surface brightness in the image is 58.5 mJy beam^{-1}. The synthesised beam, shown at the lower right of the Figure, corresponds to a resolution of $21'' \times 18''$. A line of constant Galactic latitude and the axis of symmetry for the SNR are shown as in Figure 3.1. Regions A, B and C, as discussed in the text, are indicated.

	G003.8–00.3	G350.0–02.0
VLA pointing centres[a]	$17^{\rm h}55^{\rm m}30^{\rm s}$, $-25°51'00''$	(1) $17^{\rm h}28^{\rm m}30^{\rm s}$, $-38°37'30''$ (2) $17^{\rm h}27^{\rm m}20^{\rm s}$, $-38°27'30''$ (3) $17^{\rm h}26^{\rm m}55^{\rm s}$, $-38°10'00''$ (4) $17^{\rm h}26^{\rm m}00^{\rm s}$, $-38°23'00''$
Resolution	$15'' \times 9''$, PA $= 60°$	$21'' \times 18''$, PA $= -13°$
RMS noise (mJy beam^{-1})	0.06	0.15
Derived centre of SNR[a]	$17^{\rm h}55^{\rm m}28^{\rm s}$, $-25°50'$	$17^{\rm h}27^{\rm m}50^{\rm s}$, $-38°30'$
Derived centre of SNR[b]	003.°78, –00.°29	349.°95, –02.°03
Diameter	$13'$	$47' \times 44'$
1.4 GHz flux density (Jy)	1.7 ± 0.1	22.3 ± 0.3
Spectral index	-0.65 ± 0.05	-0.4 ± 0.1
$S_{1\,\rm GHz}$ (Jy)	2.3±0.1	25.7±0.9
$\Sigma_{1\,\rm GHz}$ (10^{-21} W m^{-2} Hz^{-1} sr^{-1})	2.0±0.1	1.7±0.1

[a]Equatorial coordinates α, δ (J2000)

[b]Galactic coordinates l, b

Table 3.3 Observational, measured and derived parameters for each SNR.

to contain multiple overlapping rings (Gray 1994). However, this appearance is most probably due to the alignment of various filaments when seen with the lower resolution of the MOST — no such features are evident in our image.

ψ is defined to be the acute angle between the symmetry axis of the SNR and the Galactic Plane. We fit the symmetry axis by eye, and estimate the uncertainty by fitting a set of possible axes to the remnant. This gives a value $\psi = 6° \pm 2°$, indicating close alignment between the symmetry axis and the Plane. More involved methods for determining ψ (e.g. Storey et al. 1992) were also implemented, giving similar results. For the accuracy required for ψ in this work, the more rigorous determinations are not warranted. Furthermore, for several sources considered in Section 3.5.3, images were not available in electronic form.

Weak linearly polarised emission fills the entire image, and it is not possible to determine how much emission is specifically associated with the remnant. We put an upper limit of 0.05 Jy on polarised emission from G003.8–00.3, corresponding to a fractional polarisation of <3%.

3.3.2 SNR G350.0–02.0

SNR G350.0–02.0 (then G350.0–01.8) was first identified from a 408 MHz survey of the Galactic Plane carried out with the Molonglo Cross (Green 1972). At the comparatively low resolution and sensitivity of the time, only the bright north-western arc was clearly delineated. For the next 20 years, this remnant received little attention: Clark et al. (1975a) suggested it was "part of an old large SNR", Caswell (1977) noted it as an example of a SNR which was brighter towards the Galactic Plane, while KC87 described it as "difficult to classify". More recent observations at 0.843 GHz (MOST; Burn & Bush 1994) and at 2.4 GHz (Parkes 64-m; Duncan et

al. 1995) have demonstrated that this SNR is of far greater extent than previously realised. Higher resolution VLA observations are shown in Figure 3.2.

Using a 2.4 GHz flux density of 18 ± 1 Jy (obtained from the single-dish measurements of Duncan et al. 1995), and the 1.4 GHz value given in Table 3.3, we derive a spectral index for G350.0–02.0 of $\alpha = -0.4 \pm 0.1$. Note that the flux density values quoted for this SNR by Clark et al. (1975a) correspond only to the bright north-west component.

The image of this SNR in Figure 3.2 shows a far more complicated morphology than previously thought. It may even correspond to multiple remnants, a possibility discussed below in Section 3.4.2. The brightest region of G350.0–02.0 (corresponding to the previously identified source G350.0–01.8, and labelled as A in Figure 3.2) consists of several overlapping filaments, with the suggestion of complex, unresolved, structure. This region, which extends over $\sim 40'$, forms a roughly circular arc with radius of curvature $\sim 55'$. In the remnant's interior is region B, separated from region A by a zone of diffuse emission of width $\sim 8'$. Region B consists of a series of wisps, considerably fainter than the emission in region A, but with a similar orientation and curvature. A third region, C, is separated from region B by another zone of diffuse emission of width $\sim 6'$. Region C consists of still more overlapping filaments, of opposite curvature to the rest of the SNR, which complete a distorted shell of emission. The outer rim of region C forms a circular arc of radius $\sim 14'$, considerably different from the radius of curvature for region A.

Although G350.0–02.0 is clearly very different to G003.8–00.3, it also has a bilateral appearance. The circumference of the remnant is bounded on two sides by regions of significant emission (namely A and C), and at perpendicular position angles the emission is considerably weaker. As for G003.8–00.3, a bilateral axis can be defined. This axis is shown in Figure 3.2, drawn perpendicular to a line joining the centres of curvature of regions A and C. For this axis, $\psi = 5^\circ \pm 2^\circ$, again a high degree of alignment with the Plane.

Clumps of linear polarisation are detected throughout the interior of G350.0–02.0. The total polarised intensity is 0.8 Jy, implying a fractional intensity of 3.6%.

3.4 Discussion

Because of the lack of information at other wavelengths and the proximity of both remnants to $l = 0^\circ$, the methods typically used to estimate distances to SNRs cannot be applied (see Green 1984). The $\Sigma - D$ relation (e.g. Caswell & Lerche 1979; Huang & Thaddeus 1985) has in the past been used to estimate distances to SNRs, but the uncertainties are large (Green 1984; Berkhuijsen 1986). Thus we conclude that the age of and distance to these SNRs remains unknown at the present time.

3.4.1 SNR G003.8–00.3

FR90 have quantified the contrast between the brightest and faintest regions of a bilateral SNR by using an "azimuthal intensity ratio", A. This is defined as the ratio between the peak of emission around the SNR shell, and the minimum value around the shell at the radius corresponding to this peak. The filamentary nature of this SNR makes it difficult to compute A in this manner, but we have made a commensurate calculation as follows. The shell of emission from the SNR lies within an annulus of inner radius $4\farcm2$ and outer radius $6\farcm7$, centred on the coordinates for G003.8–00.3 as listed in Table 3.3. We have divided this annulus into 360 azimuthal bins, and computed the average flux density in each bin. A peak of approximately 1.1 mJy beam^{-1} occurs at position angles (measured north through east) of 100° and 260°. The minimum level of emission occurs at PA $\approx 40°$, where no emission can be detected above the 3σ noise level. This corresponds to an intensity ratio of $A > 6$, at a resolution of $\sim$70 beams per diameter. For a remnant in the adiabatic phase, this is consistent with magnetic models for a bilateral appearance, but does not distinguish between field compression alone and quasi-perpendicular acceleration (FR90).

3.4.2 SNR G350.0–02.0

One interpretation for the three spatially and morphologically distinct regions of emission in G350.0–02.0 is that they are two or three separate SNRs, as has been postulated in objects such as G053.6–02.2 (3C400.2; Dubner et al. 1994) and 0547–697 (DEM L 316; Williams et al. 1997). Certainly regions B and C are of similar surface brightness, which could be interpreted as a complete shell, separate from region A.

If we consider a region on the sky defined by $330° = -30° \leq l \leq 30°$, $1.5° \leq |b| \leq 3°$ (i.e. longitudes and latitudes representative of G350.0–02.0), we find nine SNRs in the catalogue of Green (1996). Given this sky density, the probability of finding two randomly distributed remnants less than $30'$ apart (as required here) is 14%. However, this is probably a lower limit, since the small number of SNRs detected in this region may be due to the incomplete sky coverage of existing surveys. Also, SNRs are not necessarily randomly distributed, but at least for those formed from massive stars probably represent the clustering of their progenitors. Thus there is no convincing statistical argument that G350.0–02.0 is a single SNR.

Nevertheless, the centres of curvature for all three regions lie in a straight line, which bisects the three arcs of emission. The fact that regions A and C are of opposite concavity also suggests that all the emission represents common expansion from a single event. Diffuse emission from the SNR (contributed primarily by the single dish observations) delineates a single plateau of emission bounded by regions A and C. We therefore consider the most likely interpretation to be that the emission in this region is from a single object.

It is possible that the non-circular appearance could be due to the influence of a

pulsar or other compact object. An analogy could be drawn with SNR G005.4–01.2, which has a bright, flattened ridge of emission along one side (Caswell et al. 1987; Frail et al. 1994c), resembling region A of G350.0–02.0. It has been proposed that the distorted morphology of this SNR is a result of the associated pulsar PSR B1757–24 overtaking the expanding parent shell (Frail & Kulkarni 1991). While a flat-spectrum region extending from the pulsar back towards the radio shell supports such a model for SNR G005.4–1.2 (Frail & Kulkarni 1991; Frail et al. 1994c), no similar component is observed in G350.0–02.0, nor has any pulsar been detected (Manchester et al. 1985a; Kaspi et al. 1996b). Thus we consider an interaction with a compact object an unlikely explanation for the observed morphology. Given that any associated pulsar should be located near the SNR's presumed centre of expansion (Gaensler & Johnston 1995a), the area bounded by regions B and C might be a more fruitful target for future pulsar searches.

A 1.4 GHz image of SNR G166.0+04.3 (VRO 42.05.01; Landecker et al. 1982a; Pineault et al. 1987) is shown in Figure 3.3, revealing a striking resemblance between this SNR and G350.0–02.0. G166.0+04.3 is also composed of three separate regions, whose relative shape, size and orientation are similar to those in G350.0–02.0. Both SNRs are bounded on one side by a bright arc with a large radius of curvature which trails into the noise (region A), contain a fainter strip of emission parallel to A and separated from it (region B), and a series of filaments with a distinctly smaller radius of curvature and of opposite concavity to the rest of the emission, completing the outline of a shell (region C). Both SNRs are similarly aligned to the Galactic Plane: when an axis of symmetry is defined for G166.0+4.3, one finds that $\psi = 2^\circ \pm 2^\circ$.

There are notable differences between the SNRs, however. Firstly, in G350.0–02.0, regions B and C are of similar brightness but are much fainter than A, while in G166.0+04.3, the region corresponding to C (the "shell" of Landecker et al. 1982a) is of comparable brightness to that corresponding to region A (the "wing"). Secondly, the central region of G166.0+04.3 consists of linear features, while region B appears to be curved. Finally, while in G350.0–02.0 regions B and C are separated by a region of faint emission, the analogues of these two regions in G166.0+04.3 actually overlap.

Pineault et al. (1987) explain the morphology of G166.0+04.3 in terms of the interaction of an expanding remnant with a slab of pre-existing low density material. The SN explosion is believed to have occurred at or near the centre of curvature of the "shell" component, which represents the expansion of that part of the SN shock into a uniform medium. The faint linear features in the remnant's centre mark the re-energising of the slab's surface as a result of the shock breaking out into it, and the "wing" component represents the shock once again encountering dense material on the other side.

The similarity between the two remnants suggests a similar explanation for them as well. In this model, region C of G350.0–02.0 is the unperturbed component of the original SNR, which evolves independently of those parts of the remnant which encounter a more complicated structure (Falle & Garlick 1982; Tenorio-Tagle et al. 1985). Indeed, region C resembles SNR G119.5+10.2 (CTA 1; Pineault et al. 1993),

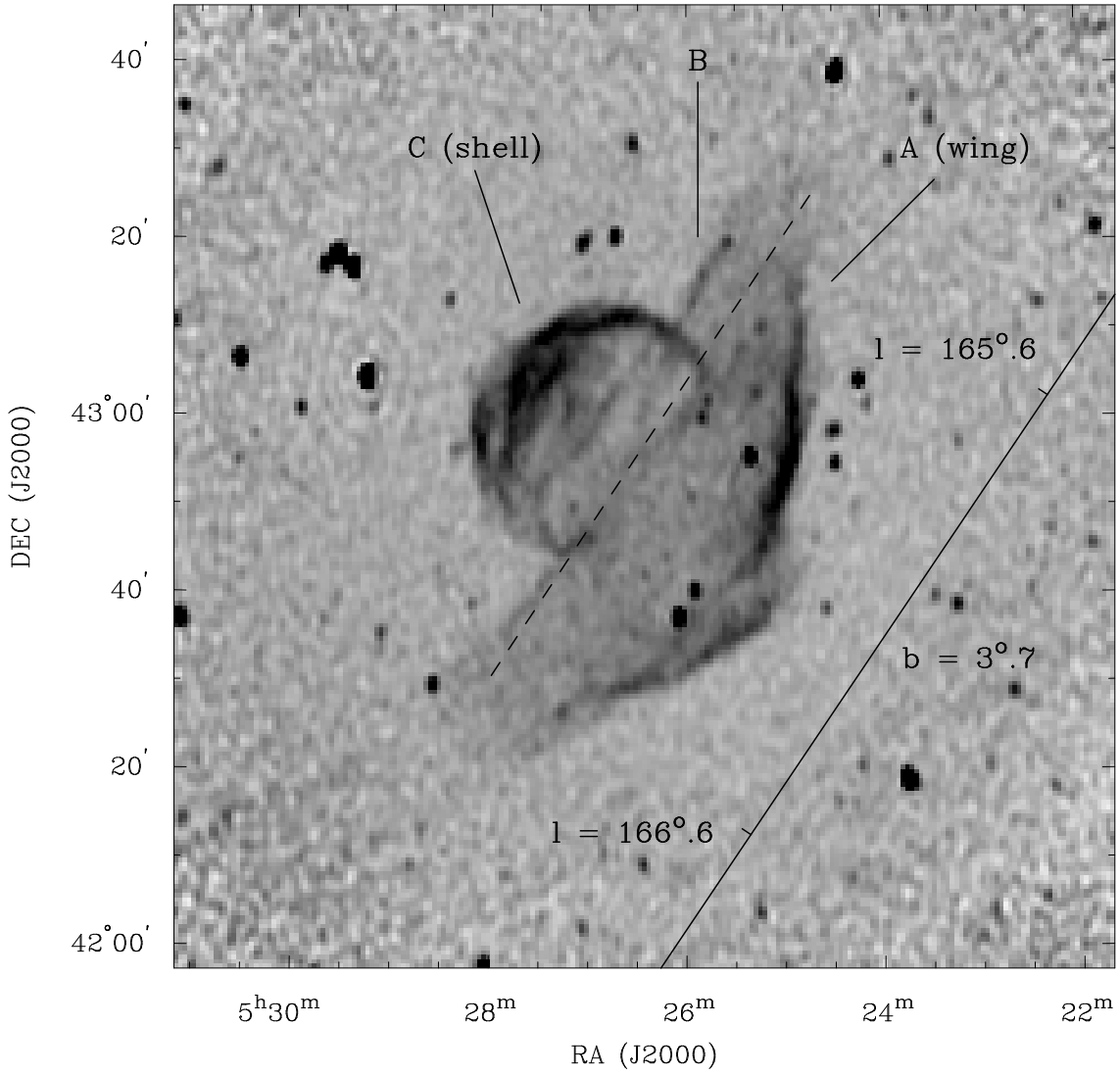

Figure 3.3 1.4 GHz image of SNR G166.0+04.3 (VRO 42.05.01), reproduced from Pineault et al. (1987) and precessed to J2000 coordinates. A line of constant Galactic latitude and the axis of symmetry for the SNR are shown as in Figure 3.1. The "wing" and "shell" components as defined by Landecker et al. (1982a) are shown.

a partial shell for which there is evidence that a breakout has occurred but for which the remainder of the SN shock is not visible. Region B of G350.0–02.0 represents the boundary of a low density slab. That it is concave and not linear and does not overlap with region C, suggests that the details of the 3D geometry differ from that in the case of G166.0+04.3. Region A is that component of the shock which has traversed the slab and continues to propagate beyond it.

3.5 The Galactic Population of Bilateral SNRs

3.5.1 Selection Criteria

Although previous studies have argued that no alignment exists between the axes of bilateral SNRs and the Galactic Plane, it is interesting that G003.8–00.3, G350.0–02.0 and G166.0+04.3 should all have such low values of ψ. This similarity prompted an examination of other bilateral SNRs.

We have therefore reviewed the Galactic SNR catalogue of Green (1996), which currently contains 215 remnants. The criteria for a SNR to be classed as bilateral are as follows:

- It must be of the shell or composite class.
- The highest resolution image available must have a minimum of 10 beams across its diameter.
- The SNR must have clear minima in emission separated by position angles of $180^\circ \pm 30^\circ$ relative to the assumed centre of the SNR. The presence of opposed minima is the main criterion for classification, as it is these minima which define the bilateral axis.
- The SNR must have well-defined maxima, similarly opposed, and at approximately perpendicular position angles to the minima.
- A clear bilateral axis should be identifiable, passing through the two minima and through the centre of the SNR. Objects with a large uncertainty ($\gtrsim 20^\circ$) in the position angle of the axis are excluded — this requirement is critical in defining the objects in the sample.

We do not quantify the azimuthal intensity ratio, A, of FR90 as a threshold. Such a measurement is both difficult and misleading, because of the various presentations of images in the literature, and of the differing nature of the observations involved. As FR90 have pointed out, the value of A depends strongly on the resolution of an image, so that the appearance of bilaterality will increase with resolution. Also, the lack of large-scale emission present in some interferometric images can cause a further over-estimation of this parameter. Thus using this ratio as a threshold will not result in a consistent criterion.

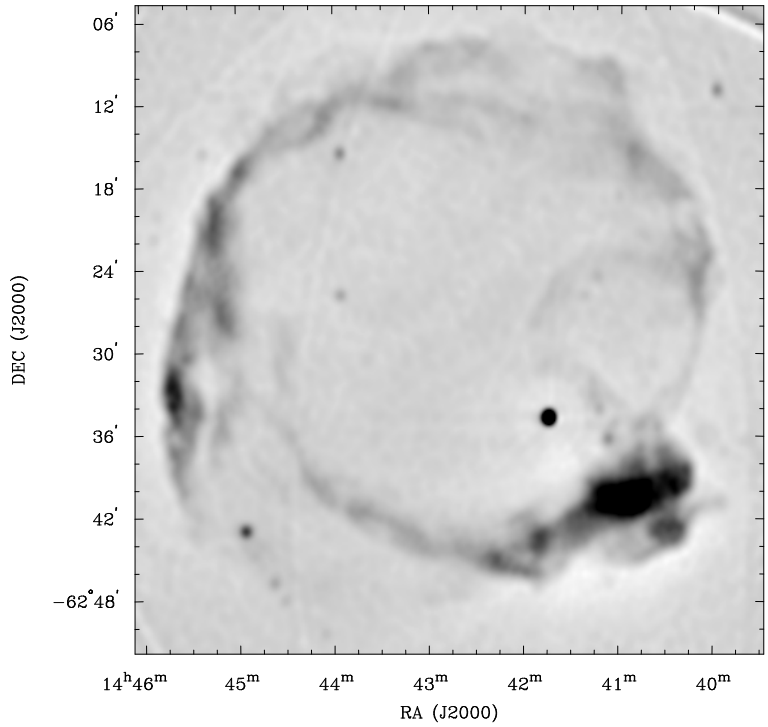

Figure 3.4 0.843 GHz image of SNR G315.4–02.3 (RCW 86), reproduced from WG96.

3.5.2 Non-bilateral SNRs

There are 198 SNRs in Green's (1996) SNR catalogue which do not meet our criteria. This is in strong contrast to KC87, who found that 63% of all SNRs had some element of "barrel" structure. This primarily reflects the strictness of our criteria. For example, consider G315.4–02.3 (RCW 86; Figure 3.4) and G332.4–00.4 (RCW 103; Figure 3.5), both of which are described by KC87 as "well developed barrels". The former has no opposed maxima or minima. The latter is a marginal case (Dickel et al. 1996 describe it is an "incipient barrel"), but lacks the distinctive minima and symmetry properties of the best examples of the class.

Improved observations over the last ten years have allowed a more precise classification of many remnants. For the MOST, substantial improvements to both hardware (Amy & Large 1990, 1992) and data reduction techniques (Cram & Ye 1995) since the observations of KC87 were made have significantly reduced the effect of artifacts, increased the sensitivity, and generally improved image quality.

3.5.3 Bilateral SNRs

There remain 17 remnants in the catalogue which can be classed as clearly bilateral from our criteria. A list of these bilateral SNRs is given in Table 3.4. For each remnant a bilateral axis is defined by eye, as for the SNRs in Section 3.3. This axis passes through the two minima, corresponding closely to an axis of mirror symmetry.

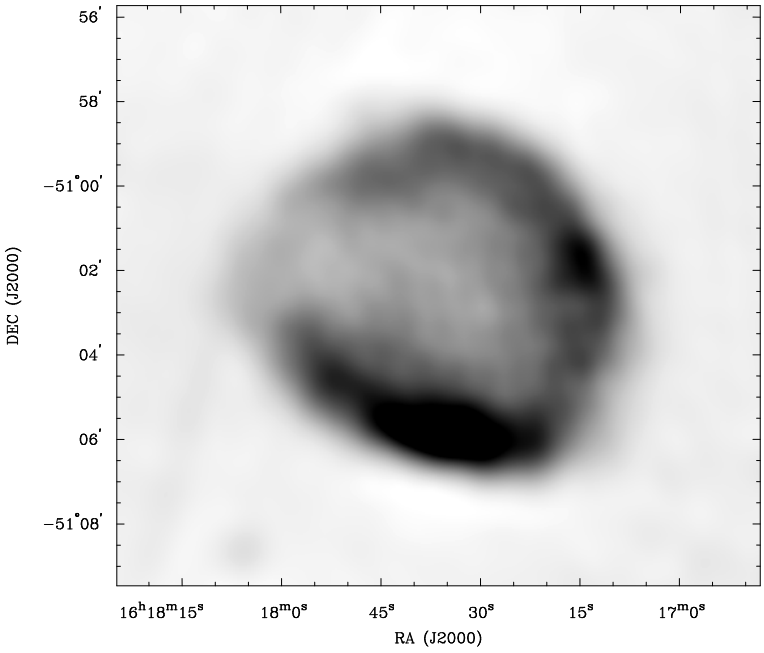

Figure 3.5 0.843 GHz image of SNR G332.4–00.4 (RCW 103), reproduced from WG96.

Some examples of SNRs which we have classed as bilateral are shown in Figures 3.6 through 3.11, with the bilateral axis of each remnant shown. In each case, we have measured the acute angle, ψ, between this axis and the Galactic Plane. Values of ψ for each SNR are shown in Table 3.4.

The reader is encouraged to examine these (and other) SNRs in order to verify that the classifications made are reasonable. We should emphasise that if there is any doubt, a SNR is *excluded* from our class. If a preferential alignment exists, it will remain apparent if some bilateral SNRs are excluded from the sample (provided that the statistics are still meaningful), but will be masked if too many remnants which do not satisfy the criteria are included.

3.5.4 Orientation with respect to the Galactic Plane

A histogram of the distribution in ψ from Table 3.4 is shown in Figure 3.12. This distribution has a median of $\psi_m = 12^{\circ}{}^{+3^{\circ}}_{-2^{\circ}}$, where the uncertainty corresponds to the maximum shift in median should two objects be discarded from the sample. This result suggests an alignment of bilateral SNRs with the Galactic Plane: the probability of this distribution occurring by chance is now discussed.

Assume cylindrical symmetry for bilateral SNRs, and represent the three dimensional axis of such a remnant by a vector in Cartesian space, with spherical coordinates θ, ϕ as shown in Figure 3.13. The observer views the system along the r axis, and the l and b axes represent increasing Galactic longitude and latitude respectively in the plane of the sky. Note that the observed axis is a projection

SNR	Other Name	ψ	Figure	Reference
G003.8–00.3		$6° \pm 2°$	3.1	This Chapter
G046.8–00.3		$21° \pm 3°$	3.6	1
G078.2+02.1	γ Cygni	$10° \pm 2°$		2
G093.3+06.9	DA 530	$15° \pm 1°$		3
G127.1+00.5		$3° \pm 3°$		4
G156.2+05.7		$64° \pm 4°$		5
G166.0+04.3	VRO 42.05.01	$2° \pm 2°$	3.3	6, 7
G296.5+10.0	PKS 1209–51/52	$80° \pm 3°$	3.7	8, 9
G302.3+00.7		$42° \pm 2°$		10
G308.8–00.1		$9° \pm 3°$		10
G318.2+00.1		$12° \pm 3°$		10
G320.4–01.2	RCW 89, MSH 15–5*2*	$7° \pm 3°$	3.8	10
G327.6+14.6	SN 1006	$86° \pm 2°$	3.9	8, 9
G332.0+00.2		$25° \pm 4°$	3.10	10
G336.7+00.5		$46° \pm 1°$		10
G350.0–02.0		$5° \pm 2°$	3.2	This Chapter
G356.3–01.5		$2° \pm 2°$	3.11	11

(1) Dubner et al. (1996) (2) Pineault & Chastenay (1990) (3) Lalitha et al. (1984) (4) Joncas et al. (1989) (5) Reich et al. (1992) (6) Landecker et al. (1982a) (7) Pineault et al. (1987) (8) KC87 (9) Roger et al. (1988) (10) WG96 (11) Gray (1994)

Table 3.4 Bilateral SNRs and their orientation with respect to the Galactic Plane.

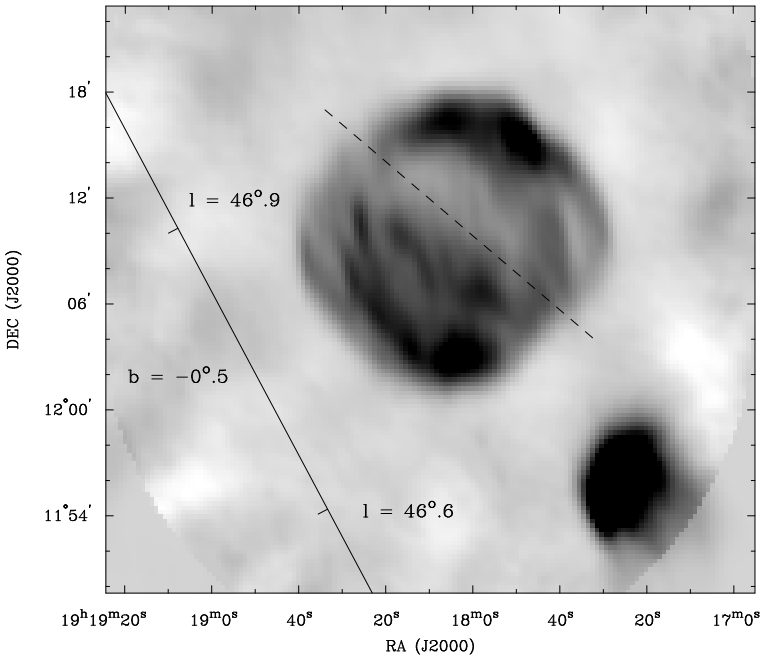

Figure 3.6 1.4 GHz image of G046.8–00.3, reproduced from Dubner et al. (1996) and precessed to J2000. Annotations to the image are as in Figure 3.1.

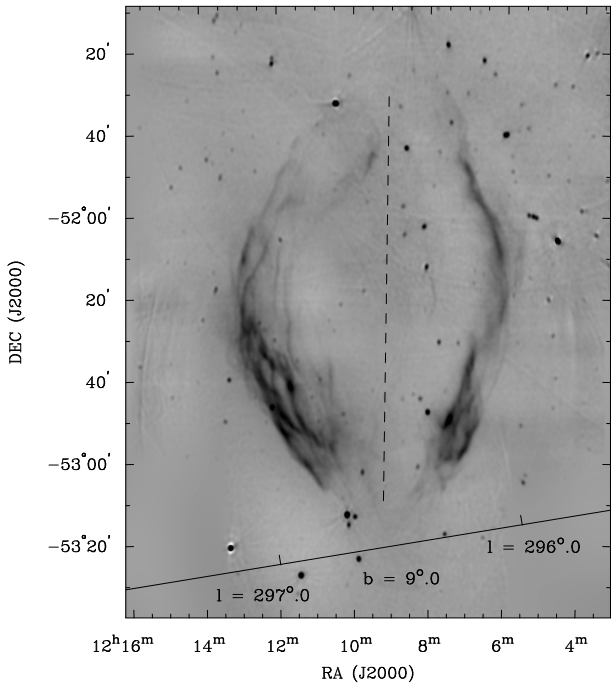

Figure 3.7 0.843 GHz image of SNR G296.5+10.0 (PKS 1209–51/52), reproduced from KC87 and precessed to J2000. Annotations to the image are as in Figure 3.1.

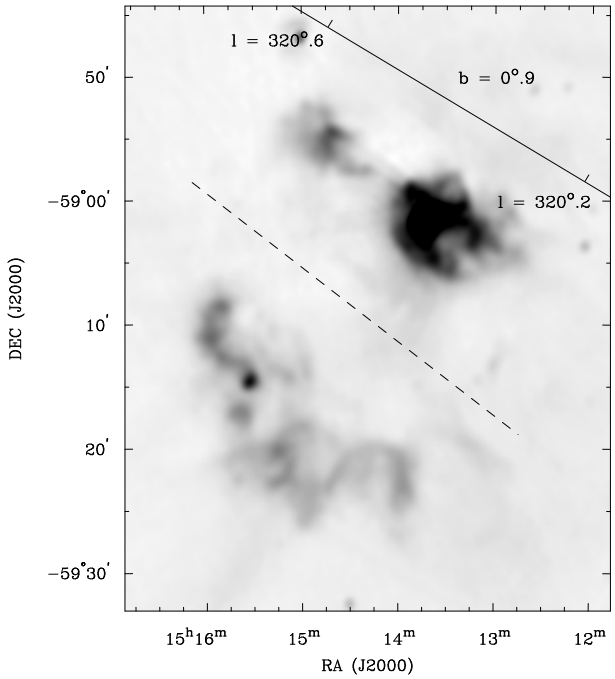

Figure 3.8 0.843 GHz image of SNR G320.4–01.2 (MSH 15–5*2*), reproduced from WG96. Annotations to the image are as in Figure 3.1.

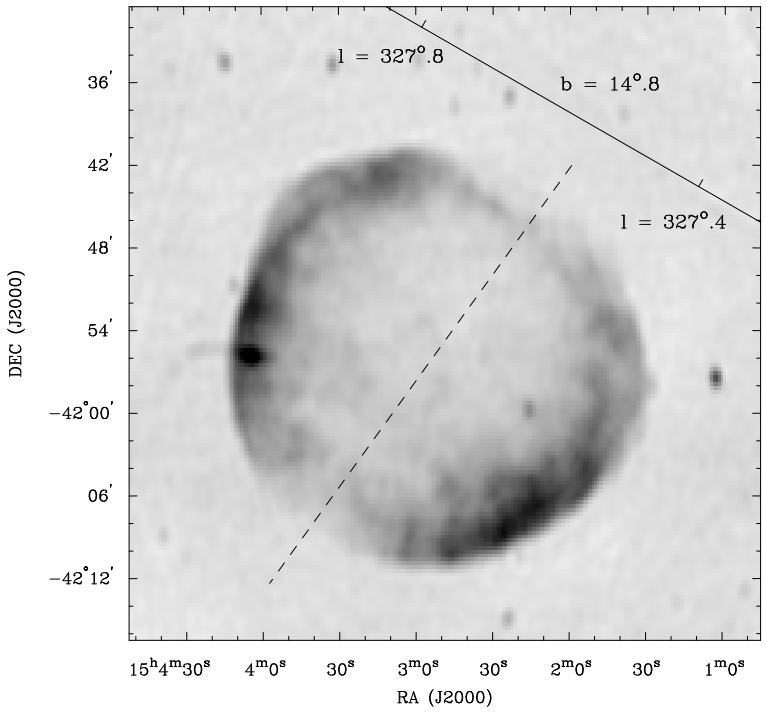

Figure 3.9 0.843 GHz image of SNR G327.6+14.6 (SN 1006), reproduced from KC87 and precessed to J2000. Annotations to the image are as in Figure 3.1.

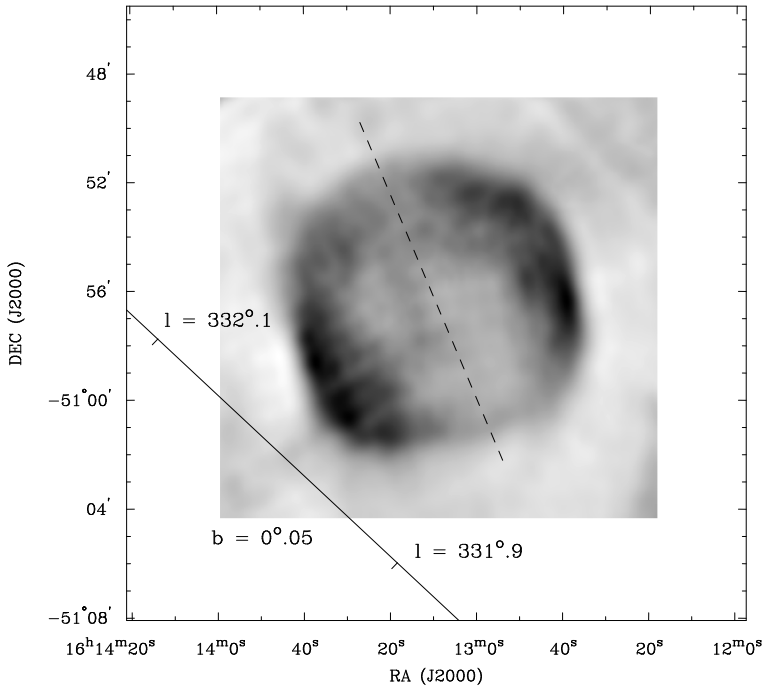

Figure 3.10 0.843 GHz image of SNR G332.0+00.2, reproduced from WG96. Annotations to the image are as in Figure 3.1.

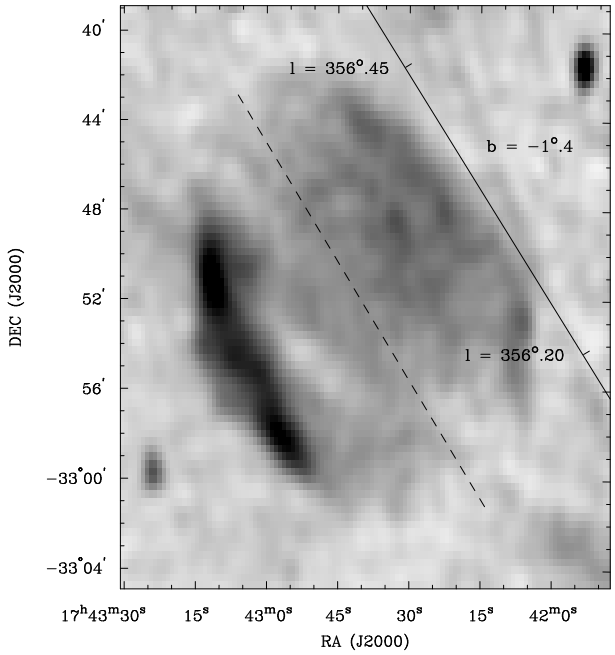

Figure 3.11 0.843 GHz image of SNR G356.3–01.5, reproduced from Gray (1994). Annotations to the image are as in Figure 3.1.

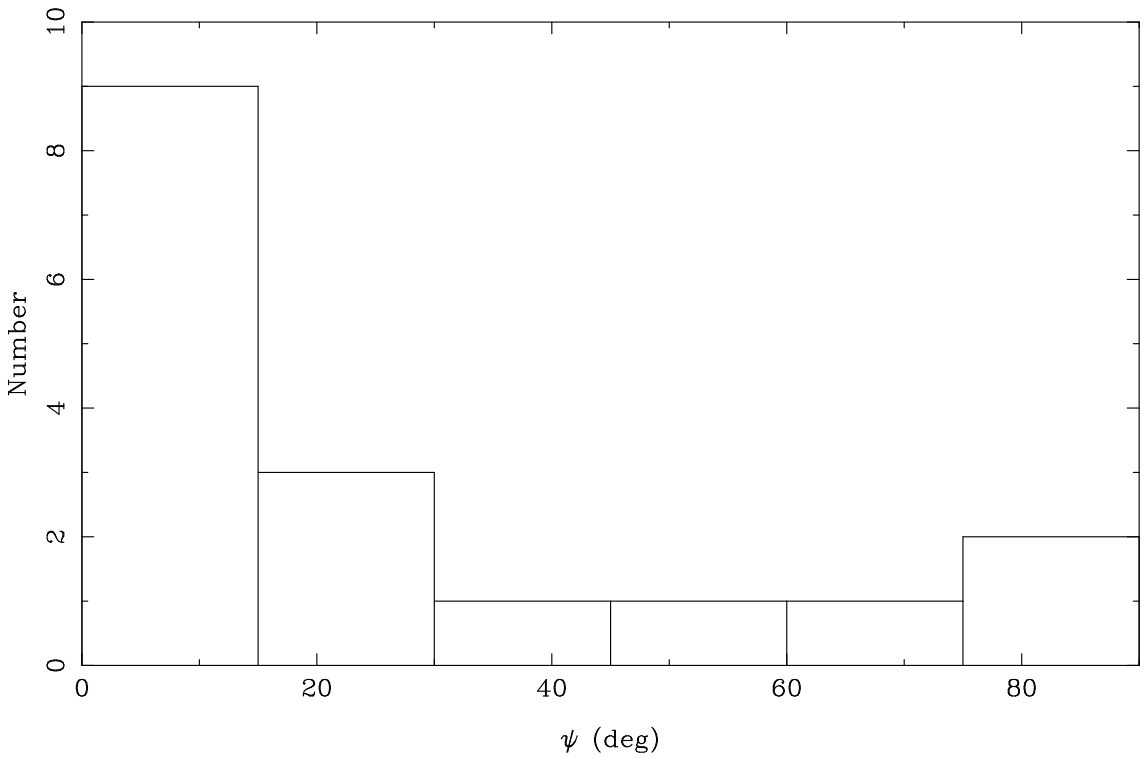

Figure 3.12 Histogram of the distribution of ψ, the acute angle between the bilateral axis of a SNR and the Galactic Plane, for SNRs listed in Table 3.4.

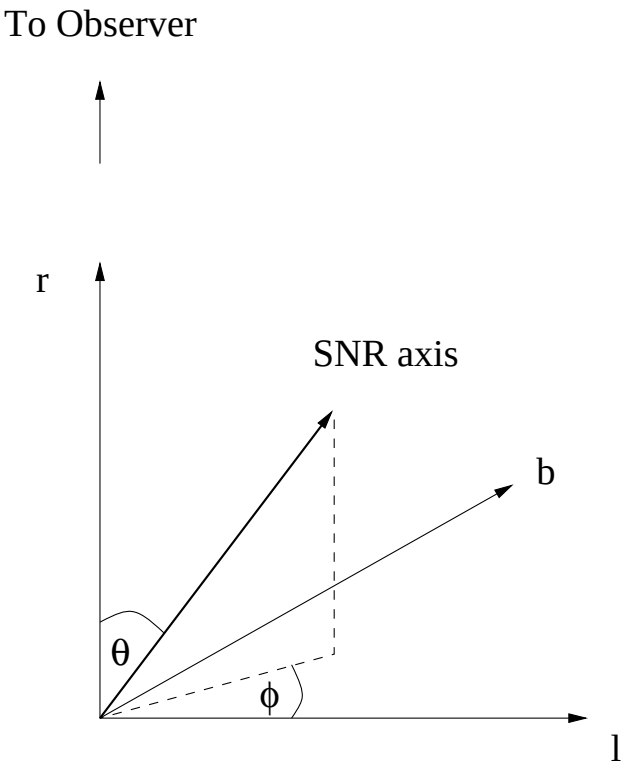

Figure 3.13 Representation of a bilateral SNR in Cartesian space. The vector corresponds to the axis of the remnant, assuming cylindrical symmetry. The observed angle between the projected axis and the Galactic Plane is $\psi = |\phi|$.

onto the $l - b$ plane of the true axis, and that a remnant will only have a bilateral appearance provided that $\theta > \theta_c$, where θ_c depends on the details of the geometry (KC87). We only consider values in the range $|\phi| \leq 90°$, since the other hemisphere is equivalent. Randomly oriented vectors will have a uniform distribution in ϕ and hence in ψ. Thus all values of ψ are equally likely, independent of θ_c.

Using the binomial theorem, we can calculate that the probability of a randomly oriented sample having the observed median is $0.7^{+4.7}_{-0.1} \times 10^{-3}$. We argue in Section 3.6.3 that G296.5+10.0 and G327.6+14.6 may be distinct from the other objects in Table 3.4, as a consequence of their large distance from the Plane. These two remnants have the highest values of ψ, and if they are excluded from the sample, the probability is even more tightly constrained.

This calculation shows that the probability of the distribution being randomly oriented is low. *We therefore consider our data to demonstrate strong evidence that bilateral SNRs align with the Galactic Plane.*

Given that no correlation between the Galactic Plane and the rotational axes of SNR progenitors has been observed (Slettebak 1949; Huang & Struve 1954), intrinsic models for the bilateral appearance (as listed in Section 3.1.2) are not consistent with the observed distribution of ψ. These models are probably better suited to explain the appearance of other classes of remnant morphology. For example, a toroidal

explosion may be appropriate for G292.0+01.8 (Tuohy et al. 1982), a high velocity progenitor could describe G357.7–00.1 (Shaver et al. 1985; Becker & Helfand 1985), outflows from a central source are appropriate for G039.7–02.0 (W 50 and SS 433; Elston & Baum 1987), while the properties of the CSM perhaps only cause a bilateral appearance at an early age, such as is observed in the radio remnant of SN 1987A (see Chapter 2).

3.6 Models for Bilateral SNRs

3.6.1 A Magnetic Model

As discussed in Section 3.1.3, an alignment of bilateral SNRs can be interpreted as evidence for magnetic models (Shaver 1969; Manchester 1987). In order for such mechanisms to be effective, the surrounding magnetic field must be well-ordered and the ISM into which the SNR is expanding must be reasonably homogeneous. The small number of bilateral remnants may indicate that this condition rarely occurs, as will be discussed further below.

There is some support for the magnetic model from polarisation measurements. Specifically, in the field compression scenario (Whiteoak & Gardner 1968), one expects the magnetic field direction in the emitting regions to be oriented tangentially. Such a phenomenon is observed in the bilateral SNRs G296.5+10.0 (Milne & Haynes 1994) and G093.3+06.9 (Lalitha et al. 1984). A tangential magnetic field need not always be observed, however, since in younger SNRs other factors may cause the magnetic field to be oriented radially (Reynolds & Gilmore 1993; Jun & Norman 1996) or be generally disordered (FR90; Moffett & Reynolds 1994).

One argument against magnetic models is that the typical energy density in the ambient magnetic field is many orders of magnitude less than the kinetic energy of a typical SNR shock (Manchester 1987; Bisnovatyi-Kogan et al. 1990). However, these arguments only pertain to whether the *shape* of a remnant can be influenced by the surrounding field. The brightness distribution can be significantly affected by the ambient field, even if the field is dynamically unimportant (FR90).

3.6.2 An Alternative to the Magnetic Model

While magnetic models can simply explain bilateral SNRs which have a circular rim and two opposed limbs of similar shape and brightness (e.g. G003.8–00.3 and G327.6+14.6), we now argue that difficulties are encountered when one considers whether such models can also account for the detailed morphologies of other objects in Table 3.4. As will be discussed below, an alternative explanation is the effect of the ISM.

Asymmetric SNRs

There are objects in Table 3.4 which align closely with the Plane, but for which the flux density and morphology of the bright opposed limbs is very different. The most striking examples of this class are G320.4–01.2 (Figure 3.8) and G308.8–00.1, but this asymmetry is also present to a lesser extent in G078.2+02.1, G127.1+00.5, G350.0–02.0 (Figure 3.2) and G356.3–01.5 (Figure 3.11). In the magnetic model, this morphology can be explained by a gradient in the field strength across the remnant (Caswell & Lerche 1979; Reynolds & Fulbright 1990).

Alternatively, for both G320.4–01.2 and G308.8–00.1, it has been suggested that this appearance is due to the influence of a central pulsar on the surrounding shell (Manchester & Durdin 1983; Kaspi et al. 1992; Brazier & Becker 1997), or because one side of the remnant encounters a region of higher density (Seward et al. 1983; Kaspi et al. 1992). In the latter case, the low value of ψ for these remnants suggests the presence of density gradients perpendicular to the Plane. There is no clear tendency for the limb closest to the Plane to be the brighter of the two. This is contrary to the suggestion of Caswell (1977), although he noted that this may only apply for remnants at large $|z|$.

Distorted SNRs

Some objects are significantly distorted from a circular or elliptical shape, for example G350.0–02.0 (Figure 3.2) and G166.0+04.3 (Figure 3.3). Observations of the latter at radio (Landecker et al. 1982a, 1989), X-ray (Burrows & Guo 1994; Guo & Burrows 1997) and optical (Pineault et al. 1985) wavelengths, are all consistent with the model of Pineault et al. (1987). As discussed in Section 3.4.2, this explains the morphology in terms of the shock encountering a hot low density tunnel lying along the Galactic Plane, before propagating into dense material beyond. We have noted that G350.0–02.0 has a similar appearance, which by analogy might also be explained in terms of such a model. The gross morphology of these remnants can be reproduced by magnetic models, but an abrupt change in density by a factor of 100, along an interface parallel to the Galactic Plane, is still required (Mineshige & Shibata 1990).

Elongated SNRs

Some objects in Table 3.4 are significantly extended along their symmetry axis, most notably G356.3–01.5 (Figure 3.11) and G296.5+10.0 (Figure 3.7). This appearance can be explained by tension associated with the ambient magnetic field, which would cause remnants to preferentially expand along field lines (Insertis & Rees 1991; Mineshige et al. 1993; Różyczka & Tenorio-Tagle 1995). However, for typical values of the explosion energy and ambient field strength, the shape of a SNR will not be appreciably distorted by the magnetic field until it reaches a diameter of $\gtrsim$100 pc (Mineshige & Shibata 1990; Norman 1993), at which stage a remnant is nearing the end of its observable lifetime (e.g. Shull et al. 1989). In order for tension in the

magnetic field to account for the observed extension, one must invoke a low explosion energy ($\lesssim 10^{50}$ erg) and/or a high magnetic field ($\gtrsim 100\,\mu$G). An alternative magnetic explanation for this elongation has been proposed by Roger et al. (1988). In the case of G296.5+10.0, they speculate that the SNR shock may not couple to newly swept up material when the magnetic field is parallel to the direction of propagation. As the remnant evolves, the shock speed is dependent on the angle with the magnetic field and the remnant will elongate.

Bisnovatyi-Kogan et al. (1990) consider a non-magnetic explanation for G296.5+10.0, wherein both the elongation and the bilateral appearance of the SNR are the result of it having expanded into a similarly extended pre-existing cavity. For this mechanism to apply for SNRs with low values of ψ, however, such cavities must lie with their major axis along the Plane.

An ISM Model

In the above discussion, we have considered three classes of objects which can be more comfortably accounted for by the surrounding ISM than by the magnetic model. We have considered objects with one side brighter than the other as might be due to a density gradient, a breakout morphology due to the presence of hot tunnels, and elongated remnants which might be due to an extended cavity. In order for any of these explanations to be valid, the observed distribution of ψ requires that structures in the ISM must be consistently parallel to the Plane.

As a mechanism for the bilateral appearance, we propose that the Galactic magnetic field produces density stratifications parallel to the Galactic Plane. Evidence to support this hypothesis is now presented.

The first issue to consider is whether stellar wind-bubbles can be elongated by the surrounding field. Consider a homogeneous ISM of gas density n_H, in which there is a uniform magnetic field of strength B_0. The bubble produced by an isotropic wind will expand more rapidly along field lines than across them, and will begin to be significantly distorted when the internal pressure in the bubble falls below the external magnetic pressure (Königl 1982). Adapting the result of Stone & Norman (1992) for a wind from a proto-star, this will occur after a time t_1, given by :

$$\left(\frac{t_1}{Myr}\right) \approx 2 \left(\frac{B_0}{3\,\mu\mathrm{G}}\right)^{-5/2} \left(\frac{L_w}{10^{35}\,\mathrm{erg\ s^{-1}}}\right)^{1/2} \left(\frac{n_H}{\mathrm{cm^{-3}}}\right)^{3/4}, \qquad (3.1)$$

where M is the mass of the star, v_w is the velocity of the wind and $L_w = \frac{1}{2}\dot{M}v_w^2$ is the associated mechanical luminosity. Therefore as a rough criterion, a wind bubble will become significantly elongated along ambient field lines if $t_0 \gg t_1$, where t_0 is the main-sequence lifetime of the star.

Chevalier & Liang (1989) tabulate the properties of stellar wind-bubbles for different spectral types, from which we find that in a typical environment ($B_0 = 3\,\mu$G, $n_H = 1\,\mathrm{cm^{-3}}$), a main-sequence wind-bubble will be dominated by the ambient field for a star of spectral type O9 or later. Such stars comprise the vast majority of

the stellar population, and indeed Lozinskaya (1988) notes that wind-blown bubbles are often elongated. Since $t_1 \propto B_0^{-5/2}$, only a slightly higher field than assumed above ($\gtrsim 10$ μG) is required to distort wind-bubbles produced by even the most massive stars. Note that the extra energy input in the late phases of stellar evolution may complicate the simple picture presented here.

On larger scales, Heiles (1979) has found that H I shells within 10° of the Plane appear elongated in the longitudinal direction, which he suggests could also be due to the ambient field. Also, simulations of magnetised superbubbles (Tomisaka 1990, 1992; Mineshige et al. 1993) and old SNRs (Norman 1993) show that such structures also become elongated along field lines, but over larger length and time scales than for stellar wind bubbles.

To summarise, we propose that where the magnetic field is oriented parallel to the Galactic disc, structures will be produced extended in the longitudinal direction, on approximately the same scale as SNRs. Thus close to the Plane, the structure of the Galactic ISM might take the form of tunnels, gradients and cavities all elongated in the disc of the Galaxy. When a SNR interacts with this structure, a bilateral appearance is produced (as in the model proposed by Bisnovatyi-Kogan et al. 1990), with the axis aligned parallel to the Plane.

A remnant formed from a massive progenitor will interact at its earliest stages with a complex and extensive CSM. During this period, a SNR can take on some aspects of bilaterality (Chapter 2 of this thesis; Igumenshchev et al. 1992; Blondin et al. 1996; Zhang et al. 1996), but no alignment with the Galactic Plane will be observed (unless the progenitor wind-bubble is elongated along the Plane through the process discussed above). Only once the shock propagates beyond its CSM and begins to interact with the ambient ISM should any trend in ψ manifest itself. Type Ia SNRs such as G327.6+14.6 may interact with the ambient medium at a much earlier stage, however. At the other end of the scale, as a remnant ages and expands, it becomes more and more likely to encounter complex inhomogeneities in the ISM which will distort its appearance. Hence, this mechanism for the bilateral appearance is most relevant for middle-aged remnants, rather than young or old ones. The uncertainty in SNR age estimates prevents us from demonstrating this property in the observed sample. However, rough estimates for the ages of SNRs in Table 3.4 (using the $\Sigma - t$ relation; Caswell & Lerche 1979) give that most are between 1000 and 10 000 years old.

3.6.3 Exceptional Cases: SNRs G296.5+10.0 and G327.6+14.6

SNRs G296.5+10.0 (Figure 3.7) and G327.6+14.6 (Figure 3.9) are discrepant in their values of ψ, both being oriented at almost right angles to the Plane. However, these two remnants are also notable in that they are both at a significant height above the Plane (175–350 pc and 450 pc, respectively; Roger et al. 1988).

For bilateral SNRs at low latitudes, we have proposed ISM structures running parallel to the Plane. At higher latitudes, the ISM is dominated by perpendicular structures in the form of chimneys (Norman & Ikeuchi 1989; Normandeau et al.

1996) and "worms" (Heiles 1984; Koo et al. 1992). Stellar polarisation measurements demonstrate the existence of large-scale loops of magnetic field also extending perpendicular to the Plane (Mathewson & Ford 1970). Thus that bilateral SNRs might tend to have $\psi \sim 90^\circ$ at large distances from the Plane is consistent with the extrinsic models described in Sections 3.6.1 and 3.6.2. SNRs G296.5+10.0 and G327.6+14.6 can therefore still be incorporated within the proposed model. One can speculate that bilateral SNRs at intermediate scale heights might be in transition between remnants with $\psi \sim 0^\circ$ and those for which $\psi \sim 90^\circ$. However, the uncertainty in the distances to SNRs in our sample prevents us from making meaningful conclusions on any latitude dependence at present.

These two SNRs are regarded as the prototypes for the bilateral morphology (e.g. KC87; Roger et al. 1988). That the most striking examples of bilaterality constitute 50% of known remnants for which $|b| \geq 10^\circ$ may be indicative of the homogeneity of the environment far from the Plane. It is highly likely that the radio all-sky surveys currently being carried out (Large et al. 1994; Condon et al. 1998) will discover new high latitude SNRs. Whether such remnants also have a well-ordered appearance and a high degree of symmetry will be useful (but not conclusive) evidence regarding the model we have proposed.

We note that intrinsic models have also been proposed for these two SNRs: Storey et al. (1992) argue that the symmetry present in G296.5+10.0 over a wide range of spatial scales generally argues against magnetic models for this object, while Willingale et al. (1996) hypothesise that a central compact object with opposed jets could generate the morphology of G327.6+14.6. Whether these remnants represent an extrinsic mechanism operating at high Galactic latitude, or intrinsic effects, either way, their high value of ψ is not at odds with the alignment observed in the remainder of the sample.

3.6.4 Explanations for Non-bilateral Structure

As noted in Section 3.5.2, the vast majority of remnants do not have a clear bilateral appearance. The wide range of SNR morphologies observed (clearly demonstrated in the catalogue of WG96) is indicative that complex, small-scale effects can dominate the appearance of SNRs. Specifically, the absence of bilaterality can be explained by any of the following conditions:

- A dominant component of the field along the line of sight, so that the projection of the emitting region is no longer two distinct arcs of emission. KC87 estimate that a SNR with a cylindrical 3D geometry will appear as a uniform ring of emission with no bilateral appearance if $\theta < 25^\circ$, and will be "confused" if $25^\circ < \theta < 45^\circ$. This results in 24% (rounded to 30% in KC87) of SNRs having a non-bilateral appearance, simply due to orientation.
- An inhomogeneous ISM. In this case, encounters with molecular clouds, cavities, and other inhomogeneities distort a remnant sufficiently so that no symmetrical structure can be observed (e.g. Pineault et al. 1993; Reynolds &

Moffett 1993; Koo & Moon 1997).

- A disordered ambient magnetic field, so that in the magnetic model, no position angle around the circumference has enhanced emissivity. It is suggestive that some bilaterals are highly polarised (e.g. Lalitha et al. 1984; Milne & Haynes 1994), indicating a well-ordered magnetic field.

3.7 Conclusion

We have presented 1.4 GHz radio observations of two southern supernova remnants, G003.8–00.3 and G350.0–02.0. The morphologies of these two SNRs are distinct — G003.8–00.3 shows a filamentary two-arc appearance in a classic "barrel" shape, while G350.0–02.0 strongly resembles the breakout morphology of G166.0+04.3 (VRO 42.05.01).

Despite their differences, both remnants have a clear bilateral appearance. Furthermore, the axis defined by this classification in both cases aligns almost exactly with the Galactic Plane. On examination of the entire sample of known Galactic SNRs, we find 17 SNRs with a high level of bilateral morphology, of which nine are oriented to the Plane at 12° or less. With a minimum of assumptions regarding the three-dimensional geometry, the probability of this occurring by chance is 7×10^{-4}. Considering SNRs G296.5+10.0 and G327.6+14.6 as distinct from the remainder of the sample reduces this probability even further.

This trend rules out "intrinsic" models for the bilateral morphology, all of which involve an axis defined by the orientation or motion of the progenitor star. Such models are not expected to produce remnants which align in any consistent way with the Galactic Plane.

The general alignment of bilateral remnants with the Plane can be explained by "magnetic" models, whereby an ambient magnetic field generates bright regions around the SNR shell where the shock normal is perpendicular to the field. This is a result of either enhanced field compression or preferential electron acceleration in these regions. However, distorted morphologies in bilateral SNRs can be better explained if the ISM into which these remnants expand consists of structures preferentially elongated in the longitudinal direction. We propose that this occurs in the form of expanding wind-bubbles distorted by the surrounding magnetic field.

The majority of SNRs do not have a distinct bilateral appearance. For some SNRs, this can be explained as an orientation effect, when the bilateral axis is close to the line of sight. The effects of a disordered magnetic field and an inhomogeneous ISM can further account for the observed diversity in morphologies.

This study has demonstrated the value of high resolution observations of Galactic SNRs. Further observations, in particular of the polarisation and environment of bilateral SNRs, are needed to test the proposed models. Undoubtedly there also remain more examples of bilateral SNRs to be discovered, particularly in the first quadrant and at high Galactic latitudes, which will improve the available statistics.

While theoretical modelling of the evolution of stellar wind bubbles is quite sophisticated (García-Segura et al. 1996 and references therein), the effect of external magnetic fields is generally ignored. The simple calculations made here suggest that such fields can have a significant effect on the dynamics of a bubble and should be included in subsequent modelling. Similarly, the interaction of SNRs with surrounding material usually assumes spherical symmetry (Chevalier & Liang 1989; Tenorio-Tagle et al. 1991); detailed simulations of the interaction of remnants with the (non-spherical) structures proposed here would be highly desirable.

An interesting extension of the results described would be to determine whether bilateral SNRs in other edge-on spiral galaxies are aligned along preferred position angles, and whether these angles correlate with measurements of the corresponding galactic magnetic field. Of particular interest is NGC 4631 which largely has a magnetic field oriented perpendicular to the disc (Hummel et al. 1991; Golla & Hummel 1994). At present, existing observations of SNRs in other spiral galaxies (e.g. Duric et al. 1993; Muxlow et al. 1994) are of insufficient resolution to derive a bilateral subset. However, the planned upgrade to the VLA (Bastian & Bridle 1996) will provide sufficient improvement in sensitivity and resolution to produce images of SNRs in these galaxies of a quality comparable to existing Galactic observations.

Chapter 4

Radio Continuum and H I Observations of SNR G296.8–00.3

This Chapter has also appeared as Gaensler et al., 1998a, "Radio continuum and H I observations of supernova remnant G296.8–00.3", MNRAS, **296**, 813.

4.1 Introduction

The expanding shock front produced by a supernova (SN) explosion is best delineated in the radio continuum, where we observe the synchrotron emission from ultra-relativistic electrons at or near the expanding shock. Few supernova remnants (SNRs) appear circular and undistorted, but whether this distortion is a result of the distribution of the ejecta driving the shock front, the mass-loss history of the progenitor, the structure of the surrounding interstellar medium (ISM) or some complex combination of all of these, is a difficult question to answer. Of the 215 known SNRs in the Galaxy (Green 1996), many have now been observed at sub-arcmin resolution at radio frequencies (e.g. Whiteoak & Green 1996). However, without knowledge of their physical properties interpretation of their appearance is difficult.

Although detected in early radio surveys of the Galactic Plane (Hill 1968; Thomas & Day 1969), G296.8–00.3 was first identified as a supernova remnant by Large & Vaughan (1972) on the basis of its spectral index and rough shell-like morphology. These authors claimed an association with the pulsar B1154–62, $13'$ from the remnant's centre, which has since been considered unlikely on the basis of the pulsar's large timing age of 1.6×10^6 yr (Gaensler & Johnston 1995c; Johnston et al. 1996). A recent higher resolution image ($43'' \times 49''$) of this SNR has been made at 843 MHz by Whiteoak & Green (1996), showing a complicated multi-ringed structure, brightest to the north-west.

In X-rays, Hwang & Markert (1994) report a 4-σ detection of SNR G296.8–00.3 with the *ROSAT* Position Sensitive Proportional Counter (PSPC). They ascribe the weakness of the X-ray emission to significant absorption along the line of sight, and consequently estimate a distance of $\sim$10 kpc. There is no detectable infrared

emission associated with the SNR (Arendt 1989; Saken et al. 1992), and examination of the Digitized Sky Survey and of the corresponding ESO R field shows no optical counterpart.

As part of a programme to determine the basic properties of southern SNRs with unusual features, we present here 1.3-GHz continuum and H I absorption observations towards SNR G296.8–00.3. We describe our observations and analysis in Section 4.2 and present our results in Section 4.3. In Section 4.4 we derive physical properties for the SNR and discuss possible causes for the remnant's unusual morphology. We also consider the possibility of an association between SNR G296.8–00.3 and PSR B1154–62.

4.2 Observations and Data Reduction

Observations were made with the Australia Telescope Compact Array (ATCA; Frater et al. 1992), a synthesis telescope near Narrabri, New South Wales. The ATCA consists of five 22-m-diameter antennas located on a 3-km east-west track, with a fixed sixth antenna located 3 km further west. A pointing centre RA (J2000) $11^{\rm h}58^{\rm m}43^{\rm s}$, Dec. (J2000) $-62^\circ34'29''$ was observed with three different array configurations, as shown in Table 4.1. For the compact configurations used here, correlations involving the sixth antenna were not used. Continuum and H I line observations were made simultaneously; the continuum data consisted of 32 channels centred at 1.344 GHz with a total bandwidth of 128 MHz, and the line data comprised 1024 channels centred at 1.420 GHz, with a total bandwidth of 4 MHz (a channel separation of 0.83 km s^{-1}). All four Stokes parameters were recorded in continuum, while only total-intensity data were recorded in the H I line. Amplitudes were calibrated using the revised scale of Reynolds (1994), assuming a flux density for PKS B1934–638 of 15.0 and 14.9 Jy, at 1.344 and 1.420 GHz respectively. Phases were calibrated using PKS B1549–790, which was observed for approximately 3 min for each hour of observation.

Date	Array Configuration	Maximum Baseline (m)	Time on Source (h)
1996 Jan 19	0.75C	750	12
1996 Feb 02	0.75B	765	11
1996 Feb 24	1.5C	1485	14

Table 4.1 ATCA observations of G296.8–00.3.

Reduction and analysis were carried out using the `MIRIAD` (Sault et al. 1995) and `KARMA` (Gooch 1996) packages. Data were edited and calibrated using standard techniques (Sault & Killeen 1998). The calibrator PKS B1549–790 ($S_{1.3\,\rm GHz} = 5.4$ Jy) was confused by the source PKS B1547–795 ($S_{1.3\,\rm GHz} = 0.8$ Jy), $27'$ distant. Thus a

point-source model for the calibrator was not appropriate, and antenna gains were determined by comparing the measured visibilities to those corresponding to a model including both sources, in effect carrying out a self-calibration of the calibrator field.

4.2.1 Continuum Data

A total-intensity continuum image of a $65' \times 65'$ region was formed using multi-frequency synthesis (Sault & Wieringa 1994), uniform weighting and a cell size of $5''$. The image was then deconvolved using a maximum entropy algorithm (Gull & Daniell 1978) with 500 iterations. To improve estimates of the antenna gains, three iterations of amplitude and phase self-calibration were applied, with a solution interval of 5 min. The resulting model was smoothed with a Gaussian restoring beam, and the final image then corrected for the mean primary beam response of the ATCA antennas.

Images were also formed in Stokes Q, U and V. To minimise the effects of bandwidth depolarisation, 13 Q and U images were made, each using a bandwidth of 8 MHz, covering the central 104 MHz of the band. Stokes Q, U and V images were then deconvolved using the `CLEAN` algorithm (Clark 1980), then restored and primary-beam corrected as for Stokes I above. For each pair of Stokes Q and U images, a linear polarisation image, L, was formed and corrected for non-Gaussian noise statistics (Killeen et al. 1986). A mean of the 13 L planes was then formed. This image was then clipped at pixels where polarised emission fell below the 5-σ level, and also where the total intensity was less than 5 σ.

4.2.2 Line Data

Continuum emission was subtracted from the line data in the $u-v$ plane using the `MIRIAD` task `UVLIN` (van Langevelde & Cotton 1990; Sault 1994), and spectra then smoothed to a velocity resolution of 3.3 km s^{-1}. Data at projected $u-v$ spacings shorter than 1 kλ were discarded to filter out broad-scale structure, and line images were then formed in velocity planes ranging from –200 to +200 km s^{-1} (LSR). The peak emission was faint, with no obvious sidelobes, and it was consequently unnecessary to deconvolve the resulting images.

The H I cube was then weighted by the continuum image. Absorption spectra against continuum sources were produced by integrating over the corresponding region of the cube, and then renormalising appropriately to give units of fractional absorption.

The RMS noise, σ, in each spectrum was estimated using the flux in line-free channels. The brightness temperature of Galactic H I in this direction ($\sim$100 K; Caswell et al. 1975b) increases the thermal noise in channels containing line emission by a factor of $\sim$2 (cf. Dickey 1997). In the spectra presented we thus show a threshold corresponding to 6σ as an indication of the believability of features.

4.3 Results

4.3.1 Total Intensity

SNR G296.8–00.3

Total-intensity images of SNR G296.8–00.3 in Figure 4.1 show a complicated structure similar to that seen with lower resolution at 843 MHz (Whiteoak & Green 1996). The SNR consists of multiple loops of emission, brightest in the north-west, where there is a sharp outer boundary. While the western edge is particularly well defined, the eastern perimeter is fainter and more diffuse.

Running through the centre of the remnant is a peculiar, slightly curved strip of emission, beginning beyond the remnant's northern boundary and extending up, or close, to its southern perimeter. This structure shows no limb-brightening, and has an essentially uniform appearance across its extent except for a possible fading to the south. Although appearing rather artificial, this feature is also seen in the 843-MHz image made with the Molonglo Observatory Synthesis Telescope (MOST; Whiteoak & Green 1996). Although both are synthesis telescopes, the ATCA and the MOST produce quite different artifacts (Robertson 1991) and we conclude that this feature corresponds to genuine emission.

Derived parameters for the SNR are given in Table 4.2. The flux density for the remnant and its uncertainty were determined by integrating the emission within multiple polygons enclosing the remnant. A background correction was made and the RMS noise in the image measured by similarly integrating over nearby source-free regions.

Resolution	$24\farcs3 \times 22\farcs4$, PA 14°
RMS noise in image	170 (Stokes I)
(μJy beam^{-1})	40 (Stokes V)
Geometric centre (α, δ; J2000)	$11^{\rm h}58^{\rm m}25^{\rm s}$ –62°36′
Geometric centre (l, b)	296.°87 –00.°35
Diameter	$18' \times 12'$
Flux density at 1.3 GHz (Jy)	7.0 ± 0.3
Spectral index	-0.65 ± 0.08

Table 4.2 Observational and derived parameters for G296.8–00.3.

We compute a spectral index for SNR G296.8–00.3 using the total flux density measurements shown in Table 4.3. Fitting a power law of the form $S_\nu \propto \nu^\alpha$ to the data, we obtain a spectral index $\alpha = -0.65 \pm 0.08$, consistent with earlier determinations (Large & Vaughan 1972; Caswell et al. 1975a).

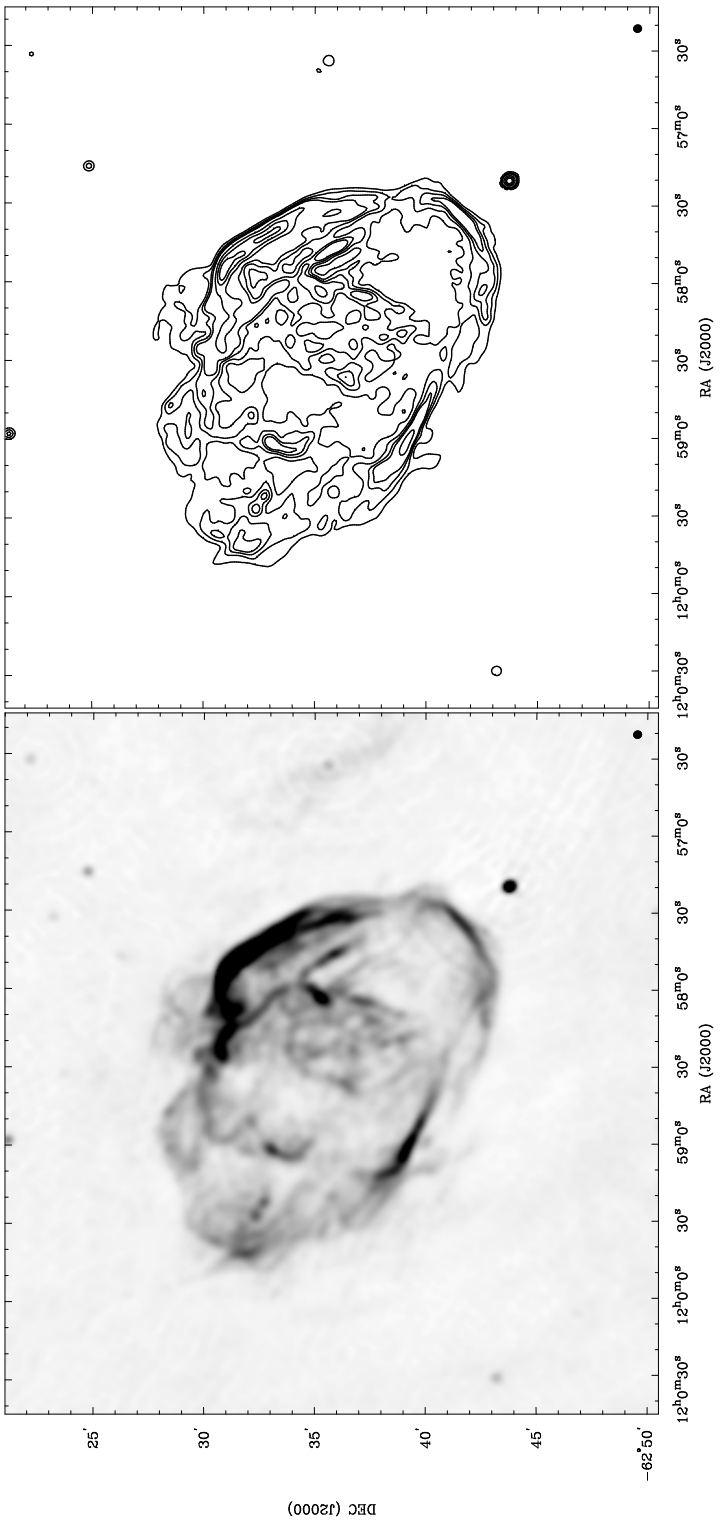

Figure 4.1 Grey-scale and contour images of SNR G296.8–00.3 at 1.3 GHz. The grey-scale range is –1 to 20 mJy beam^{-1}, while the contour levels are 2.5, 5, 7.5, 10, 20, 30 and 40 mJy beam^{-1}. The FWHM of the Gaussian restoring beam is shown at the lower right of each image.

ν (GHz)	Telescope	S_ν (Jy)	Reference
0.408	Mills Cross	15.0 ± 1.5	1
0.843	MOST	9.2 ± 0.9	2
1.344	ATCA	7.0 ± 0.3	This Chapter
1.420	Parkes 64-m	6 ± 1	1,3
2.650	Parkes 64-m	4 ± 1	4
5.000	Parkes 64-m	3.2 ± 1	5

(1) Large & Vaughan (1972) (2) Whiteoak & Green (1996) (3) Hill (1968) (4) Thomas & Day (1969) (5) Caswell et al. (1975a)

Table 4.3 Flux density measurements of SNR G296.8–00.3. Where not specified by the authors, errors have been taken to be 10% or 1 Jy, whichever is larger.

Other Sources in the Field

An image of the entire field is shown in Figure 4.2. The properties of four sources of note are summarised in Table 4.4.

Source 1 can be identified with the 400-ms pulsar B1154–62 (Large et al. 1969; Siegman et al. 1993). We measure an integrated flux density for the pulsar of 9.7 ± 0.3 mJy, agreeing with previous measurements (Johnston et al. 1996).

Source	Position		$S_{1.3\,\mathrm{GHz}}$	Spectral index[a]	Other name
	Equatorial (J2000)	Galactic	(Jy)	(α, $S_\nu \propto \nu^\alpha$)	
1	$11^\mathrm{h}57^\mathrm{m}15^\mathrm{s}$ $-62°24'50''$	$296.^\circ70$ $-00.^\circ20$	0.01	–2.6	PSR B1154–62
2	$11^\mathrm{h}57^\mathrm{m}20^\mathrm{s}$ $-62°43'50''$	$296.^\circ78$ $-00.^\circ51$	0.08	–0.5	
3	$11^\mathrm{h}59^\mathrm{m}32^\mathrm{s}$ $-62°07'19''$	$296.^\circ90$ $-00.^\circ14$	0.62	–0.9	PMN J1159–6207
4	$12^\mathrm{h}01^\mathrm{m}21^\mathrm{s}$ $-62°36'44''$	$297.^\circ21$ $-00.^\circ30$	0.11	–0.6	

[a] Calculated between 1.344 GHz (this Chapter) and 843 MHz (Green et al. 1998).

Table 4.4 Selected sources in the vicinity of SNR G296.8–00.3. All sources are unresolved.

4.3.2 Polarisation

PSR B1154–62

As a test of the polarimetric quality of our data, we first consider PSR B1154–62, whose polarisation properties we can compare with existing data.

PSR B1154–62 is significantly linearly polarised: we measure a linear polarisation $L = 2.5 \pm 0.3$ mJy ($26 \pm 4\%$), agreeing well with previous measurements (McCulloch

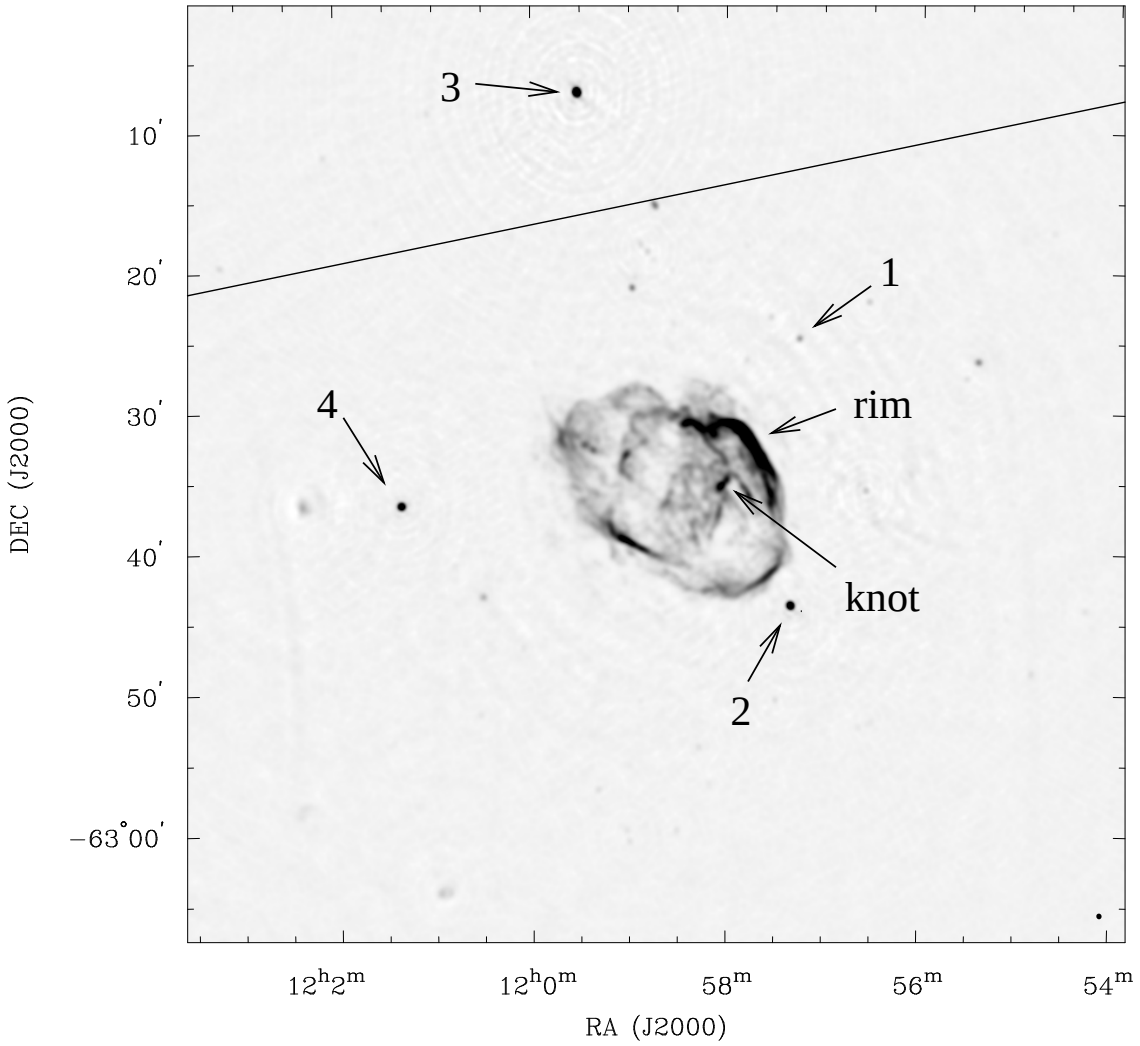

Figure 4.2 A total-intensity image of the field surrounding SNR G296.8–00.3. In order to give uniform noise across the image, the image has not been corrected for the ATCA primary beam response. Sources listed in Table 4.4 are indicated, as well as the two regions of the SNR against which H I absorption was obtained. The line to the north of the SNR represents the Galactic Plane.

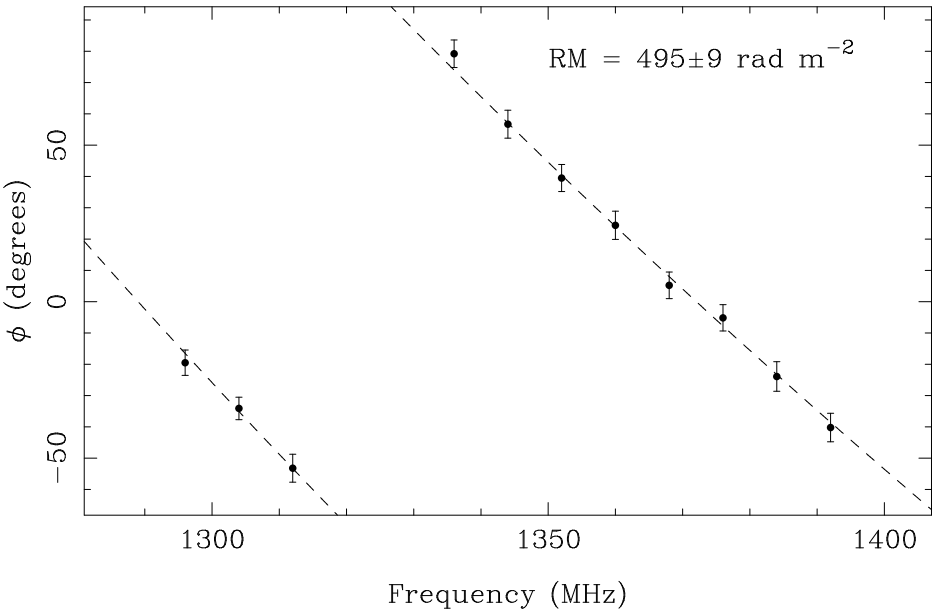

Figure 4.3 A plot of the Faraday rotation across the band for PSR B1154–62. The plotted points correspond to position angles measured at 8-MHz intervals (gaps at 1320 and 1328 MHz correspond to bad data), while the line corresponds to the best fitting curve of the form $\phi = \phi_0 + \mathrm{RM}\,c^2/\nu^2$.

et al. 1978; Manchester et al. 1980; van Ommen et al. 1997).

The ATCA generates instrumental linear polarisation proportional to the strength of a source in total intensity. This response is negligible at the phase centre, but becomes significant towards the edges of the field. The primary-beam corrected linear polarisation for the pulsar caused by this effect is of the order of 0.2% of the total intensity and makes a minor contribution to the value obtained.

The multi-frequency capability of the ATCA allows us to measure the variation in position angle, ϕ, of the pulsar's linearly polarised emission across the observing bandwidth, as shown in Figure 4.3. This can be attributed to Faraday rotation, and we can hence derive a rotation measure for the pulsar. Fitting a curve with functional form $\phi = \phi_0 + \mathrm{RM}\,c^2/\nu^2$ to the data gives a rotation measure $\mathrm{RM} = 495 \pm 9$ rad m^{-2}. Within the uncertainties, this agrees with the published value of 508 ± 5 rad m^{-2} (Taylor et al. 1993).

PSR B1154–62 is left-hand circularly polarised with a flux density 1.2 ± 0.2 mJy (12 ± 2% of the total). This is again consistent with earlier work.

In summary, we conclude that the observed polarisation properties of PSR B1154–62 agree well with previous measurements.

SNR G296.8–00.3

No circular polarisation is detected from SNR G296.8–00.3. An image of the linear polarisation from the remnant is shown in Figure 4.4. We estimate a lower limit on

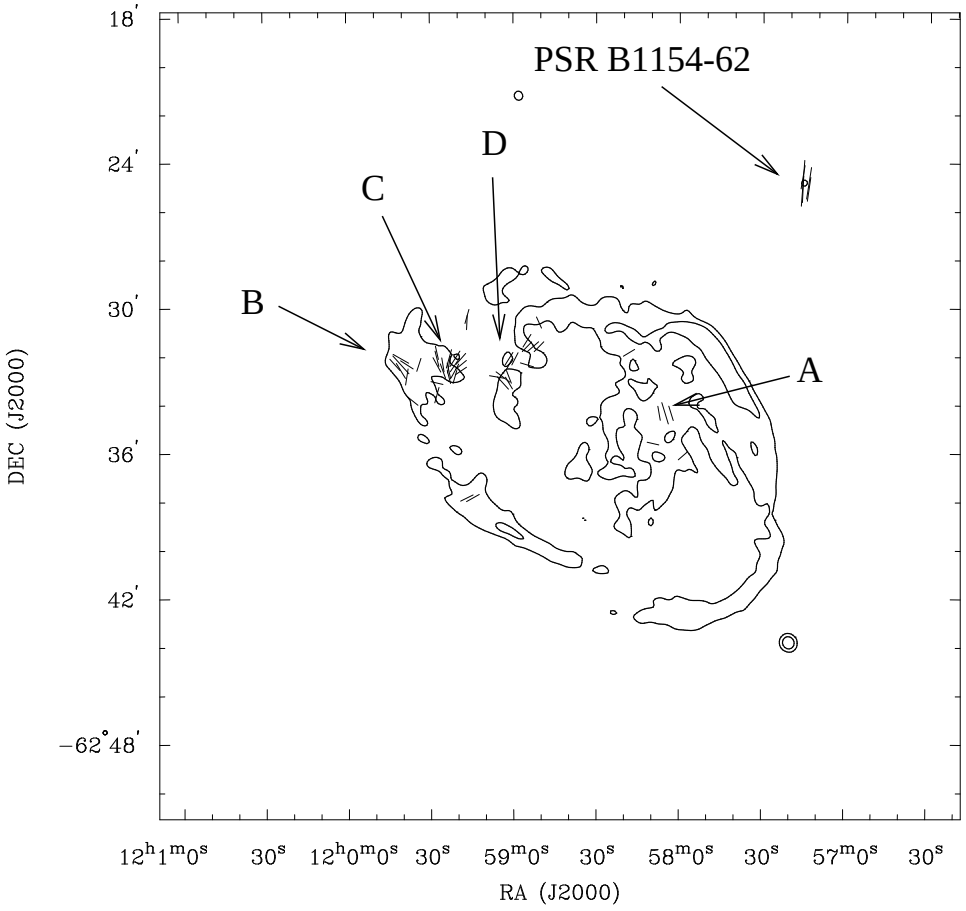

Figure 4.4 Linearly polarised emission from G296.8–00.3. The orientation of vectors indicate the position angle of the electric field in an 8-MHz channel centred on 1376 MHz. Lengths of vectors are proportional to the surface brightness in linear polarisation at that position, the longest vector corresponding to $L = 2.5$ mJy beam^{-1}. Contours represent total intensity, and are drawn at 5 and 20 mJy beam^{-1}. The labelled regions correspond to the plots in Figure 4.5.

the linearly polarised flux density from the remnant of 35 ± 5 mJy, a fractional polarisation of 0.5% (instrumental polarisation contributes less than 0.1%). Polarisation from the SNR occurs in a few discrete cells, predominantly near the north-eastern edge of the SNR (note that region 'A' is not coincident with the compact knot in this region of the SNR). Within a cell there appears to be some correlation in position angle but adjacent cells have quite different orientations. There is no correlation between total and polarised intensity over the SNR. In fact the brightest regions of the SNR, namely the north-west, south-west and south edges, have no significant polarised emission.

In Figure 4.5 we show the position angle as a function of frequency for four regions of significant linear polarisation. As for PSR B1154–62, a change in position angle of the electric field vectors is seen across the band. Averaging over regions of sufficiently

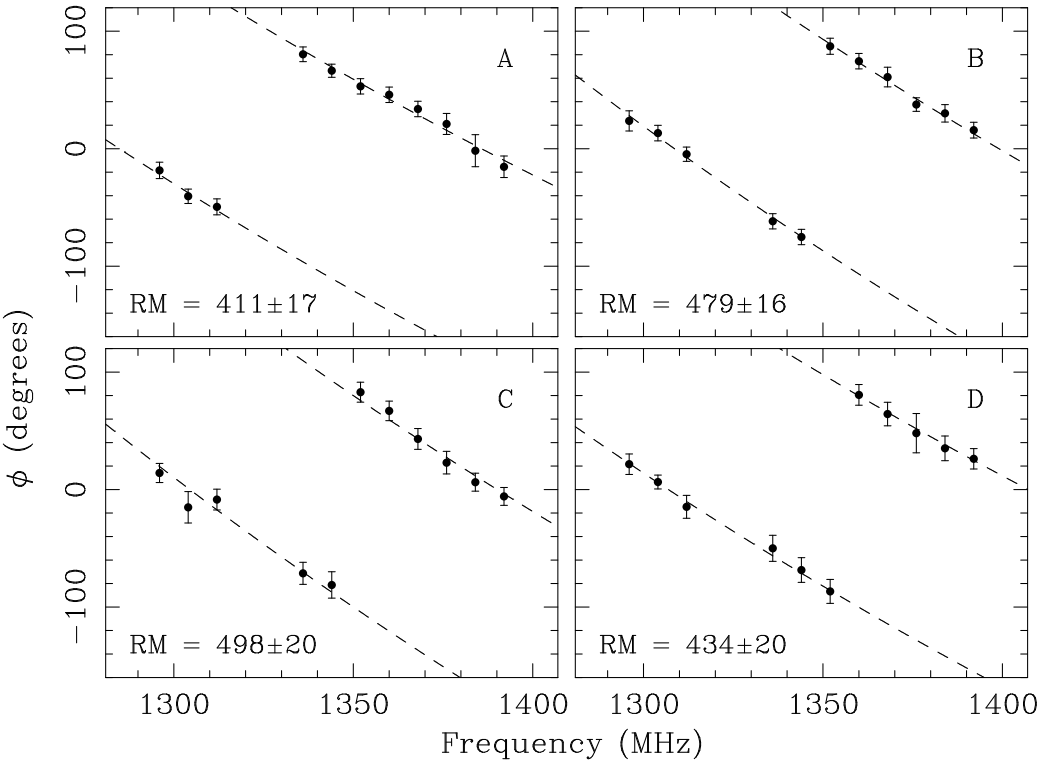

Figure 4.5 Faraday rotation and rotation measures (in rad m^{-2}) for four regions marked in Figure 4.4. Properties of the plots are as for Figure 4.3.

strong polarisation, we obtain a mean RM for the remnant of 430 rad m^{-2}, with a scatter of 40 rad m^{-2}.

In theory, one can use the rotation measure to determine the intrinsic position angle of the polarised radiation, ϕ_0. However, the accuracy, $\delta\phi_0$, of this measurement is limited by the uncertainty in RM, δ(RM). Typical values of δ(RM) across the SNR are 20–30 rad m^{-2}, corresponding to $\delta\phi_0 \approx \delta(\mathrm{RM})\, c^2/\nu^2 \approx 1$. Thus we cannot determine intrinsic position angles, effectively because of the narrow bandwidth across which we have made our measurements.

Other Sources

After correcting for instrumental polarisation, sources 2, 3 and 4 are 0.2%, 2.7% and 1.4% linearly polarised respectively. No circular polarisation is detected from any of these sources.

4.3.3 H I Line

In the following discussion we establish upper and lower limits on the systemic velocity of SNR G296.8–00.3 by measuring the H I velocities of absorbing clouds along the line of sight and combining these with an appropriate model for Galactic

rotation to derive a kinematic distance to the remnant (see Burton 1988 for a review). We compare absorption against the remnant to adjacent emission and absorption spectra; the former is obtained from nearby regions devoid of continuum emission, while the latter is seen towards sources 2 and 4.

We define the lower limit on the systemic velocity, V_L, to be that corresponding to the most distant absorption feature seen against the SNR, and the upper limit, V_U, to be the nearest strong emission feature in the region not seen in absorption (e.g. Frail & Weisberg 1990). We adopt an uncertainty of ± 7 km s^{-1} in V_U and V_L, representative of the random motion of H I clouds (Shaver et al. 1982; Belfort & Crovisier 1984); uncertainties associated with estimating velocities from our spectra are somewhat smaller than this. When translating velocities into distances, we adopt standard IAU parameters (Kerr & Lynden-Bell 1986) for the solar orbital velocity ($\Theta_0 = 220$ km s^{-1}) and the distance to the Galactic Centre ($R_0 = 8.5$ kpc).

The lack of short $u - v$ spacings in our ATCA observations means that it is difficult to produce an emission spectrum from these data. However, we can compare ATCA absorption spectra to the emission spectrum seen towards PSR B1154–62 (Johnston et al. 1996), only $7'$ from the brightest part of the SNR. This spectrum is shown in Figure 4.6, together with the single-dish absorption towards the pulsar and the rotation curve in this direction. The emission spectrum contains strong ($T_b > 35$ K) features at –35, –5, +15, +30 and +50 km s^{-1}. Similar emission profiles are seen in the direction of the nearby H II regions G298.2–00.3 and G298.9–00.4 (Goss et al. 1972) and in the H I survey of Kerr et al. (1986).

Point Sources

Absorption was measured against the nearby sources 2 and 4, with spectra shown in Figure 4.7. The absorption spectrum obtained towards source 3 was noisy and not considered useful.

The most negative velocity absorption feature seen in the spectrum of source 2 is at –35 km s^{-1}, agreeing well with the measured tangent velocity in this direction (Kerr et al. 1986; Malhotra 1995). Significant absorption is also seen at –5, +15 and +30 km s^{-1}. A weak feature at +100 km s^{-1} is of low significance.

Source 4 shows similar structure to source 2 at negative velocities. At positive velocities, strong absorption is seen at +15 km s^{-1}, and a forest of weaker features is visible at +30, +40, +50, +65 and +110 km s^{-1}. Although each feature individually is of marginal significance, together they suggest true absorption rather than random fluctuations.

SNR G296.8–00.3

Spectra of reasonable signal-to-noise were seen against the two regions of the SNR indicated in Figure 4.2: the bright rim along the SNR's north-west edge, and a nearby knot in the interior. These spectra are shown in Figure 4.7.

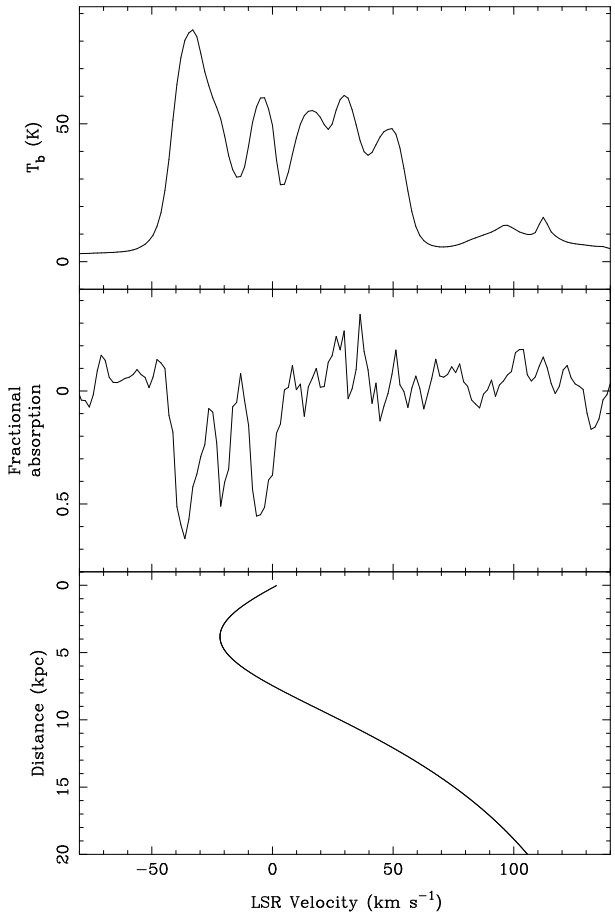

Figure 4.6 H I emission and absorption towards PSR B1154–62, and the variation of velocity with distance from the sun in this direction (Johnston et al. 1996).

Against the rim of the SNR, absorption seen at negative velocities corresponds to emission seen towards the pulsar and absorption towards sources 2 and 4. At positive velocities, clear absorption is seen at +15 km s^{-1} and a weaker feature at +35 km s^{-1}. Beyond this the spectrum is consistent with noise. Absorption towards the knot at negative velocities is similar to that towards the rim. Strong absorption is also seen at +15 km s^{-1} but not beyond this point.

The weak feature seen against the rim at +35 km s^{-1} matches the +30-km s^{-1} feature clearly seen towards source 2 only approximately. While this difference in velocity is within the uncertainties associated with H I, emission towards the pulsar, much closer to the rim than source 2, also shows a feature peaking at +30 km s^{-1}. This seems to indicate a genuine discrepancy in velocity between the +35-km s^{-1} feature towards the SNR and +30-km s^{-1} absorption towards source 2. Furthermore, while the two SNR spectra are otherwise similar the +35-km s^{-1} feature is not seen against the knot, despite its proximity to the rim. One could argue that the knot is an unrelated foreground source but we think it more likely that the +35-km s^{-1} feature represents fluctuations in emission rather than true absorption, and assign

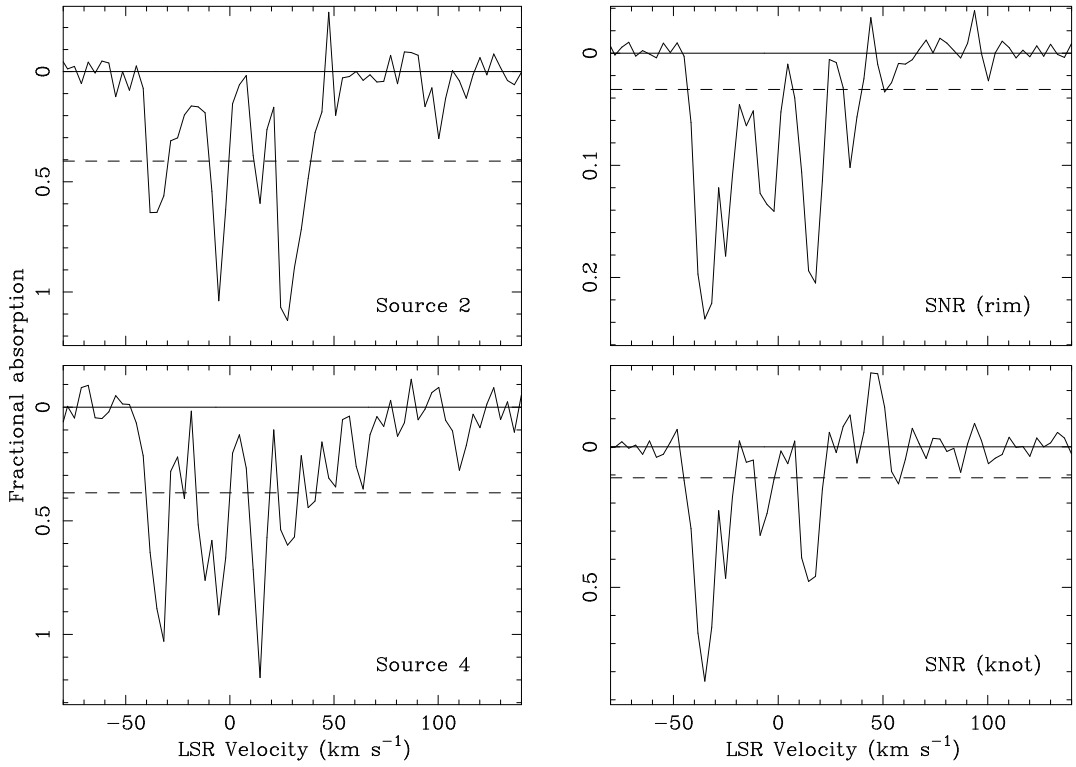

Figure 4.7 H I absorption spectra towards sources 2 and 4 and towards the regions of SNR G296.8–00.3 indicated in Figure 4.2. The dashed line represents absorption at the 6-σ level, where σ is calculated from the emission in line-free channels.

lower and upper limits to the remnant of $V_L = +15$ km s^{-1}and $V_U = +30$ km s^{-1} respectively. Given an uncertainty of ± 7 km s^{-1}, we can assign an overall systemic velocity to the SNR of $V_{\rm SNR} = 23 \pm 7$ km s^{-1}.

4.4 Discussion

4.4.1 SNR G296.8–00.3

Physical Parameters

Adopting the best fitting model for Galactic rotation of Fich et al. (1989), we use the velocity determined for the SNR in Section 4.3.3 to derive a kinematic distance of 9.6 ± 0.6 kpc, putting it on the far side of the Carina arm. This is consistent with Hwang & Markert's (1994) estimate based on the lack of X-ray emission. A distance of 9.7 kpc has also been estimated from the $\Sigma - D$ relation (Caswell & Barnes 1983). However, given the large uncertainties in this method (Green 1984), this agreement is certainly fortuitous.

Using the brightest regions ('ring 1' — see Figure 4.8) to define a single SNR shell, we find a radius for G296.8–00.3 of 17 ± 1 pc. An upper limit on the remnant's

age can consequently be obtained by assuming that it has expanded into the ambient ISM. For an ambient density n_0 cm^{-3}, the mass swept up by the SNR is $\sim 500 n_0\, M_\odot$. Typical values of n_0 then imply that the ejecta have swept up many times their own mass and that the remnant is no longer freely expanding. If we assume that the remnant is in the adiabatic (Sedov–Taylor) phase, we can derive an age $t_{\rm SNR} = (22 \pm 3)\,(n_0/E_{51})^{1/2} \times 10^3$ yr, where E_{51} is the kinetic energy of the explosion in units of 10^{51} erg. Frail et al. (1994b) suggest typical values $n_0 = 0.2$ and $E_{51} = 1$, implying that $t_{\rm SNR} = (10 \pm 2) \times 10^3$ yr.

We derive a lower limit on the remnant's age by assuming free expansion, as would occur if the remnant is propagating through the main-sequence wind bubble of a massive progenitor (Chevalier & Liang 1989; Tenorio-Tagle et al. 1990). Free expansion at $(0.3 - 1.0) \times 10^4$ km s^{-1} gives an age in the range 1600–6000 yr.

Polarisation

The rotation measure of 430 rad m^{-2} derived for the SNR in Section 4.3.2 differs from the value of ~ 100 rad m^{-2} measured by Dickel & Milne (1976) over the north-east part of the remnant. Given that we obtain polarisation data for PSR B1154–62 consistent with earlier measurements, we have confidence in our results. In any correction for Faraday rotation, there is always an ambiguity of $n\pi$ ($n = 0, \pm1, \pm2, \ldots$). The discrepancy in rotation measures can be accounted for if Dickel & Milne's result (obtained using data at 2.7 and 5 GHz) is out by a half-turn, causing them to underestimate the rotation measure by 360 rad m^{-2}. It is unlikely that there is any further ambiguity in the data: at the 8-MHz frequency resolution of the ATCA observations, a further half-turn would increase the RM by ~ 5000 rad m^{-2}.

Although the theoretical fractional polarisation of synchrotron radiation is 70%, this SNR is quite typical in having a much lower value, indicating that the remnant has been depolarised. We can immediately rule out bandwidth depolarisation as a possible cause since, by imaging the polarised emission in several frequency planes before combining, we have reduced Faraday rotation across each channel to $< 20°$.

The cell structure of the polarised emission, with significant changes in position angle between adjacent regions, suggests that the SNR has been beam depolarised, i.e. that large changes in position angle are occurring on scales smaller than the resolution element. This could be a result of differential Faraday rotation in the ISM, or may correspond to intrinsic structure in the SNR's magnetic field. The former possibility is certainly reasonable, given that it requires fluctuations in RM within a beam of only $\sim$20 rad m^{-2}, comparable to the variation in RM seen across the source. However, to determine conclusively which mechanism applies will require observations at higher frequencies, where effects caused by Faraday rotation are minimal.

Using the Galactic electron density distribution of Taylor & Cordes (1993), we compute an electron column density along the line of sight to the SNR of 260–330 pc cm^{-3}. Assuming that Faraday rotation internal to the SNR makes only a small contribution to the total rotation measure, we compute an averaged line-of-

sight interstellar magnetic field of 1.7 ± 0.3 μG, directed towards us.

Morphology

The morphology of SNR G296.8–00.3 is not that seen in a typical shell SNR, and we suggest three possible explanations to account for its complicated and multi-shelled appearance. First, the SNR could be two separate objects. Second, it may have a double-ringed morphology corresponding to an underlying biannular symmetry in the progenitor system, as proposed by Manchester (1987). Finally, G296.8–00.3 may owe its appearance to the surrounding ISM. We now consider these various possibilities.

Given that the lifetime of a supernova progenitor exceeds the observable lifetime of a SNR by 2–3 orders of magnitude, it is highly unlikely that we are seeing two SNRs from the same stellar association in temporal co-existence. It is possible that we are seeing two SNRs lying at different distances but along the same line of sight, but we think that this too is unlikely as it would require the centres of the only two SNRs in the field to virtually coincide. Further circumstantial evidence against G296.8–00.3's being multiple SNRs is that H I absorption from the rim and the knot give consistent systemic velocities, and that the rotation measure is roughly uniform across the SNR. Thus the possibility of multiple SNRs cannot be ruled out by our data, but is unlikely.

It is now well-established that the slow wind from the red supergiant (RSG) phase of massive stars can possess axial symmetry (Blondin et al. 1996 and references therein). Manchester (1987) proposed that expansion of a SNR into such a medium can produce a biannular, or double-ringed morphology, similar to models proposed for planetary nebulae (Kahn & West 1985; Balick 1987). Theory (Igumenshchev et al. 1992; Blondin et al. 1996) and observations (see Chapter 2) both support the argument that this axisymmetric RSG wind can indeed affect the shape and morphology of a remnant expanding through it. Typical parameters for the RSG phase are a wind speed $v_{\rm RSG} = 20$ km s^{-1}, a mass loss rate $\dot{M}_{\rm RSG} = 10^{-7} - 10^{-5}$ $M_\odot$ yr^{-1} and a life-time $t_{\rm RSG} = 3 \times 10^5$ yr (Smith 1994). This generates a potentially asymmetric medium around a supernova of radius <5 pc. Assuming such an environment for SNR G296.8–00.3, we find that the remnant, with a radius of $\sim$17 pc, has expanded well beyond this region and into the main-sequence wind of the progenitor. In the spherically symmetric case, this wind is predominantly hot, isobaric and consequently isotropic (Weaver et al. 1977), and we expect a SNR propagating through it to rapidly become spherical (Bisnovatyi-Kogan & Blinnikov 1982). For such a SNR to retain the brightness distribution induced in it by the RSG wind requires a mechanism by which shock acceleration preferentially occurs in the biannular emitting regions (Manchester 1987). A more likely explanation is the presence of asymmetry in the main sequence wind: for example, the effect of rotation in the progenitor can concentrate such a wind along the equatorial plane (Bjorkman & Cassinelli 1993; Owocki et al. 1994). To summarise, SNR G296.8–00.3 is well beyond the size at which biannular structure could

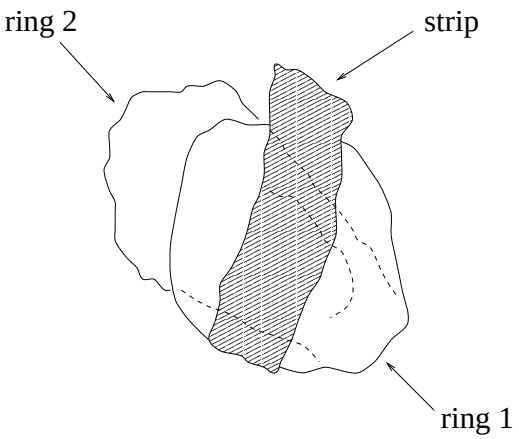

Figure 4.8 A sketch of the morphology of SNR G296.8–00.3, showing some pertinent features.

be imprinted upon it by asymmetric mass loss in a RSG progenitor wind. If its appearance is caused by the structure of circumstellar material, then we require either the SNR to have somehow retained a biannular morphology while expanding into an isotropic medium, or the progenitor's main-sequence wind to have possessed axial symmetry.

Manchester (1987) also suggests that a biannular SNR could be formed by the preferential distribution of ejecta along the polar axis. However, evidence suggests that asymmetric ejecta do not produce an unusually shaped remnant (Chapter 2 of this thesis; Bisnovatyi-Kogan & Blinnikov 1982; Blondin et al. 1996).

A further means of producing biannular structure is through jets from a central pulsar or binary system, which then hit the surface of the expanding remnant (Manchester 1987). Our radio observations of SNR G296.8–00.3 show no evidence for a centrally located point source either in total or polarised intensity, nor for outflows from such a source. The X-ray observations also show no central emitting region which might correspond to a central star or nebula. Apart from B1154–62, no pulsar has been detected in or near this remnant (Manchester et al. 1985a; Kaspi et al. 1996b). We conclude that there is no evidence for a central source or related outflows in SNR G296.8–00.3.

We now consider the possibility that the SNR is interacting with the ambient medium. In order to propose a simple model of the SNR's appearance, we denote the main features in the SNR as follows, illustrated schematically in cartoon form in Figure 4.8:

1. a bright, sharp-edged, and almost complete ring of emission in the south-west ('ring 1'). In the absence of other structure, this component would appear as

a typical shell SNR;

2. a rectangular strip of emission running north-south through the centre of the SNR. This strip is not a typical SNR feature — it is almost linear, is uniform in brightness over its extent, with projected dimensions of ∼40 pc north-south and ∼13 pc east-west (at a distance of 10 kpc);
3. a faint, ragged partial ring ('ring 2'), extending beyond ring 1 to the north-east and possibly connecting with filaments in the south.

Ring 1 seems compatible with a SNR expanding into a homogeneous medium. We suggest that the strip corresponds to a tunnel or tube of significantly lower density. This is of appropriate dimensions to be an old SNR or stellar-wind bubble, its elongated appearance caused by tension in external (Chapter 3 of this thesis; Stone & Norman 1992) or internal (Cox & Smith 1974; Landecker et al. 1989) magnetic field lines. On encountering such a region, an expanding shock will re-energise it, rapidly propagating both across the tube and up and down its length. As it does so, electrons in the walls are shock-accelerated and emit synchrotron radiation (Pineault et al. 1987), giving a filled, linear structure as observed here.

Ring 2 is fainter than ring 1, extends beyond the latter's boundary, and has a more poorly defined outer edge. This suggests that it represents a region of break-out into an adjacent cavity, perhaps created by another massive star. In such a case the shock will rapidly expand to take on the dimensions of the region, creating the multiple shell appearance observed (Braun & Strom 1986)

It has been argued that the morphologies of SNRs G166.0+04.3 (VRO 42.05.01) and G350.0–02.0 both result from a supernova shock re-energising a tube or tunnel and then propagating on to the other side to form a second shell (Chapter 3 of this thesis; Pineault et al. 1987). In both these SNRs, the three components are all approximately in the plane of the sky. We suggest that SNR G296.8–00.3 may represent a similar situation, but in this case where the explosion site, the low-density tunnel and the second shell all lie roughly along the line of sight.

4.4.2 PSR B1154–62

Physical Properties

The similarity in the rotation measures of the SNR and the pulsar suggests that they are at roughly the same distance. The poor signal-to-noise in the absorption spectrum shown in Figure 4.6 suggests that while the Johnston et al. (1996) lower limit on the kinematic distance of 4 kpc (inferred from absorption out to the tangent point) is valid, their upper limit of 9 kpc, based on lack of absorption at positive velocities, can be questioned. Indeed an early H I absorption spectrum towards the pulsar suggested absorption out to +30 km s^{-1} (Ables & Manchester 1976). Putting the pulsar at a similar distance to the SNR gives agreement with the dispersion measure distance derived from the model of Taylor & Cordes (1993). Thus we propose a distance for the pulsar of 10 kpc.

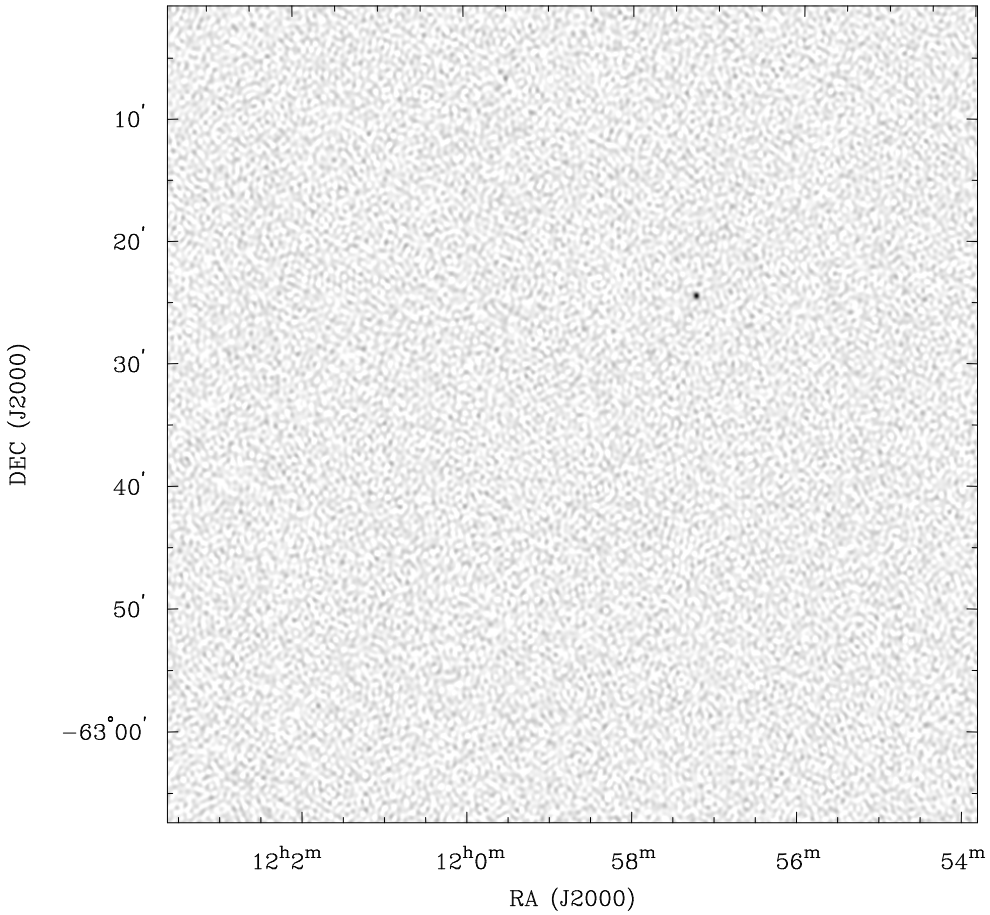

Figure 4.9 An image of the field in circular polarisation. PSR B1154–62 is the only detectable source.

Polarisation

A Stokes V image of the entire field is shown in Figure 4.9. Because the ATCA has linear feeds, the instrumental response in Stokes V is negligible. Apart from the pulsar, the image is devoid of emission, with a noise (40 μJy beam^{-1}) commensurate with that expected from the radiometer equation alone.

The signal-to-noise of the pulsar in Stokes V ($\sim 30\sigma$) is comparable to that in total intensity, yet the circularly polarised signal-to-noise of all other sources in the field is zero. Indeed pulsars are generally $\sim$10% circularly polarised (e.g. Qiao et al. 1995), while other sources tend not to emit in circular polarisation. We therefore suggest that examination of Stokes V images may be a fruitful method of finding new pulsars, particularly those which are too weak, too dispersed, too scattered or have a period too short or too long to be found by traditional searches for pulsed emission.

4.4.3 Other Sources

Absorption against source 2 (Figure 4.7) is not seen at +50 km s^{-1}, where emission is seen in Figure 4.6. However, at this distance absorbing clouds are of small angular scale and may not lie along this line of sight. This source has no counterpart in *IRAS* 60-μm emission, which, combined with its intermediate spectral index and low linear and circular polarisation, is consistent with its being a background radio galaxy. Source 4's H I absorption suggests that it too is extragalactic, consistent, as for source 2, with its spectral, infrared and polarisation properties. While no absorption was obtainable against source 3, the available evidence is also consistent with an extragalactic origin.

4.4.4 An Association between SNR G296.8–00.3 and PSR B1154–62?

An association between SNR G296.8–00.3 and PSR B1154–62 was originally proposed by Large & Vaughan (1972), primarily based on the spatial coincidence of the two objects. This association has subsequently been regarded as unlikely on the basis of the pulsar's large timing age $\tau_c = 1.6 \times 10^6$ yr (Gaensler & Johnston 1995c; Johnston et al. 1996), clearly incompatible with the age for the SNR derived above. However, the timing age of a pulsar is only an upper limit on the true age, since it assumes that the initial period of the pulsar was much smaller than the present value. If a pulsar is born spinning slowly (Vivekanand & Narayan 1981; Emmering & Chevalier 1989; Narayan & Ostriker 1990), it can be much younger than τ_c. Given the evidence presented above that the distances of the SNR and the pulsar are compatible, we now reconsider the likelihood of an association.

If the pulsar is as young as $t_{\rm SNR} \lesssim 10^4$ yr, its position well outside the remnant argues strongly against a physical association. The pulsar is removed from the remnant's centre by approximately double the SNR radius. Such a large displacement is statistically improbable for an association of this age (Gaensler & Johnston 1995a). The implied projected velocity is >3500 km s^{-1}, a speed similar to that claimed by Caraveo (1993) in order to associate PSR B1610–50 with G332.4+00.1, but well in excess of typical pulsar velocities (Lyne & Lorimer 1994; Frail et al. 1994b). We note, however, that the implied proper motion of 80 mas yr^{-1} cannot be ruled out; comparison of timing positions derived by Newton et al. (1981) and Siegman et al. (1993) gives an upper limit on the proper motion of 150 mas yr^{-1}.

An alternative is that the remnant is much older than the age calculated above. If we suppose that the remnant has an age of 10^5 yr, then the pulsar's inferred projected velocity ($\sim$400 km s^{-1}) becomes quite reasonable, as does its position (Gaensler & Johnston 1995b). However, this requires that $n_0/E_{51} \sim 25$, an usually high value (cf. Frail et al. 1994b). The high pulsar velocity and ambient density required for an association would be expected to generate a wind nebula or bow shock trailing out behind the pulsar (e.g. Frail & Scharringhausen 1997). No such structure is visible around the pulsar in our radio image, and comparison of the

integrated flux density (Table 4.4) with the pulsed flux (Johnston et al. 1996) puts an upper limit on emission from any unresolved nebula of $\lesssim 0.1$ mJy. Furthermore, the pulsar would still have to be born spinning slowly: for a braking index $n = 3$ (Manchester & Taylor 1977), $t = 10^5$ yr requires an initial period $P_0 = 388$ ms (compared with a current period of 400 ms).

Thus, we conclude that, apart from an agreement in distance, there is no evidence in favour of a physical relationship between SNR G296.8–00.3 and PSR B1154–62. Most likely their spatial proximity is by chance and the pulsar is a much older object.

4.5 Conclusion

We have presented 1.3-GHz continuum and H I observations of SNR G296.8–00.3. These data (resolution $\sim 20''$) represent the highest resolution at which this SNR has been observed. The remnant is weakly polarised at a lower limit of 0.5%. We attribute this to beam depolarisation, possibly a result of differential Faraday rotation in the ISM. The ATCA's capacity to measure many channels across the continuum band allows a measurement to be made of the change in polarisation position angle as a function of frequency. We consequently derive a rotation measure towards the SNR of 430 rad m^{-2}. This disagrees with the earlier results of Dickel & Milne (1976), and we argue that these authors incorrectly accounted for an ambiguity in the rotation.

H I absorption towards the SNR gives lower and upper limits on its systemic velocity of +15 and +30 km s^{-1} respectively, corresponding to a distance 9.6±0.6 pc. We consequently estimate an age for the remnant of $(2 - 10) \times 10^3$ yr, and a mean interstellar magnetic field along the line of sight of 1.7 ± 0.3 μG.

SNR G296.8–00.3 seems consistent with its being the remnant of a single explosion. Two explanations for its morphology seem possible. One is that the remnant has a biannular appearance induced by axial symmetry in the progenitor wind. However, the SNR is much larger than the RSG wind of a SN progenitor, and it must either be able to "remember" its environment from an earlier stage of evolution, or be propagating through a main-sequence wind which is also axisymmetric. The other possibility is that the SNR's complex appearance results from the inhomogeneous ISM into which it is expanding. In this context, an unusual linear feature running north-south through the remnant may represent a low-density tunnel which has been re-energised by encounter with the SN shock, while a partial ring of emission to the north-east may indicate a break-out into an adjacent bubble. A detailed H I emission study of the region, using a combination of compact ATCA configurations and single-dish data, may give further insight into the remnant and its environment.

We also detect the pulsar PSR B1154–62, $13'$ from the remnant's centre, and find its measured properties to agree with those found in previous observations. On the basis of its H I absorption, rotation measure and dispersion measure, we argue that the pulsar is at a distance of ∼10 kpc, compatible with the distance to the SNR.

However, the pulsar's large timing age and large displacement from the remnant's centre make a physical association highly unlikely.

The pulsar is 12% circularly polarised and its detection through such emission is straightforward. Other sources in the field show no circular polarisation and the nature of the ATCA means that instrumental effects in Stokes V are minimal. This suggests that detection through Stokes V is a useful method for finding new pulsars.

Chapter 5

G309.2–00.6 and Jets in SNRs

This Chapter has also appeared as Gaensler et al., 1998b, "G309.2–00.6 and jets in supernova remnants", MNRAS, **299**, 812.

5.1 Introduction

Radio observations of supernova remnants (SNRs) demonstrate a vast range of shapes (e.g. Whiteoak & Green 1996). While most SNRs have a distorted and complicated appearance reflecting their interaction with an inhomogeneous interstellar medium (ISM), some SNRs have striking symmetry properties which require other explanations (e.g. Chapter 3 of this thesis; Manchester 1987; Roger et al. 1988; Różyczka et al. 1993).

G309.2–00.6 was first identified as a SNR on the basis of its non-thermal spectrum (Green 1974; Clark et al. 1975a). Subsequent higher resolution observations (Caswell et al. 1981; Kesteven & Caswell 1987; Whiteoak & Green 1996) have shown a distorted shell with two opposed, symmetric bright ends, and a weak compact source in the interior. Continuing a programme to study unusual southern SNRs (see Chapter 4), we present high resolution 1.3-GHz continuum and H I absorption observations of G309.2–00.6, as well as observations of the region in Hα, in X-rays and in the near-infrared. In Section 5.2 we briefly describe our observations and analysis, before presenting our results in Section 5.3. In Section 5.4 the morphology of SNR G309.2–00.6 is discussed, and is compared to that of other SNRs.

5.2 Radio Observations and Reduction

Radio observations were carried out with the Australia Telescope Compact Array (ATCA; Frater et al. 1992), a six-element synthesis telescope near Narrabri, New South Wales. Three different array configurations were used, as shown in Table 5.1. Observations were made simultaneously in the radio continuum (centre frequency 1.344 GHz) and in the H I line (centre frequency 1.420 GHz, channel separation 0.83 km s^{-1}) towards a pointing centre RA (J2000) $13^{\rm h}46^{\rm m}35^{\rm s}$, Dec. (J2000)

$-62°53'48''$. All other details of the observations, calibration and analysis are as in Chapter 4.

Date	Array Configuration	Maximum Baseline (m)	Time on Source (h)
1996 Jan 18	0.75C	750	13
1996 Feb 03	0.75B	765	12
1996 Feb 25	1.5C	1485	13

Table 5.1 ATCA observations of G309.2–00.6.

5.3 Results

5.3.1 Total Intensity

Figure 5.1 shows total intensity images of G309.2–00.6, while Figure 5.2 shows an image of the entire field. Properties of sources of note are given in Table 5.2. Source 3 corresponds to the H II region G309.548–0.737 (Haynes et al. 1979; Caswell & Haynes 1987).

The remnant is comprised of two morphological components: firstly two roughly circular arcs of emission to the south-east and north-west which we subsequently refer to as the 'shell', and secondly two bright, sharply curved arcs to the south-west and north-east (the 'ears'). The two parts of each component are diametrically opposed with respect to the SNR's geometric centre, and the two components are oriented at position angles perpendicular to each other. Although no connecting structure is apparent, the two arcs of the shell can be construed to form a single circular ring.

Within the remnant, to the north-east of centre, is a slightly extended source which we designate ATCA J134649–625235. At the available resolution ($\sim 20''$ — see Table 5.3), this source has a cometary appearance, with a tail trailing out to the west. In Figure 5.3 is shown an image of ATCA J134649–625235 made using the observations in Table 5.1, but including the sixth ATCA antenna, 3 km west of the track upon which the other five antennas are stationed. This increases the maximum baseline to $\sim$5000 m, corresponding to a resolution of $5''$. (Note that this gives a significant gap in the $u - v$ coverage between 1500 m and 5000 m, and so is not appropriate for imaging the entire remnant.) At this higher resolution, the source breaks into a double source to the east, and a fainter extended source to the west.

To the north of the remnant is a narrow column of emission. Extending northwards from the SNR's north-eastern ear, this column bends around to the west and

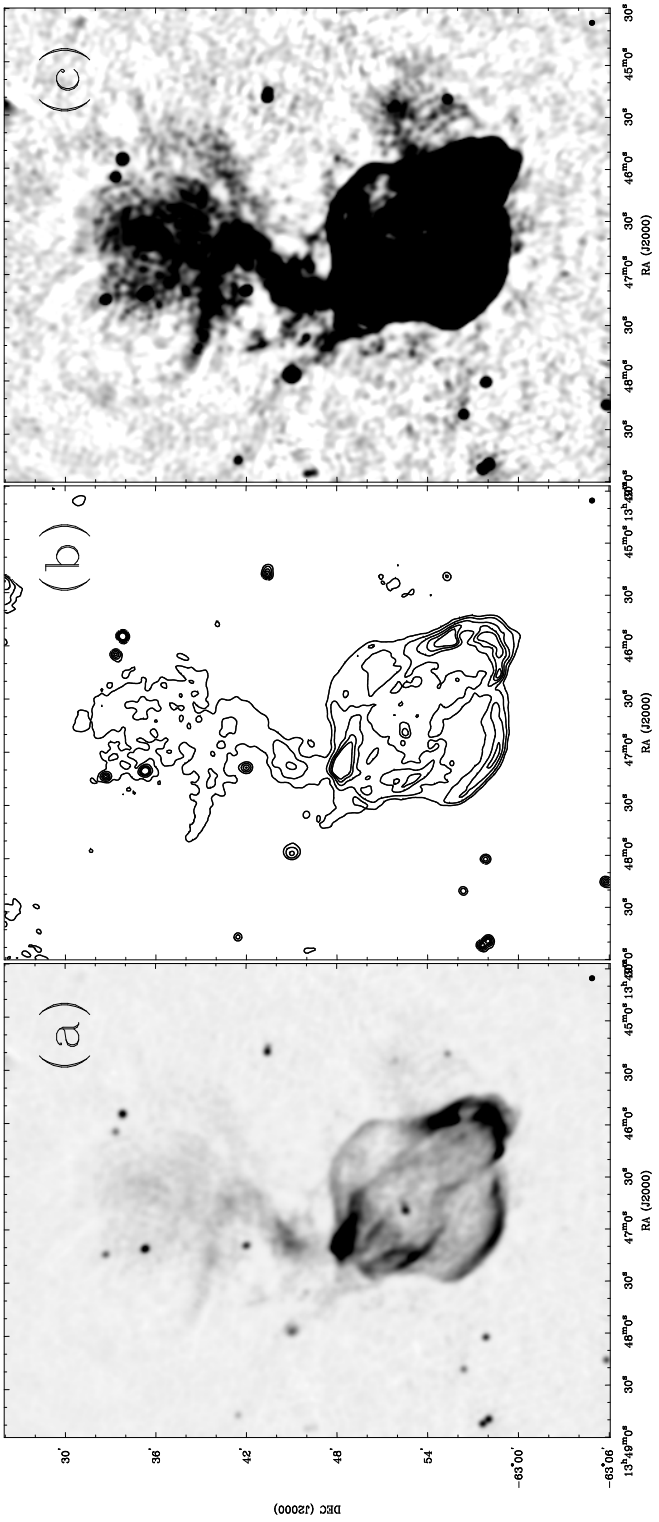

Figure 5.1 ATCA images of SNR G309.2–00.6 at 1.3 GHz: (a) grey scale representation, ranging from –1 to 15 mJy beam^{-1}; (b) contours with levels at 2, 5, 10, 15 and 20 mJy beam^{-1}; (c) grey scale with range –0.1 to 1.5 mJy beam^{-1}, shown to emphasise faint structure. The grey scales have not been corrected for the ATCA primary beam response, in order to give uniform noise across the image. The FWHM of the Gaussian restoring beam is shown at lower right of each panel.

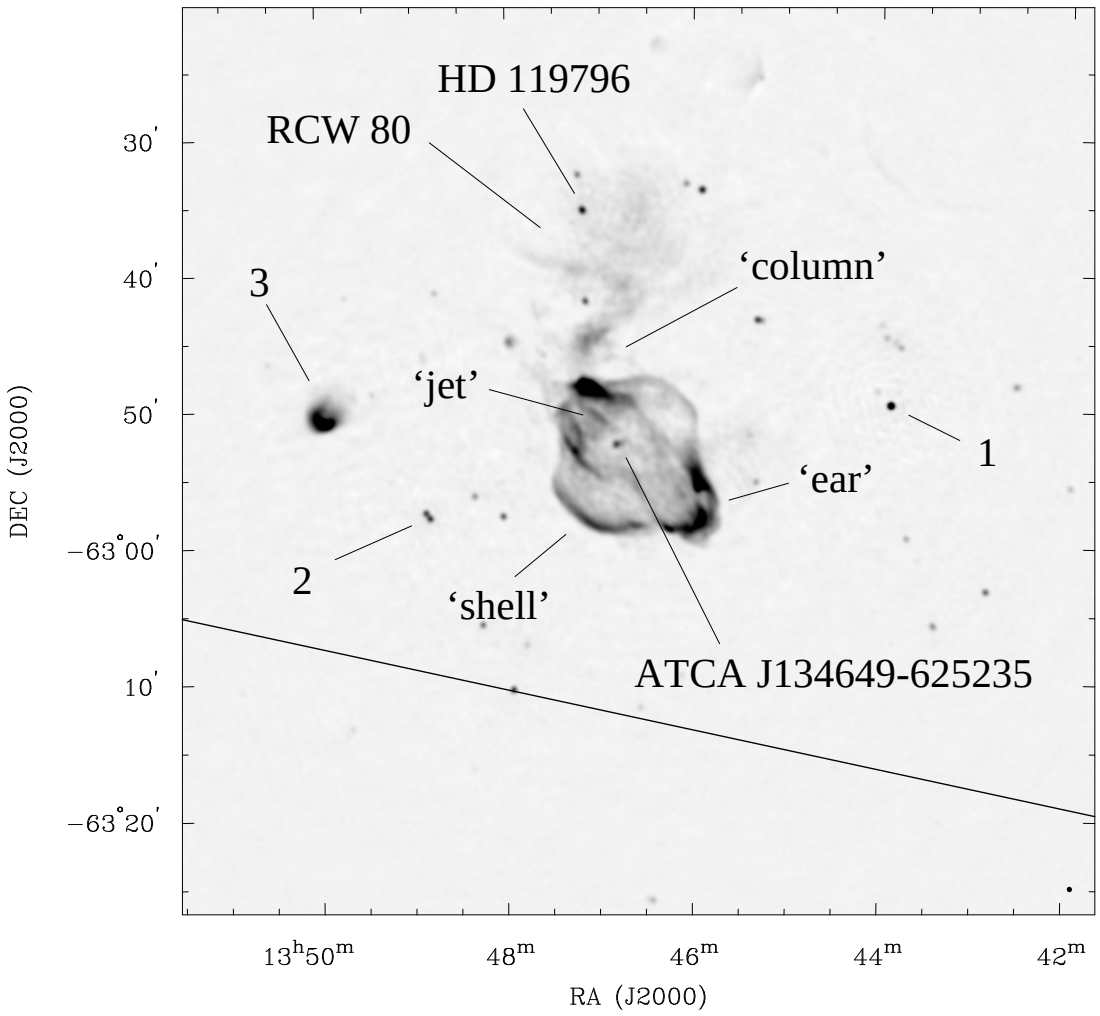

Figure 5.2 A total intensity image of the field surrounding SNR G309.2–00.6. The image has not been corrected for the ATCA primary beam response. Sources listed in Table 5.2 are indicated, as well as some of the main features associated with the SNR. The diagonal line running across the image corresponds to a Galactic latitude $b = -1°$.

Source	Position		$S_{1.3\,\mathrm{GHz}}$	Spectral index[a]	Other names
	Equatorial (J2000)	Galactic	(Jy)	(α, $S_\nu \propto \nu^\alpha$)	
1	$13^{\mathrm{h}}43^{\mathrm{m}}53^{\mathrm{s}}$ –62°49′41″	308°.88 –00°.56	0.08	−0.7	
central source	$13^{\mathrm{h}}46^{\mathrm{m}}49^{\mathrm{s}}$ –62°52′35″	309°.20 –00°.68	0.02	+0.6±0.6	ATCA J134649–625235
HD 119796	$13^{\mathrm{h}}47^{\mathrm{m}}10^{\mathrm{s}}$ –62°35′20″	309°.30 –00°.41	0.06	0.0	HR 5171, IRAS 13436–6220
RCW 80	$13^{\mathrm{h}}47^{\mathrm{m}}$ –62°38′	309°.3 –00°.4	0.7	+0.3±0.5	Gum 48d
column	$13^{\mathrm{h}}47^{\mathrm{m}}$ –62°45′	309°.2 –00°.6	0.6	–0.6±0.5	
jet	$13^{\mathrm{h}}47^{\mathrm{m}}$ –62°50′	309°.2 –00°.6	0.02	—	
2	$13^{\mathrm{h}}48^{\mathrm{m}}50^{\mathrm{s}}$ –62°57′51″	309°.40 –00°.82	0.06	−1.0	
3	$13^{\mathrm{h}}50^{\mathrm{m}}$ –62°50′	309°.6 –00°.7	1.7	−0.1	G309.548–0.737, PMN J1349–6250

[a] Calculated between 1.344 GHz (this Chapter) and 843 MHz (Green et al. 1998).

Table 5.2 Selected sources in the vicinity of SNR G309.2–00.6.

Resolution	$24\farcs1 \times 22\farcs7$, PA 14°
RMS noise in image	160 (Stokes I)
(μJy beam^{-1})	50 (Stokes V)
Geometric centre (α, δ; J2000)	$13^{\rm h}46^{\rm m}37^{\rm s}$ –62°53′
Geometric centre (l, b)	309.°17 –00.°68 (l, b)
Diameter	12′ × 10′, PA –40°(shell)
	14′ × 6′, PA +45°(ears)
Flux density at 0.4 GHz (Jy)[a,d]	10 ± 1
Flux density at 0.8 GHz (Jy)[b,d]	6.0 ± 0.6
Flux density at 1.3 GHz (Jy)[c]	5.2 ± 0.2
Spectral index	-0.53 ± 0.09

[a]Mills Cross data (Green 1974)
[b]MOST data (Whiteoak & Green 1996)
[c]ATCA data (this Chapter)
[d]Errors of 10% have been assumed in Mills Cross and MOST data

Table 5.3 Observational and derived parameters for G309.2–00.6.

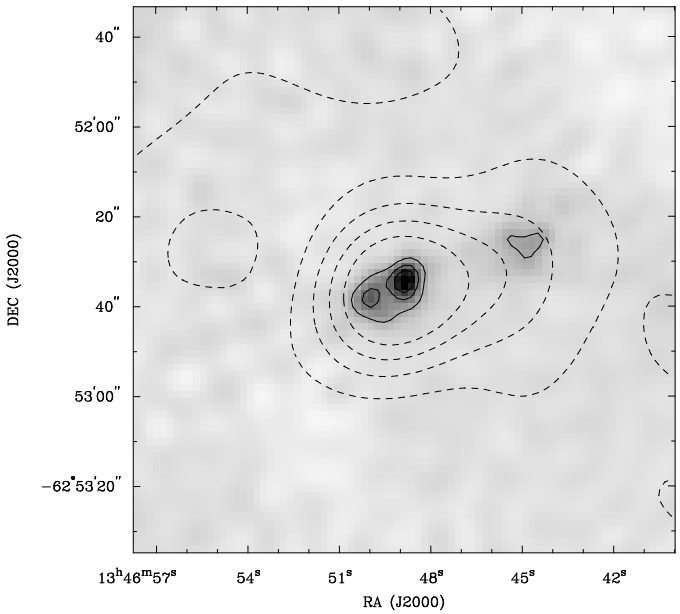

Figure 5.3 An image of the source ATCA J134649–625235 within G309.2–00.6, using all six ATCA antennas. The grey-scale runs from –0.5 to 4 mJy beam^{-1}, with solid contours at 1, 2, 3 and 4 mJy beam^{-1}. The dashed contours correspond to the lower resolution image shown in Figure 5.1(b), and are at levels of 2, 4, 6 and 8 mJy beam^{-1}.

then to the north again, before opening up into a broader diffuse region forming a semi-circular arc. The arc is coincident with the Hα nebula RCW 80 (Rodgers et al. 1960; Georgelin et al. 1988), while within it is a point source coincident with the position of the double star HD 119796 (Humphreys et al. 1971; Hirshfeld & Sinnott 1985).

Between ATCA J134649–625235 and the north-eastern ear, is a collimated feature extending away from the SNR's centre, which we dub the 'jet'. There is a distinct break in the emission from the north-eastern ear where it intersects the jet. The jet and the break both lie along the symmetry axis defined by the two ears. The bright linear component of the jet is $1\farcm5$ long. At its south-west end the jet abruptly fades, although a faint continuation can be seen extending to the SNR's centre. Beyond the break in the north-eastern ear is faint emission extending $3'$ beyond the SNR.

The south-west ear also shows a break, although it is less distinct, and does not lie along the symmetry axis. Faint emission which might correspond to a less distinct and less collimated counterpart to the jet is seen just within this ear.

Derived parameters for the SNR are given in Table 5.3, and were determined by methods described in Chapter 4. Total flux density measurements of G309.2–00.6 are shown in Table 5.3 — we exclude single dish observations (Day et al. 1969; Clark et al. 1975a; Duncan et al. 1995), which are confused by emission from RCW 80 to the north. We consequently compute a spectral index for SNR G309.2–00.6 of $\alpha = -0.53 \pm 0.09$, where $S_\nu \propto \nu^\alpha$. The spectral index calculated here is somewhat steeper than previous results ($\alpha = -0.37$; Clark et al. 1975a), probably due to confusion with RCW 80. We note that the largest spatial scale sampled in our image is $17'$, only slightly larger than the remnant. Although our data include additional spacings corresponding to scales of $13'$ and $10'$, one could argue that we are missing some of the SNR's flux density, and that its spectrum is consequently flatter than that we have just determined. However, the ATCA flux density is greater than that extrapolated from lower frequency data, and we argue that little flux is missing.

Although ATCA J134649–625235, RCW 80 and the column feature are of low surface brightness, we can put rough constraints on their spectra, as listed in Table 5.2. The lack of resolution in the MOST image of Whiteoak & Green (1996) prevents a calculation of the jet's 843 MHz flux density and hence of its spectrum.

5.3.2 Polarisation

SNR G309.2–00.6

Images of polarised emission were produced as in Chapter 4, the effects of bandwidth depolarisation being minimised by imaging Stokes Q and U in 13 distinct frequency channels, forming $L = (Q^2 + U^2)^{1/2}$ for each channel, and then combining. No circular polarisation was detected from G309.2–00.6; linear polarisation from the SNR is shown in Figure 5.4. We put a lower limit of 75 mJy on its linear polarisation,

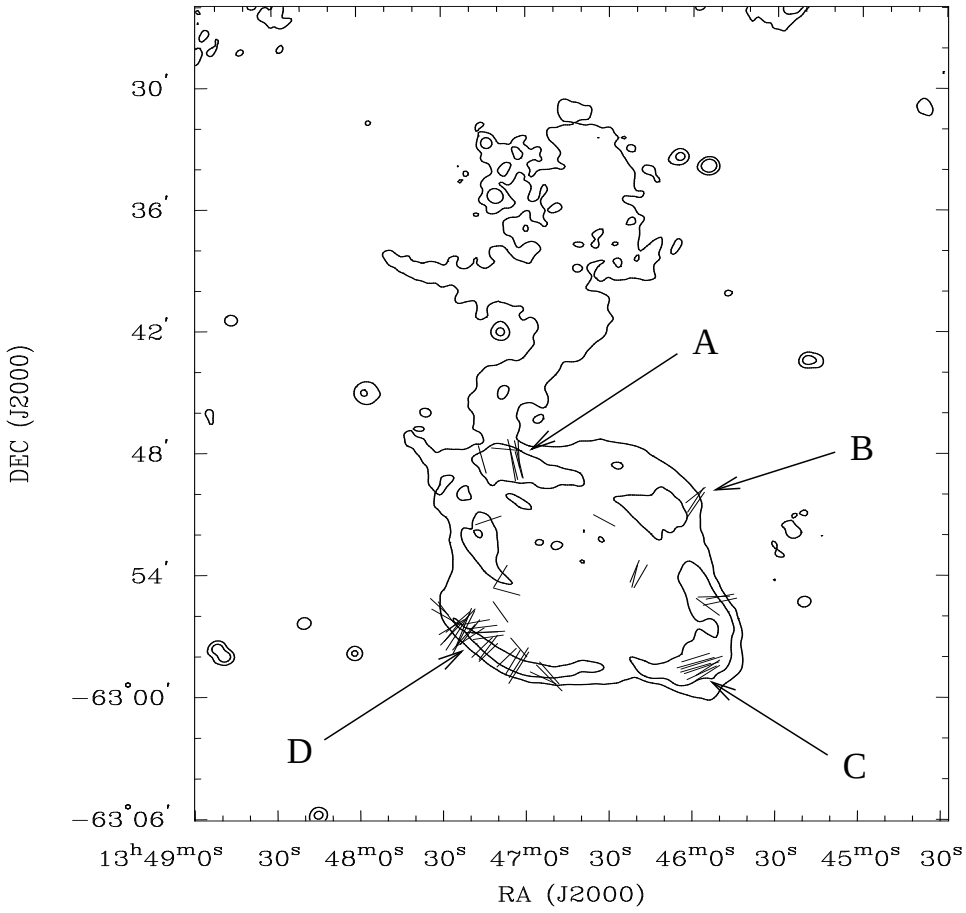

Figure 5.4 Linearly polarised emission from G309.2–00.6. The orientation of vectors indicate the position angle of the electric field in an 8 MHz channel centred on 1376 MHz. Lengths of vectors are proportional to the surface brightness in linear polarisation at that position, the longest vector corresponding to $L = 2.0$ mJy beam^{-1}. Contours representing total intensity are drawn at 2 and 10 mJy beam^{-1}. Labelled regions correspond to the plots in Figure 5.5.

corresponding to an overall fractional polarisation of 1.4% (instrumental polarisation at the field centre is negligible). However, as a function of position, the fractional polarisation in some places reaches the theoretical maximum of 70%. Much of the SNR's outer edge is polarised, correlating roughly with total intensity, with a rough consistency in position angle over a given region. There is no suggestion that the ear components have different polarimetric properties from the shell. No polarisation is detectable from ATCA J134649–625235 or from the jet.

As demonstrated in Chapter 4, the multiple channels recorded in the ATCA's continuum mode can be used to derive a rotation measure (RM) towards linearly polarised sources. In Figure 5.5 we show the frequency dependence of polarisation position angle for four regions of the SNR. Towards the two shell components and towards the north-eastern ear, we find a consistent RM of –930 rad m^{-2} with fluc-

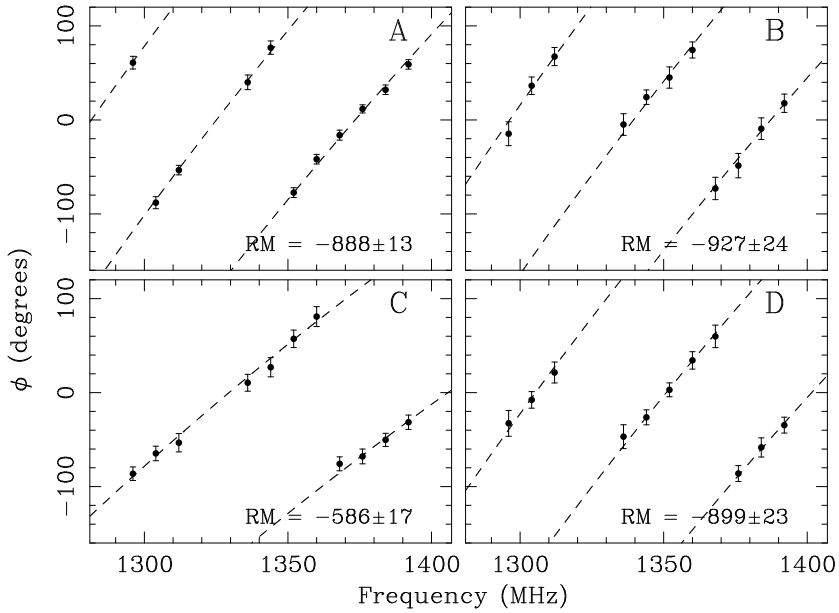

Figure 5.5 Faraday rotation across the observing band for four regions of SNR G309.2–00.6 indicated in Figure 5.4. The data correspond to position angles of the electric field at 8 MHz intervals; gaps at 1320 and 1328 MHz are due to data corrupted by interference. The broken line represents the best-fit curve of the form $\phi = \phi_0 + \mathrm{RM}\,c^2/\nu^2$; the fitted rotation measures are given in rad m^{-2}.

tuations (1σ) of 60 rad m^{-2}. The south-western ear has a distinctly different RM of –570 rad m^{-2}, with 20 rad m^{-2} fluctuations. As discussed in Chapter 4, the frequency range across which measurements have been made is relatively small, resulting in large errors when extrapolating the position angles to infinite frequency. Thus from the current data we cannot determine the intrinsic orientation of polarisation vectors in the source.

Other Sources

No linear polarisation is detected from RCW 80 or from the column, either formally at the 5-σ level, or by eye at any lower level. Sources 1 and 3 are both 4% linearly polarised after correction for instrumental polarisation. Source 2 and HD 119796 are less than 3% linearly polarised. No circular polarisation is detected from any source in the field.

5.3.3 H I Line

As in Chapter 4, we convert systemic LSR velocities into distances using the best fitting model for Galactic rotation of Fich et al. (1989), and assume ±7 km s^{-1} uncertainties in velocities. We adopt a solar orbital velocity $\Theta_0 = 220$ km s^{-1} and a distance to the Galactic Centre $R_0 = 8.5$ kpc, as recommended by Kerr &

Lynden-Bell (1986).

Our ATCA observations lack the $u-v$ data at short spacings required to produce useful H I emission spectra. Thus in considering H I absorption towards sources of interest, we compare with emission seen towards the nearby ($\sim 2^\circ$) SNR G311.5–00.3 (Caswell et al. 1975b). Their profile shows continuous emission from –60 km s^{-1} up to 0 km s^{-1}, then a strong peak at +35 km s^{-1} and weaker emission near +100 km s^{-1}. Emission in the surveys of Jackson (1976) and Kerr et al. (1986) shows similar structure.

Nearby Sources

Absorption was measured against sources 1, 2 and 3; the results are shown in Figure 5.6. Absorption towards source 1 is seen down to –50 km s^{-1}, corresponding well to the observed tangent velocity in this direction (Jackson 1976; Kerr et al. 1986), and to that expected from the rotation curve of Fich et al. (1989). Absorption towards source 1 is also seen at –5 km s^{-1}, and then again at +40 km s^{-1}. These features are similar to those seen in emission towards G311.5–00.3 as described above. Towards source 2, significant absorption is seen at negative velocities out to –60 km s^{-1}. A weak feature is seen at +40 km s^{-1}. Absorption against source 3 is detected between –50 km s^{-1} and –40 km s^{-1}, then at –25 km s^{-1} and –5 km s^{-1}. No absorption is detected at positive velocities. Other sources in the image, including the column, HD 119796 and RCW 80, were too weak or too far from the phase centre to obtain useful absorption against.

SNR G309.2–00.6

Useful absorption spectra were obtained against three parts of the remnant: towards each ear, and towards the south-east shell component, as shown in Figure 5.6.

Absorption towards the south-western ear is seen between –50 and –25 km s^{-1}, possibly at –10 km s^{-1} and then at 0 km s^{-1}. No convincing absorption is seen at positive velocities. Towards the north-eastern ear, absorption is detected at –50 km s^{-1} and –25 km s^{-1}. Along the south-eastern shell component, we see absorption only between –60 km s^{-1} and –25 km s^{-1}.

Examination of individual velocity channels clearly shows the outline of the SNR in absorption, demonstrating that it is indeed continuum emission from the SNR which is being absorbed and not background H I features (cf. Landecker et al. 1982b). In any case, the brightness temperature of the SNR in the relevant regions is 20–25 K, significantly brighter than typical H I emission features.

5.3.4 Other Wavelengths

Optical Observations

A field containing G309.2–00.6 was observed by A. J. Walker on 1997 Apr 30, as part of a wide-field Hα survey of the Southern Galactic Plane being carried out at Siding

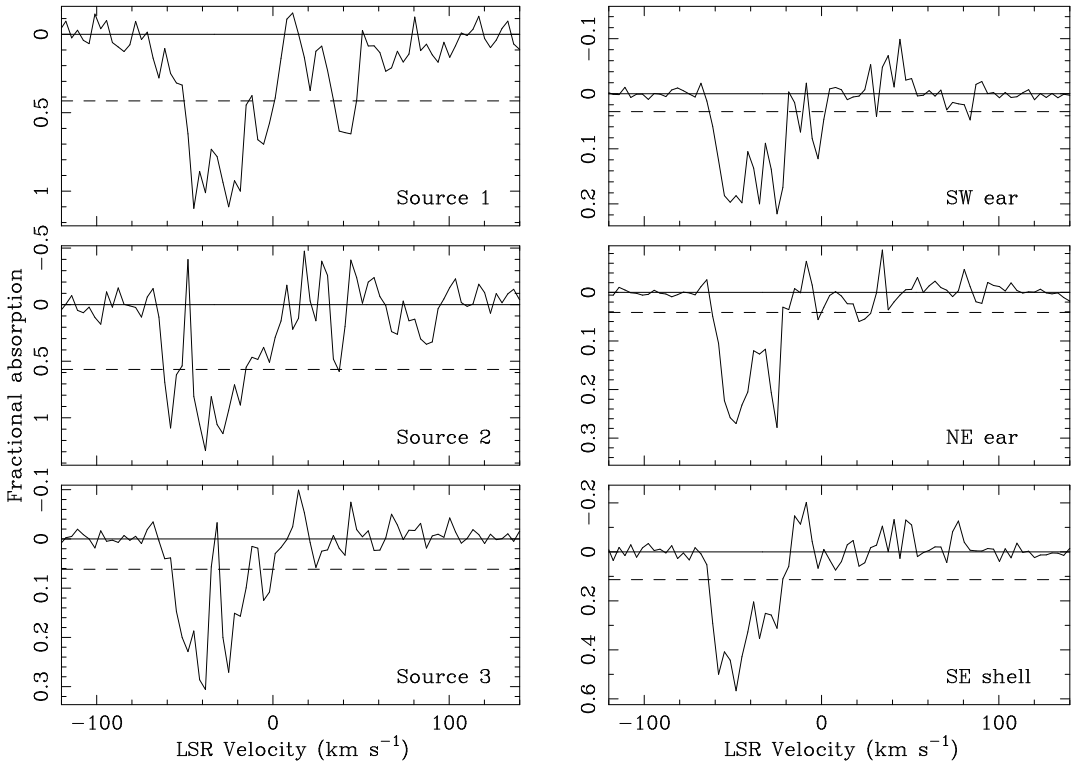

Figure 5.6 H I absorption spectra towards sources 1, 2 and 3, and towards three parts of the SNR. The dashed line represents absorption at the 6-σ level, where σ is calculated from the signal in line-free channels.

Spring Observatory (Buxton et al. 1998). Three 10 min exposures were made with a 400 mm, f/4.5 Nikkor-Q lens, through a filter centred at 657.0 nm with a width of 1.5 nm. The detector was a 2048×2048 CCD with a resolution of 12″ pixel^{-1}. The images were bias and dark subtracted, flat-fielded and then combined with a median filter. A final image, without continuum subtraction, is shown in Figure 5.7(a).

RCW 80 is clearly delineated in Hα, having a similar arc-like appearance to its radio morphology. As in the radio, HD 119796 is visible at the centre of this region. No Hα emission from the SNR or from the column to its north is apparent. The open cluster NGC 5281 is visible in the remnant's interior, at RA (J2000) $13^{\rm h}46^{\rm m}30^{\rm s}$, Dec. (J2000) $-62°55'$. Its distance has been estimated to be 1.3 kpc (Moffat & Vogt 1973).

X-ray Observations

SNR G309.2–00.6 was observed by the *ROSAT* Position Sensitive Proportional Counter (PSPC) in 1992 Aug for 3931 sec; the data are now available from the *ROSAT* public archive. In the energy range 0.1–0.4 keV, only a slight enhancement above the background is seen towards the SNR. However, in Figure 5.7(b) is shown emission in the range 0.4–2.4 keV, where the compact X-ray source 1WGA J1346.5–

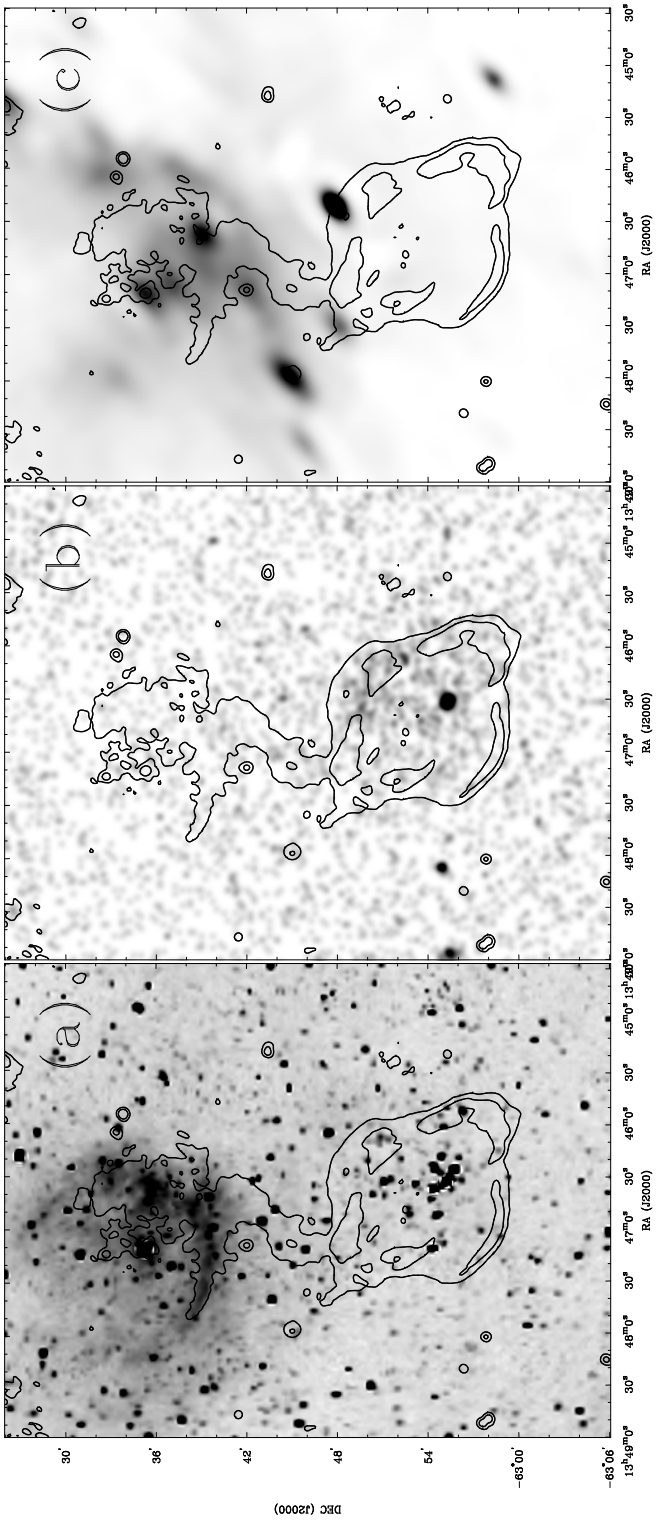

Figure 5.7 Multi-wavelength observations of the region surrounding G309.2–00.6. The grey scales correspond to: (a) Hα emission; (b) X-ray (*ROSAT* PSPC) emission in the energy range 0.5–2.0 keV, smoothed with a 25″ Gaussian; (c) 60 μm (*IRAS* HIRES) emission. Contours correspond to 1.3 GHz ATCA data at the levels of 2 and 10 mJy beam^{-1}.

6255 (White et al. 1994a,b) can be seen near the remnant's centre, and weak diffuse emission can be associated with the rest of the SNR. No significant emission can be seen along the column or from RCW 80.

Infrared Observations

An *IRAS* 60 μm image of the region, processed with the `HIRES` algorithm (Aumann et al. 1990), is shown in Figure 5.7(c). Strong IR emission is coincident with RCW 80 and with HD 119796 (= IRAS 13436–6220), but no obvious emission can be associated with the SNR or with the column to its north. The point source on the north-western edge of the SNR is IRAS 13428–6232.

5.4 Discussion

5.4.1 Field Sources

H I absorption at +40 km s^{-1} towards source 1 puts it at a distance of at least 14 kpc. Although no absorption is seen at +100 km s^{-1} corresponding to emission seen towards G311.5–00.3, this may be due to the small angular size of absorbing clouds at this large distance. Source 1's spectral index and low level of linear polarisation is consistent with it being a background radio source. Similar arguments apply to source 2, which in addition has the characteristic double-lobed morphology of a radio galaxy.

Source 3 (G309.548–00.737) shows absorption out to the tangent point. Using a recombination line velocity towards it of –43 km s^{-1} (Caswell & Haynes 1987), we can thus (within the uncertainties) put this source at the tangent point, corresponding to a distance 5.4±1.6 kpc. The source's morphology and flat spectrum are in accord with its identification as an H II region. The low level of linear polarisation we detect from it is not, however. Either there is a previously unidentified synchrotron component to its emission, or the instrumental polarimetric response of the ATCA is not being characterised correctly at this large distance from the phase centre. Examination of the position angle of polarised emission on a channel-by-channel basis shows no evidence for Faraday rotation as is observed towards the SNR. We thus consider instrumental effects to be a more likely explanation. We note that instrumental response near the phase centre is both minimal and well-characterised, and that polarimetry in that part of the field is reliable (cf. Chapter 4).

The infrared and Hα emission associated with RCW 80 and its flat spectrum are all consistent with it being a thermal H II region. A radial velocity $V_{\rm LSR} \approx -48$ km s^{-1} (Georgelin & Georgelin 1970; Avedisova & Palouš 1989; Avedisova 1997) puts it at the tangent point ($d = 5.4 \pm 1.6$ kpc). One of the components of HD 119796 has been proposed as the exciting star for RCW 80 (Georgelin et al. 1988), but its photometric distance of 3.2 kpc (Humphreys et al. 1971) suggests that it may be unrelated.

5.4.2 SNR G309.2–00.6

Physical Parameters

The three absorption spectra obtained towards the SNR are all consistent, showing absorption out to the tangent point, but not at positive velocities. Thus we assign a lower velocity limit to the SNR of $V_L = V_{\rm tangent} \approx -50$ km s^{-1}, and an upper limit $V_U = +40$ km s^{-1}, corresponding to emission seen at this velocity towards G311.5–00.3 (Caswell et al. 1975b) and to absorption seen against source 1 and weakly against source 2.

These lower and upper limits on the kinematic velocity correspond to respective distances of 5.4±1.6 kpc and 14.1±0.7 kpc. This result immediately confirms NGC 5281 as an unrelated foreground object. Using the shell component to define the extent of the SNR, we thus find SNR G309.2–00.6 to have a diameter between 17 and 45 pc. Through arguments as in Chapter 4, this corresponds to an age between 1000 yr (assuming the lower limit on the distance and free expansion) and 20 000 yr (assuming the upper limit and a SNR in the adiabatic phase). The low level of X-ray emission towards the SNR suggests a line-of-sight column density of $\sim 10^{22}$ cm^{-2} (cf. Hwang & Markert 1994, who made marginal and non-detections of SNRs using comparable exposure times), which for typical ISM densities is consistent with the distance range determined using H I absorption. The Scutum-Crux arm of the Galaxy lies in this direction at distances between 5 and 9 kpc (Georgelin & Georgelin 1976; Georgelin et al. 1988), which weakly favours a distance to G309.2–00.6 in the lower half of the quoted range.

Polarisation

SNR G309.2–00.6 is only weakly polarised; as for G296.8–00.3 in Chapter 4, this is most simply explained in terms of differential Faraday rotation within the beam, consistent with the observed fluctuations in RM and typical of polarimetric observations at this low frequency.

The RM measured towards most of the SNR (regions A, B and D of Figure 5.4), when combined with a model for the Galactic electron density distribution (Taylor & Cordes 1993), corresponds to a mean interstellar magnetic field along the line of sight in the range 1–9 μG, directed away from us. Figure 5.5 demonstrates a distinct difference in RM between the south-western ear (region C) and the rest of the SNR, however. We now consider whether this difference can be explained in terms of conditions internal to the remnant.

We first require a well-ordered field within the SNR, and indeed the electric field vectors in this region are particularly uniform. For a distance to the SNR of $d = 10 d_{10}$ kpc, the length of the line of sight through the tip of the south-west ear is $l \lesssim 9 d_{10}$ pc. We assume a line-of-sight magnetic field within this region of $B = 10 B_{10}$ μG, consistent with adiabatic compression of the interstellar magnetic field by the SNR shock. The resultant thermal electron density required over the entire region is then at least $5 (B_{10} d_{10})^{-1}$ cm^{-3}, an improbably high value. Even when

invoking turbulent amplification of the magnetic field, or compression by a radiative shock or by the outflow proposed below, it is difficult to see how such a large change in RM can be produced along such a small line of sight. A greatly amplified magnetic field would also cause depolarisation resulting from internal Faraday rotation, yet the level of fractional polarisation in region C is not significantly different from regions A, B or D. We thus ascribe the differences in RM to variations in fields and ionised gas in the ambient ISM along the line of sight. Variations (and even reversal of sign) of the RM have certainly been observed across other remnants (Dickel & Milne 1976).

Morphology

The shell and ear components of G309.2–00.6 have comparable H I absorption spectra and (at least for the north-eastern ear) similar rotation measures, and are of comparable angular size. Also, the shell component cannot be seen at the position angles of the ears. This leads us to conclude that we are unlikely to be seeing two structures superimposed, and in further discussion we assume G309.2–00.6 to be a single object.

SNRs with multiple loops and/or significant variations in radius and brightness are reasonably common — a perusal of the catalogue of Whiteoak & Green (1996) suggests that ∼20% of SNRs have some sort of multi-ringed structure, corresponding to ∼45 Galactic SNRs of the 215 currently identified (Green 1996). Such structures are usually interpreted in terms of expansion into multiple cavities in the ISM (Braun & Strom 1986; Pineault et al. 1987; Milne et al. 1989; Dubner et al. 1994). It is possible that G309.2–00.6 represents such a system: the shell component alone is quite undistorted and would represent the original SNR, while the ears would trace an ellipsoidal cavity into which the blast wave has then expanded. However, the centres of the shell and ear components coincide to within 30″. For two interlocking cavities, we estimate the probability of such close alignment of their centres to the line of sight to be 3×10^{-3}. Thus even if all multi-ringed SNRs are due to multiple cavities, it is unlikely that even one such remnant would show as good an alignment as seen for G309.2–00.6. We therefore consider it unlikely that the SNR's appearance can be explained by simply invoking the inhomogeneity of the ISM.

The striking symmetry of the two ears in terms of brightness, shape and opposed positions around the shell suggest that the mechanism responsible for them has a characteristic axis. For example, a SNR evolving in a strong ambient magnetic field will become considerably elongated along the field direction (Insertis & Rees 1991; Różyczka & Tenorio-Tagle 1995), perhaps resembling the ears of G309.2–00.6. However, such a model cannot explain the round and symmetric shell component, and in any case requires an ambient field 1000 times stronger than encountered in the ambient ISM. Another possibility is that the axis is defined by the progenitor star: Blondin et al. (1996) show that expansion of a SNR into a progenitor wind of axisymmetric density distribution causes the shell to develop opposed protuberances, producing a morphology quite like that of G309.2–00.6. However, as we have

discussed in Chapter 4, this shaping occurs when the remnant is very young, and it is not clear how the SNR might "remember" the effects of its progenitor wind as it expands to large sizes.

The alternatives we have just discussed cannot be ruled out, but we argue that the appearance of G309.2–00.6 can be best explained if the SNR contains a central source which produces collimated outflows or jets in two opposed directions. The shell component represents the original, undistorted SNR. The outflows collide with the expanding remnant, their pressure distorting and brightening the two opposite sides and thus producing the ears. G309.2–00.6 is then similar to SNR G039.7–02.0 (W 50), in which the centrally located X-ray binary SS 433 generates opposed jets which distort the surrounding shell (Elston & Baum 1987; Murata & Shibazaki 1996). G309.2–00.6 is much younger than W 50 (age $50-100\times10^3$ yr), and indeed a rough progression in morphology can be seen from the former to the latter. G309.2–00.6 has a distinct, almost circular shell with ears protruding $\sim 30\%$ of the radius beyond it; in W 50, however, the original shell is much fainter and filamentary, with ears extending up to twice the radius of the shell from the remnant's centre (Elston & Baum 1987).

Outflows such as those claimed here are generally associated with jets produced by an accreting binary system (Hjellming & Johnston 1988; Fender et al. 1997), but can also be produced by an isolated neutron star (Sulkanen & Lovelace 1990; Hester et al. 1995; Bell 1997). An obvious candidate for such a source in SNR G309.2–00.6 is ATCA J134649–625235 (Figure 5.3). No X-ray counterpart to ATCA J134649–625235 is apparent, and examination of the Digitized Sky Survey shows no optical source within $8''$. While the source's radio morphology is suggestive of the episodic ejections seen in the X-ray binaries GRS 1915+10 (Mirabel & Rodriguez 1994) and SS 433 (Vermeulen et al. 1993), the axis so defined is not aligned with the axis for outflow implied by the SNR morphology, nor does the source itself lie on this symmetry axis. We thus think it most likely that this source is not associated with the SNR.

We put a 5-σ upper limit of 0.4 mJy on the 1.3 GHz flux density of any other central source. No X-ray counterpart is apparent either; while 1WGA J1346.5–6255 is suggestive, it is spatially coincident with and is probably associated with one or more stars in NGC 5281. The uncertainty in position, the low Galactic latitude and the proximity to NGC 5281 all make optical identification difficult. We thus find no observational evidence for the postulated central source. However, the radio upper limit is consistent with a binary system in a quiescent state (cf. GRO J1655–40; Hjellming 1997) or an isolated pulsar which is beaming away from us, while the lack of X-rays can be attributed to absorption in the Galactic Plane, confusion with diffuse soft emission from the SNR, and the comparatively short exposure time. X-ray observations at higher energies and with greater sensitivity with *ASCA* or *AXAF* may be more successful (cf. Gotthelf et al. 1997).

The jet feature seen in our radio image aligns with the axis of symmetry defined by the two ears, and can be traced back faintly to the centre of the SNR. Thus it can be argued that this structure (and its less distinct counterpart in the remnant's

south-west) is indeed emission representing or surrounding a jet, and that it delineates the proposed outflow. That the brightest emission from the jet is produced along a segment just within the original SNR shell may be due to a sudden change in the jet's environment, may represent episodic ejections of material, or may demarcate the progress of a reverse shock generated when the outflow collides with the SNR shell (Murata & Shibazaki 1996). There is no evidence for an outflow in X-rays comparable to the X-ray lobes seen in the interior of W 50 (Seward et al. 1980; Watson et al. 1983; Yamauchi et al. 1994). However, the *ROSAT* observations described in Section 5.3.4 extend only up to 2.4 keV, so that absorption along the line of sight may prevent detection. As for the central source, hard X-ray observations may overcome this problem.

Comparison of our observations with the 843 MHz image of Whiteoak & Green (1996) shows no evidence that the ears have a different spectral index to the rest of the shell. The lack of sufficient separation in frequency between the 843 MHz and our observations prevents a sensitive analysis of spatial spectral index variations (e.g. Anderson & Rudnick 1993). However, we note that the ears contribute ∼50% of the total flux density of SNR G309.2–00.6: thus if we demand the ears to have a significantly flatter spectral index than the mean for the SNR, the rest of the remnant must be steeper by the same amount. No such effect is apparent in the data, and it is thus unlikely that the brightening observed in the ears is due to an injection of relativistic particles from the central outflow.

The distinct break in the north-eastern ear at the point where it is crossed by the jet suggests that the pressure of the outflow carries emitting particles away from the point of impact, thus producing the apparent break in emission. Faint emission seen along the axis of the jet, just outside the north-eastern ear, may represent emitting electrons which were once part of the shell.

It is interesting to note that the brightest region of the north-eastern ear is immediately adjacent to the break; a similar situation exists for the south-western ear. This may be a result of additional shocks and turbulence driven into the shocked region of the SNR by the outflow. The resulting enhanced particle acceleration in these regions then produces the bright ears (cf. Frail et al. 1997).

The column appears to attach to the SNR at the break in the north-eastern ear, and may join with the jet in the remnant's interior. The bends and turns along the column make it difficult to see how it might be a direct extension of the jet, but we note that radio emission associated with the possible jet in Vela X has a similarly twisted appearance (Frail et al. 1997). One possibility is that the column could represent an interaction between the jet and a distorted old star trail (Nicholls & Le Strange 1995). This can explain the bends seen along the length of the column, and also why no such structure is seen beyond the opposite ear.

The column broadens at its northern end to overlap with RCW 80 at the apex of its arc, suggesting that it joins onto RCW 80. If the column is unassociated with the SNR, one could interpet it and RCW 80 as being a single, complex thermal region. The lack of optical and infrared emission associated with the column might then be explained by absorption due to associated molecular material.

On the other hand, if the column is associated with both the SNR and the H II region, then we have a single system, where the outflow and/or column connects the SNR with the thermal arc. Associating G309.2–00.6 with RCW 80 puts the SNR at the lower limit of the distance range inferred from its H I absorption, and implies a shell radius of 9 ± 3 pc. Assuming expansion into a homogeneous medium of density n_0 cm^{-3}, we find that the remnant has swept up between 20 and 170 $M_\odot$, and is thus most likely in a transition between free expansion and the subsequent Sedov-Taylor phase. Assuming $n_0 = 0.2$ and $E_{51} = 1$ as adopted in Chapter 4 (where E_{51} is the kinetic energy of the explosion in units of 10^{51} erg), we derive an upper limit on the remnant's age of 4000 yr.

5.4.3 Other SNRs with Jets

G309.2–00.6 bears a remarkable resemblance to G332.4+00.1 (Kes 32), a roughly circular shell which is distorted and brightened at one end. A flat-spectrum collimated structure extends through a break in the shell in the region of greatest distortion, broadening and kinking before terminating well outside the remnant in an extended thermal 'plume' (Roger et al. 1985; Kesteven et al. 1987). Higher resolution ATCA observations of G332.4+00.1 (M. J. Kesteven 1997, private communication) show a collimated feature within the shell near the break. Thus both G309.2–00.6 and G332.4+00.1 have an undistorted shell component, a distorted and brightened ear component containing both a jet feature and a break in the shell, and a winding column which attaches the SNR to a thermal nebula. The main difference between the two SNRs is that G309.2–00.6 appears to be affected by twin outflows, while G332.4+00.1 seems to involve only a one-sided jet. The 'column' component of G309.2–00.6 may have a steeper spectrum than the equivalent component of G332.4+00.1, but the uncertainties in the former's spectral index are large because of its low flux density.

G309.2–00.6 also has some resemblance to G320.4–01.2 (MSH 15-5*2*), X-ray observations of which show a one-sided synchrotron jet emanating from the central pulsar B1509–58, which then appears to collide with the Hα nebula RCW 89 (Chapter 6 of this thesis; Tamura et al. 1996; Brazier & Becker 1997). As for G309.2–00.6 and G332.4+00.1, the radio morphology of the remnant is significantly distorted where the outflow intersects the shell.

We summarise the SNRs which we have argued are similar to G309.2–00.6 in the first half of Table 5.4. In the second half of Table 5.4 we suggest some further candidates for such interactions. While somewhat speculative, they each satisfy at least some of the morphological criteria observed in G309.2–00.6 and in the other remnants discussed above. We now briefly discuss these additional candidates.

0540–693 (Hen N 158A): This young ($\sim$1000 yr) composite SNR is in the Large Magellanic Cloud, and is associated with the Crab-like pulsar PSR B0540–69. The shell component of this remnant is distinctly brightest in the east

SNR	Other name	Jets?	Reference
G039.7–02.0	W 50 / SS 433	XR	1, 2
G309.2–00.6		R	This Chapter
G320.4–01.2	MSH 15–5*2*	X	3, 4; Chapter 6
G332.4+00.1	Kes 32, MSH 16–5*1*	R	5, 6
0540–693	Hen N 158A	R?	7
G109.1–01.0	CTB 109	X	8
G290.1–01.8	MSH 11–6*1*A	X?	This Chapter
G308.8–00.1		–	9
G315.9–00.0		R	6
G327.6+14.6	SN 1006	–	10

(1) Seward et al. (1980) (2) Hjellming & Johnston (1981b) (3) Tamura et al. (1996) (4) Brazier & Becker (1997) (5) Roger et al. (1985) (6) Kesteven et al. (1987) (7) Manchester et al. (1993) (8) Gregory & Fahlman (1983) (9) Kaspi et al. (1992) (10) Willingale et al. (1996)

Table 5.4 SNRs proposed to contain jet/shell interactions. 'X' and 'R' refer to the existence of X-ray and radio jets respectively. A reasonable case can be made for the first four SNRs, while the remaining sources are more speculative.

in both radio (Manchester et al. 1993) and X-ray (Seward & Harnden Jr. 1994) images, with possible connecting structure to the central pulsar and its associated synchrotron nebula. Manchester et al. (1993) propose that injection of particles from the pulsar into the shell may cause the observed morphology.

G109.1–01.0 (CTB 109): This SNR is associated with the long-period, possibly accreting pulsar 1E 2259+586. Gregory & Fahlman (1983) propose that a collimated X-ray feature and the unusual radio morphology are consistent with precessing jets originating from the pulsar. More recent observations (e.g. Rho & Petre 1997) do not support this interpretation, however.

*G290.1–01.8 (MSH 11–6*1*A)*: A radio image of this remnant (Whiteoak & Green 1996) shows it to have two opposed radio lobes protruding approximately 50% of the SNR radius beyond its otherwise circular shell, resembling the 'ears' observed in W 50 and claimed here for G309.2–00.6. We thus propose this SNR as a possible new example of a shell SNR with jets. A distance to G290.1–01.8 of 7 kpc (Rho 1995; Rosado et al. 1996) corresponds to an age ∼10 000 yr (Rho 1995), similar to that of G309.2–00.6. In X-rays, an *ASCA* spectrum of G290.1–01.8 shows emission lines characteristic of hot plasma in the remnant's interior (Rho 1995). However, there is the suggestion in an earlier *Einstein* image of faint extensions along the axis defined by the lobes (Seward 1990), and we speculate that these may be possible analogues of the X-ray jets seen in W 50. We note that the inclusion of G290.1–01.8 in this class is mutually exclusive with a tentative association between it and the

pulsar PSR J1105–6107, $\sim 20'$ from the remnant's centre (Kaspi et al. 1997). Demonstration of either hypothesis would conclusively rule out the other.

G308.8–00.1: This SNR consists of two opposed arcs of completely different morphology. The northern arc has a bright, possibly filled-centre appearance, which Kaspi et al. (1992) suggest may be due to an outflow from the associated pulsar PSR B1338–62.

G315.9–00.0: This faint shell has a narrow collimated protrusion extending well beyond its boundary (Kesteven et al. 1987). The shell is brightest where the protrusion joins onto it.

G327.6+14.6 (SN 1006): The remnant of SN 1006 is a classic barrel SNR. Willingale et al. (1996) argue that its symmetric, bilateral appearance is produced by twin electron beams originating from an unseen central engine. We note, however, that many other explanations have been proposed (Chapter 3 of this thesis; Kesteven & Caswell 1987; Roger et al. 1988; Reynolds 1996).

There thus may be as many as ten SNRs for which jets from a central source interact with, brighten and/or distort the surrounding shell. Along with SNRs in which an associated pulsar or other source is detected directly (Kaspi 1996; Brazier & Johnston 1999), there is now a large and diverse collection of SNRs for which the presence of a compact stellar remnant can be *inferred*: there are SNRs affected by jets and outflows as discussed above, remnants which are distorted and re-energised by the passage of an associated pulsar through the shell (Shull et al. 1989) and SNRs containing traditional pulsar-powered components ('plerions'; e.g. Helfand & Becker 1987). Evidence that plerions may also be powered by jets (Hester et al. 1995; Brazier & Becker 1997) suggests that the various interactions between a SNR and a compact source may all be manifestations of the same phenomenon, the differences depending on the details of the environment and position of the source within the SNR.

The fraction of SNRs in which a central source is observed or can be inferred is still well below the $\sim$80% of supernovae that are of type Ib or II (van den Bergh & Tammann 1991) and thus expected to produce such sources. This discrepancy has traditionally been explained in terms of a population of radio pulsars of low luminosity or which are not beaming towards us (Manchester & Taylor 1977; Taylor & Stinebring 1986; Manchester 1987). However, we are now aware of a variety of new complications which prevent such detections:

1. Observational selection effects may prevent the detection of a pulsar or its associated nebula. As mentioned above luminosity and beaming may account for a lack of associations, while emission from a pulsar nebula may be swamped by emission from the surrounding shell or from other sources. An instance in which several of these effects are operating simultaneously is PSR B1853+01 in the SNR G034.7–00.4 (W 44): the pulsar is particularly faint (Wolszczan et al. 1988), and its surrounding nebula is difficult to distinguish against the rest of the SNR in radio (Frail et al. 1996) and in X-rays (Harrus et al. 1996).

SN 1987A may be another object in which emission from the remnant prevents detection of any central neutron star (McCray 1993), while we have argued above that SNR G309.2–00.6 also falls into this category;

2. The environment surrounding a neutron star may prevent production of a detectable nebula and/or jets. For example, Bhattacharya (1990) has argued that the lack of a radio plerion around PSR B1509–58 can be explained if its progenitor supernova exploded into a low-density cavity;

3. A compact stellar remnant may be given a high spatial velocity by its supernova explosion. Once such a source passes well beyond its SNR's boundaries, it may not be identified as associated with the remnant, and will probably no longer influence the remnant's morphology (e.g. Gaensler & Johnston 1995b). A possible example of such a system is the X-ray binary Circinus X-1, which has been associated with the nearby SNR G321.9–00.3 (Clark et al. 1975b; Stewart et al. 1993);

4. Some compact remnants may not produce detectable emission and/or may not interact appreciably with their environment. Examples include 'injected' neutron stars, born spinning slowly, and 'magnetars', neutron stars born with high magnetic fields which cause them to slow down at a rapid rate (see Frail 1998 for a review and discussion). Such sources may not emit radio pulses (Chen & Ruderman 1993; Baring & Harding 1998), and their nebulae will rapidly fade below detectability (Bhattacharya 1990). An uncertain fraction of supernovae will produce isolated black holes (Brown & Bethe 1994), which are also undetectable and which are expected to show no interaction with their remnant.

5.5 Conclusion

We have presented H I and 1.3-GHz continuum observations of SNR G309.2–00.6, as well as Hα, *ROSAT* PSPC and *IRAS* 60 μm data on the region. We put a lower limit on linear polarisation from the SNR of 1.4%, a low level which we attribute to beam depolarisation. We find a rotation measure towards most of the SNR of –930 rad m^{-2}, but a distinctly different RM of –570 rad m^{-2} towards one component. This difference is best explained in terms of ISM differences rather than by conditions within the SNR itself. H I absorption puts lower and upper limits on the SNR's systemic velocity of –50 km s^{-1} and +40 km s^{-1} respectively, putting it at a distance between 5.4±1.6 and 14.1±0.7 kpc and implying an age in the range $(1 - 20) \times 10^3$ yr. The nearby H II region G309.548–00.737 shows absorption out to the tangent point, consistent with its recombination line velocity and putting it at a distance 5.4±1.6 kpc.

SNR G309.2–00.6 appears to be a typical shell SNR but with two brightened and distorted 'ears' at opposed position angles, which have a similar spectral index to the rest of the shell. No emission corresponding to the remnant is apparent in

the infrared or in Hα, while diffuse emission can be seen in X-rays. The compact X-ray source 1WGA J1346.5–6255 within the SNR is probably associated with the foreground open cluster NGC 5281.

We consider various explanations for the morphology of SNR G309.2–00.6, and argue that the remnant's appearance is best explained by the presence of opposed jets from a central source which collide with and distort the surrounding shell. We propose G309.2–00.6 as a possible younger analogue to the X-ray binary SS 433 and its associated SNR W 50. A faint jet-like structure oriented along the symmetry axis of G309.2–00.6 may correspond to the outflow itself, while breaks in the ears along this axis may represent this outflow travelling beyond the shell. The weak source ATCA J134649–625235 in the SNR's interior is unlikely to be associated with the remnant. We do not detect any other central source in either X-rays or in radio. The former can be attributed to a lack of sensitivity in the observations and to absorption along the line of sight, while the latter may indicate a binary system in a quiescent state or a pulsar with radio beams directed away from us.

To the SNR's north is an unusual column of radio emission, which at one end may connect with the proposed outflow from the SNR's centre and, at the other end, with the H II region RCW 80. Such an association puts the SNR at a distance 5.4±1.6 kpc and corresponds to an age of less than 4000 yr. The details of the physical process behind such an interaction are unclear, but we note that a similar combination of outflow, distortion and termination in a thermal region has been claimed for both G332.4+00.1 (Kes 32) and G320.4–01.2 (MSH 15–5*2*).

Further observations of SNR G309.2–00.6 will be required to determine whether our interpretation for its appearance is valid. Higher frequency radio observations can be used to provide higher resolution images of the 'ear' and 'jet' regions and the interaction between them, to better study the polarimetric properties of the SNR and, together with lower frequency data, to better constrain any spectral index differences between the different components of the remnant. If G309.2–00.6 is similar to W 50, X-ray observations of greater sensitivity and at higher energies should be able to detect both a central source and evidence for outflow from it.

Apart from G309.2–00.6, we find at least eight other SNRs in which the shell may be affected in some way by jets or outflows from an associated compact source, and suggest G290.1–01.8 (MSH 11–6*1*A) as a possible further example. While the characteristic morphology associated with such outflow may become another means of determining which supernovae have massive star progenitors, there is good reason to believe that a significant fraction of SNRs harbour compact remnants which, for various reasons, we still have not detected.

Chapter 6

G320.4–01.2 and PSR B1509–58: A Complex Interacting system

A slightly shorter version of this chapter will appear as Gaensler et al., 1999, "SNR G320.4–01.2 and PSR B1509–58: New radio observations of a complex interacting system", MNRAS, in press.

6.1 Introduction

A massive star ends its life in a supernova. This usually produces a supernova remnant (SNR) and an associated neutron star, the latter sometimes observable as a pulsar. However, associations between SNRs and pulsars are rare: 30 years of effort have provided fewer than ten convincing cases (Kaspi 1998). Such associations can clarify questions regarding pulsar velocities, ages, magnetic fields and initial spin periods, and can help us to understand the evolution and appearance of SNRs. Thus establishing the validity of an association is of great interest, as are subsequent studies of a particular pulsar/remnant pairing.

Of such systems, one of the best studied but least understood is that involving the peculiar SNR G320.4–01.2 and the energetic young pulsar B1509–58. In the rest of this Section we review previous observations of these sources and outline the issues regarding them which are still to be resolved. In Section 6.2 we describe our new radio study, and in Section 6.3 detail the associated data reduction. The resulting images and spectra are presented in Section 6.4. In Section 6.5 we discuss our results in the context of previous observations, and show how they can answer the questions outlined below.

6.1.1 Previous Observations

Radio

The radio source G320.4–01.2 (MSH 15–5*2*, Kes 23) was detected in the earliest radio surveys of the southern sky (Mills et al. 1960; Komesaroff 1966; Hill 1968;

Kesteven 1968; Day et al. 1969), and was soon classified as a SNR on the basis of its non-thermal spectrum and lack of hydrogen recombination lines (Milne et al. 1969; Milne 1970; Shaver & Goss 1970b). Early images of the source (Shaver & Goss 1970a; Milne 1972; Milne & Dickel 1975) showed (at least) two distinct components: a bright double source to the north-west, and fainter extended structure to the south-east. Subsequent observations at sub-arcmin resolution (Caswell et al. 1981; Manchester & Durdin 1983; Whiteoak & Green 1996) showed the north-western component to be dominated by a central clumpy ring, and the south-eastern source to be comprised of complex filamentary structure, as shown in Figure 6.1. Both components are extended along a direction parallel to the Galactic Plane, with a distinct gap between them. Wide-field observations of the region (Milne et al. 1993; Whiteoak & Green 1996) reveal a pair of polarised radio arcs $\sim 30'$ to the south-east of G320.4–01.2, which have been designated G320.6–01.6. It is not clear whether this structure is a "blow-out" from G320.4–01.2 or is a separate SNR.

X-ray

The first X-ray image of the region revealed a surprise: a 150-ms pulsar B1509–58 within the SNR (Seward & Harnden Jr. 1982). The pulsar was subsequently detected in the radio (Manchester et al. 1982) and γ-ray (Wilson et al. 1992; Ulmer et al. 1993) bands. Radio timing observations (Manchester et al. 1985b; Kaspi et al. 1994) show PSR B1509–58 to have the highest period derivative ($\dot{P} = 1.5 \times 10^{-12}$), the second lowest characteristic age ($\tau_c = 1700$ yr) and the third highest spin-down luminosity ($\dot{E} = 1.8 \times 10^{37}$ erg s^{-1}) of any known pulsar.

The X-ray morphology of the SNR is shown in Figure 6.1. The pulsar is embedded in a $5'$–$10'$ non-thermal nebula (region "SN" of Figure 6.1) (Seward et al. 1984; Greiveldinger et al. 1995; Marsden et al. 1997), presumed to be synchrotron emission from a pulsar wind nebula (PWN). There is no obvious radio counterpart to this PWN. To the north-west of the pulsar is an extended thermal X-ray source (region "NN") (Seward et al. 1983; Trussoni et al. 1996; Tamura et al. 1996), whose position and morphology closely correspond to the brightest radio emission (Brazier & Becker 1997). A diffuse bridge of emission joins the "SN" and "NN" regions. Another bridge connects the "SN" region to X-ray emission south-east of the pulsar (region "T"). Region "T" appears to coincide in position and morphology with the south-eastern component of the radio SNR (Trussoni et al. 1996). The lowest level X-ray contour envelopes the entire SNR (region "CDN").

Optical and Infrared

The bright north-western X-ray and radio source coincides with the collection of irregular filaments which make up the Hα nebula RCW 89 (Rodgers et al. 1960; Seward et al. 1983). Other nearby nebulosities are probably unrelated to the SNR (Lortet et al. 1987). The infrared point source IRAS 15099–5856 is coincident with the pulsar, but its nature is uncertain (Arendt 1991).

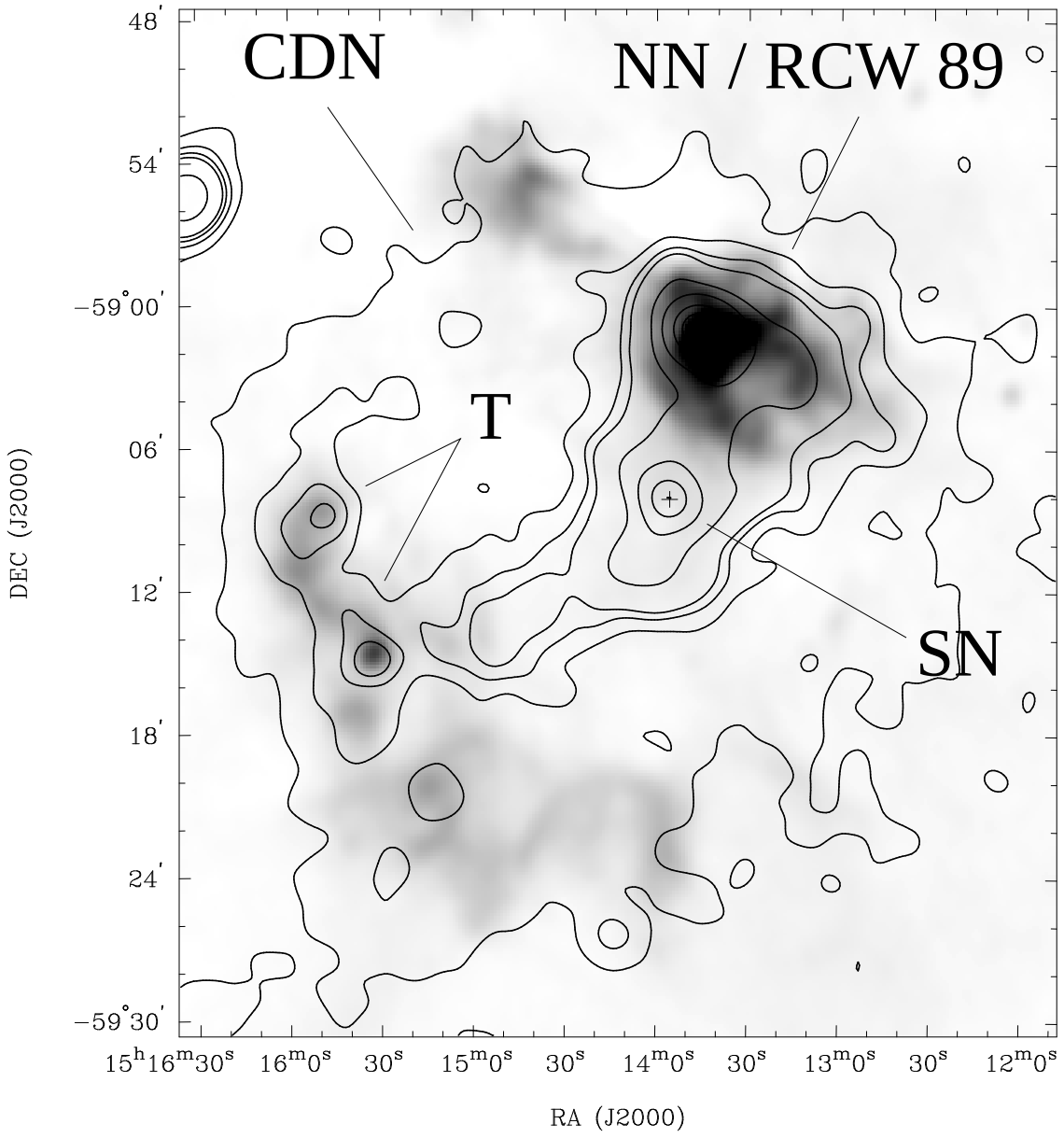

Figure 6.1 A radio/X-ray comparison of G320.4–01.2. The grey-scale corresponds to 36-cm MOST observations (Whiteoak & Green 1996), while the contours represent smoothed *ROSAT* Position Sensitive Proportional Counter (PSPC) data of Trussoni et al. (1996) [their Figure 2(a)]. Contour levels (in arbitrary units) are at levels of 0.5, 1, 1.5, 2, 5, 10, 20, 30 and 40. Selected regions designated by Trussoni et al. (1996) are indicated. Here (and in subsequent figures), the position of PSR B1509–58 is marked by a "+" symbol. G320.6–01.6 is to the south-east of G320.4–01.2 and is outside the field of view shown here.

6.1.2 Is There a Radio PWN Around PSR B1509–58?

The one fact about this system which conforms to expectations is the presence of an X-ray PWN around the pulsar (Seward et al. 1984). However, the system is unlike other young pulsars in SNRs in that there is no apparent radio counterpart to this PWN. This can be explained by rapid expansion of the supernova ejecta into a low-density bubble, which causes severe adiabatic losses in the PWN and a consequent rapid fading of its radio emission (Bhattacharya 1990). While this seems plausible, existing observations are not of sufficient quality to put good observational limits on the flux from a radio PWN. A tongue of emission apparently extends southwards from RCW 89 towards the pulsar (Manchester & Durdin 1983), but it is not clear whether this structure is associated with the pulsar, or is unrelated and obscures any faint radio PWN.

6.1.3 What is G320.4–01.2?

The radio morphology of G320.4–01.2 is unusual. Its two well-separated components can only be considered a single shell in the broadest of interpretations; the unusual collections of knots and filaments, and the distinct gaps in emission to the north-east and south-west, need to be explained. The region is probably the site of many supernovae in the recent past (Lortet et al. 1987), and one possibility is that the components of G320.4–01.2 may actually be multiple SNRs.

In order to explain RCW 89's bright appearance in X-rays, Seward et al. (1983) suggested that it is powered by an outflow of energy from the pulsar. Tamura et al. (1996) revive this interpretation, showing that the X-ray bridge joining the pulsar and RCW 89 has a non-thermal spectrum. They propose that this bridge is a jet flowing out from the pulsar and illuminating RCW 89. Manchester & Durdin (1983) and Manchester (1987) describe a related idea, noting that the two components of the radio remnant can be mapped onto opposed cones emanating from PSR B1509–58. They suggest that the radio morphology of the SNR may be generated by opposed beams of particles originating from the pulsar and colliding with the surface of a surrounding cavity. Brazier & Becker (1997) provide X-ray evidence for this model, pointing out that the PWN has a cross-shaped appearance, possibly corresponding to a highly inclined version of the "torus + jets" geometry of the Crab Nebula in X-rays (Hester et al. 1995). The "jets" align with the axis of proposed outflow (presumed also to be the pulsar's rotation axis) and one of them maps onto the ring of X-ray knots seen at the peak of RCW 89.

There are two main problems with the argument that the RCW 89 region is powered purely by an outflow from the pulsar. First, the total thermal energy in RCW 89 (4×10^{49} erg; Tamura et al. 1996) exceeds the *entire* energy lost by the pulsar over its lifetime for any but very rapid initial periods. Second, the mechanism by which a large thermal nebula might be created at the termination of such an outflow is unclear (Tamura et al. 1996). Both these issues must be resolved if this model is to be considered a possibility.

6.1.4 Are G320.4–01.2 and B1509–58 Associated?

PSR B1509–58 is a young pulsar located near the centre of a SNR. At first glance, a physical association with G320.4–01.2 seems assured. However, such a claim should be treated with caution: a young pulsar need not have an associated SNR (Kafatos et al. 1980; Braun et al. 1989), and line-of-sight coincidences are rife (Gaensler & Johnston 1995a,b). There are several criteria by which an association can be judged. The most useful are agreement in distance and age estimates, a reasonable implied transverse velocity for the pulsar, evidence from the pulsar's proper motion, and any indication of an interaction between the pulsar and the SNR.

Distances

H I absorption towards RCW 89 (Caswell et al. 1975b) puts the SNR at a distance of 4.2 kpc, slightly less than the pulsar's distance of 5.9±0.6 kpc as derived from its dispersion measure (Taylor & Cordes 1993). Strom (1994) argues that the pulsar is at a greater distance than the SNR based on a claim that the hydrogen column density towards the pulsar is significantly greater than that to the remnant. Evidence from X-ray spectral data (Trussoni et al. 1996) shows that in fact the opposite is true, and that in any case such a discrepancy need not imply that the two are at different distances.

Ages

A more serious discrepancy lies in the ages of the two systems. Unless one invokes a time-variable braking index, PSR B1509–58 can be no older than 1700 yr (Kaspi et al. 1994). But assuming standard supernova and interstellar medium (ISM) parameters, Seward et al. (1983) calculate an age for the SNR in the range $(6 - 21) \times 10^3$ yr. Proper motion measurements of the optical filaments in RCW 89 also imply a remnant age much greater than that of the pulsar (van den Bergh & Kamper 1984). Identification of G320.4–01.2 with the historical supernova SN 185 (Thorsett 1992) makes its age almost compatible with that of PSR B1509–58, but this claim has been disputed by several other authors (Schaefer 1993; Strom 1994; Chin & Huang 1994). One way of reconciling the SNR and pulsar ages is by invoking rapid expansion of the SNR shell into a cavity, followed by an encounter with dense surrounding material (Seward et al. 1983; Manchester 1992).

Velocity and Proper Motion

Calculating the transverse pulsar velocity implied by an association requires a determination of the pulsar birthplace. This is straightforward when the SNR is a near-circular shell, but is more difficult for the complex morphology of G320.4–01.2. Suffice to say that the pulsar's current position well within the SNR's perimeter implies a projected velocity somewhere between 0 km s^{-1} (Srinivasan et al. 1982)

and 3000 km s^{-1} (Kaspi 1996). No proper motion has yet been detected (Kaspi et al. 1994).

Interaction and Morphology

As discussed in Section 6.1.3, several authors have proposed that the pulsar and SNR are interacting. Du Plessis et al. (1995) argue against an association on the basis that the radio emission from RCW 89 is spectrally and morphologically distinct from the X-ray emission from the PWN. However, this is entirely consistent with RCW 89 and the PWN corresponding to the shell and "plerionic" components respectively of a composite SNR (e.g. Milne et al. 1979), and does not imply that the two are unassociated.

6.2 New Observations

Clearly, many things are still not understood about SNR G320.4–01.2 and PSR B1509–58. This has prompted us to carry out a wide range of new radio observations. With high-resolution continuum images at well-separated frequencies, we can look for morphological, polarimetric and spectral evidence for interaction between the pulsar and SNR. H I observations can confirm the kinematic distance obtained by Caswell et al. (1975b) for RCW 89, and can be used to see if other components of the radio emission are at this distance as well. Pulsar-gated observations allow us to accurately locate the pulsar, and thus measure or constrain its proper motion. Detection of hydrogen recombination lines can be used to identify any thermal sources in the region, while OH maser emission at 1720 MHz is a pointer to interaction between the SNR shock and a molecular cloud (Frail et al. 1994a).

All observations were carried out with the Australia Telescope Compact Array (ATCA; Frater et al. 1992), a synthesis telescope located near Narrabri, NSW, Australia. It consists of five movable 22-m antennas on a 3-km east-west track, with a fixed sixth antenna stationed 3 km further west.

Five types of observations were carried out:

1. continuum observations at 20 cm (1.3 GHz) and 6 cm (4.8 and 5.8 GHz);
2. pulsar-gated observations, similar to continuum mode, but where data were sampled every 4.7 ms and then folded at the apparent period of PSR B1509–58;
3. observations in the H I spectral line;
4. observations in the 1720-MHz OH maser line (carried out as part of the survey of Green et al. 1997, and reprocessed here);
5. observations in the H140α recombination line (2371.1 MHz).

These observations are detailed in Table 6.1. H I and ungated continuum observations at 20 cm consisted of two fields covering the entire SNR. Continuum observations at 6 cm were a mosaic of eight fields, covering RCW 89, a region around

B1509–58 and part of the south-eastern component. OH, H140α and pulsar-gated observations consisted of a single pointing towards RCW 89. All four Stokes parameters were recorded in continuum, while total-intensity alone was recorded for line observations. The flux density scale of all data was tied to the revised scale of Reynolds (1994) using observations of PKS B1934–638. Antenna gains were determined using regular observations of MRC 1613–586 (20-cm continuum, H I and H140α), PKS B1740–517 (6-cm continuum) and PKS B0823–500 (OH).

Date	Array Config.	Maximum Baseline (m)	ν_1 (MHz)	ν_2 (MHz)	Time on Source (h)
1995 Nov 03	6A	5939	1344	1420[a]	4
1995 Nov 11	6A	”	1721[b]	—	3
1996 Feb 01	0.75B	765	1344	1420[a]	3
1996 May 10	1.5D	1439	1376	1420[a]	16
1996 May 12	1.5D	”	4790	5824	6
1996 May 13	0.75D	719	4790	5824	9
1996 May 16	0.75D	”	1344	1420[a]	12
1996 May 17	0.75D	”	4790	5824	12
1996 Nov 10	0.75A	735	2371[c]	1376[d]	13
1997 Apr 18	0.375	459	1344	1420[a]	11
1997 Apr 20	0.375	”	4800	5824	13

[a] H I observations (1024 channels across 4 MHz)

[b] OH observations (1024 channels across 4 MHz)

[c] H140α observations (256 channels across 8 MHz)

[d] Pulsar-gated observations

Table 6.1 ATCA observations of G320.4–01.2. Except where noted, all observations were in continuum mode, involving 32 channels across a 128 MHz bandwidth.

6.3 Data Reduction

Reduction and analysis were carried out within the `MIRIAD` package (Sault et al. 1995). Data were edited and calibrated using standard techniques (Sault & Killeen 1998). The field of the calibrator MRC 1613–586 contains several weak confusing sources, and antenna gains for this source were determined using a model of all the sources in the relevant field (cf. Chapter 4).

6.3.1 Continuum Data

At both 20 and 6 cm, a mosaic image of the field was formed using multi-frequency synthesis (Sault & Wieringa 1994), uniform weighting and cell sizes of $4''$ and $2''$ respectively. Data from the 6-km antenna were excluded. Each image was deconvolved using the maximum entropy algorithm (Gull & Daniell 1978), all pointings in the mosaic being handled simultaneously (Sault et al. 1996). No constraints were placed on the deconvolution as to the total flux density of the region. The resulting models were smoothed using a Gaussian restoring beam, and then corrected for the mean primary response of the ATCA antennas and for the appropriate mosaic pattern. The resolution and noise in the final images are given in Table 6.2.

Wavelength (cm)	20		6
Resolution	$24\farcs1 \times 20\farcs8$		$15\farcs0 \times 10\farcs4$
Measured RMS noise	250	(Stokes I)	250
(μJy beam^{-1})	75	(Stokes V)	100
G320.4–01.2 :			
Flux density (Jy)	28 ± 1	(north)	10 ± 1
	18 ± 1	(south)	—
	46 ± 2	(total)	—
PSR B1509–58 :			
Flux density (mJy)	1.3 ± 0.3		< 0.5
Position (J2000)	RA $15^{\rm h}13^{\rm m}55\fs61 \pm 0\fs02$, Dec. $-59°08'08\farcs67 \pm 0\farcs26$		
G320.6–00.9 (Source 1 in Figure 6.2) :			
Flux density (Jy)	0.35 ± 0.05		≈ 0.1
Position (J2000)	RA $15^{\rm h}15^{\rm m}0^{\rm s}$, Dec. $-58°46'53''$		

Table 6.2 Observational and derived parameters for ATCA continuum data.

The pulsar-gated data were analysed by de-dispersing at a dispersion measure of 253.2 pc cm^{-3} (Kaspi et al. 1994). On- and off-pulse data-sets were formed, and the off-pulse data subtracted from the on-pulse data so that only pulsed emission remained.

Images of the region were also formed in Stokes Q, U and V. At 20 cm, Faraday rotation across the observing band is significant ($\sim$4 radians across 128 MHz in some regions), and can cause depolarisation of the emission. This effect was minimised by making multiple pairs of Q and U images across the 20-cm band, each of bandwidth 8 MHz. At 6-cm bandwidth depolarisation is minimal (< 0.5 radians), and we made a single pair of Q and U images for the entire frequency band.

Although mosaic images can be formed in polarisation as described for total-intensity data above, Q, U and V data are not positive everywhere and thus cannot be deconvolved using maximum entropy techniques as used for Stokes I. For our 20-cm data we thus deconvolved images of polarised emission using the "individual" approach (see Sault & Killeen 1998), whereby each pointing is deconvolved separately using the `CLEAN` algorithm (Clark 1980), and final images in Q, U or V are then formed by combining each `CLEAN`ed pointing. However, the "individual" approach results in an image greatly lacking in extended structure when compared to "joint" deconvolution techniques (Cornwell 1988). At 20 cm most of the emission is well sampled by the unmosaiced $u-v$ coverage, and this effect is minimal. However, at 6 cm the image quality resulting from the individual approach is poor. Thus at 6 cm we formed dirty polarisation images using the joint algorithm as in total intensity, but made no attempt to deconvolve them.

A linear polarisation image L was formed from each pair of Q and U images and corrected for non-Gaussian noise statistics. At 20 cm, each L image was clipped where the polarised emission or the total intensity was less than 5σ, and the final image formed by taking a mean across the observing band.

6.3.2 Spectral Index

Spatial variations in the spectral index, α (where $S_\nu \propto \nu^\alpha$), of a SNR can be used as evidence of inhomogeneities in the surrounding ISM (Keohane et al. 1997), to indicate a "plerionic" component (Milne et al. 1979), to demonstrate an interaction between the pulsar and the SNR shell (Frail et al. 1994c), or to identify distinct components or separate sources (Kassim et al. 1991). These possibilities are all of particular interest for G320.4–01.2, but existing spectral index studies of this source have had low spatial resolution and have produced a wide range of conflicting results (see du Plessis et al. 1995). Using our high-resolution 20- and 6-cm observations, as well as the lower resolution 36-cm observations of Whiteoak & Green (1996), we can (in principle) accurately calculate the spatial distribution of α for G320.4–01.2.

However, when computing spectral indices, it is crucial that the images being compared contain the same spatial scales. If not, any calculation could be biased by flux on scales which are present in one image but not in the other. Indeed the $u-v$ coverage of each data-set is quite different, and spatial filtering must be applied to each so that those spatial scales which are not shared between each data-set are discarded. Assuming that the deconvolution process at each frequency accurately fills in the $u-v$ plane in some range $w_{\rm min} \leq (u^2+v^2)^{1/2} \leq w_{\rm max}$, this filtering can be simply achieved by smoothing the higher resolution image to the resolution of the lower, and discarding extended structure in whichever image extends to shorter projected baselines. The spatial distribution of spectral index can then be determined using the method of "T–T" (temperature-temperature) plots (Turtle et al. 1962). In this method, two images $S_{\nu_1}(x,y)$ and $S_{\nu_2}(x,y)$ are plotted against each other on a pixel-by-pixel basis in some small sub-region of the image. Provided any DC offset is constant over this region, the data will follow a

linear relationship of the form:

$$S_{\nu_1} = m\, S_{\nu_2} + b, \tag{6.1}$$

where b is the contribution caused by the DC offset, and m is related to the spectral index, α, by

$$\alpha = \frac{\ln m}{\ln(\nu_1/\nu_2)}. \tag{6.2}$$

A linear fit to the data gives a value of m and thus of α.

We first ensured this method's validity by generating a series of test images of varying extents and shapes, and of known spectral index. After simulating observations of these objects at 20 and 6 cm and spatially filtering the resulting images appropriately, we found that the input spectral index could be recovered to within 1σ whenever the corresponding T–T plot showed a simple, linear relation.

We then applied this method to our 20- and 6-cm data on G320.4–01.2 to produce a pair of images of resolution $24''$, and also to the lower resolution 36-cm image of Whiteoak & Green (1996) in conjunction with our 20- and 6-cm images to produce a trio of images at resolution $50''$.

Because there are many pixels per beam area in each image, adjacent pixels are correlated, which will cause the uncertainty in the linear fit to a T–T plot to be underestimated (Green 1990). To correct for this effect, each image was re-binned by choosing every ith pixel, where there are i pixels per beam in each dimension. T–T plots of ν_1 vs ν_2 were then produced in square regions of side $2'$, and a linear least squares fit applied to each plot to determine m, and hence α via Equations (6.1) and (6.2). The uncertainty in α was determined by standard propagation of errors, incorporating contributions from the finite bandwidths at ν_1 and ν_2, and from the uncertainty in m caused by the fitting process. The process was repeated for ν_2 vs ν_1 to avoid any bias (Anderson & Rudnick 1993), and the two values for α averaged, weighted by their uncertainties.

6.3.3 Spectral Line Data

For the H I observations, continuum emission was subtracted from the line data in the $u-v$ plane (van Langevelde & Cotton 1990; Sault 1994), and spectra were then smoothed to a velocity resolution of 3.3 km s^{-1}. Diffuse emission was removed by discarding $u-v$ spacings shorter than 1 kλ, and a line cube was then formed for velocities between –200 and +200 km s^{-1} (LSR). The peak emission in the resulting images was deemed sufficiently faint that deconvolution was not required.

The H I cube was then weighted by multiplying it by the 20-cm continuum image. H I spectra towards sources of interest were generated by integrating over the relevant region of the cube, and then renormalised to give units of fractional absorption.

The RMS noise, σ, in each spectrum was determined from the flux in line-free channels. The presence of extended H I emission in the Galactic Plane raises the

thermal noise in the H I line to approximately double this value (e.g. Dickey 1997), and so we choose 6σ as the threshold above which features are considered believable.

Continuum emission was subtracted from OH and H140α data as for H I. Cubes were formed at various velocity resolutions and then searched for emission.

6.4 Results

6.4.1 Continuum Images

Total-intensity images of SNR G320.4–01.2 at 20 and 6 cm are shown in Figures 6.2 and 6.3 respectively. The brightest region is that coincident with RCW 89, and can be seen to form a ring of knots (region 4 in Figure 6.2) superimposed on a horseshoe-shaped plateau of emission (region 5). A bridge of emission running parallel to the Galactic Plane connects RCW 89 with another clump of emission, comprised of a compact source at its south-west end (region 3) and becoming more diffuse to the north-east (region 2). South-east of RCW 89 is a twisted, filamentary arc (incorporating regions 7 and 9), with one distinctly compact region near its northern end (region 8).

The 20-cm flux density of G320.4–01.2 and its associated uncertainty are given in Table 6.2, and were measured by integrating polygons around each component of the source then applying a background correction. The shortest antenna spacing at 20 cm is 31 m, corresponding to a spatial scale of $\sim 25'$. However, the mosaic allows us to recover information on larger scales (Cornwell 1988; Sault et al. 1996), in this case up to $\sim 35'$. If the SNR contains structure larger than this, these missing spacings will result in a significant underestimate in the true flux density. However, the 20-cm flux densities in Table 6.2 are in excellent agreement with single-dish observations at this frequency (Milne et al. 1969; Milne 1972). Furthermore, a high-contrast image of the field shown in Figure 6.4 demonstrates that there is no negative bowl around the SNR, as would be expected if large-scale structure were missing. Finally, our ATCA image, when smoothed to the appropriate resolution, is indistinguishable from a 20-cm image made with the Parkes 64-m radio telescope (A. R. Duncan 1996, private communication). All these points are good evidence that the ATCA observations contain all the flux and structure from the SNR.

At 6 cm, we are sensitive only to scales smaller than $9'$, even after mosaicing. Thus we expect the flux density determined in Table 6.2 (for the northern component only) to be an underestimate. Indeed if we take the flux density at 20 cm and scale it by a mean spectral index $\alpha = -0.45$ (Milne et al. 1993), we expect a 6-cm flux density for the northern region of 15 Jy, significantly greater than the value in Table 6.2. This missing flux is clearly evident in Figure 6.3, which, compared to Figure 6.2, lacks significant extended structure.

The position and 20-cm flux density of PSR B1509–58 are given in Table 6.2 and were determined by fitting in the $u-v$ plane to the pulsed data-set formed from the pulsar-gated data. This position is marked by a "+" symbol on appropriate Figures.

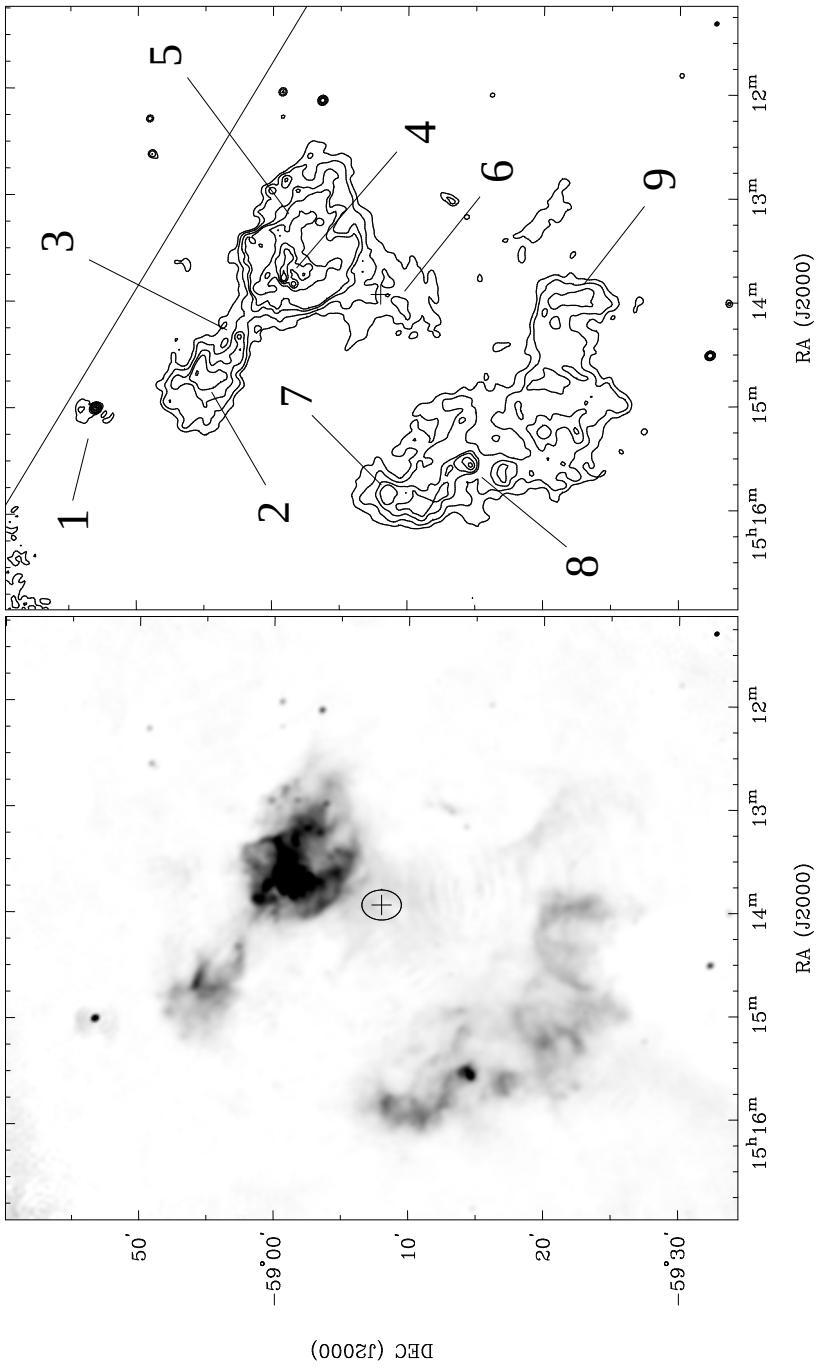

Figure 6.2 Grey-scale and contour images of SNR G320.4–01.2 at 20 cm, corrected for the primary beam response of the telescope. The grey-scale range is 0 to 75 mJy beam^{-1}, while the contours are at 5, 10, 20, 30, 60, 90, 120 and 150 mJy beam^{-1}. The FWHM of the Gaussian restoring beam is shown at the lower right of each image. The diagonal line above the SNR runs parallel to the Galactic Plane. Various regions of interest are marked. The ellipse in the left panel shows the 1σ error ellipse for the pulsar's birth-place.

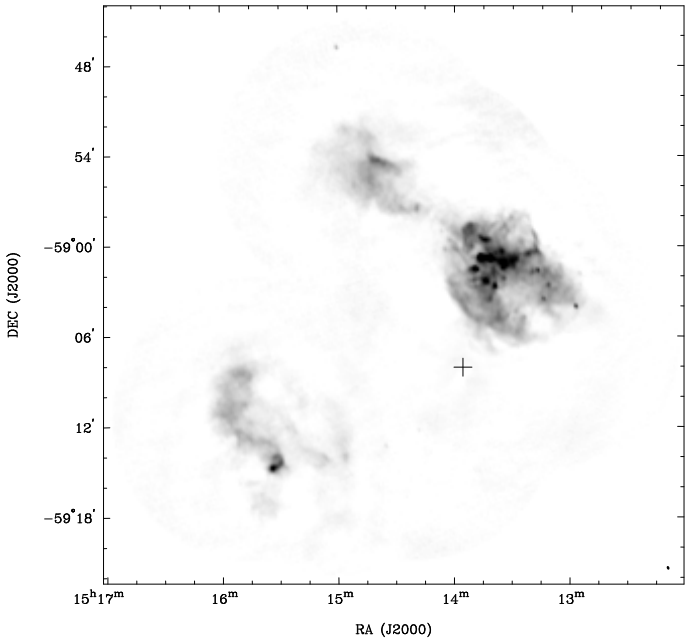

Figure 6.3 Grey-scale image of part of SNR G320.4–01.2 at 6 cm. The image has been tapered towards the edges to give uniform noise across the image, and shows emission in the range 0 to 20 mJy beam^{-1}. The FWHM of the Gaussian restoring beam is shown at lower right.

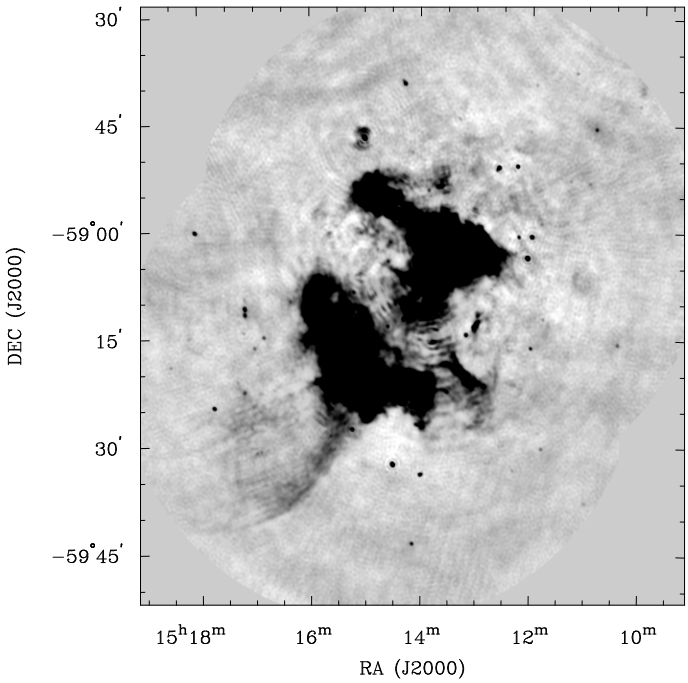

Figure 6.4 20-cm ATCA image of G320.4–01.2, with grey-scale range –1 to 4 mJy beam^{-1}. A taper has been applied to give constant noise across the field.

The pulse-profile is similar to that obtained by Manchester et al. (1982), consisting of a single main pulse occupying ∼15% (FWHM) of the period. The pulsar was not detected in (ungated) 6-cm observations.

The position of the pulsar given in Table 6.2 is consistent, within the uncertainties, with that derived by Manchester et al. (1985b) 14.4 yr earlier. This allows us to put 1-σ upper limits on the pulsar's proper motion of 39 mas yr^{-1} in RA and 52 mas yr^{-1} in Dec.. The corresponding 1-σ error ellipse for the distance travelled in 1700 yr is shown in Figure 6.2, limiting its birth-place to somewhere south of RCW 89 and well within the SNR.

An image of the region surrounding the pulsar is given in Figure 6.5, where the grey-scale range has been chosen to show faint radio emission in the region. The pulsar is seen to lie within a tongue-like plateau of emission extending 6′ south-east from RCW 89 (region 6 of Figure 6.2); a channel of depressed emission in this tongue can be seen surrounding and to the south-east of the pulsar. This tongue and the channel within it are clearly evident in MOST observations of the same region (Manchester & Durdin 1983; Whiteoak & Green 1996), but under conditions of lower resolution, poorer sensitivity and reduced dynamic range. It is also just visible in our 6-cm data, but is poorly imaged as a result of the lack of short spacings. X-ray emission in the region (as imaged by *ROSAT* PSPC) is shown as contours in Figure 6.5. A comparison between X-ray and radio data clearly shows that a narrow X-ray feature (part of the PWN powered by PSR B1509–58) runs along the channel of reduced radio emission.

In Figure 6.6 we compare radio emission from the centre of the RCW 89 region with the *ROSAT* High Resolution Imager (HRI) data of Brazier & Becker (1997). The ring of knots seen at the radio peak of RCW 89 shows a marked correspondence with the X-ray emission.

To the north of the SNR is source 1, an unresolved core surrounded by a patchy plateau of emission of diameter ∼ 3′. This source was classified as a SNR candidate, G320.6–00.9, by Whiteoak & Green (1996). Its position and 20- and 6-cm flux densities are given in Table 6.2. Its flux density at 6 cm is difficult to estimate, as the correction for the primary beam response is large. Furthermore, the extended component was not imaged by the 6-cm $u-v$ coverage, and thus the corresponding flux density pertains only to the core region.

In the high-contrast image of the entire field shown in Figure 6.4, to the south-east of the burnt-out regions, is a diffuse arc of emission extending beyond the field of view. This emission corresponds to G320.6–01.6, the full extent of which can be seen in other images (Milne et al. 1993; Whiteoak & Green 1996). Structure in this arc is almost certainly not fully sampled by our $u-v$ coverage.

6.4.2 Polarisation

Images of linear polarisation L at 20 and 6 cm are shown in Figures 6.7 and 6.8 respectively. The 20-cm image shows diffuse patchy polarisation over the SNR, with noticeable peaks in regions 4, 6, 8 and 9. Polarised intensity at 6 cm shows similar

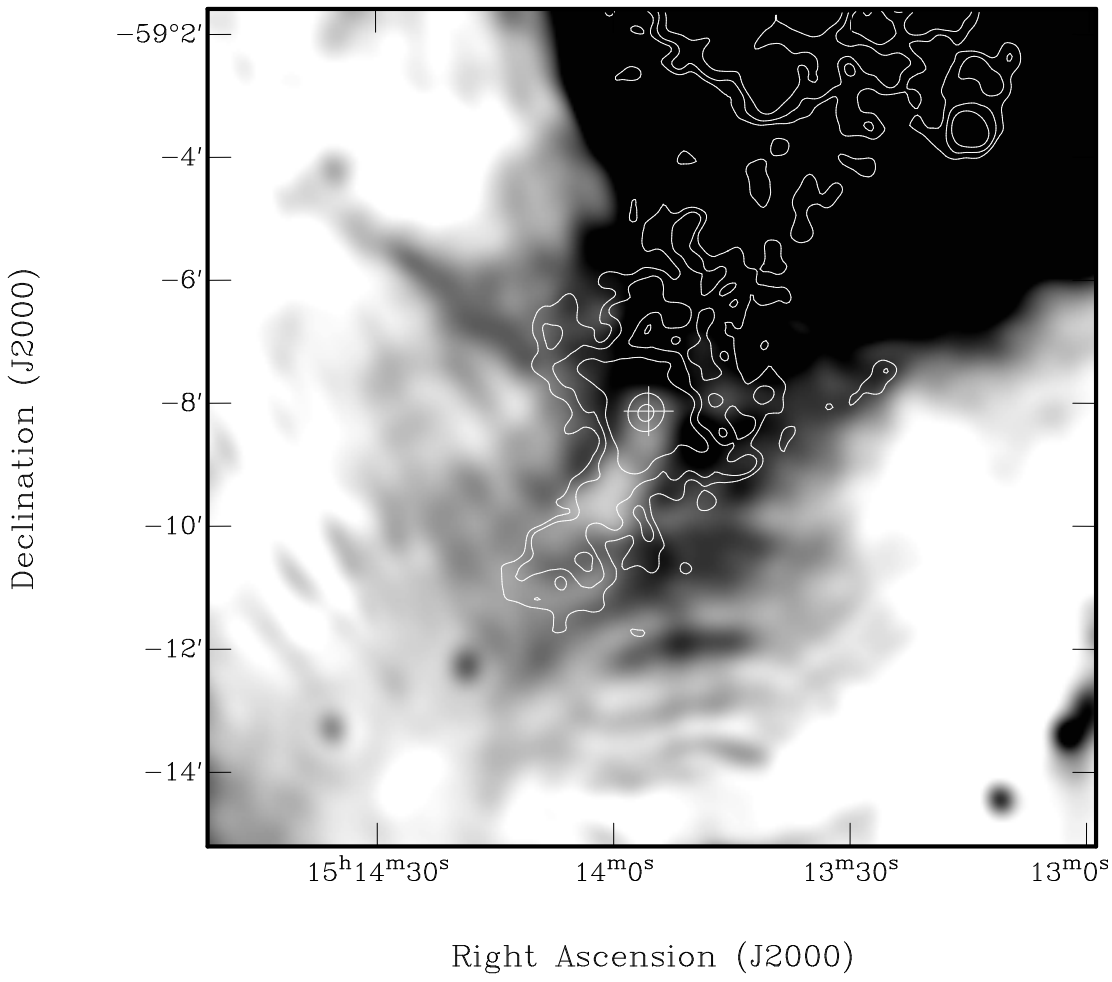

Figure 6.5 Radio/X-ray comparison of the region near PSR B1509–58. The grey-scale corresponds to a sub-region of Figure 6.2, but showing 20-cm emission in the range 1 to 10 mJy beam^{-1}. The contours represent the *ROSAT* PSPC data of Greiveldinger et al. (1995), with levels (in arbitrary units) at 1.5, 2, 3, 15, 30. Corrugations seen in the radio emission are low-level artifacts of the deconvolution process.

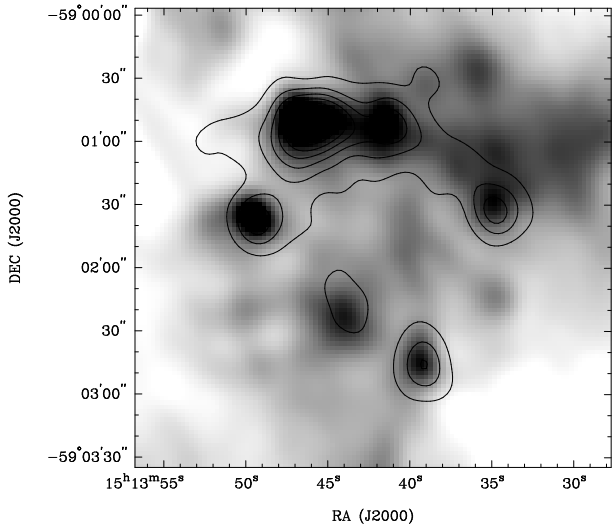

Figure 6.6 A high-resolution radio/X-ray comparison of the RCW 89 region. The grey-scale delineates 6-cm ATCA observations, while contours correspond to the *ROSAT* HRI data of Brazier & Becker (1997), smoothed to the resolution of the 6-cm image. Contour levels (in arbitrary units) are at levels of 5, 10, 15, ..., 40.

peaks but at higher resolution. Although emission at 6 cm in region 6 is affected by sidelobes from region 4, a channel of reduced emission extending south of the pulsar is visible, just as is seen in total intensity in Figure 6.5. In Table 6.3 we summarise the fractional polarisation in the two images, showing a general increase at 6 cm compared with 20 cm.

Region	Fractional polarisation (%)	
	20 cm	6 cm
1	< 3	< 3
2	17	40
3	5	25
4	10	18
5	5	20
6	60	120
7	13	28
8	7	30
9	32	—

Table 6.3 Peak linear polarisation of regions indicated in Figure 6.2.

ATCA continuum observations involve the recording of many adjacent frequency channels. These can be used to extract the Faraday rotation across the observing band, from which an accurate rotation measure (RM) can be derived (see Chapter 4).

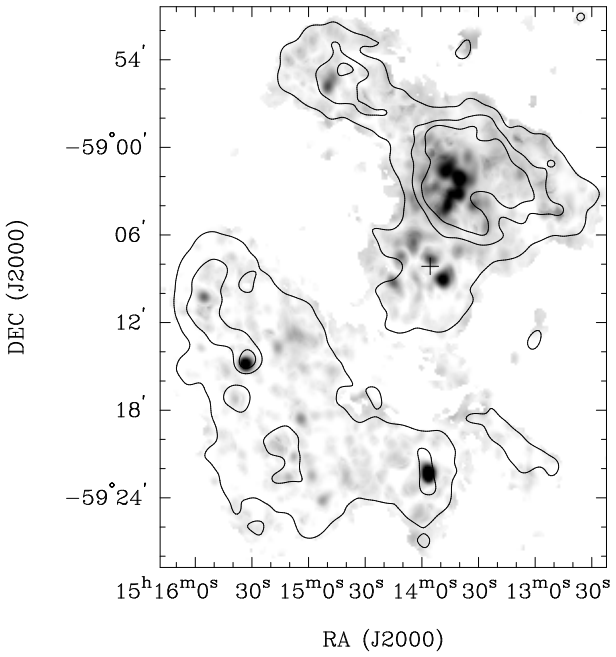

Figure 6.7 Polarised emission from G320.4–01.2 at 20 cm. The grey-scale runs from 1.2 to 5.0 mJy beam^{-1}. Contours represent total intensity at 20 cm smoothed to 50′ resolution, and are at levels of 20, 100 and 200 mJy beam^{-1}.

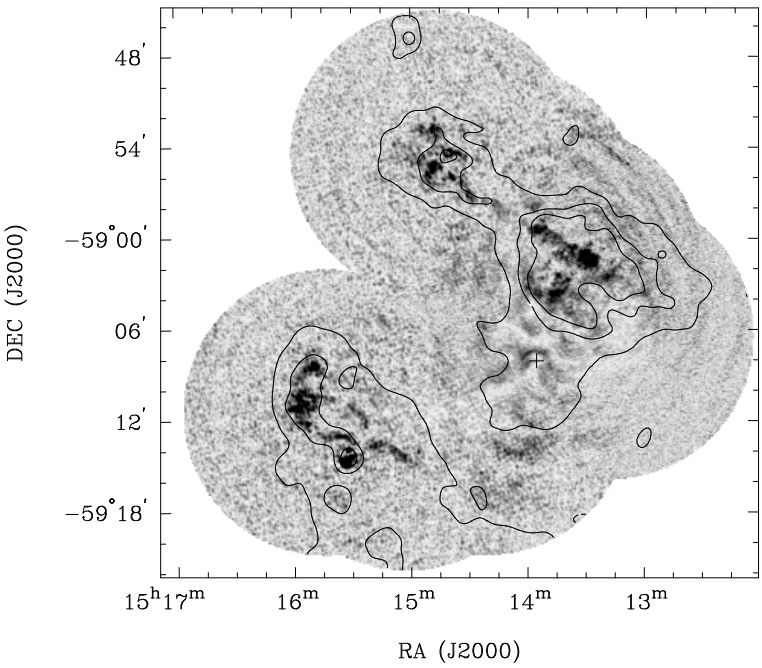

Figure 6.8 Polarised emission from G320.4–01.2 at 6 cm (with no deconvolution or clipping applied). A taper has been applied to keep the noise constant across the image. The grey-scale runs from 0 to 1 mJy beam^{-1} and contours are as in Figure 6.7.

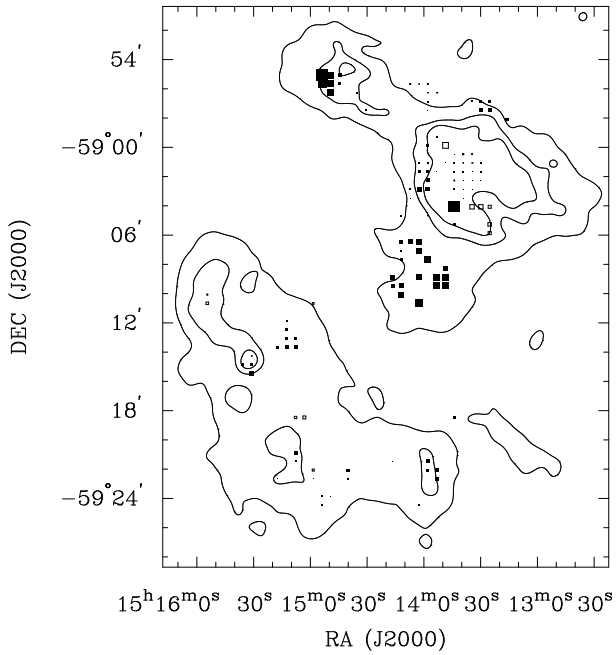

Figure 6.9 Rotation measures towards G320.4–01.2. The linear size of each box indicates the magnitude of the RM, solid boxes indicating positive RM's and open boxes negative. The largest box visible corresponds to +400 rad m^{-2}. Contours are as in Figure 6.7.

In Figure 6.9 we show RMs for the SNR, determined from Faraday rotation across the 20-cm band. Rotation measures are generally low ($|RM| < 100$ rad m^{-2}) except in regions 2 and 6 and on the southern edge of region 4. The RM of the SNR at the position of B1509–58 is 210±30 rad m^{-2}, very similar to the value of 215±2 rad m^{-2} for the pulsar (F. Crawford 1998, private communication). The pulsar is too weak to contaminate the value measured for the remnant.

The fractional bandwidth at 20 cm is insufficient to accurately determine intrinsic position angles (see Chapter 4), while as discussed in Section 6.3.1, the 6-cm L image cannot be easily deconvolved. Thus we cannot derive intrinsic position angles of linear polarisation from the SNR, and refer the reader to the lower resolution results of Milne et al. (1993). In particular, we note that their results show that the magnetic field in the highly polarised region 6 is oriented along the axis defined by the collimated X-ray feature and the associated radio channel both seen in Figure 6.5

The clumpy nature of polarised emission at 20 cm, along with the significant variations in RM seen across the remnant, suggest that the low levels of L/I seen at 20 cm can be explained by beam depolarisation, in which the position angle of polarised emission varies across the sky on scales smaller than the beam. As expected, the fractional polarisation is significantly higher at 6 cm, a result of both the increased resolution and the reduced Faraday rotation at shorter wavelengths. Since our RMs are derived using up to 13 independent data points across the 20-cm band, it is unlikely that there is any ambiguity in their determination. There is

reasonable agreement between the RMs determined here and those derived by Milne et al. (1993) using only two data points, and thus one can have confidence in the intrinsic position angles which Milne et al. derive.

At 6 cm, radio emission near PSR B1509–58 (region 6) has the unphysical value of $L/I = 1.2$. This can be understood in terms of the spatial filtering applied by an interferometer to the sky distribution of emission. In 6-cm total intensity, region 6 is poorly imaged by the ATCA because it is dominated by extended structure to which the telescope is not sensitive. But in polarisation, variations in position angle (either intrinsic to the source or resulting from differential Faraday rotation) shift power in the polarised images into smaller-scale structure to which the interferometer is sensitive. Polarised emission thus appears to be of greater surface brightness than the total intensity (see Wieringa et al. 1993). Although the fractional polarisation of region 6 is also high at 20 cm, it does not suffer from this effect as the observations are sensitive to all relevant spatial scales (see Section 6.4.1). The high fractional polarisation at 20 cm thus shows that there is minimal beam depolarisation in this region, indicating a well-ordered magnetic field.

No linear polarisation is detected from G320.6–00.9 (source 1 in Figure 6.2). In circular polarisation, the 20-cm image shows emission only from PSR B1509–58, while the 6-cm image contains no discernible sources.

6.4.3 Spectral Index

Appropriate spatial filtering of the 20- and 6-cm data results in a pair of images both of which contain emission on scales between 24″ (the resolution at 20 cm) and 520″ (corresponding to the shortest spacings at 6 cm), and have no structure outside this range. T–T plots were produced for the various regions of G320.4–01.2 marked in Figure 6.2. Several plots were produced for each region by shifting the box in which data were considered by a few pixels each time. In all cases adjacent boxes produced consistent results. Two spectral indices were determined for each region: between 20 and 6 cm and between 36 and 6 cm. An example is given in Figure 6.10, where T–T plots are shown for regions 4 and 7 between 20 and 6 cm. It can be seen in Figure 6.10 that the data in each region follow a linear relationship, and that the corresponding slopes (and hence spectral indices) are different. Meaningful spectral indices could not be determined between 36 and 20 cm because of the small wavelength separation between these observations.

The results of the T–T fitting are shown in Table 6.4. No value of α could be calculated for source 1 using this method, both because of the small number of pixels available for the fit and because of the large uncertainties in the primary beam correction near the edge of the field; simply using the total flux density at 20 and 6 cm we estimate $\alpha = -0.5 \pm 0.1$. No value of α_6^{36} could be calculated for region 3 because of a poor linear fit to the data. Region 6 was only barely imaged at 6 cm because of lack of short spacings in the array; we attempted to calculate a spectral index for it between 20 and 36 cm, but its low surface brightness and the nearness of the two wavelengths prevents us from constraining its spectrum any more tightly

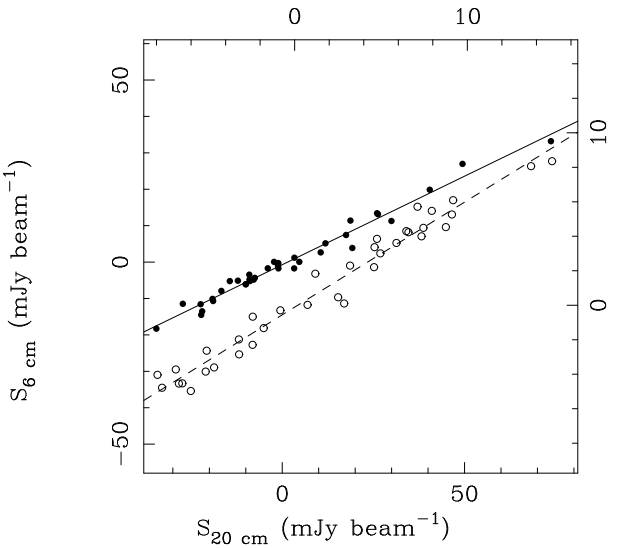

Figure 6.10 T–T plots for G320.4–01.2 between 20 and 6 cm. Data-points for region 4 are represented by solid circles and correspond to the bottom and left axes, while the resulting linear fit is shown by a solid line of slope 0.49 ± 0.01. Data for region 7 are shown by the open circles and correspond to the top and right axes. They are fitted by the broken line of slope 0.62 ± 0.02. (The data can take on negative values as a result of the spatial filtering described in Section 6.3.2.)

than $-1 < \alpha_{20}^{36} < 0$. Region 9 was outside the region of the 6-cm mosaic, and we roughly estimate $\alpha_{20}^{36} = -0.5 \pm 0.2$.

Although for each region α_6^{20} and α_6^{36} agree to within 1–2σ, in all cases α_6^{36} is of greater magnitude than α_6^{20}. Such a systematic effect suggests an error in the absolute flux density scale of one or more of the images. We expect the flux density scale of the MOST and ATCA images used here to be accurate to 5% and 3% respectively, an uncertainty sufficient to account for the discrepancies observed. While uncertainties in absolute flux calibration will always limit the accuracy with which α itself can be calculated, this effect biases the spectral index of all regions by the same amount, and thus does not affect our ability to comment on spatial variations in α. Errors caused by applying a single primary beam correction on images formed from a large fractional bandwidth (as is the case at both 20 and 6 cm) can bias α towards the edges of the field, but the effect is negligible ($\Delta\alpha \lesssim 0.01$) compared to the uncertainties quoted.

Thus results from both sets of data in Table 6.4 indicate that the spectrum of region 4 is 2–3σ steeper than that of regions 2 and 5, and 3–4σ steeper than the spectra of regions 7 and 8.

Region	α_6^{20}	α_6^{36}
1	—	
2	-0.40 ± 0.03	-0.47 ± 0.04
3	-0.45 ± 0.04	—
4	-0.52 ± 0.04	-0.57 ± 0.04
5	-0.42 ± 0.04	-0.50 ± 0.03
6	—	
7	-0.34 ± 0.03	-0.37 ± 0.04
8	-0.33 ± 0.03	-0.41 ± 0.03
9	—	

Table 6.4 Spectral indices for regions marked in Figure 6.2.

6.4.4 H I Line

One usually compares absorption spectra with emission spectra from an adjacent patch of the sky. However, a useful emission spectrum is difficult to extract from our ATCA data because of insufficient $u - v$ coverage on the large spatial scales where emission dominates. We thus compare our results to the emission spectrum in this direction obtained by Caswell et al. (1975b). This spectrum shows significant emission at LSR velocities of –70 km s^{-1}, –55 km s^{-1}, from –15 to +30 km s^{-1}, then at +80 km s^{-1}.

Of unrelated sources near G320.4–01.2, only G320.6–00.9 (source 1 in Figure 6.2) has enough signal-to-noise ratio to obtain a useful absorption spectrum. This spectrum is shown in Figure 6.11, where significant absorption is seen at –75 and –55 km s^{-1} and between –10 and +20 km s^{-1}, with a lower level feature at +65 km s^{-1}. We thus put a lower limit on the systemic velocity of G320.6–00.9 of $V_L = +20$ km s^{-1}. We use the best fitting model for Galactic rotation of Fich et al. (1989), adopt standard IAU parameters (Kerr & Lynden-Bell 1986) for the solar orbital velocity ($\Theta_0 = 220$ km s^{-1}) and distance to the Galactic Centre ($R_0 = 8.5$ kpc), and assume an uncertainty of ± 7 km s^{-1} in systemic velocities, representative of the random motion of H I clouds (Shaver et al. 1982; Belfort & Crovisier 1984). We can thus derive a lower limit on the distance to G320.6–00.9 of 14.8 ± 0.7 kpc.

Thus G320.6–00.9 is at a large distance, is unpolarised, and has a comparatively steep spectral index, and its core is unresolved at our highest resolution ($2''$ using the 6-km antenna at 6 cm). Thus it seems likely that this source is not a SNR as proposed by Whiteoak & Green (1996), but rather is a background radio galaxy. The nature of its extended envelope is unclear.

In Figure 6.11 we also show H I spectra towards three parts of G320.4–01.2. Regions 2 and 4, both in the northern part of the SNR, show the same main features in absorption: strong absorption at –55 km s^{-1} and then at –15 km s^{-1} (region 2) or –5 km s^{-1} (region 4). Other spectra towards the northern part of the SNR are similar, all showing absorption out to –55 km s^{-1}. Region 8, in the south of the

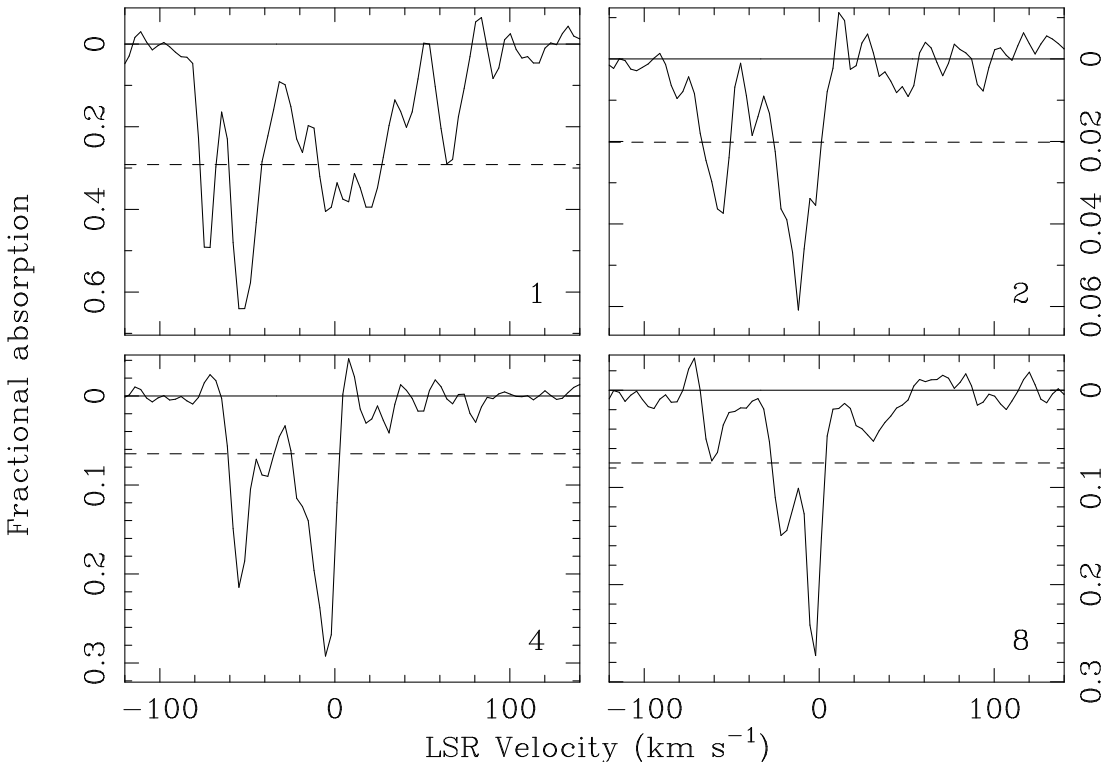

Figure 6.11 H I absorption spectra towards four regions in the field marked in Figure 6.2. The dashed line marks absorption at the 6σ level, where σ is the noise in line-free channels.

SNR, shows significant absorption only at –25 km s^{-1} and –5 km s^{-1}. A feature at –60 km s^{-1} is at the limit of significance. The signal-to-noise of absorption towards other parts of the SNR was too low to make any useful measurements.

6.4.5 OH and H140α

Neither OH nor H140α emission was detected towards G320.4–01.2. The 3-σ upper limit on the surface brightness of OH is 23 mJy beam^{-1} at 4 km s^{-1} resolution, consistent with the survey results of Green et al. (1997) but at a slightly more stringent limit. Limits for H140α are 6 mJy beam^{-1} (15 km s^{-1} resolution) and 4.5 mJy beam^{-1} (40 km s^{-1} resolution). At the peak of the radio emission from RCW 89, the H140α non-detection corresponds to an upper limit on the line-to-continuum ratio of $\sim$4%.

6.5 Discussion

6.5.1 How Many SNRs?

Although there are several distinct components to the radio emission from G320.4–01.2, each part can be matched up to part of the X-ray emission in the region.

1. Based on the correspondence shown in Figure 6.6, the north-western radio region (which appears to be a single object based on the similarity of H I spectra for regions 2 and 4) can be associated with the X-ray region "NN".
2. The morphological correspondence seen in Figure 6.5 between radio region 6 and the X-ray region "SN" argues a connection between them.
3. Figure 6.1 demonstrates a match between the "T" region in X-rays and regions 7 and 8 in the radio.

Trussoni et al. (1996) have shown that the spectra of and absorption towards these X-ray regions are consistent with their all being part of a single SNR. Since each of the main radio regions corresponds to part of this X-ray remnant, we therefore argue that *the entire G320.4–01.2 region in radio and X-rays is a single SNR.*

6.5.2 A Distance to G320.4–01.2

Absorption spectra for regions 2 and 4 of the SNR are consistent with that of Caswell et al. (1975b): absorption is seen at –55 km s^{-1} but not at more negative velocities. We thus adopt $V_L = -55$ km s^{-1}, corresponding to a lower limit on the distance of 3.8 ± 0.5 kpc. An upper limit is the tangent point at ~ -70 km s^{-1} (Caswell et al. 1975b; Kerr et al. 1986), which is at a kinematic distance 6.6 ± 1.4 kpc. Region 8's spectrum can only be considered consistent with those of regions 2 and 4 if absorption at –60 km s^{-1} is genuine. However, region 8 is several arcmin away from the other sources, and the distribution of H I clouds along the line of sight may be quite different. Indeed, values for the hydrogen column density towards the SNR inferred from photoelectric absorption indicate significant gradients across the SNR (Trussoni et al. 1996). Thus the H I spectra can all be considered consistent with a distance for SNR G320.4–01.2 of 5.2 ± 1.4 kpc. This agrees with the distance derived by Caswell et al. (1975b), but has more realistic uncertainties. In further discussion we adopt a distance to the SNR of $5d_5$ kpc.

6.5.3 Radio Emission near PSR B1509–58

Region 6 has the same RM as the pulsar (quite different from that of RCW 89), has a distinctly higher fractional polarisation than RCW 89, and shows a morphological correspondence with X-ray emission associated with the pulsar nebula. Thus there is good evidence that region 6 is directly associated with PSR B1509–58, as originally suggested by Manchester & Durdin (1983). Despite this claim, we would argue that this region of radio emission is *not* a radio PWN in the traditional sense, since the radio emission is not centred on the pulsar, nor are the X-ray-bright regions bright in the radio. Indeed any radio PWN is expected to be faint: comparison with the Crab Nebula gives an expected flux density at 20 cm of ∼100 mJy (Srinivasan et al. 1984), while extrapolation from the X-ray spectrum of the "SN" region implies a flux density ∼1 mJy (Seward et al. 1984). If we assume that this radio PWN is of the same extent as the X-ray PWN (although in fact we expect the radio source

to be larger because of the longer synchrotron lifetimes), we expect a 20-cm mean surface brightness at $1'$ resolution of 0.02–2 mJy beam^{-1}, completely undetectable against the background in this region of $\gg$20 mJy beam^{-1}.

The morphology of the X-ray PWN, together with the appearance of the surrounding SNR, have led several authors to propose that the pulsar's wind is focused into relativistic jets or outflows, generated along an axis aligned approximately north-west/south-east (Seward et al. 1983; Manchester & Durdin 1983; Tamura et al. 1996; Brazier & Becker 1997). There are collimated X-ray features along this axis on both sides of the pulsar. In the south-east, Figure 6.5 shows that radio emission is enhanced along the sides of the collimated X-ray feature, but not within it. We argue that this anti-correspondence can be explained if the X-ray feature is indeed a jet or outflow along the previously proposed axis; radio emission is then produced by shocks generated in a cylindrical sheath around the jet, as seen for SS 433 (Hjellming & Johnston 1986, 1988) and possibly for the X-ray jet in Vela X (Frail et al. 1997). A jet interpretation is also favoured by the polarisation properties of the sheath: the magnetic field in the region is well-ordered and oriented parallel to the axis of the proposed outflow (Section 6.4.2 above; Milne et al. 1993), similar to the field structure seen surrounding the jets associated with both the Crab (Hester et al. 1995) and Vela (Markwardt & Ögelman 1995; Milne 1995) pulsars.

We assume the radio sheath to be a hollow cylinder, the inner and outer diameters of which correspond to the diameters of the X-ray jet and radio sheath respectively. From *ROSAT* PSPC and HRI data we estimate the inner diameter of the sheath to be $60''$–$75''$, while from 20-cm ATCA data we determine an outer diameter of $210''$. We assume that the jet is inclined to the line of sight at 70° (Brazier & Becker 1997) and that the radio emission in the sheath is optically thin. We then expect the radio emission along lines of sight through the X-ray jet to be 0.7 as bright as the radio emission along the edges of the jet, consistent with the observed value of 0.5–0.8. The sheath is too faint for us to put any useful constraint on its spectral index, but we expect it to have $\alpha \lesssim -0.5$, indicative of shock acceleration (Frail et al. 1997).

The abrupt fading of the sheath to the south-east (see Figure 6.4) is difficult to explain, but appears to coincide with a similar termination in X-rays seen in Figure 6.5. Clearly, conditions within or surrounding the jet change in some way beyond this point.

The cross-shaped morphology of the X-ray PWN and its resemblance to the Crab Nebula (Hester et al. 1995; Brazier & Becker 1997) both argue for the presence of a second jet to the north-west of the pulsar. This jet appears to be less collimated than the south-eastern jet and has no obvious radio depression associated with it. While there is no clear explanation for this difference, we note that conditions on the north and south sides of the pulsar may be quite different (see Section 6.5.7 below), and that asymmetries are also observed in the outflows associated with the Crab and Vela pulsars (Pelling et al. 1987; Markwardt & Ögelman 1995).

6.5.4 The Knots in RCW 89

The north-western jet which we have just discussed appears to map onto the ring of X-ray/radio knots seen in Figure 6.6 (Brazier & Becker 1997). Thus rather than argue that the entire RCW 89 region is powered by the pulsar outflow (Manchester & Durdin 1983; Tamura et al. 1996), we now consider the alternative that the interaction region is confined just to the ring of knots.

The radio knots within RCW 89 are significantly linearly polarised, show no recombination lines and have the steepest spectral index of any emission from the SNR. Thus there seems little doubt that the emission mechanism associated with the radio features is synchrotron radiation. Taking the brightest knot to be a sphere of radius $15''$ and flux density 0.2 Jy at 20 cm, we can use standard minimum energy arguments (Pacholczyk 1970) to infer a magnetic field for it of $1.5(1+k)^{2/7}\phi^{-2/7}d_5^{-2/7}$ μG, where ϕ is the filling factor of emitting particles and fields and k is the ratio of energy in heavy particles to that in electrons. This is not significantly different from the field strengths of 7 μG and 2.5 μG inferred for the overall X-ray PWN (Seward et al. 1984) and for the X-ray jet (Tamura et al. 1996) respectively. The corresponding total energy of this knot in magnetic fields and relativistic particles is $1.3(1+k)^{4/7}\phi^{3/7}d_5^{17/7} \times 10^{42}$ erg, a tiny fraction of the total spin-down energy released by the pulsar in its life-time ($> 10^{48}$ erg). The steep spectrum of the knots is the opposite to what we might expect if injection of particles from the pulsar was directly contributing to their emission (cf. Frail et al. 1994c). Rather, it seems that the collision between the jet and pre-existing material drives shocks into the latter at the working surface, producing clumps of enhanced synchrotron emission.

X-ray observations of RCW 89 as a whole show it to be thermal (Seward et al. 1984; Tamura et al. 1996), but the X-ray/radio correspondence seen in Figure 6.6 suggests that X-ray emission from the knots might be synchrotron emission as in the radio. A single power law of spectral index $-0.6 \lesssim \alpha \lesssim -0.5$ (from Table 6.4) can indeed be extrapolated between the radio flux of the knots as observed here and the X-ray count rates quoted by Brazier & Becker (1997). No spectral break as might be caused by synchrotron losses is required, which implies a magnetic field strength < 10 μG consistent with the determination from minimum energy above. While RCW 89 is predominantly thermal in X-rays, the available spectral data lack the spatial resolution to determine whether the thermal spectrum of the region corresponds to the knots as well as the more extended component in which they are embedded. Comparison of the count-rate for the entire RCW 89 region (Trussoni et al. 1996) with those of the knots alone (Brazier & Becker 1997) shows that soft X-ray emission is dominated by the extended component, and thus at low energies a power-law spectrum associated with the knots might be hidden. Indeed observations in hard X-rays (Tamura et al. 1996) show non-thermal emission at their position. However, the spatial resolution of these data is not sufficient to separate the knots from more diffuse emission in the area; high-resolution observations with *AXAF* will be required to clarify the issue. Whether thermal or non-thermal, the energy in the knots is far smaller than that in the whole RCW 89 region, and so can

be comfortably accounted for by the pulsar spin-down.

The horseshoe-shaped plateau in RCW 89 appears to have a similar shape to the ring it envelopes, and may represent material diffusing away from the point(s) of impact. However, the size of this region is then somewhat large: from the ring to the edge of this plateau region is $2'$, which requires emission to have travelled outwards from the ring at a projected mean velocity of $2100 d_5$ km s^{-1}. One possibility suggested by Tamura et al. (1996) is that the pulsar jet has precessed or narrowed in opening angle.

To summarise, the problems raised at the end of Section 6.1.3 can be resolved if just the X-ray/radio knots, rather than the whole of RCW 89, are interpreted as the point of interaction between the pulsar outflow and the SNR. The energy in these knots can be easily accommodated by the pulsar spin-down, and it is easier to understand how these features, rather than the whole extended nebula, might be the termination of an energetic outflow. A more likely possibility to account for the surrounding RCW 89 region is that it originates from the SNR blast wave, and is not related to any outflow from the pulsar.

6.5.5 The South-Eastern Component of the SNR

It can be seen in Figure 6.7 that regions 8 and 9 of the SNR contain compact polarised clumps, resembling the knots seen in RCW 89. These features may be evidence for an interaction between the south-eastern jet and the south-eastern half of the SNR, although, compared to that with the RCW 89 region, the impact is greatly reduced. In Figure 6.12 we show an extension of the model proposed by Brazier & Becker (1997), where we speculatively project an additional cone of emission onto the south-eastern part of the SNR.[1] It is interesting to note that this second cone happens to intersect the SNR at the location of these two highly polarised clumps. It can be seen in Figure 6.1 that while the X-ray emission joining the "SN" and "T" regions might make up one edge of this cone, the other edge is missing. However, the latter region lies right along a rib of the PSPC and so may have had minimal exposure.

6.5.6 Spectral Index Variations

Results presented in Section 6.4.3 indicate that the compact knots at the peak of RCW 89 have a steeper radio spectrum than the diffuse emission surrounding them, which are again steeper than the south-eastern part of the SNR. While the phenomenon of spatial spectral index variations in SNRs is not well understood, there is the suggestion that young remnants generally show a steeper spectrum in their brightest, most compact components (Anderson & Rudnick 1993), as observed here. For example, in G260.4–03.4 (Puppis A) the steepest spectrum part of the

[1] This projection is qualitatively similar to that of Manchester & Durdin (1983) and Manchester (1987), but maps onto a smaller region of each half of the SNR.

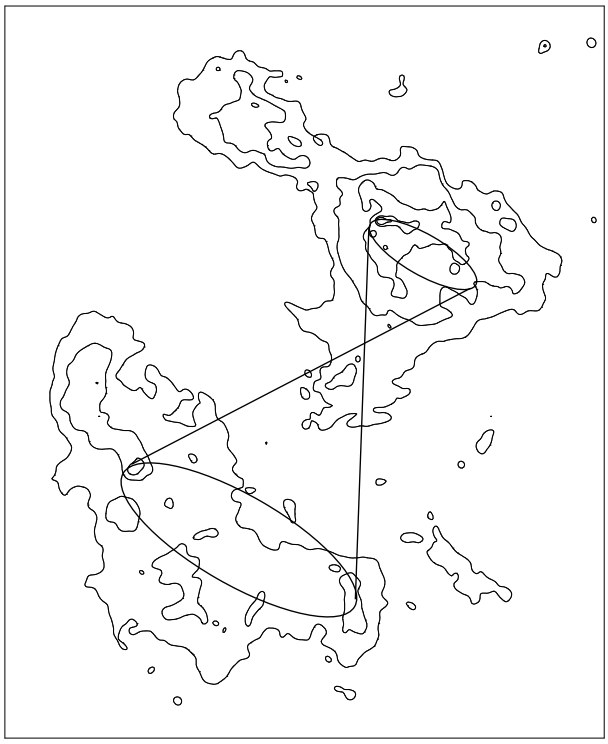

Figure 6.12 Speculative geometry for outflow in G320.4–01.2. Contours represent 20-cm continuumm, and are at 5, 20, 60, 120 and 150 mJy beam^{-1}.

shell is where it has been apparently decelerated by a collision with a dense cloud (Dubner et al. 1991), while in G111.7–02.1 (Cassiopeia A), the steep spectrum regions tend to be bow-shocks driven by clumps of fast-moving material (Anderson et al. 1991). We note that both these effects may be occurring in G320.4–01.2: significant deceleration of the RCW 89 region is argued for in Section 6.5.7 below, while the pulsar outflow may accelerate small clumps of material to high velocity, which then drive bow-shocks as in Cas A.

6.5.7 Finale: What is SNR G320.4–01.2?

The distance to the SNR of 4.2 kpc as derived by Caswell et al. (1975b) was used in the calibration of the electron distribution model of Taylor & Cordes (1993). Thus comparisons between the pulsar's distance as derived from this model and any distance estimate to the SNR are not entirely meaningful. Rather, we estimate the pulsar's distance as follows.

While PSR B1509–58 itself is too weak to show H I absorption, PSRs B1240–64, B1323–58, B1323–62, B1356–60 and B1557–50 are all within 20° of PSR B1509–58, have comparable dispersion measures and have independent distance estimates from H I absorption (Frail & Weisberg 1990; Saravanan et al. 1996). Distances and dispersion measures for these pulsars suggest a mean electron density along

this line of sight of between 0.03 and 0.06 cm^{-3}, corresponding to a distance for PSR B1509–58 in the range 4.2 to 8.4 kpc.

This distance for the pulsar is consistent with the distance we have determined for SNR G320.4–01.2 through H I absorption, resolving any previous discrepancy. Furthermore, despite the large variation in RM across the SNR (–200 to +400 rad m^{-2}), its RM at the position of the pulsar agrees with that of the pulsar itself. Finally, we discussed in Section 6.5.4 that the pulsar appears to be interacting with the surrounding SNR. Thus we argue strongly that *PSR B1509–58 and SNR G320.4–01.2 are associated*. The age discrepancy outlined in Section 6.1.4 must then be resolved.

A first possibility to account for this apparent age difference is that B1509–58 has had an unusual spin-down history, and is much older than it seems (Blandford & Romani 1988). However, all observations suggest that B1509–58 is a typical young pulsar, but that G320.4–01.2 is an anything-but-typical remnant. Although the possibility that B1509–58 is old cannot be ruled out, disagreement between a relatively well-determined pulsar age and a crudely estimated SNR age gives little cause to look to the pulsar as the culprit. Thus in future discussion we assume that the age of the system is $\lesssim$1700 yr. We now attempt to account for this age in terms of the properties of the supernova and its environment.

We take the south-eastern component of the SNR (incorporating regions 7, 8 and 9) as that part most representative of a "normal" shell SNR. Assuming the site of the supernova explosion to be within the 1-σ error-box derived from the pulsar's proper motion, we estimate the radius of the south-eastern component of the SNR to be $17' \pm 2'$. For an SNR age of 1700 yr, this implies a mean expansion velocity of $(14 \pm 2) d_5 \times 10^3$ km s^{-1}. If this component represents freely expanding material, we find a kinetic energy for the explosion of $E_{51} = (2.0 \pm 0.3) M_{\rm ej} d_5^2$, where $M_{\rm ej}$ is the ejected mass in units of $M_\odot$ and E_{51} is in units of 10^{51} erg. Alternatively, if we assume expansion in the adiabatic (Sedov-Taylor) phase then the size of the SNR implies $(E_{51}/n_1) \sim (1100 \pm 600) d_5^5$, where n_1 is the ambient density into which this component of the SNR is expanding. To fully enter this phase the SNR must sweep up 20 times its own mass (Fabian et al. 1983; Dohm-Palmer & Jones 1996), implying a density $n_1 > (0.012 \pm 0.003) M_{\rm ej} d_5^{-3}$ cm^{-3} to give $E_{51} \gtrsim (3.3 \pm 2.9) M_{\rm ej} d_5^2$.

Thus regardless of the evolutionary state of the SNR, an age of 1700 yr implies a value of $E_{51}/M_{\rm ej}$ which is 10–100 times higher than typical values (Berkhuijsen 1988; Smith 1988). This problem has been overcome in the past by invoking a large ($E_{51} \sim 10 - 100$) kinetic energy for the supernova (Seward et al. 1983; Katz 1983). While such a value for E_{51} seems uncomfortably high, it is comparable to the energy estimated for the recent Type Ic supernova SN 1998bw (Iwamoto et al. 1998; Woosley et al. 1998). However, we propose the more likely explanation that the progenitor of PSR B1509–58 was a helium star. Such a star explodes in a Type Ib supernova, ejecting a low amount of mass ($M_{\rm ej} \sim 1.5$) but with a typical supernova energy ($E_{51} \sim 1 - 2$) (Woosley et al. 1995), as required here. While the optical filaments in RCW 89 show no evidence of helium rich ejecta (Dopita et al. 1977; Seward et al. 1983), we show below that this component of the SNR is considerably evolved and is now dominated by swept-up material. Spectroscopy of any optical

emission which can be associated with the south-eastern component of G320.4–01.2 would be of great interest.

Helium stars start off as extremely massive stars, but lose their hydrogen envelopes either through a strong stellar wind or through transfer of mass to a binary companion (Woosley et al. 1993, 1995). The latter possibility is interesting, particularly as the O star Muzzio 10 (Muzzio 1979; Seward et al. 1983) is just 18″ north of the pulsar, and is at a comparable distance (∼5 kpc; Arendt 1991). We thus speculate that Muzzio 10 is the former companion of PSR B1509–58. This possibility is easily tested: assuming a pulsar age of 1700 yr, the association predicts a proper motion for the pulsar of 11 mas yr^{-1} along a position angle 168° (N through E), corresponding to a transverse velocity $260 d_5$ km s^{-1}.

It is clear from Figure 6.4 that there is no radio emission which can trace an entire shell and thus join the two components of the SNR. It was argued in Chapter 3 that the "bilateral" or "barrel" morphology which results (and the observed alignment of the bilateral axis with the Galactic Plane) is produced when a SNR expands into an elongated low-density cavity, radio emission being produced where the shock has recently encountered the walls. Thus a bilateral appearance can be considered evidence that n_1 is low ($\sim$ 0.01 cm^{-3}); such a value for n_1 can also account for the faintness of the radio PWN (Bhattacharya 1990), and is consistent with the cavities expected due to the presence of other massive stars in the region (Lortet et al. 1987). For $M_{\rm ej} = 1.5$, this ambient density corresponds to the south-eastern component beginning to enter the adiabatic phase.

Limits on the pulsar proper motion as indicated in Figure 6.2 demonstrate that the SNR is distributed highly asymmetrically about the site of the explosion. Intuitively, this suggests that the supernova explosion was near the edge of the proposed cavity, and that, while the south-eastern half of the SNR has expanded relatively unimpeded, the north-western half has decelerated significantly. A high-density environment for this component is also argued for by its high X-ray and radio brightness and by the small proper motion of associated optical filaments (Seward et al. 1983; Manchester 1992).

Gull (1973) has modelled the deceleration of a young SNR, and provides means of scaling his solution to arbitrary values of density and $E_{51}/M_{\rm ej}$. We take the radius of the north-western component to be $7' \pm 2'$, and adopt $E_{51}/M_{\rm ej} \sim 2$ as argued for above. Scaling to Figure 3 of Gull (1973), we find that the north-western component of the SNR is well into the adiabatic phase, and that the ambient density in this region is in the range $n_2 = 1 - 5$ cm^{-3}. This is consistent with the non-detection of OH, as the 1720 MHz maser line will be shock-excited into emission only at much higher densities (Elitzur 1976).

To summarise, we find that a number of observed properties of the SNR, particularly its bilateral appearance, faint radio PWN, asymmetric distribution about the pulsar and large size (and possibly also the slow optical expansion of filaments in RCW 89) can all be explained in a model in which an explosion of high energy or low mass occurred near the edge of a cavity elongated parallel to the Galactic Plane. The density of the cavity is $\sim$ 0.01 cm^{-3}: the south-eastern component of

the SNR has expanded rapidly across the cavity and has recently collided with the other side, while to the north-west, the shock has encountered denser (1–5 cm^{-3}) material, causing the SNR to decelerate significantly. To the north-east and south-west the shock is still propagating through the cavity and produces no observable emission.

While at low resolution G320.6–01.6 appears to be an extension of G320.4–01.2 (Milne et al. 1993), it is impossibly large to have expanded to its current size in 1700 yr. Its morphology and surface brightness are in complete contrast to those of G320.4–01.2, and we conclude that it is an unrelated older SNR along the same line of sight.

6.6 Conclusion

We have reported on an extensive set of ATCA observations of G320.4–01.2 and PSR B1509–58. The main results of this study are as follows.

1. The disparate radio components of G320.4–01.2 are all part of a single SNR at a distance of 5.2 ± 1.4 kpc and with an age of $\sim$1700 yr.
2. PSR B1509–58 is physically associated with G320.4–01.2. The pulsar emits twin jets or collimated outflows of relativistic particles, one of which interacts with the SNR in the form of radio/X-ray knots within RCW 89.
3. SNR G320.4–01.2 was formed in a supernova of high kinetic energy or low ejected mass ($E_{51}/M_{\mathrm{ej}} \sim 2$) which occurred near the edge of a low-density cavity.

A variety of further observations can support or refute these conclusions. For example, the cavity we propose may be visible in H I emission, while forthcoming *AXAF* observations will allow a detailed study of the physical conditions within the knots.

While we have offered answers to the questions outlined in Section 6.1, the picture is far from complete. First, we lack an understanding of the physical details of how the pulsar outflow is generating the peculiar knots in RCW 89, and of how the pulsar is interacting with the south-eastern half of the SNR. Similar interactions through outflows or jets have been proposed for a variety of other SNRs (Chapter 5 of this thesis; Roger et al. 1985; Manchester 1987), although an associated pulsar is yet to be detected in most cases. We have also side-stepped the whole issue of why PSR B1509–58 generates such large-scale jets and how general this situation might be. Certainly the theoretical expectation has been for some time that pulsars should generate collimated outflows (Benford 1984; Michel 1985; Sulkanen & Lovelace 1990). The Crab, Vela, PSR B1509–58 and possibly PSR B1951+32 (Hester 1998; J. J. Hester et al. 1998, in preparation) all show evidence that this is indeed the case, while various jet-like features have been proposed around other pulsars (Bell 1997). We must now therefore accept that spherically symmetric pulsar winds are a gross over-simplification.

Chapter 7

Conclusions

7.1 Summary of Results

In this thesis I have made sensitive high-resolution radio observations of several SNRs, and with these data have attempted to account for the radio morphology of these remnants. I have also demonstrated various techniques associated with synthesis imaging, including super-resolution, addition of single-dish data, determination of spatially resolved spectral indices, and extraction of rotation measures via multi-frequency synthesis.

There are many conclusions and implications from this work; these are all discussed in detail in each Chapter (and in the corresponding publications), and so will not be fully repeated here. Below I give a brief summary of the results which are directly relevant to the themes of this thesis.

The radio properties of SN 1987A can all be interpreted in terms of the SN shock encountering a denser component of the progenitor's stellar wind. The bilateral appearance of this young remnant demonstrates the same axis of symmetry as inferred for the progenitor system, and I interpret the radio morphology as resulting from a progenitor wind which is densest in the equatorial plane and/or elongated along its polar axis. Differences between the two hotspots may be due to a directional anisotropy in the SN explosion. At the current rate of expansion, the SNR will collide with the surrounding optical ring in 2006 ± 3.

I have demonstrated a highly significant alignment between the symmetry axes of 17 bilateral SNRs and the Galactic Plane, immediately ruling out intrinsic explanations for their appearance. Instead, I propose that SNRs appear bilateral as a result of the Galactic magnetic field. While both the basic "barrel" appearance and the observed alignment can be explained by a dependence of field compression or shock acceleration on the angle between the shock and the field, the different varieties of bilateral SNR can be better explained if the barrel shape predominantly results from expansion into elongated cavities in the ISM. To explain the alignment of bilateral SNRs with the Galactic Plane, I propose that these elongated cavities are formed by stellar wind-bubbles expanding into a well-ordered ambient field. Lo-

cal inhomogeneities in the magnetic field and/or ISM, as well as orientation effects, can explain why most SNRs do not appear bilateral.

ATCA observations of G296.8–00.3 show a complex multi-shelled SNR with an unusual rectangular strip running through its centre. Using H I absorption, I derive a distance to the SNR of ∼10 kpc, which implies a radius for the remnant of 17 pc. I argue that most supernova progenitors show anisotropic mass loss only late in their lives, and that any resulting asymmetric component of the CSM is far smaller than the extent of G296.8–00.3. Thus the double-ringed appearance of this SNR can only be explained by intrinsic effects if either the SNR can "remember" its environment from an earlier stage of its evolution, or more likely, if the main sequence wind of the progenitor is also anisotropic. The alternative, extrinsic, explanation is that the morphology of G296.8–00.3 is controlled by extrinsic factors, and that the two rings of emission (as well as the strip running through the middle) result from a break-out of the SN shock into an adjacent cavity.

SNR G309.2–00.6 is a near-circular shell but with two brightened and distorted arcs of emission on opposite sides. On the basis of this morphology I argue that it is a younger analogue of the W 50 / SS 433 system, and that its unusual appearance is a result of opposed jets or outflows from a central source. A jet-like feature and breaks in the shell can both be seen along the axis of proposed outflow, providing further support for this interpretation. The central source itself is not detected. The SNR may be interacting with the adjacent H II region RCW 80 through an extension of the proposed outflow beyond the SNR shell.

Based on a comparison between radio and X-ray observations, I argue that the two main radio components of G320.4–01.2 (MSH 15–5*2*) are a single SNR, which H I absorption indicates is at a distance of ∼5 kpc. A high-resolution correspondence between radio and X-rays argues that the pulsar is interacting with the SNR via an opposed pair of collimated outflows. One outflow is seen as an elongated X-ray feature surrounded by a highly polarised radio sheath, while the other interacts with the SNR in a ring of radio/X-ray knots within the optical nebula RCW 89. I conclude that SNR G320.4–01.2 and PSR B1509–58 are associated and have an age of $\lesssim$1700 yr. I propose that the SNR resulted from a high-energy or low-mass supernova which occurred near the edge of an elongated cavity. Such a model can account for the SNR's bilateral appearance, its large apparent age, the significant offset of the pulsar from the SNR's centre and the faintness of the pulsar-powered nebula at radio wavelengths.

7.2 Application to Other SNRs

SN 1987A is obviously a unique object, and its specific interpretation results from our detailed knowledge of the progenitor star, its environment, and the supernova event itself. However, it seems reasonable to infer from the results in Chapter 2 that the appearance of other remnants in the earliest stages of evolution (e.g. SN 1986J and SN 1993J) is similarly dominated by the structure of their progenitor wind, and

possibly also by anisotropies in the explosion.

Explanations for the bilateral morphology are numerous, and clearly there are at least some SNRs (e.g. SN 1987A) whose barrel appearance cannot be explained by expansion into elongated cavities as proposed in Chapter 3. Nevertheless, this interpretation most likely applies to the majority of such remnants. This is a major step forward in understanding SNR morphology: for the first time, a whole category of remnants, as well as differences between individual SNRs within this category, can be explained by a single, simple model.

Unlike bilateral SNRs, double-ringed SNRs are not an easily defined and distinct category. However, the radius of 17 pc derived for G296.8–00.3 is a typical size for a SNR. Thus the conclusions made in Chapter 4 on possible intrinsic and extrinsic explanations for this SNR's appearance can most probably be applied to other biannular SNRs of comparable extent.

While W 50 has long been the one clear case where outflows from a central source have a significant effect on the radio morphology of the associated SNR, our results in Chapters 5 and 6 on SNRs G309.2–00.6 and G320.4–01.2 provide convincing evidence that such behaviour is not restricted to this one system. Furthermore, the interaction between PSR B1509–58 and G320.4–01.2 demonstrates that isolated pulsars, as well as accreting binary systems, can generate such outflows. The observational consequences of such interactions are quite distinctive, and are not seen in most SNRs. Thus for now, this mechanism cannot be used to interpret whole categories of SNR morphology. However, as observations of high resolution and sensitivity are carried out on an increasing number of SNRs, it may become apparent that many one-sided or distorted SNRs owe their appearance to one or more outflows from a central source.

7.3 Intrinsic vs Extrinsic Effects

SN 1987A demonstrates that the morphology of a young type Ib/II SNR is completely dominated by intrinsic effects. The CSM around SN 1987A extends for several parsecs beyond the radio remnant, and it will be hundreds of years before the ambient ISM and magnetic field play any part in its evolution.

Our interpretation of bilateral SNRs is that their morphologies largely result from extrinsic effects. There is no reason to think that these SNRs were not influenced by their progenitor winds early in their evolution as is the case for SN 1987A. Hence we are left to conclude that these SNRs "forget" their early environment, and that effects such as the progenitor wind and supernova explosion no longer contribute to their appearance. I have argued that bilateral SNRs result from elongated cavities in the ISM. One can then extend this result to infer that other roughly shell-like SNRs, regardless of the details of their specific appearance, are shaped by the variety of structures into which they expand. I therefore conclude that extrinsic effects dictate the appearance of most SNRs. While the possibility of a SNR being "imprinted" by its CSM at an early age (as considered for G296.8–00.3) is an interesting one,

the mechanism by which this might occur is still unclear. Amongst mature SNRs, only for G296.5+10.0 has a strong case been made that this mechanism might be occurring (see Storey et al. 1992).

SNRs which are affected by outflows from a central source are an obvious exception to the claim that extrinsic effects dominate most SNRs, but systems in which there is good evidence for such an interaction appear to be in the minority. We actually expect most SNRs to be associated with a neutron star or other compact remnant: it is not clear whether these objects indeed interact only rarely with their surrounding shells, or if this paucity is better explained by observational selection effects such as orientation to the line of sight.

7.4 Future Outlook

ATCA studies of SN 1987A will continue. The improvement in resolution and frequency coverage offered by the approaching millimetre upgrade promises much greater insight into this unique object, while forthcoming missions such as *AXAF* and *NGST* will improve our understanding at other wavelengths of the ejecta and their environment. Some time in the next decade, the collision between the SN ejecta and dense surrounding material should result in an exciting new phase in the remnant's evolution.

The SNRs of which I have made individual studies can all benefit from a multi-wavelength approach. Radio, optical, X-ray and infrared images, along with spectral studies in H I emission and in various molecular lines, can trace a SNR's environment and allow us to study the effect on the SNR of its interaction with this surrounding material. Such an observational project is a significant undertaking and may only be appropriate for particular remnants.

The Galactic SNR population is still sorely in need of radio observations at resolution substantially better than $1'$. For example, features such as the "jet" in G309.2–00.6 and the X-ray / radio correspondences in G320.4–01.2 (all of which proved important in the interpretation of their associated SNRs) could not easily be discerned from the lower resolution images previously available. High resolution observations are also needed in hard X-rays — emission from many interesting SNRs is absorbed in the *ROSAT* energy band, and is detected but poorly resolved by *ASCA*. With the launches of *AXAF* and *XMM* this situation should soon be rectified.

As demonstrated for G296.8–00.3 and G320.4–01.2, an interpretation depends critically on knowing the distance to the remnant. However, distance estimates to most SNRs are in a parlous state, particularly at southerly declinations. Many of these SNRs are easily bright enough for H I absorption measurements, and a concerted programme of observations (with simultaneous high resolution imaging and polarimetry) would be of great benefit.

Our results on the statistics of bilateral SNRs demonstrate the value of accruing moderate resolution images of a large sample of SNRs. The significant improvements in resolution and sensitivity offered by the proposed VLA upgrade and the Square

Kilometre Array (SKA) will allow us to extend such studies to other galaxies, where the large-scale magnetic field and ISM structure are better defined than in the Milky Way, and whose SNRs are all at a known distance.

Finally, our understanding of SNR morphology and evolution should benefit from continued developments on the theoretical side. There is now considerable evidence for collimated outflows from pulsars and binary systems, and further consideration is needed of how such structures form and how they interact with their associated remnant. Many of the classic results on SNRs and their interaction with the ISM come from one- or two-dimensional simulations and analytical work. Computing capability has now reached the point where complicated three-dimensional treatments are feasible, allowing a more realistic and detailed comparison between theory and observations.

Bibliography

Ables, J. G. & Manchester, R. N., 1976, A&A, **50**, 177.

Amy, S. W. & Large, M. I., 1990, Proc. Astr. Soc. Aust., **8**, 308.

Amy, S. W. & Large, M. I., 1992, Aust. J. Phys., **45**, 105.

Anderson, M. C. & Rudnick, L., 1993, ApJ, **408**, 514.

Anderson, M., Rudnick, L., Leppik, P., Perley, R., & Braun, R., 1991, ApJ, **373**, 146.

Arendt, R. G., 1989, ApJS, **70**, 181.

Arendt, R. G., 1991, AJ, **101**, 2160.

Aumann, H. H., Fowler, J. W., & Melnyk, M., 1990, AJ, **99**, 1674.

Avedisova, V. S., 1997, Baltic Astronomy, **6**, 307.

Avedisova, V. S. & Palouš, J., 1989, Bull. Astron. Inst. Czechosl., **40**, 42.

Baade, W. & Zwicky, F., 1934, Proc. Nat. Acad. Sci., **20**, 254.

Bailes, M. & Johnston, S., 1993, in *Review of Radio Science 1990–1992,* edited by W. R. Stone, p. 677, Oxford University Press, Oxford.

Balick, B., 1987, AJ, **94**, 671.

Ball, L. & Kirk, J. G., 1992, ApJ, **396**, L39.

Ball, L. & Kirk, J. G., 1995, A&A, **303**, L57.

Ball, L., Campbell-Wilson, D., Crawford, D. F., & Turtle, A. J., 1995a, ApJ, **453**, 864.

Ball, L., Campbell-Wilson, D., & Staveley-Smith, L., 1995b, MNRAS, **276**, 944.

Barbon, R., Ciatti, F., & Rosino, L., 1979, A&A, **72**, 287.

Baring, M. G. & Harding, A. K., 1998, in *Proceedings of the Fourth Compton Symposium (AIP Conference Proceedings 410),* edited by C. D. Dermer, M. S. Strickman, & J. D. Kurfess, p. 638, American Institute of Physics, New York.

Bartel, N., Rupen, M. P., Shapiro, I. I., Preston, R. A., & Rius, A., 1991, Nature, **350**, 212.

Bartel, N., Bietenholz, M. F., Rupen, M. P., Conway, J. E., Beasley, A. J., Sramek, R. A., Romney, J. D., Titus, M. A., Graham, D. A., Altunin, V. I., Jones, D. L., Rius, A., Venturi, T., Umana, G., Francis, R. L., McCall, M. L., Richer, M. G., Stevenson, C. C., Weiler, K. W., Van Dyk, S. D., Panagia, N., Cannon, W. H., Popelar, J., & Davis, R. J., 1994, Nature, **368**, 610.

Bastian, T. S. & Bridle, A. H., 1996, *The VLA Development Plan,* NRAO, Socorro.

Beck, R., Brandenburg, A., Moss, D., Shukurov, A., & Sokoloff, D., 1996, ARA&A, **34**, 155.

Becker, R. H. & Helfand, D. J., 1985, Nature, **313**, 115.

Begelman, M. C., Sarazin, C. L., Hatchett, S. P., McKee, C. F., & Arons, J., 1980, ApJ, **238**, 722.

Belfort, P. & Crovisier, J., 1984, A&A, **136**, 368.

Bell, A. R., 1978, MNRAS, **182**, 443.

Bell, J. F., 1997, Vistas Astron., **41**, 87.

Benford, G., 1984, ApJ, **282**, 154.

Berkhuijsen, E. M., 1986, A&A, **166**, 257.

Berkhuijsen, E. M., 1988, A&A, **192**, 299.

Beuermann, K., Brandt, S., & Pietsch, W., 1994, A&A, **281**, L45.

Bhattacharya, D., 1990, JA&A, **11**, 125.

Bisnovatyi-Kogan, G. S., 1971, Sov. Astron., **14**, 652.

Bisnovatyi-Kogan, G. S. & Blinnikov, S. I., 1982, Sov. Astron., **26**, 530.

Bisnovatyi-Kogan, G. S. & Silich, S. A., 1995, Rev. Mod. Phys., **67**, 661.

Bisnovatyi-Kogan, G. S., Lozinskaya, T. A., & Silich, S. A., 1990, Ap&SS, **166**, 277.

Bjorkman, J. E. & Cassinelli, J. P., 1993, ApJ, **409**, 429.

Blandford, R. D. & Ostriker, J. P., 1978, ApJ, **221**, L29.

Blandford, R. D. & Romani, R. W., 1988, MNRAS, **234**, 57P.

Blondin, J. M., 1994, in *Circumstellar Media in the Late Stages of Stellar Evolution,* edited by R. E. S. Clegg, W. P. S. Meikle, & I. R. Stevens, p. 139, Cambridge University Press, Cambridge.

Blondin, J. M. & Lundqvist, P., 1993, ApJ, **405**, 337.

Blondin, J. M., Lundqvist, P., & Chevalier, R. A., 1996, ApJ, **472**, 257.

Bodenheimer, P. & Woosley, S. E., 1983, ApJ, **269**, 281.

Branch, D., 1986, ApJ, **300**, L51.

Braun, R. & Strom, R. G., 1986, A&A, **164**, 193.

Braun, R., Goss, W. M., & Lyne, A. G., 1989, ApJ, **340**, 355.

Brazier, K. T. S. & Becker, W., 1997, MNRAS, **284**, 335.

Brazier, K. T. S. & Johnston, S., 1999, MNRAS, in press (astro-ph/9803176).

Briggs, D. S., 1994, in *The Restoration of HST Images and Spectra II,* edited by R. J. Hanisch & R. L. White, p. 250, Space Telescope Science Institute, Baltimore.

Briggs, D. S., 1995, PhD thesis, New Mexico Institute of Mining and Technology.

Brighenti, F. & D'Ercole, A., 1994, MNRAS, **270**, 65.

Brown, G. E. & Bethe, H. A., 1994, ApJ, **423**, 659.

Burbidge, E. M., Burbidge, G. R., Fowler, R. A., & Hoyle, F., 1957, Rev. Mod. Phys., **29**, 547.

Burderi, L. & King, A. R., 1995, MNRAS, **276**, 1141.

Burn, D. & Bush, B., 1994, unpublished.

Burrows, D. N. & Guo, Z., 1994, ApJ, **421**, L19.

Burrows, C. J., Krist, J., Hester, J. J., Sahai, R., Trauger, J. T., Stapelfeldt, K. R., Gallagher, J. S., Ballester, G. E., Casertano, S., Clarke, J. T., Crisp, D., Evans, R. W., Griffiths, R. E., Hoessel, J. G., Holtzman, J. A., Mould, J. R., Scowen, P. A., Watson, A. M., & Westphal, J. A., 1995, ApJ, **452**, 680.

Burton, W. B., 1988, in *Galactic and Extragalactic Radio Astronomy (2nd edition),* edited by G. L. Verschuur & K. I. Kellermann, p. 295, Springer-Verlag, New York.

Buxton, M., Bessell, M., & Watson, B., 1998, Publ. Astr. Soc. Aust., **15**, 24.

Cameron, A. G. W., 1957, PASP, **69**, 201.

Cappellaro, E., Turatto, M., Tsvetkov, D. Y., Bartunov, O. S., Pollas, C., Evans, R., & Hamuy, M., 1997, A&A, **322**, 431.

Caraveo, P. A., 1993, ApJ, **415**, L111.

Caswell, J. L., 1977, Proc. Astr. Soc. Aust., **3**, 130.

Caswell, J. L. & Barnes, P. J., 1983, ApJ, **271**, L55.

Caswell, J. L. & Haynes, R. F., 1987, A&A, **171**, 261.

Caswell, J. L. & Lerche, I., 1979, MNRAS, **187**, 201.

Caswell, J. L., Clark, D. H., & Crawford, D. F., 1975a, Aust. J. Phys. Astr. Supp., **37**, 39.

Caswell, J. L., Murray, J. D., Roger, R. S., Cole, D. J., & Cooke, D. J., 1975b, A&A, **45**, 239.

Caswell, J. L., Milne, D. K., & Wellington, K. J., 1981, MNRAS, **195**, 89.

Caswell, J. L., Kesteven, M. J., Komesaroff, M. M., Haynes, R. F., Milne, D. K., Stewart, R. T., & Wilson, S. G., 1987, MNRAS, **225**, 329.

Caswell, J. L., Kesteven, M. J., Stewart, R. T., Milne, D. K., & Haynes, R. H., 1992, ApJ, **399**, L151.

Chen, K. & Ruderman, M., 1993, ApJ, **402**, 264.

Chevalier, R. A., 1977, in *Supernovae,* edited by D. N. Schramm, p. 53, Reidel, Dordrecht.

Chevalier, R. A., 1982a, ApJ, **258**, 790.

Chevalier, R. A., 1982b, ApJ, **259**, 302.

Chevalier, R. A., 1992a, Nature, **355**, 617.

Chevalier, R. A., 1992b, Nature, **360**, 628.

Chevalier, R. A. & Dwarkadas, V. V., 1995, ApJ, **452**, L45, (CD95).

Chevalier, R. A. & Fransson, C., 1987, Nature, **328**, 44.

Chevalier, R. A. & Liang, E. P., 1989, ApJ, **344**, 332.

Chevalier, R. A. & Luo, D., 1994, ApJ, **421**, 225.

Chin, Y.-N. & Huang, Y.-L., 1994, Nature, **371**, 398.

Ciotti, L. & D'Ercole, A., 1989, A&A, **215**, 347.

Clark, B. G., 1980, A&A, **89**, 377.

Clark, D. H., Caswell, J. L., & Green, A. J., 1975a, Aust. J. Phys. Astr. Supp., **37**, 1.

Clark, D. H., Parkinson, J. H., & Caswell, J. L., 1975b, Nature, **254**, 674.

Condon, J. J., Cotton, W. D., Greisen, E. W., Yin, Q. F., Perley, R. A., Taylor, G. B., & Broderick, J. J., 1998, AJ, **115**, 1693.

Cordes, J. M. & Chernoff, D. F., 1998, ApJ, **505**, 315.

Cornwell, T. J., 1988, A&A, **202**, 316.

Cornwell, T. J., Holdaway, M. A., & Uson, J. M., 1993, A&A, **271**, 697.

Cowsik, R. & Sarkar, S., 1984, MNRAS, **207**, 745.

Cox, D. P. & Smith, B. W., 1974, ApJ, **189**, L105.

Cram, L. & Ye, T., 1995, Aust. J. Phys., **48**, 113.

Cropper, M., Bailey, J., McCowage, J., Cannon, R. D., Couch, W. J., Walsh, J. R., Strade, J. O., & Freeman, F., 1988, MNRAS, **231**, 695.

Crotts, A. P. S. & Heathcote, S. R., 1991, Nature, **350**, 683.

Crotts, A. P. S., Kunkel, W. E., & Heathcote, S. R., 1995, ApJ, **438**, 724.

Day, G. A., Thomas, B. M., & Goss, W. M., 1969, Aust. J. Phys. Astr. Supp., **11**, 11.

Dickel, J. R. & Jones, E. M., 1985, ApJ, **288**, 707.

Dickel, J. R. & Milne, D. K., 1976, Aust. J. Phys., **29**, 435.

Dickel, J. R., Green, A., Ye, T., & Milne, D. K., 1996, AJ, **111**, 340.

Dickey, J. M., 1997, ApJ, **488**, 258.

Dohm-Palmer, R. C. & Jones, T. W., 1996, ApJ, **471**, 279.

Dopita, M. A., Mathewson, D. S., & Ford, V. L., 1977, ApJ, **214**, 179.

Downes, A. J. B., Pauls, T., & Salter, C. J., 1986, MNRAS, **218**, 393.

du Plessis, I., de Jager, O. C., Buchner, S., Nel, H. I., North, A. R., Raubenheimer, B. C., & van der Walt, D. J., 1995, ApJ, **453**, 746.

Dubner, G. M., Braun, R., Winkler, P. F., & Goss, W. M., 1991, AJ, **101**, 1466.

Dubner, G. M., Giacani, E. B., Goss, W. M., & Winkler, P. F., 1994, AJ, **108**, 207.

Dubner, G. M., Giacani, E. B., Goss, W. M., Moffett, D. A., & Holdaway, M., 1996, AJ, **111**, 1304.

Duffy, P., Ball, L., & Kirk, J. G., 1995, ApJ, **447**, 364, (DBK).

Duncan, A. R., Stewart, R. T., Haynes, R. F., & Jones, K. L., 1995, MNRAS, **277**, 36.

Duric, N., Viallefond, F., Goss, W. M., & van der Hulst, J. M., 1993, A&AS., **99**, 217.

Duyvendak, J. J. L., 1942, PASP, **54**, 91.

Elitzur, M., 1976, ApJ, **203**, 124.

Ellis, R. S. & Axon, D. J., 1978, Ap&SS, **54**, 425.

Elston, R. & Baum, S., 1987, AJ, **94**, 1633.

Emmering, R. T. & Chevalier, R. A., 1989, ApJ, **345**, 931.

Fabian, A. C., Brinkmann, W., & Stewart, G. C., 1983, in *Supernova Remnants and Their X-Ray Emission (IAU Symposium 101),* edited by J. Danziger & P. Gorenstein, p. 119, Reidel, Dordrecht.

Falle, S. A. & Garlick, A. R., 1982, MNRAS, **201**, 635.

Fender, R. P., Bell Burnell, S. J., & Waltman, E. B., 1997, Vistas Astron., **41**, 3.

Ferrière, K. M. & Zweibel, E. G., 1991, ApJ, **383**, 602.

Fich, M., Blitz, L., & Stark, A. A., 1989, ApJ, **342**, 272.

Frail, D. A., 1998, in *NATO Advanced Study Institute: "The Many Faces of Neutron Stars",* edited by A. Alpar, R. Buccheri, & J. van Paradijs, Kluwer, Dordrecht, in press.

Frail, D. A. & Kulkarni, S. R., 1991, Nature, **352**, 785.

Frail, D. A. & Moffett, D. A., 1993, ApJ, **408**, 637.

Frail, D. A. & Scharringhausen, B. R., 1997, ApJ, **480**, 364.

Frail, D. A. & Weisberg, J. M., 1990, AJ, **100**, 743.

Frail, D. A., Goss, W. M., & Slysh, V. I., 1994a, ApJ, **424**, L111.

Frail, D. A., Goss, W. M., & Whiteoak, J. B. Z., 1994b, ApJ, **437**, 781.

Frail, D. A., Kassim, N. E., & Weiler, K. W., 1994c, AJ, **107**, 1120.

Frail, D. A., Giacani, E. B., Goss, W. M., & Dubner, G., 1996, ApJ, **464**, L165.

Frail, D. A., Bietenholz, M. F., Markwardt, C. B., & Ögelman, H., 1997, ApJ, **475**, 224.

Frater, R. H., Brooks, J. W., & Whiteoak, J. B., 1992, J. Electr. Electron. Eng. Aust., **12**, 103.

Fulbright, M. S. & Reynolds, S. P., 1990, ApJ, **357**, 591, (FR90).

Gaensler, B. M., 1998, ApJ, **493**, 781.

Gaensler, B. M. & Johnston, S., 1995a, Publ. Astr. Soc. Aust., **12**, 76.

Gaensler, B. M. & Johnston, S., 1995b, MNRAS, **275**, L73.

Gaensler, B. M. & Johnston, S., 1995c, MNRAS, **277**, 1243.

Gaensler, B. M., Manchester, R. N., Staveley-Smith, L., Tzioumis, A. K., Reynolds, J. E., & Kesteven, M. J., 1997, ApJ, **479**, 845.

Gaensler, B. M., Manchester, R. N., & Green, A. J., 1998a, MNRAS, **296**, 813.

Gaensler, B. M., Green, A. J., & Manchester, R. N., 1998b, MNRAS, **299**, 812.

Gaensler, B. M., Brazier, K. T. S., Manchester, R. N., Johnston, S., & Green, A. J., 1999, MNRAS, in press (astro-ph/9901262).

García-Segura, G., Langer, N., & Mac Low, M.-M., 1996, A&A, **316**, 133.

Gardner, F. F. & Milne, D. K., 1965, AJ, **70**, 754.

Georgelin, Y. P. & Georgelin, Y. M., 1970, A&A, **6**, 349.

Georgelin, Y. M. & Georgelin, Y. P., 1976, A&A, **49**, 57.

Georgelin, Y. M., Boulesteix, J., Georgelin, Y. P., Le Coarer, E., & Marcelin, M., 1988, A&A, **205**, 95.

Golla, G. & Hummel, E., 1994, A&A, **284**, 777.

Gooch, R., 1996, in *Astronomical Data Analysis Software and Systems V,* edited by G. H. Jacoby & J. Barnes, p. 80, ASP Conference Series, Volume 101, San Francisco.

Gorenstein, P., Hughes, J. P., & Tucker, W. H., 1994, ApJ, **420**, L25.

Goss, W. M., Radhakrishnan, V., Brooks, J. W., & Murray, J. D., 1972, ApJS, **24**, 123.

Gottesman, S. T., Broderick, J. J., Brown, R. L., Balick, B., & Palmer, P., 1972, ApJ, **174**, 383.

Gotthelf, E. V., Petre, R., & Hwang, U., 1997, ApJ, **487**, L175.

Gray, A. D., 1994, MNRAS, **270**, 847.

Green, A. J., 1972, PhD thesis, University of Sydney.

Green, A. J., 1974, A&AS., **18**, 267.

Green, D. A., 1984, MNRAS, **209**, 449.

Green, D. A., 1990, AJ, **100**, 1927.

Green, D. A., 1996, *A Catalogue of Galactic Supernova Remnants (1996 August Version),* Mullard Radio Astronomy Observatory, Cambridge, (http://www.mrao.cam.ac.uk/surveys/snrs/).

Green, D. A. & Scheuer, P. A. G., 1992, MNRAS, **258**, 833.

Green, A. J., Frail, D. A., Goss, W. M., & Otrupcek, R., 1997, AJ, **114**, 2058.

Green, A. J., Cram, L. E., Large, M. I., & Ye, T., 1998, ApJS, in press.

Gregory, P. C. & Fahlman, G. G., 1983, in *Supernova Remnants and their X-ray Emission (IAU Symposium 101),* edited by J. Danziger & P. Gorenstein, p. 429, Reidel, Dordrecht.

Greisen, E. (ed.), 1996, *The* `AIPS` *Cookbook,* National Radio Astronomy Observatory, Charlottesville.

Greiveldinger, C., Caucino, S., Massaglia, S., Ögelman, H., & Trussoni, E., 1995, ApJ, **454**, 855.

Gull, S. F., 1973, MNRAS, **161**, 47.

Gull, S. F. & Daniell, G. J., 1978, Nature, **272**, 686.

Guo, Z. & Burrows, D. N., 1997, ApJ, **480**, L51.

Hanuschik, R. W. & Dachs, J., 1987, A&A, **182**, L29.

Harris, D. E., 1962, ApJ, **135**, 661.

Harrus, I. M., Hughes, J. P., & Helfand, D. J., 1996, ApJ, **464**, L161.

Hartquist, T. W., 1994, Ap&SS, **216**, 185.

Hasinger, G., Aschenbach, B., & Trümper, J., 1996, A&A, **312**, L9.

Haynes, R. F., Caswell, J. L., & Simons, L. W. J., 1979, Aust. J. Phys. Astr. Supp., **48**, 1.

Heiles, C., 1979, ApJ, **229**, 533.

Heiles, C., 1984, ApJS, **55**, 585.

Helfand, D. J. & Becker, R. H., 1987, ApJ, **314**, 203.

Herbst, W. & Assousa, G. E., 1977, ApJ, **217**, 473.

Hester, J. J., 1998, in *Neutron Stars and Pulsars: Thirty Years after the Discovery,* edited by N. Shibazaki, N. Kawai, S. Shibata, & T. Kifune, p. 431, Universal Academy Press, Tokyo.

Hester, J. J., Scowen, P. A., Sankrit, R., Burrows, C. J., Gallagher, III, J. S., Holtzman, J. A., Watson, A., Trauger, J. T., Ballester, G. E., Casertano, S., Clarke, J. T., Crisp, D., Evans, R. W., Griffiths, R. E., Hoessel, J. G., Krist, J., Lynds, R., Mould, J. R., O'Neill, Jr., E. J., Stapelfeldt, K. R., & Westphal, J. A., 1995, ApJ, **448**, 240.

Hewish, A., Bell, S. J., Pilkington, J. D. H., Scott, P. F., & Collins, R. A., 1968, Nature, **217**, 709.

Hill, E. R., 1968, Aust. J. Phys., **21**, 735.

Hirshfeld, A. & Sinnott, R. W., 1985, *Sky Catalogue 2000.0, Volume 2,* Cambridge University Press, Cambridge.

Hjellming, R. M., 1997, in *Accretion Phenomena and Related Outflows (IAU Colloquium 163),* edited by D. T. Wickramasinghe, L. Ferrario, & G. V. Bicknell, p. 53, Astronomical Society of the Pacific, San Francisco.

Hjellming, R. M. & Johnston, K. J., 1981a, ApJ, **246**, L141.

Hjellming, R. M. & Johnston, K. J., 1981b, Nature, **290**, 100.

Hjellming, R. M. & Johnston, K. J., 1986, in *The Physics of Accretion onto Compact Objects,* edited by K. O. Mason, M. G. Watson, & N. E. White, p. 287, Springer-Verlag, Berlin.

Hjellming, R. M. & Johnston, K. J., 1988, ApJ, **328**, 600.

Huang, S.-S. & Struve, O., 1954, Annales d'Astrophysique, **17**, 85.

Huang, Y.-L. & Thaddeus, P., 1985, ApJ, **295**, L13.

Hummel, E., Beck, R., & Dahlem, M., 1991, A&A, **248**, 23.

Humphreys, R. M., Strecker, D. W., & Ney, E. P., 1971, ApJ, **167**, L35.

Hwang, U. & Markert, T. H., 1994, ApJ, **431**, 819.

Igumenshchev, I. V., Tutokov, A. V., & Shustov, B. M., 1992, Sov. Astron., **36**, 241.

Insertis, F. M. & Rees, M. J., 1991, MNRAS, **252**, 82.

Iwamoto, K., Mazzalli, P. A., Nomoto, K., Umeda, H., Nakamura, T., Patat, F., Danziger, I. J., Young, T. R., Suzuki, T., T., S., Augusteijn, T., Doublier, V., Gonzalez, J.-F., Boehnhardt, H., Brewer, J., Hainaut, O. R., Lidman, C., Leibundgut, B., Cappellaro, E., Turatto, M., Galama, T. J., Vreeswijk, P., Kouveliotou, C., van Paradijs, J., Pian, E., & Frontera, F., 1998, Nature, **395**, 672.

Jackson, P. D., 1976, A&AS., **25**, 433.

Jakobsen, P., Albrecht, R., Barbieri, C., Blades, J. C., Boksenberg, A., Crane, P., Deharveng, J. M., Disney, M. J., Kamperman, T. M., King, I. R., Macchetto, F., Mackay, C. D., Paresce, F., Weigelt, G., Baxter, D., Greenfield, P., Jedrzejewski, R., Nota, A., Sparkes, W. B., Kirshner, R. P., & Panagia, N., 1991, ApJ, **369**, L63.

Johnston, S., Koribalski, B. S., Weisberg, J., & Wilson, W., 1996, MNRAS, **279**, 661.

Jokipii, J. R., 1987, ApJ, **313**, 842.

Joncas, G., Roger, R. S., & Dewdney, P. E., 1989, A&A, **219**, 303.

Jun, B.-I. & Norman, M. L., 1996, ApJ, **472**, 245.

Kafatos, M., Sofia, S., Bruhweiler, F., & Gull, S., 1980, ApJ, **242**, 294.

Kahn, F. D. & West, K. A., 1985, MNRAS, **212**, 837.

Karovska, M., Koechlin, L., Nisenson, P., Papaliolios, C., & Standley, C., 1989, in *Highlights of Astronomy, Volume 8,* edited by D. McNally, p. 193, Kluwer, Dordrecht.

Kaspi, V. M., 1996, in *Pulsars: Problems and Progress (IAU Colloquium 160),* edited by S. Johnston, M. A. Walker, & M. Bailes, p. 375, Astronomical Society of the Pacific, San Francisco.

Kaspi, V. M., 1998, in *Neutron Stars and Pulsars: Thirty Years after the Discovery,* edited by N. Shibazaki, N. Kawai, S. Shibata, & T. Kifune, p. 401, Universal Academy Press, Tokyo.

Kaspi, V. M., Manchester, R. N., Johnston, S., Lyne, A. G., & D'Amico, N., 1992, ApJ, **399**, L155.

Kaspi, V. M., Manchester, R. N., Siegman, B., Johnston, S., & Lyne, A. G., 1994, ApJ, **422**, L83.

Kaspi, V. M., Bailes, M., Manchester, R. N., Stappers, B. W., & Bell, J. F., 1996a, Nature, **381**, 584.

Kaspi, V. M., Manchester, R. N., Johnston, S., Lyne, A. G., & D'Amico, N., 1996b, AJ, **111**, 2028.

Kaspi, V. M., Bailes, M., Manchester, R. N., Stappers, B. W., Sandhu, J. S., Navarro, J., & D'Amico, N., 1997, ApJ, **485**, 820.

Kassim, N., Baum, S. A., & Weiler, K. W., 1991, ApJ, **374**, 212.

Katz, J. I., 1983, A&A, **128**, L1.

Keohane, J. W., Petre, R., Gotthelf, E. V., Ozaki, M., & K., K., 1997, ApJ, **484**, 350.

Kerr, F. J. & Lynden-Bell, D., 1986, MNRAS, **221**, 1023.

Kerr, F. J., Bowers, P. F., Jackson, P. D., & Kerr, M., 1986, A&AS., **66**, 373.

Kesteven, M. J. L., 1968, Aust. J. Phys., **21**, 369.

Kesteven, M. J. & Caswell, J. L., 1987, A&A, **183**, 118, (KC87).

Kesteven, M. J., Caswell, J. L., Roger, R. S., Milne, D. K., Haynes, R. F., & Wellington, K. J., 1987, Aust. J. Phys., **40**, 855.

Killeen, N. E. B., Bicknell, G. V., & Ekers, R. D., 1986, ApJ, **302**, 306.

Kirshner, R. P. & Kwan, J., 1974, ApJ, **193**, 27.

Komesaroff, M. M., 1966, Aust. J. Phys., **19**, 75.

Königl, A., 1982, ApJ, **261**, 115.

Koo, B.-C. & Moon, D.-S., 1997, ApJ, **475**, 194.

Koo, B.-C., Heiles, C., & Reach, W. T., 1992, ApJ, **390**, 108.

Kouveliotou, C., Dieters, S., Strohmayer, T., van Paradijs, J., Fishman, G. J., Meegan, C. A., Hurley, K., Kommers, J., Smith, I., Frail, D., & Murakami, T., 1998, Nature, **393**, 235.

Koyama, K., Petre, R., Gotthelf, E. V., Hwang, U., Matsura, M., Ozaki, M., & Holt, S. S., 1995, Nature, **378**, 255.

Lalitha, P., Salter, C. J., Mantovani, F., & Tomasi, P., 1984, A&A, **131**, 196.

Lamport, L., 1994, *LaTeX: A Document Preparation System,* Addison-Wesley, Reading, Massachusetts.

Landecker, T. L., Pineault, S., Routledge, D., & Vaneldik, J. F., 1982a, ApJ, **261**, L41.

Landecker, T. L., Roger, R. S., & Dewdney, P. E., 1982b, AJ, **87**, 1379.

Landecker, T. L., Pineault, S., Routledge, D., & Vaneldik, J. F., 1989, MNRAS, **237**, 277.

Large, M. I. & Vaughan, A. E., 1972, Nature Phys. Sci., **236**, 117.

Large, M. I., Vaughan, A. E., & Mills, B. Y., 1968, Nature, **220**, 340.

Large, M. I., Vaughan, A. E., & Wielebinski, R., 1969, Astrophys. Lett., **3**, 123.

Large, M. I., Campbell-Wilson, D., Cram, L. E., Davison, R. G., & Robertson, J. G., 1994, Proc. Astr. Soc. Aust., **11**, 44.

Leckband, J. A., Spangler, S. R., & Cairns, I. H., 1989, ApJ, **338**, 963.

Lloyd, H. M., O'Brien, T. J., & Kahn, F. D., 1995, MNRAS, **273**, L19.

Lortet, M. C., Georgelin, Y. P., & Georgelin, Y. M., 1987, A&A, **180**, 65.

Lozinskaya, T. A., 1988, in *Supernova Remnants and the Interstellar Medium (IAU Colloquium 101),* edited by R. S. Roger & T. L. Landecker, p. 95, Cambridge University Press, Cambridge.

Lundmark, K., 1921, PASP, **33**, 225.

Luo, D. & McCray, R., 1991, ApJ, **379**, 659.

Luo, D., McCray, R., & Slavin, J., 1994, ApJ, **430**, 264.

Lyne, A. G. & Lorimer, D. R., 1994, Nature, **369**, 127.

Malhotra, S., 1995, ApJ, **448**, 138.

Manchester, R. N., 1974, ApJ, **188**, 637.

Manchester, R. N., 1987, A&A, **171**, 205.

Manchester, R. N., 1988, Proc. Astr. Soc. Aust., **7**, 548.

Manchester, R. N., 1992, Nature, **356**, 660.

Manchester, R. N. & Durdin, J. M., 1983, in *Supernova Remnants and Their X-Ray Emission (IAU Symposium 101),* edited by J. Danziger & P. Gorenstein, p. 421, Reidel, Dordrecht.

Manchester, R. N. & Peterson, B. A., 1996, ApJ, **456**, L107.

Manchester, R. N. & Taylor, J. H., 1977, *Pulsars,* Freeman, San Francisco.

Manchester, R. N., Hamilton, P. A., & McCulloch, P. M., 1980, MNRAS, **192**, 153.

Manchester, R. N., Tuohy, I. R., & D'Amico, N., 1982, ApJ, **262**, L31.

Manchester, R. N., D'Amico, N., & Tuohy, I. R., 1985a, MNRAS, **212**, 975.

Manchester, R. N., Durdin, J. M., & Newton, L. M., 1985b, Nature, **313**, 374.

Manchester, R. N., Staveley-Smith, L., & Kesteven, M. J., 1993, ApJ, **411**, 756.

Marcaide, J. M., Alberdi, A., Ros, E., Diamond, P., Schmidt, B., Shapiro, I. I., Baath, L., Davis, R. J., de Bruyn, A. G., Elósegul, P., Guirado, J. C., Jones, D. L., Krichbaum, T. P., Mantovani, F., Preston, R. A., Ratner, M. I., Rius, A., Rogers, A. E. E., Schilizzi, R. T., Trigilio, C., Whitney, A. R., Witzel, A., & Zensus, A., 1995a, Nature, **373**, 44.

Marcaide, J. M., Alberdi, A., Ros, E., Diamond, P., Shapiro, I. I., Guirado, J. C., Jones, D. L., Krichbaum, T. P., Mantovani, F., Preston, R. A., Rius, A., Schilizzi, R. T., Trigilio, C., Whitney, A. R., & Witzel, A., 1995b, Science, **270**, 1475.

Markwardt, C. B. & Ögelman, H., 1995, Nature, **375**, 40.

Marsden, D., Blanco, P. R., Gruber, D. E., Heindl, W. A., Pelling, M. R., Peterson, L. E., Rothschild, R. E., Rots, A. H., Jahoda, K., & Macomb, D. J., 1997, ApJ, **491**, L39.

Martin, C. L. & Arnett, D., 1995, ApJ, **447**, 378.

Mathewson, D. S. & Ford, V. L., 1970, MRAS, **74**, 139.

Mayall, N. U. & Oort, J. H., 1942, PASP, **54**, 95.

McCray, R., 1993, ARA&A, **31**, 175.

McCray, R. & Lin, D. N. C., 1994, Nature, **369**, 378.

McCulloch, P. M., Hamilton, P. A., Manchester, R. N., & Ables, J. G., 1978, MNRAS, **183**, 645.

Méndez, M., Clocchiatti, A., Benvenuto, O. G., Feinstein, C., & Marraco, H. G., 1988, ApJ, **334**, 295.

Michel, F. C., 1985, ApJ, **288**, 138.

Michel, F. C., 1991, *Theory of Neutron Star Magnetospheres,* University of Chicago Press, Chicago.

Mills, B. Y., Slee, O. B., & Hill, E. R., 1960, Aust. J. Phys., **13**, 676.

Milne, D. K., 1970, Aust. J. Phys., **23**, 425.

Milne, D. K., 1972, Aust. J. Phys., **25**, 307.

Milne, D. K., 1995, MNRAS, **277**, 1435.

Milne, D. K. & Dickel, J. R., 1975, Aust. J. Phys., **28**, 209.

Milne, D. K. & Haynes, R. F., 1994, MNRAS, **270**, 106.

Milne, D. K., Wilson, T. L., Gardner, F. F., & Mezger, P. G., 1969, Astrophys. Lett., **4**, 121.

Milne, D. K., Goss, W. M., Haynes, R. F., Wellington, K. J., Caswell, J. L., & Skellern, D. J., 1979, MNRAS, **188**, 437.

Milne, D. K., Caswell, J. L., Kesteven, M. J., Haynes, R. F., & Roger, R. S., 1989, in *Supernova Shells and their Birth Events, Lecture Notes in Physics 316,* edited by W. Kundt, p. 98, Springer-Verlag, Berlin.

Milne, D. K., Caswell, J. L., & Haynes, R. F., 1993, MNRAS, **264**, 853.

Mineshige, S. & Shibata, K., 1990, ApJ, **355**, L47.

Mineshige, S., Shibata, K., & Shapiro, P. R., 1993, ApJ, **409**, 663.

Mirabel, I. F. & Rodriguez, L. F., 1994, Nature, **371**, 46.

Moffat, A. F. J. & Vogt, N., 1973, A&AS., **10**, 135.

Moffett, D. A. & Reynolds, S. P., 1994, ApJ, **425**, 668.

Murata, K. & Shibazaki, N., 1996, Proc. Astr. Soc. Jap., **48**, 819.

Muxlow, T. W. B., Pedlar, A., Wilkinson, P. N., Axon, D. J., Sanders, E. M., & de Bruyn, A. G., 1994, MNRAS, **266**, 455.

Muzzio, J. C., 1979, AJ, **84**, 639.

Napier, P. J., Thompson, A. R., & Ekers, R. D., 1983, Proc. I. E. E. E., **71**, 1295.

Narayan, R. & Nityananda, R., 1986, ARA&A, **24**, 127.

Narayan, R. & Ostriker, J. P., 1990, ApJ, **352**, 222.

Newton, L. M., Manchester, R. N., & Cooke, D. J., 1981, MNRAS, **194**, 841.

Nicholls, J. & Le Strange, E. T., 1995, ApJ, **443**, 638.

Nomoto, K., 1987, in *The Origin and Evolution of Neutron Stars (IAU Symposium 125),* edited by D. J. Helfand & J.-H. Huang, p. 281, Reidel, Dordrecht.

Norman, M. L., 1993, in *Back To The Galaxy: AIP Conference Proceedings 278,* edited by S. S. Holt & F. Verter, p. 552, American Institute of Physics, New York.

Norman, C. A. & Ikeuchi, S., 1989, ApJ, **345**, 372.

Normandeau, M., Taylor, A. R., & Dewdney, P. E., 1996, Nature, **380**, 687.

Öpik, E. J., 1953, Irish Astr. J., **2**, 219.

Owocki, S. P., Cranmer, S. R., & Blondin, J. M., 1994, ApJ, **424**, 887.

Pacholczyk, A. G., 1970, *Radio Astrophysics,* Freeman, San Francisco.

Pacini, F. & Salvati, M., 1973, ApJ, **186**, 249.

Panagia, N., Scuderi, S., Gilmozzi, R., Challis, P. M., Garnavich, P. M., & Kirshner, R. P., 1996, ApJ, **459**, L17.

Pearson, T. J., 1997, `PGPLOT` *Graphics Subroutine Library,* California Institute of Technology, Pasadena, (http://astro.caltech.edu/~tjp/pgplot/).

Pelling, R. M., Paciesas, W. S., Peterson, L. E., Makishima, K., Oda, M., Ogawara, Y., & Miyamoto, S., 1987, ApJ, **319**, 416.

Perley, R. A., 1989, in *Synthesis Imaging In Radio Astronomy,* edited by R. A. Perley, F. R. Schwab, & A. H. Bridle, p. 259, ASP Conference Series, Volume 6, San Francisco.

Perlmutter, S., Aldering, G., Della Valle, M., Deustua, S., Ellis, R. S., Fabbro, S., Fruchter, A., Goldhaber, G., A., G., Groom, D. E., Hook, I. M., Kim, A. G., Kim, M. Y., Knop, R. A., Lidman, C., McMahon, R. G., Nugent, P., Pain, R., Panagia, N., Pennypacker, C. R., Ruiz-Lapuente, P., Schaefer, B., & Walton, N., 1998, Nature, **391**, 51.

Petre, R., Becker, C. M., & Winkler, P. F., 1996, ApJ, **465**, L43.

Pineault, S. & Chastenay, P., 1990, MNRAS, **246**, 169.

Pineault, S., Pritchet, C. J., Landecker, T. L., Routledge, D., & Vaneldik, J. F., 1985, A&A, **151**, 52.

Pineault, S., Landecker, T. L., & Routledge, D., 1987, ApJ, **315**, 580.

Pineault, S., Landecker, T. L., Madore, B., & Gaumont-Guay, S., 1993, AJ, **105**, 1060.

Pineault, S., Landecker, T. L., Swerdlyk, C. M., & Reich, W., 1997, A&A, **324**, 1152.

Plait, P. C., Lundqvist, P., Chevalier, R. A., & Kirshner, R. P., 1995, ApJ, **439**, 730.

Podsiadlowski, P., Fabian, A. C., & Stevens, I. R., 1991, Nature, **354**, 43.

Pun, C. S. J., Kirshner, R. P., Challis, P., & Garnavich, P., 1995, BAAS, **27**, 1308.

Qiao, G. J., Manchester, R. N., Lyne, A. G., & Gould, D. M., 1995, MNRAS, **274**, 572.

Rand, R. J. & Kulkarni, S. R., 1989, ApJ, **343**, 760.

Ratkiewicz, R., Axford, W. I., & McKenzie, J. F., 1994, A&A, **291**, 935.

Reich, W., Füst, E., & Arnal, E. M., 1992, A&A, **256**, 214.

Reid, M. J. & Silverstein, E. M., 1990, ApJ, **361**, 483.

Reynolds, S. P., 1988, in *Galactic and Extragalactic Radio Astronomy (2nd edition),* edited by G. L. Verschuur & K. I. Kellermann, p. 439, Springer-Verlag, New York.

Reynolds, J. E., 1994, ATNF Technical Document Series, **39.3040**.

Reynolds, S. P., 1996, ApJ, **459**, L13.

Reynolds, S. P. & Chevalier, R. A., 1984, ApJ, **278**, 630.

Reynolds, S. P. & Fulbright, M. S., 1990, in *Proceedings of the 21st International Cosmic Ray Conference,* edited by R. J. Protheroe, p. 72, University of Adelaide, Adelaide.

Reynolds, S. P. & Gilmore, D. M., 1993, AJ, **106**, 272.

Reynolds, S. P. & Moffett, D. A., 1993, AJ, **105**, 2226.

Reynolds, J. E., Jauncey, D. L., Tzioumis, A. K., de Vegt, C., Zacharias, N., Perryman, M. A. C., van Leeuwen, F., King, E. A., McCulloch, P. M., Russell, J. L., Johnston, K. J., Hindsley, R., Malin, D. F., Argue, A. N., Manchester, R. N., Kesteven, M. J., White, G. L., & Jones, P. A., 1995, A&A, **304**, 116.

Rho, J., 1995, PhD thesis, University of Maryland.

Rho, J. & Petre, R., 1997, ApJ, **484**, 828.

Robertson, J. G., 1991, Aust. J. Phys., **44**, 729.

Rodgers, A. W., Campbell, C. T., & Whiteoak, J. B., 1960, MNRAS, **121**, 103.

Roger, R. S. & Costain, C. H., 1976, A&A, **51**, 151.

Roger, R. S., Milne, D. K., Kesteven, M. J., Haynes, R. F., & Wellington, K. J., 1985, Nature, **316**, 44.

Roger, R. S., Milne, D. K., Kesteven, M. J., Wellington, K. J., & Haynes, R. F., 1988, ApJ, **332**, 940.

Rosado, M., Ambrocio-Cruz, P., Le Coarer, E., & Marcelin, M., 1996, A&A, **315**, 243.

Różyczka, M. & Tenorio-Tagle, G., 1995, MNRAS, **274**, 1157.

Różyczka, M., Tenorio-Tagle, G., Franco, J., & Bodenheimer, P., 1993, MNRAS, **261**, 674.

Saken, J. M., Fesen, R. A., & Shull, J. M., 1992, ApJS, **81**, 715.

Sankrit, R. & Hester, J. J., 1997, ApJ, **491**, 796.

Saravanan, T. P., Deshpande, A. A., Wilson, W., Davies, E., McCulloch, P. M., & McConnell, D., 1996, MNRAS, **280**, 1027.

Sault, R. J., 1994, A&AS., **108**, 55.

Sault, R. J. & Killeen, N. E. B., 1998, *The* `MIRIAD` *User's Guide,* Australia Telescope National Facility, Sydney, (http://www.atnf.csiro.au/computing/software/miriad/).

Sault, R. J. & Wieringa, M. H., 1994, A&AS, **108**, 585.

Sault, R. J., Teuben, P. J., & Wright, M. C. H., 1995, in *Astronomical Data Analysis Software and Systems IV,* edited by R. Shaw, H. Payne, & J. Hayes, p. 433, ASP Conference Series, Volume 77, San Francisco.

Sault, R. J., Staveley-Smith, L., & Brouw, W. N., 1996, A&AS., **120**, 375.

Schaefer, B. E., 1993, PASP, **105**, 1238.

Sedov, L. I., 1959, *Similarity and Dimensional Methods in Mechanics,* Academic Press, New York.

Seward, F. D., 1990, ApJS, **73**, 781.

Seward, F. D. & Harnden Jr., F. R., 1982, ApJ, **256**, L45.

Seward, F. D. & Harnden Jr., F. R., 1994, ApJ, **421**, 581.

Seward, F., Grindlay, J., Seaquist, E., & Gilmore, W., 1980, Nature, **287**, 806.

Seward, F. D., Harnden Jr., F. R., Murdin, P., & Clark, D. H., 1983, ApJ, **267**, 698.

Seward, F. D., Harnden Jr., F. R., Szymkowiak, A., & Swank, J., 1984, ApJ, **281**, 650.

Shaver, P. A., 1969, Observatory, **89**, 227.

Shaver, P. A., 1982, A&A, **105**, 306.

Shaver, P. A. & Goss, W. M., 1970a, Aust. J. Phys. Astr. Supp., **14**, 77.

Shaver, P. A. & Goss, W. M., 1970b, Aust. J. Phys. Astr. Supp., **14**, 133.

Shaver, P. A., Radhakrishnan, V., Anantharamaiah, K. R., Retallack, D. S., Wamsteker, W., & Danks, A. C., 1982, A&A, **106**, 105.

Shaver, P. A., Salter, C. J., Patnaik, A. R., van Gorkom, J. H., & Hunt, G. C., 1985, Nature, **313**, 113.

Shklovskii, I. S., 1970, Sov. Astron., **13**, 562.

Shull, J. M., Fesen, R. A., & Saken, J. M., 1989, ApJ, **346**, 860.

Siegman, B. C., Manchester, R. N., & Durdin, J. M., 1993, MNRAS, **262**, 449.

Slettebak, A., 1949, ApJ, **110**, 498.

Smith, A., 1988, in *Supernova Remnants and the Interstellar Medium (IAU Colloquium 101),* edited by R. S. Roger & T. L. Landecker, p. 119, Cambridge University Press, Cambridge.

Smith, L. J., 1994, in *Circumstellar Media in the Late Stages of Stellar Evolution,* edited by R. E. S. Clegg, W. P. S. Meikle, & I. R. Stevens, p. 64, Cambridge University Press, Cambridge.

Sofue, Y. & Fujimoto, M., 1983, ApJ, **265**, 722.

Sofue, Y., Fujimoto, M., & Wielebinski, R., 1986, ARA&A, **24**, 459.

Spyromilio, J., 1994, MNRAS, **266**, L61.

Srinivasan, G., Dwarakanath, K. S., & Radhakrishnan, V., 1982, Curr. Sci., **51**, 596.

Srinivasan, G., Bhattacharya, D., & Dwarakanath, K. S., 1984, JA&A, **5**, 403.

Staelin, D. H. & Reifenstein, III, E. C., 1968, Science, **162**, 1481.

Stathakis, R. A., 1996, PhD thesis, University of Sydney.

Staveley-Smith, L., Manchester, R. N., Kesteven, M. J., Campbell-Wilson, D., Crawford, D. F., Turtle, A. J., Reynolds, J. E., Tzioumis, A. K., Killeen, N. E. B., & Jauncey, D. L., 1992, Nature, **355**, 147, (Paper S1).

Staveley-Smith, L., Manchester, R. N., Kesteven, M. J., Tzioumis, A. K., & Reynolds, J. E., 1993a, Proc. Astr. Soc. Aust., **10**, 331, (Paper S2).

Staveley-Smith, L., Briggs, D. S., Rowe, A. C. H., Manchester, R. N., Reynolds, J. E., Tzioumis, A. K., & Kesteven, M. J., 1993b, Nature, **366**, 136, (Paper S3).

Staveley-Smith, L., Manchester, R. N., Tzioumis, A. K., Reynolds, J. E., & Briggs, D. S., 1996, in *Supernovae and Supernova Remnants (IAU Colloquium 145),* edited by R. McCray & Z. Wang, p. 309, Cambridge University Press, Cambridge, (Paper S4).

Stewart, R. T., Caswell, J. L., Haynes, R. F., & Nelson, G. J., 1993, MNRAS, **261**, 593.

Stone, J. M. & Norman, M. L., 1992, ApJ, **389**, 297.

Storey, M. C. & Manchester, R. N., 1987, Nature, **329**, 421.

Storey, M. C., Staveley-Smith, L., Manchester, R. N., & Kesteven, M. J., 1992, A&A, **265**, 752.

Strom, R. G., 1994, MNRAS, **268**, L5.

Sulkanen, M. E. & Lovelace, R. V. E., 1990, ApJ, **350**, 732.

Suzuki, T., Shigeyama, T., & Nomoto, K., 1993, A&A, **274**, 883.

Tammann, G. A., Löffler, W., & Schröder, A., 1994, ApJS, **92**, 487.

Tamura, K., Kawai, N., Yoshida, A., & Brinkmann, W., 1996, Proc. Astr. Soc. Jap., **48**, L33.

Taylor, J. H. & Cordes, J. M., 1993, ApJ, **411**, 674.

Taylor, J. H. & Stinebring, D. R., 1986, ARA&A, **24**, 285.

Taylor, J. H., Manchester, R. N., & Lyne, A. G., 1993, ApJS, **88**, 529.

Tenorio-Tagle, G., Bodenheimer, P., & Yorke, H. W., 1985, A&A, **145**, 70.

Tenorio-Tagle, G., Bodenheimer, P., Franco, J., & Różyczka, M., 1990, MNRAS, **244**, 563.

Tenorio-Tagle, G., Różyczka, M., Franco, J., & Bodenheimer, P., 1991, MNRAS, **251**, 318.

Thomas, B. M. & Day, G. A., 1969, Aust. J. Phys. Astr. Supp., **11**, 3.

Thornton, K., Gaudlitz, M., Janka, H.-T., & Steinmetz, M., 1998, ApJ, **500**, 95.

Thorsett, S. E., 1992, Nature, **356**, 690.

Tomisaka, K., 1990, ApJ, **361**, L5.

Tomisaka, K., 1992, Proc. Astr. Soc. Jap., **44**, 177.

Trussoni, E., Massaglia, S., Caucino, S., Brinkmann, W., & Aschenbach, B., 1996, A&A, **306**, 581.

Tuohy, I. R., Clark, D. H., & Burton, W. B., 1982, ApJ, **260**, L65.

Turtle, A. J., Pugh, J. F., Kenderdine, S., & Pauliny-Toth, I. I. K., 1962, MNRAS, **124**, 297.

Turtle, A. J., Campbell-Wilson, D., Bunton, J. D., Jauncey, D. L., Kesteven, M. J., Manchester, R. N., Norris, R. P., Storey, M. C., & Reynolds, J. E., 1987, Nature, **327**, 38.

Ulmer, M. P., Matz, S. M., Wilson, R. B., Finger, M. J., Hagedon, K. S., Grabelsky, D. A., Grove, J. E., Johnson, W. N., Kinzer, R. L., Kurfess, J. D., Purcell, W. R., Strickman, M. S., Kaspi, V. M., Johnston, S., Manchester, R. N., Lyne, A. G., & D'Amico, N., 1993, ApJ, **417**, 738.

Utrobin, V. P., Chugai, N. N., & Andronova, A. A., 1995, A&A, **295**, 129.

van den Bergh, S. & Kamper, K. W., 1984, ApJ, **280**, L51.

van den Bergh, S. & Tammann, G. A., 1991, ARA&A, **29**, 363.

van den Bergh, S., McClure, R. D., & Evans, R., 1987, ApJ, **323**, 44.

van der Laan, H., 1962a, MNRAS, **124**, 125.

van der Laan, H., 1962b, MNRAS, **124**, 179.

van Langevelde, H. J. & Cotton, W. D., 1990, A&A, **239**, L5.

van Ommen, T. D., D'Alesssandro, F. D., Hamilton, P. A., & McCulloch, P. M., 1997, MNRAS, **287**, 307.

Vermeulen, R. C., Schilizzi, R. T., Spencer, R. E., Romney, J. D., & Fejes, I., 1993, A&A, **270**, 177.

Vivekanand, M. & Narayan, R., 1981, JA&A, **2**, 315.

Walker, A. R. & Suntzeff, N. B., 1990, PASP, **102**, 131.

Wallace, B. J., Landecker, T. L., Taylor, A. R., & Pineault, S., 1997, A&A, **317**, 212.

Wang, L. & Mazzali, P. A., 1992, Nature, **355**, 58.

Watson, M. G., Willingale, R., Grindlay, J. E., & Seward, F. D., 1983, ApJ, **273**, 688.

Weaver, R., McCray, R., Castor, J., Shapiro, P., & Moore, R., 1977, ApJ, **218**, 377.

Weiler, K. W. & Sramek, R. A., 1988, ARA&A, **26**, 295.

Weiler, K. W., Sramek, R. A., Panagia, N., van der Hulst, J. M., & Salvati, M., 1986, ApJ, **301**, 790.

Weiler, K. W., Van Dyk, S. D., Sramek, R. A., & Panagia, N., 1996, in *Supernovae and Supernova Remnants (IAU Colloquium 145),* edited by R. McCray & Z. Wang, p. 283, Cambridge University Press, Cambridge.

Wheeler, J. C., Mazurek, T. J., & Sivaramakrishnan, A., 1980, ApJ, **237**, 781.

White, N. E., Giommi, P., & Angelini, L., 1994a, BAAS, **185**, 4111.

White, N. E., Giommi, P., & Angelini, L., 1994b. IAU Circ. No. 6100.

Whiteoak, J. B. & Gardner, F. F., 1968, ApJ, **154**, 807.

Whiteoak, J. B. Z. & Green, A. J., 1996, A&AS., **118**, 329, (WG96; http://www.physics.usyd.edu.au/astrop/wg96cat).

Wieringa, M. H., de Bruyn, A. G., Jansen, D., Brouw, W. N., & Katgert, P., 1993, A&A, **268**, 215.

Wilkinson, P. N. & de Bruyn, A. G., 1990, MNRAS, **242**, 529.

Williams, R. M., Chu, Y.-H., Dickel, J. R., Beyer, R., Petre, R., Smith, R. C., & Milne, D. K., 1997, ApJ, **480**, 618.

Willingale, R., West, R. G., Pye, J. P., & Stewart, G. C., 1996, MNRAS, **278**, 749.

Wilner, D. J., Reynolds, S. P., & Moffett, D. A., 1998, AJ, **115**, 247.

Wilson, R. B., Finger, M. H., Fishman, G. J., Meegan, C. A., & Paciesas, W. S., 1992. IAU Circ. No. 5429.

Wolszczan, A., Cordes, J. M., Dewey, R. J., & Blaskiewicz, M., 1988. IAU Circ. No. 4694.

Woltjer, L., 1972, ARA&A, **10**, 129.

Woltjer, L., Salvati, M., Pacini, F., & Bandiera, R., 1997, A&A, **325**, 295.

Woosley, S. E. & Weaver, T. A., 1986, ARA&A, **24**, 205.

Woosley, S. E., Langer, N., & Weaver, T. A., 1993, ApJ, **411**, 823.

Woosley, S. E., Langer, N., & Weaver, T. A., 1995, ApJ, **448**, 315.

Woosley, S. E., Eastman, R. G., & Schmidt, B. P., 1998, ApJ, submitted (astro-ph/9806299).

Yamauchi, S., Kawai, N., & Aoki, T., 1994, Proc. Astr. Soc. Jap., **46**, L109.

Ye, T., Turtle, A. J., & Kennicutt Jr., R. C., 1991, MNRAS, **249**, 722.

Zhang, Q.-C., Wang, Z., & Chen, Y., 1996, ApJ, **466**, 808.